



Investigation of the Influence of Correlations on  
Photovoltaic Energy Conversion in Hot Polaron Solar  
Cells

**Dissertation**

zur Erlangung des mathematisch-naturwissenschaftlichen Doktorgrades  
'Doctor rerum naturalium'  
der Georg-August-Universität  
im Promotionsstudiengang ProPhys  
der Georg-August University School of Science (GAUSS)

vorgelegt von

**Birte Kressdorf**  
aus Hannover

Göttingen, 2022

### **Betreuungsausschuss**

Prof. Dr. Christian Jooß, Institut für Materialphysik

Prof. Dr. Michael Seibt, IV. Physikalisches Institut

Prof. Dr. Claus Ropers, IV. Physikalisches Institut

### **Mitglieder der Prüfungskommission**

Referent: Prof. Dr. Christian Jooß, Institut für Materialphysik

Korreferent: Prof. Dr. Michael Seibt, IV. Physikalisches Institut

### **Weitere Mitglieder der Prüfungskommission**

Prof. Dr. Peter E. Blöchl, Institut für Theoretische Physik

Prof. Dr. Hans-Christian Hofsäss, II. Physikalisches Institut

Prof. Dr. Vasily Moshnyaga, I. Physikalisches Institut

Prof. Dr. Martin Wenderoth, IV. Physikalisches Institut

**Tag der mündlichen Prüfung: 14.03.2022**

# Contents

<b>1</b>	<b>Introduction</b>	<b>3</b>
1.1	Third-generation Photovoltaics . . . . .	4
1.2	Hot Carrier Aspects in Metal Halide Perovskites . . . . .	8
1.3	Manganite Perovskite for Hot Polaron Solar Cells . . . . .	10
1.4	Thesis Objectives and Outline . . . . .	12
<b>2</b>	<b>Theoretical Background</b>	<b>15</b>
2.1	Thermodynamic Approach to Photovoltaic Energy Conversion . . . . .	15
2.1.1	Detailed Balance and the SQ Limit . . . . .	15
2.1.2	The Solar Cell as a Heat Engine . . . . .	19
2.2	Structural and Electronic Properties . . . . .	22
2.2.1	3D Manganite System: $\text{Pr}_{1-x}\text{Ca}_x\text{MnO}_3$ . . . . .	22
2.2.2	2D Manganite RP System: $\text{Pr}_{0.5}\text{Ca}_{1.5}\text{MnO}_4$ . . . . .	25
2.3	Tuning of Interface Properties in Manganite Heterojunctions . . . . .	26
<b>3</b>	<b>Experimental Methods</b>	<b>31</b>
<b>4</b>	<b>Room-temperature Hot-polaron Photovoltaics in the Charge-ordered State of a Layered Perovskite Oxide Heterojunction</b>	<b>37</b>
<b>5</b>	<b>Orbital-order Phase Transition in <math>\text{Pr}_{1-x}\text{Ca}_x\text{MnO}_3</math> probed by Photovoltaics</b>	<b>47</b>
<b>6</b>	<b>Power Density and Spectral Photovoltaic Response in a Hot Polaron Solar Cell</b>	<b>69</b>
<b>7</b>	<b>General Discussion and Summary</b>	<b>93</b>
	<b>Appendix A Supplemental Material for Room-temperature Hot-polaron Photovoltaics in the Charge-ordered State of a Layered Perovskite Oxide Heterojunction</b>	<b>101</b>

<b>Appendix B Supplemental Material for Orbital-order Phase Transition in <math>\text{Pr}_{1-x}\text{Ca}_x\text{MnO}_3</math> probed by Photovoltaics</b>	<b>107</b>
<b>Appendix C Supplemental Material for Power Density and Spectral Photovoltaic Response in a Hot Polaron Solar Cell</b>	<b>119</b>
<b>Bibliography</b>	<b>125</b>
<b>Author Contribution</b>	<b>137</b>
<b>List of abbreviations</b>	<b>141</b>
<b>Danksagung</b>	<b>143</b>

# Chapter 1

## Introduction

In 1839, Edmond Becquerel was, reportedly, the first person to discover the photovoltaic process of converting light into electricity on a device consisting of silver chloride in an electrolyte [1]. The first solar cell, composed of selenium with gold electrodes, was developed by Charles Fritts in 1883. More than half a century later, in 1954, the first silicon-based solar cell was built by Chapin, Fuller and Pearson of Bell Laboratories [2, 3]. Since then, solar cell research and device development has progressed significantly and the solar cell has been established as a generally available and commercially recognized renewable energy conversion system [4]. In 2019, around 3 % of global electricity generation was provided by solar cell systems [5].

Most solar cells presently available on the market are *p-n* junctions composed of silicon or gallium arsenide, which are accordingly referred to as **first-generation** solar cells or **second-generation** solar cells, when thin-film technology is incorporated to lower material costs [6]. For thin-film solar cells, a variety of semiconductor materials, such as *CdS*,  $\alpha$ -*Si*, *CuInSe<sub>2</sub>*, *CdTe*, are utilized [7, 8].

Rising energy demands worldwide, dwindling resources and the negative consequences of fossil fuels on the environment call for further advancement in renewable energy sources, including fundamental research. In addition to other promising concepts such as wind energy, the solar cell, due to the abundance of solar radiation and, therefore, its capacity to meet the global energy demand, remains a viable alternative energy source and an important research topic.

In recent decades the **third-generation** of solar cells, with new concepts and working principles, including new materials, such as organic halide perovskites and novel cell designs, such as nanostructures, has emerged [9–11].

## 1.1 Third-generation Photovoltaics

Before introducing different concepts of third-generation solar cells, it is necessary to understand both the working mechanism and fundamental loss mechanism in conventional semiconductor single-junction devices. The fundamental steps involved in conversion of optical excitation into electricity are:

- I) absorption of an incident photon with energy  $E_{ph}$ ;
- II) generation of an electron–hole pair (charge carriers);
- III) charge separation utilizing a space charge region;
- IV) collection of charges at the contacts.

In this regard, incident photons with energies smaller than the band gap  $E_g$  are not absorbed and pass through the material. In contrast, photogenerated electron–hole pairs with energies higher than the band edge rapidly (on a picosecond time scale) relax towards the band edge, where they accumulate [12, 13]. The surplus of energy is converted into heat until thermal equilibrium with the lattice is established. At the band edge, the charge carriers exist in a meta-stable, long-living state and can either be extracted from the device as photocurrent or recombine. The relaxation process of charge carriers to the band edge is denoted as thermalization or cooling down and charge carriers with energies above the band gap value, i.e., higher kinetic energies than the lattice thermal energy, are referred to as **hot carriers**.

In semiconductors, the relaxation process of the hot charge carriers to the band edge is a multi-step process [14–16]. Within the first 100 fs, the carrier–carrier scattering results in a Boltzmann distribution of the hot carriers with a single fixed temperature above the lattice temperature [17]. Next, the charge carriers scatter inelastically with phonons, thereby predominantly emitting optical phonons and the now-overpopulated optical phonons decay to low-energy acoustic phonons. In the final step, the acoustic phonons decay and on the macroscopic scale, the entire process manifests through heat dissipation into the environment.

In summary, fundamental limitations for this operating principle in a single-junction solar cell are given by the two major intrinsic loss mechanisms: a) inability to absorb photons with energies below the band gap ( $E_{ph} < E_g$ ) and b) thermalization of photon energies exceeding the band gap ( $E_{ph} > E_g$ ) [18]. Together, they are responsible for more than half the loss of the incident solar energy for energy conversion [19]. Based on these

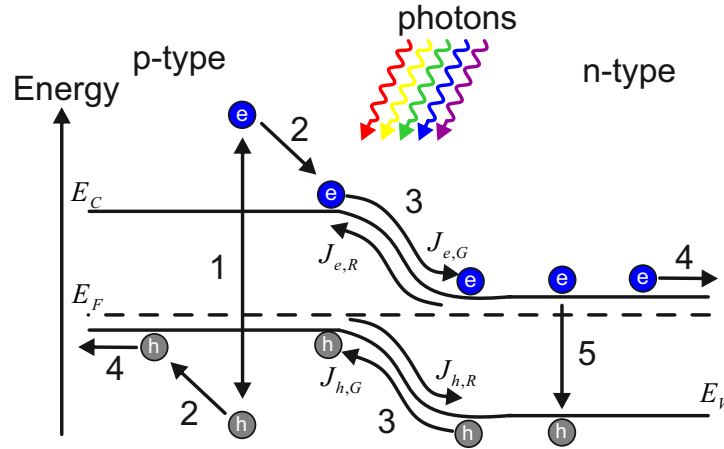


Figure 1.1: Schematic representation of the fundamental loss mechanism and steps for photovoltaic energy conversion in conventional semiconductors: (1) **excitation** of electron–hole pair through absorption of incident photon; (2) **thermalization** of the excited charge carriers to the band edge; (3) **transport** of the charge carriers across the interface (with generation current density  $J_G$  and recombination current density  $J_R$ ); (4) **extraction** of charge carriers through contacts or (5) **recombination** of the electron–hole pair.

working principles, W. Shockley and H. Queisser were the first to calculate a theoretical thermodynamic limit of energy conversion, the Shockley–Queisser (SQ) limit [20]. Within a detailed balance model, the process of incident photon absorption is in thermodynamic equilibrium with the reverse process of radiative recombination. A maximum efficiency of 30% was calculated for a silicon-based device with a 1.1 eV band gap [20]. In a real solar cell, additional extrinsic loss contributions such as recombination due to impurities and serial and parallel resistances add up to the overall higher efficiency loss.

The development of third-generation solar cells aims to produce highly efficient cells exceeding the SQ limit through new device and material design strategies. To reduce the fundamental losses, different strategies and cell concepts are being pursued [9–11]:

- **Tandem solar cells** increase the number of available energy levels [21]. For these systems, two or more cells with different fixed band gaps are stacked on top of each other and each cell converts only a narrow range of the incident solar spectrum, according to its respective band gap. The material with the largest band gap is stacked on the top and, therefore, ensures that the congruent cells receive a filtered spectrum. This strategy has been successfully applied for a variety of semiconductor and organic solar cells such as double or triple tandem cells composed



of *GaInP/GaAs/Ge* [22, 23].

- **Multiband or intermediate-level cells** exploit the same principle as the tandem cells but are applied to a single cell by strategic incorporation of specific impurities, adding one or more fixed energy levels within the band gap [24–26]. This allows for energy conversion of photons in these additional intermediate impurity states in parallel with the normal band gap conversion.
- For **carrier multiplication**, an increase in numbers of extracted charge carriers is pursued through various approaches. In **impact ionization** or **multiple exciton generation** in nanostructured semiconductors, a single high-energy photon generates more than one charge carrier pair [27–29]. Optical processes for carrier multiplication include **upconversion**, where several photons with energies below the band gap interact and generate one photon with energies above the band gap, as well as **downconversion**, where one high-energy photon is converted into multiple lower-energy photons [30, 31].
- The term **thermophotonic device** is used to describe two optically coupled and thermally isolated photovoltaic devices that are facing each other [6]. As one of the devices is heated to a higher temperature, it generates light through band-to-band recombination and thus serves as an illumination source.

The final strategy presented, which is also a topic in this thesis, are **hot carrier solar cells** (see Fig. 1.2) [32, 33]. The concept for hot carrier cells was first proposed by R. T. Ross and A. J. Nozik in 1982 and consists of two principal aspects [12]:

- I) preventing hot charge carriers from thermalization to the band edge by slowing down or eliminating charge carrier cooling;
- II) fast extraction of hot carriers prior to thermalization process.

If the cooling-down process is slowed down sufficiently, the now long-living hot carriers can be extracted without losing their excess energy. In conventional solar cells excited charge carriers with sufficiently long lifetimes are generated as a result of the existence of the band gap. If other mechanisms for stabilization are in action, no band gap is required for the hot charge carrier solar cells. Thus, the benefit of hot carrier solar cells is that they are capable of utilizing the entire energy of the photons or rather the full solar spectrum. Therefore, energy conversion in these systems is only limited by the Carnot efficiency

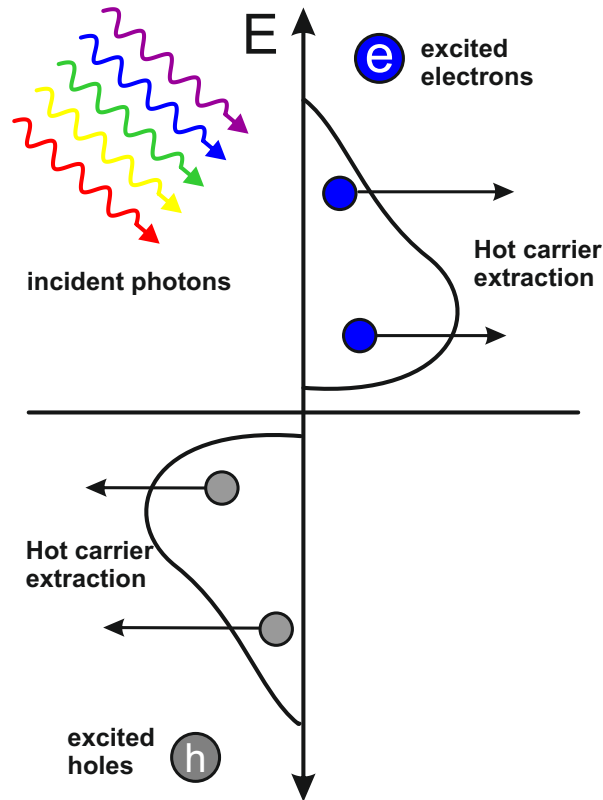


Figure 1.2: Schematic illustration of the concept for a hot charge carrier solar cell.

of thermodynamics [18]. Detailed balance calculations suggest that efficiencies up to 66 % (unconcentrated sunlight) and 85 % (concentrated sunlight) can be achieved [12, 21]. Research focuses mainly on one of the two aforementioned aspects at a time and, while many promising research findings have been discovered, the hot charge carrier cell are not yet used in applications.

In the **phonon bottleneck** strategy, the interaction of the charge carriers with phonons is suppressed at some point in the decay cascade in order to prevent the fast thermalization to the band edge [34–37]. Additionally, as carrier cooling is suppressed, overpopulation of hot phonons can build up and these phonons re-emit their energy back to the charge carriers.

The material requirements are small band gaps for broad absorption, high carrier mobility and weak electron–phonon scattering to allow for long hot carrier lifetimes [13, 38]. The biggest challenge for the material properties is given by the last condition. For example, in most semiconductor, efficient electron–phonon scattering is an intrinsic characteristic.

This is, for example, relevant for polar semiconductors with Fröhlich interaction, which features intraband cooling by emission of longitudinal optical phonons with momentum and energy conservation on timescales of picoseconds or less [19]. However, as a second step, these optical photons decay into acoustic phonons through the anharmonic or Klemens mechanism, where one optical photon decays into two acoustic photons each with almost half of the energy of the optical phonon and opposite wave vectors [39].

At this point the phonon bottleneck principle could come into play, since this step can, for example, be suppressed in materials with a phonon scattering channel, in which the phonon band gap is in the range of the acoustic phonons, this around half the energy of the optical phonons. Additionally, to slow down the cooling process, the optical phonons can re-scatter with electrons, which leads to a regaining of energy. This concept has been investigated and published for binary semiconductors  $InN$ ,  $BiN$ , quantum dots or multiple quantum wells, where thermalization times of a few hundred picoseconds (two orders of magnitude above values for conventional semiconductors) have been observed [40–45].

The second requirement for hot carrier solar cells is to achieve fast carrier extraction through, e.g., energy-selective contacts [12, 13]. As charge carriers are transported to non-energy-selective contacts for extraction, heat leakage occurs [46]. The contacts require large conductance and a specific narrow and energy-selective width [47, 48].

In addition to long-living states at the band edge of semiconductors, nanostructure devices like semiconductor quantum dots, as well as halide perovskites, can utilize long-living hot carriers. Another strategy is investigated in the material group of metallic nanostructures. Here, the utilization of plasmonic resonance is being developed through surface plasmon resonance [49]. When the frequency of incident light matches the intrinsic oscillation of free electrons within the metallic nanostructures, the generation of hot charge is one of the energy-releasing mechanisms as the plasmons disphase.

## 1.2 Hot Carrier Aspects in Metal Halide Perovskites

One prime candidate for exceeding the SQ limit is the metal halide perovskite [32, 33, 50]. Within this material class, energy conversion could be enhanced through utilization of hot carriers additionally to conventional working mechanisms, by slowing down the carrier cooling process. The model system and fundamental investigation of manganite/titanite heterojunctions within this thesis present an interesting analogue for research on metal halide perovskite—which is closer to commercial production—due to the common aspect of long-living hot carrier states in combination with correlation effects.

The use of metal halide perovskites in photovoltaics is an emerging new technology and research on this material has skyrocketed over the last decade. Through progress in material properties with respect to composition and morphology as well as device design, efficiencies have increased rapidly [51]. Currently, the maximum efficiency of 25 % is almost on level with crystalline *Si* solar cells [52].

Metal halide perovskites have a  $ABX_3$  perovskite structure. On the *A* site, monovalent organic molecular cations such as methylammonium (*MA*), formamidinium (*FA*) or inorganic alkali metal cations (*C*, *K*, *Rb*) can be found. The *B* site is occupied by divalent metal ions such as *Pb*, *Ge*, *Sn* and the *X* site by halides, for example, *I*, *Br* or *Cl* [51, 53]. As a prerequisite for solar energy conversion, the material provides good optoelectrical properties with high absorption, long carrier diffusion length and high carrier mobility [54, 55]. It is a correlated polar semiconductor, in which electronic degrees of freedom strongly couple to the lattice vibration. The band gap can be tuned through material composition to include both wide-band and narrow-band gap absorbers (1.15–3.06 eV) [51, 56]. However, to become feasible for commercial use, these metal halide perovskites must overcome several major challenges, including stability towards moisture, light and heat [53, 57, 58]. Additionally, significant effort has been put into making the solar cells eco-friendly by replacing the lead on the B site [59, 60].

In recent years, this material class has been identified as a promising candidate for hot carrier solar cells, as a number of compositions show relatively long-living hot carrier states [32, 33, 50, 61]. For example, under strong illumination (thus highly excited carrier densities) cooling rates ranging from picoseconds up to nanoseconds have been observed in  $FASnI_3$  [62–64], which drastically exceed the picosecond lifetime of hot carriers in inorganic semiconductors. The slowing down of hot charge carrier cooling has been attributed to the phonon bottleneck principle [61, 65–68]. However, the origin of slow carrier cooling is still under debate and it is likely that all the following aspects are relevant, although not with equal importance:

- The accumulation of slowly dissipating optical phonons slows down the carrier cooling process [67, 68].
- A low thermal conductivity and, thus, a short phonon lifetime [69, 70], among other things, results in decreased heat transport (in  $MAPbI_3$  acoustic phonon lifetimes are in the range of picoseconds, around two magnitudes of order shorter than in semiconductors [69]).

- Large polarons with long-range Coulomb interactions between charge carriers and ions are formed [71]. One proposed concept is the formation of a protective shield (screening) by the large polarons, which prevents optical phonon scattering [70, 72].
- In optical acoustic phonon upconversion, the decay of acoustic phonons is suppressed, which results in an increased up-transition of the acoustic phonon. The thermal energy is recycled back and reheats the charge carriers, therefore prolonging the overall cooling time [73, 74].
- For the Auger heating effect, the electron–hole recombination energy is transferred to another carrier and thus excites the carrier. Therefore, the recombination energy is re-transferred to the electronic system [74].

The charge carrier cooling rate varies widely and depends on illumination parameters such as pump energy (i.e., initial hot carrier excess energy) and fluency (i.e., excited carrier density) [33, 50, 75]. Additional material properties such as cation species, morphology and geometric confinement influence the slowing down of charge carrier cooling. For example a higher excess energy, i.e., excitation energy, as well as higher initial hot carrier densities can further increase the lifetime [75]. For the cation species it has been shown, that the exchange of iodine with lighter halides can decrease cooling lifetime as it increases the frequency of longitudinal optical phonons [33, 61, 75].

### 1.3 Manganite Perovskite for Hot Polaron Solar Cells

Within this thesis, highly correlated perovskite manganite oxides are proposed as a model system for hot carrier solar cells, since it provides insights into new pathways and mechanisms for photovoltaic energy conversion beyond conventional semiconductor systems.

Through the correlative exchange interactions of lattice orbital and spin degrees of freedom, interesting phenomena such as the colossal magnetoresistance effect (CMR) and colossal electroresistance (CER) effects emerge. The appearance of order phenomena such as purely orbital, combined charge and orbital and magnetic order phases are observed. Due to the interaction of charge carriers and lattice, i.e., strong electron–phonon coupling, a new quasi-particle, the polaron, is formed [76, 77]. For conventional semiconductors the band structure can in good approximation be described with a rigid band structure, as the modification in electronic structure due to a change in occupancy i.e. through

excitation, are small. The polaronic nature, i.e., strong coupling of atomic arrangement and electronic structure, of this material leads to deviations from the rigid band structure of semiconductors [78]. Investigations of the impact of correlation effects on optical excitation, lifetime of hot charge carriers and energy conversion, allow for fundamental insights into hot carrier stabilization and harvest [79, 80].

In p–n heterojunctions composed of manganites and titanites, the photovoltaic energy conversion has been demonstrated by several research groups [77, 81–85]. Iffland et al. established a correlation between order phenomena and photovoltaic energy conversion for two types of order phases [86]: The temperature where a strong increase of the open circuit voltage  $U_{oc}$  is observed coincides with the onset of the charge and orbital order in  $Pr_{1-x}Ca_xMnO_3$  (PCMO)  $x = 0.34$  as well as with the magnetic order in case of  $x = 0.95$ . Above the phase transition to the ordered phase, i.e., within the disorder phase, only a very small open circuit voltage is observed. However, below the phase transition, a significant value for the open circuit voltage is observed, which further increases with decreasing temperature. Additionally, Raiser et al. reported long-living states with nanosecond lifetime within the charge and orbital order phase for PCMO  $x = 0.34$  [79]. Thus, long-living hot polaron states, which can be harvested for photovoltaic energy conversion, exist due to cooperative correlation phenomena.

In the scope of this thesis, the research within this material class is extended to the orbital order  $Pr_{1-x}Ca_xMnO_3$  (PCMO)  $x = 0.1$  and a Ruddlesden–Popper (RP) 2D layered system of charge and orbital order  $Pr_{0.5}Ca_{1.5}MnO_4$  (RP PCMO). This enabled the establishment of a **new type of phonon bottleneck principle** for hot polaron manganite perovskites solar cells, which is briefly introduced here. The slowing down of carrier relaxation and the emergence of long-living states is given through strong coupling of electrons to cooperative lattice modes. Therefore, instead of suppressing the phonon interaction as proposed previously to slow down carrier cooling (Section 1.1), the strong and cooperative phonon interaction is turned into an advantage and utilized.

In an ionic model, the fivefold-degenerated  $d$  orbital in the ground state of an isolated  $MnO_6$  octahedron is split into three  $t_{2g}$  and two  $e_g$  separate states by the crystal field of the octahedron as well as through Jahn–Teller (JT) distortion (for details, see Chapter 2.2). Additionally, due to strong hybridization, the  $Mn$   $3d$  states overlap with the oxygen  $O$   $2p$  states [78]. The relaxation process of a Jahn–Teller dimer for excitation from an occupied to an unoccupied Jahn–Teller split  $Mn$   $3d$   $e_g$ – $O$   $2p$  state occurs through structural relaxation on a fast time scale, if an isolated  $MnO_6$  octahedral configuration is considered. The excited charges relax to the ground state through a conical intersection between

the energy potential surfaces [79]. However, within the confined geometry of the lattice and in the presence of cooperative long-range correlations, the energy potential surface is modified and the structural relaxation is suppressed [79]. Consequently, within the order phase, long-living hot charge carriers for photovoltaic energy conversion emerge [79]. Two transitions are relevant for photovoltaic energy conversion: on the one hand, the intraband transition between occupied and unoccupied  $e_g$  states (Jahn–Teller transition) and on the other hand, the charge transfer transition into the  $t_{2g}$  states.

## 1.4 Thesis Objectives and Outline

In this thesis, the hot polaron photovoltaic effect in junctions with different phases—in particular, different ordered phases of  $Pr_{1-x}Ca_xMnO_3$  (PCMO)  $x = 0.1$  and a 2D layered  $Pr_{0.5}Ca_{1.5}MnO_4$  (RP PCMO)—are investigated. The required high-quality, epitaxial and well-characterized manganite thin films are prepared on a variety of substrates ( $SrTiO_3$  (STO),  $Nb$  doped  $SrTiO_3$  (STNO) and  $MgO$ ) by means of ion beam sputtering (IBS) as well as metal aerosol deposition (MAD). The MAD samples were prepared by the MAD group of the 1. Phys. Institute (Group V. Moshneaga, see also [87]).

On the basis of the findings, a generalization of the **hot polaron phonon bottleneck** mechanism is established. Furthermore, the influence of order and correlation on the photovoltaic properties are explored from a mechanistic viewpoint. These topics are presented through three publications in Chapters 4–6. The thesis is structured as follows: In Chapter 2, the theoretical background on the fundamental limits of photovoltaic energy conversion, electronic and structural properties of manganites and the role of the charge separating interface to  $n$ -doped titanite is given. Information on the measurement setup for photovoltaic properties is presented in Chapter 3. The photovoltaic properties are analyzed through current density–voltage measurements in the dark and under different illumination conditions. Additionally, characteristic photovoltaic parameters open circuit voltage  $U_{oc}$  and short circuit current density  $J_{sc}$  are analyzed (see Fig. 1.3).

Chapter 4 deals with the photovoltaic and electronic properties of the 2D layered Ruddlesden–Popper (RP)  $Pr_{0.5}Ca_{1.5}MnO_4$  material system. In comparison to the 3D  $Pr_{1-x}Ca_xMnO_3$   $x = 0.34$  with a transition to the charge and orbital order phase at about 220 K, the epitaxial 2D RP PCMO thin films show a charge order transition temperature above room temperature [86, 88]. Moreover, the RP PCMO exhibits photovoltaic energy conversion above room temperature as well. Consequently, proof of principle for extending the hot polaron photovoltaics to a room temperature device has been acquired.

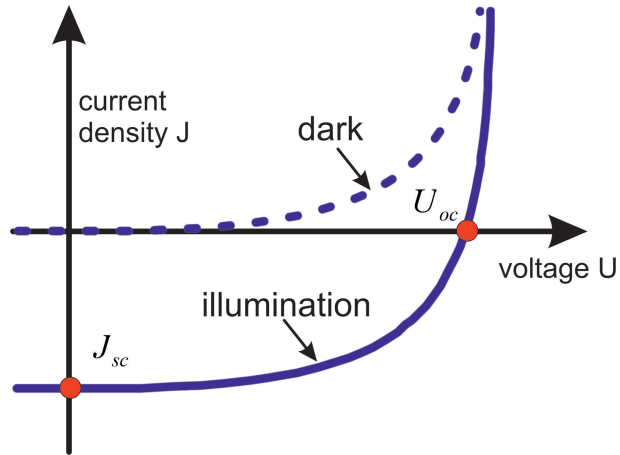


Figure 1.3: Photovoltaic effect: an exemplary current density–voltage curve in the dark and under illumination conditions. The two characteristic photovoltaic parameters of short circuit current density  $J_{sc}$  and open circuit voltage  $U_{oc}$  are marked.

In Chapter 5, the lightly doped 3D PCMO  $x = 0.1$ , which exhibits a purely orbital order phase, is investigated. This material enables the extension of hot polaron photovoltaics to a different type of order, as previous works focused on charge and orbital order, as well as magnetic order phases [86]. Additionally, according to the phase diagram by Jirak, the purely orbital order phase exists up to 800–1100 K [89]; therefore, it offers a second model system for polaronic room temperature photovoltaics. However, the onset of photovoltaic energy conversion is experimentally observed only well below room temperature. A readjustment of the phase diagram (see Fig. 2.3) for low doping is proposed and the concept of spontaneous orbital order with long-living states below room temperature and an induced orbital order of Jahn–Teller distortions at higher temperatures is discussed. This additional phase transition and the change of the phase diagram is supported by several anomalies in various physical properties, e.g., transport, magnetic, optic, ultra-fast transient excitation probe studies; change in lattice constant; and finite temperature simulations based on tight binding.

The mechanism for photovoltaic energy conversion in hot polaron systems differs in nature from conventional semiconductors. In Chapter 6, the dependence of characteristic parameters, such as the open circuit voltage and the short circuit current density on illumination conditions, including photon energy and power density, are analyzed. The interplay and influences of correlation phenomena such as phase transition orbital order phase and kinetic contributions are discussed.

A general discussion and summary is given in Chapter 7.





## Chapter 2

### Theoretical Background

This Chapter provides theoretical background for this thesis, covers thermodynamics for photovoltaic energy conversion and introduces the used material systems and their respective properties as well as strategies for tuning the interface properties of the junction.

#### 2.1 Thermodynamic Approach to Photovoltaic Energy Conversion

In this section, two different thermodynamic approaches to describe the fundamental limits of a photovoltaic energy conversion are presented. In the first subsection, the detailed balance approach is introduced in the form of Shockley–Queisser (SQ) model. The foundation of this thermodynamic model is based on material features and their corresponding limitations. Even if, in the framework of the SQ theory, many simplifications are made, it is ultimately the “real” material mechanisms of conventional semiconductors that determine the maximum efficiency. The radiation is described from an idealized thermodynamic point of view and the conventional semiconductor by the intrinsic material property of the band gap. An alternative approach on the basis of the first and second laws of thermodynamics for an ideal material is presented in the second subsection. In this case, the solar cell is approximated as a heat engine within a typical idealized Carnot and Landsberg framework.

##### 2.1.1 Detailed Balance and the SQ Limit

In 1961, Shockley and Queisser presented a theoretical approach, based on the thermodynamic principle of detailed balance, for the determination of the fundamental limits of photovoltaic energy conversion in silicon-based solar cells [20]. In this approach, the basis for this theoretical upper limit is given by physical mechanisms instead of the previously

employed phenomenological approach, in which the potential maximum efficiency is based on limits of empirical values such as lifetime. The detailed balance approach yields not only an upper efficiency limit but also a systematic formalism for the performance of a solar cell, in the context of which, for example, the current–voltage characteristics can be modelled effectively. Since then, this approach has undergone many expansions and refinements; it is widely used as a starting point for models of photovoltaic energy conversion.

In thermodynamic equilibrium, the conditions of detailed balance, i.e., that every process is in equilibrium with its inverse process, are given. Transferring this detailed balance to a solar cell translates to the following: The energy, in the form of light into and out of the system, is in equilibrium. More specifically, the detailed balance pair of photon absorption and its reverse process of radiative recombination is considered.

Within their approach, Shockley and Queisser used a highly idealized model with several simplifications [20]:

- Incident photons with energies below the band gap are not absorbed and all photons with energies above the band gap  $E_g$  are absorbed without loss (perfect absorption).
- Each absorbed photon (with energy above the band edge) creates exactly one electron–hole pair.
- All generated electron–hole pairs thermalize to the band edges without any detrimental loss contribution and end up in thermal equilibrium with the lattice.
- All charge carriers (electron–hole pairs) at the band edges are collected as current or recombine by emission of exactly one photon per electron–hole recombination process. If all charge carriers are collected (perfect collection) the internal quantum efficiency  $Q$  is a step function with  $Q = 1$  and a voltage of  $V = E_g/q$  for photons with energies above  $E_g$  and  $Q = 0$  for photons with energies below  $E_g$ .
- Non-radiative recombination channels, such as recombination at impurities, are excluded.

Consequently, as the material specific properties, only the band gap  $E_g$  and the temperature  $T$  of the cell are required for the calculation of an efficiency limit. Accordingly, the limit of efficiency is strongly influenced by the band gap.

The incident energy source, the sun, can be approximated as a black-body emitter, with a temperature of around  $T_s = 6000$  K. The spectral photon flux  $\phi$  is therefore given by

Planck's law with photon energy  $E$ , temperature  $T$  of the emitting body, Planck's constant  $h$ , speed of light  $c$  and Boltzmann constant  $k_b$ , solid angle  $\Omega$ , as [90]:

$$\phi(E, T) = \frac{2\Omega}{h^3 c^2} \frac{E^2}{\exp\left(\frac{E}{k_b T}\right) - 1}. \quad (2.1)$$

A geometrical factor is included to take, among other things, the limited angle for the solar radiation which shines on the solar cells into account [91].

In the original SQ model, this black-body approximation was applied for both the absorption and emission process. However, Würfel et al. introduced a generalized Planck's equation, in which the chemical potential of a material is included, as the photons emitted by the semiconductor material result from electron-hole recombination processes [92]. For a thermal emitter, such as the sun, the chemical potential is set as  $\mu = 0$ . The generalized Planck's equation for the spectral photon flux  $\phi(E, T, \mu)$  is given by:

$$\phi(E, T, \mu) = \frac{2\Omega}{h^3 c^2} \frac{E^2}{\exp\left(\frac{E-\mu}{k_b T}\right) - 1}. \quad (2.2)$$

Nowadays, the AM 1.5G standard global solar spectrum is often applied in addition to the black-body spectrum for the incident photon spectrum [93].

For the detailed balance, the current density is then given by the difference between absorbed  $J_{abs}$  and emitted photons  $J_{rad}$ :

$$\begin{aligned} J &= J_{abs} - J_{rad} \\ &= q \int_{E_g}^{\infty} \phi_{sun}(E, T_{sun}, \mu = 0, \Omega_{abs}) dE - q \int_{E_g}^{\infty} \phi_{cell}(E, T_{cell}, \mu, \Omega_{emit}) dE. \end{aligned} \quad (2.3)$$

If all absorbed photons from solar irradiance are collected (voltage is zero), the short circuit current density is equal to the photo-generated current density  $J_{sc} = J_{abs}$ .

In thermodynamic equilibrium, the total current density is zero and thus,  $J_{abs} = J_{rad}$  for  $V = 0$ . Under applied external voltage  $V$  and by Boltzmann approximation of the Bose-Einstein term in 2.2, this results in the idealized diode equation:

$$J = J_{0,rad} \left( \exp\left(\frac{qV}{k_b T}\right) - 1 \right) - J_{sc}, \quad (2.4)$$

with the constant prefactor of radiative saturation current density  $J_{0,rad}$ . The idealized diode  $J(V)$  equation can approximate a real solar cell effectively and is applied for many solar cell concepts. A widely used expansion of this model is the inclusion of series and

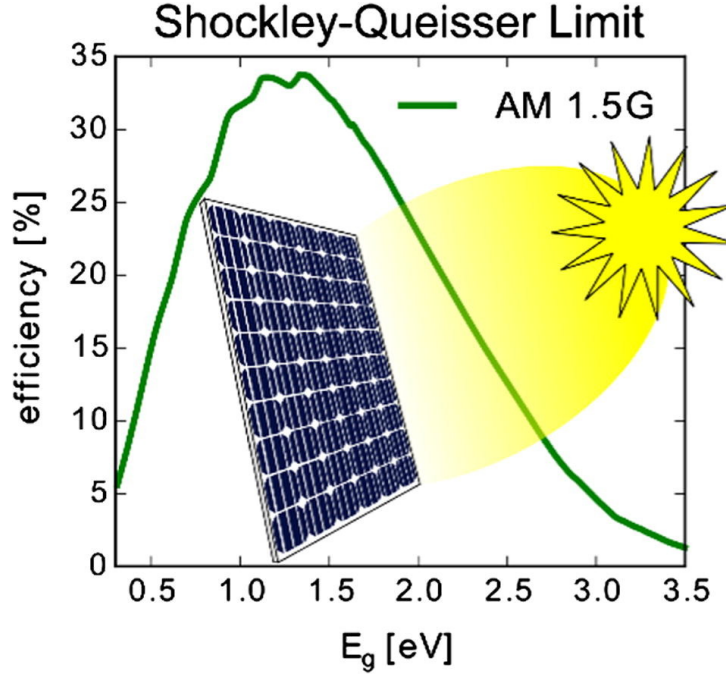


Figure 2.1: Theoretical maximum efficiency as a function of the band gap  $E_g$  in the SQ model for a Silicon-based cell operated at room temperature. The illumination was fixed to the global standard AM 1.5G spectrum (reprinted with permission [97]).

parallel resistance and the diode quality factor  $n$  to include additional loss mechanism of a real solar cell [94–96]. Within the SQ theory, the maximum efficiency  $\eta_{SQ}$  is given by the incident radiative power  $p_{in}$ , the outgoing power  $p_{out}$  and the maximum current-voltage  $J(V) \cdot V$ , according to:

$$\eta_{SQ} = \frac{p_{out}}{p_{in}} = \frac{\max(J(V) \cdot V)}{p_{in}}. \quad (2.5)$$

Consequently, the efficiency is a function of the light absorbers' band gap  $E_g$ , as shown in Fig. 2.1. A maximum efficiency of 33 % occurs at  $E_g = 1.34$  eV for global standard AM 1.5G spectral irradiance [97]. In this context, the fraction of incident solar radiation lost through thermalization  $f_{therm}$  (relaxation of photons with  $E > E_g$  to the band edge) and spectral mismatch  $f_{spec}$  (loss of photons with  $E < E_g$ ) can be described as follows [18]:

$$f_{therm} = \frac{2\Omega_{abs}}{c^2 h^3} \int_{E_g}^{\infty} \frac{E^2}{\exp\left(\frac{E}{k_b T_s}\right) - 1} (E - E_g) dE, \quad (2.6a)$$

$$f_{spec} = \frac{2\Omega_{abs}}{c^2 h^3} \int_0^{E_g} \frac{E^2}{\exp\left(\frac{E}{k_b T_s}\right) - 1} E dE. \quad (2.6b)$$

There are several publications that deal with the extension and generalization of the detailed balance approach for solar cells to include additional physical mechanisms. These revisions and refinements include additional mechanisms such as photon recycling, Auger generation and non-radiative recombination [98–100].

### 2.1.2 The Solar Cell as a Heat Engine

A different approach to determine a maximum efficiency, as well as establishing a systematic formalism, is given by the point of view of a thermodynamic heat engine. The sun emits energy, which, in turn, is converted into usable work in the solar cell. The fundamental limits of the energy conversion process are investigated using the first and second laws of thermodynamics. Among other things, these approaches could offer alternative ideas regarding hot carrier solar cells.

The most simplified and fundamental approach is, to approximate the solar cell as a Carnot heat engine. Within the idealized and reversible Carnot heat engine, the energy of the sun is absorbed and converted into electric energy within the solar cell without generating irreversible entropy. The sun, as the heat source, is represented as a black-body radiation source with temperature  $T_s$ . The output of the solar cell is characterized by the work done  $w$ , the heat flux  $q$  supplied to the system and the solar cell temperature  $T_{cell}$ , which is assumed to be equivalent to the ambient surrounding temperature. The entropy, which is due to the generated heat, is given as  $s_w$ . The first law of thermodynamics states that, for the change in internal energy  $u$  of a closed system:

$$u = w + q. \tag{2.7}$$

When  $u_s$  is given as the radiation energy of the sun, which is the input into the system, then  $w$  is the output work and  $q$  is the heat flux. This results in the Carnot efficiency  $\eta_{carnot}$  for the photovoltaic energy conversions given as:

$$\eta_{carnot} = \frac{w}{u_s} = 1 - \frac{T_{cell}}{T_s}. \tag{2.8}$$

As only the respective temperatures of the source and solar cell and no other intrinsic material properties, such as the band gap, are considered, the Carnot efficiency represents an ultimate thermodynamic upper limit. Accordingly, all photons contribute to the energy conversion, i.e., neither thermalization losses nor loss of photons with energies below the

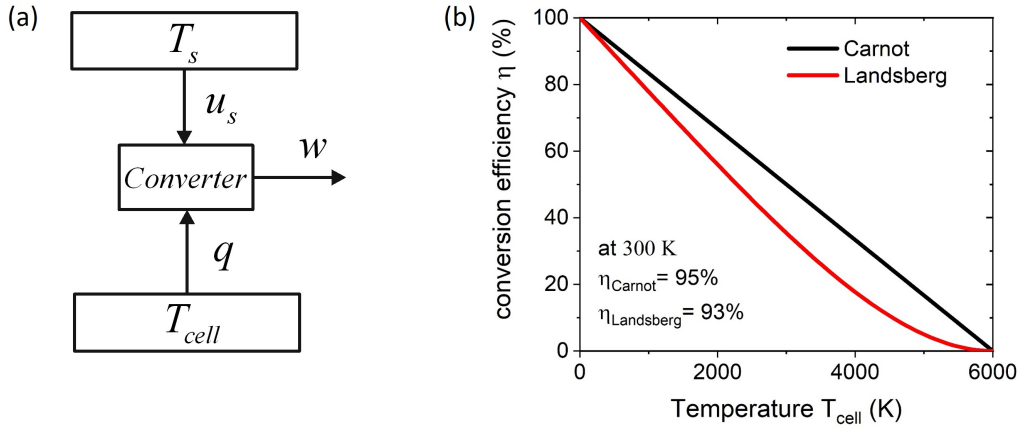


Figure 2.2: (a) A schematic diagram of the solar cell as a heat engine; (b) The Carnot and Landsberg efficiency limits for the solar cell versus the solar cell (ambient) temperature.

band gap are considered. Therefore, this represents an ideal hot carrier solar cell.

The Carnot model applies only for an idealized process because a prerequisite is that no entropy is generated. However, this already does not apply for a two-black-body scenario, as Planck reported unavoidable entropy generation [90, 101]. Various alternative and extended approaches to the Carnot heat engine are proposed for hot solar cell concepts as well as conventional semiconductor solar cells. One example is given by the Landsberg limit, where reflection losses and entropy generation are included [102]. Within this model, the emission spectrum is given by a black body radiation described by the Stefan Boltzmann law and results in the following efficiency  $\eta_{Landsberg}$  [102]:

$$\eta_{Landsberg} = 1 - \frac{4}{3} \frac{T_{cell}}{T_s} + \frac{1}{3} \left( \frac{T_{cell}}{T_s} \right)^4. \quad (2.9)$$

The efficiencies obtained in both models are shown as a function of cell temperature in Fig. 2.2. It is noticeable that the efficiency for the solar cell in the ideal heat engines models are significantly (almost a factor of three) larger than the maximum efficiency of the SQ model. Therefore, if one can succeed in eliminating the material limitations that determine the maximum efficiency in the SQ model (thermalization to the band edge and spectral mismatch), then significantly higher efficiencies are achievable.

In a heat engine model by Markvart et. al the voltage generated by the solar cell can be obtained based on the balance of entropy as well as energy for absorbed and emitted

photons [103, 104]. The light is considered as a stream of photons and the process is divided into two parts: the absorption and emission of radiation as well as the conversion of the absorbed photons into usable work. The sun emits photons with incident photon energy  $u_s$  in the form of heat, represented by a high temperature reservoir  $T_s$ . As the solar cell absorbs the photons, the radiation is converted into energy  $w$  and the corresponding heat  $q_w$  is transferred to the lower temperature reservoir of the solar cell with temperature  $T_{cell}$ . In this case, the temperature of the solar cell and ambient temperature are assumed to be equal. In accordance with energy conservation, the following dependence is given:

$$u_{in} = w + q_w. \quad (2.10)$$

Additionally, entropy  $s$  and entropy balance need to be considered and are given by the following equations:

$$s_{in} = \frac{u_s}{T_s}, \quad (2.11a)$$

$$s_{in} = \frac{q_w}{T_{cell}} - \sigma_i. \quad (2.11b)$$

The incident photons are characterized by the heat of the sun at temperature  $T_s$  (Equation 2.11a) and the entropy of the absorbed photon is composed of two parts (Equation 2.11b): the entropy transferred into the temperature reservoir of the solar cell  $T_s$  (first part of the formula) and consequently the irreversible entropy  $\sigma_i$ , which is generated in the conversion process. The energy of one photon is considered as  $u = \mu + T_s$ , in which  $\mu$  represents the chemical potential, i.e., available work per photon and can thus generate voltage within an external circuit. Consequently, the photo-generated voltage is given by:

$$qV = \mu_{out} = \left(1 - \frac{T_{cell}}{T_s}\right) u_s - T_{cell}\sigma_i. \quad (2.12)$$

The loss contributions for the voltage can be quantified through a generalized irreversible entropy generation  $\sigma_i$  [103]. This relates the maximum splitting of the Fermi levels, i.e., the open circuit voltage to the Carnot efficiency and the entropy generation. This opens up the possibility of examining fundamental losses contributions to the voltage through a thermodynamic view point, including non-radiative recombination and hot-carrier conversion [104].



## 2.2 Structural and Electronic Properties

In this section, an introduction into the structural and electronic properties of the 3D  $Pr_{1-x}Ca_xMnO_3$  and 2D layered  $Pr_{0.5}Ca_{1.5}MnO_4$  manganite perovskite systems is given.

### 2.2.1 3D Manganite System: $Pr_{1-x}Ca_xMnO_3$

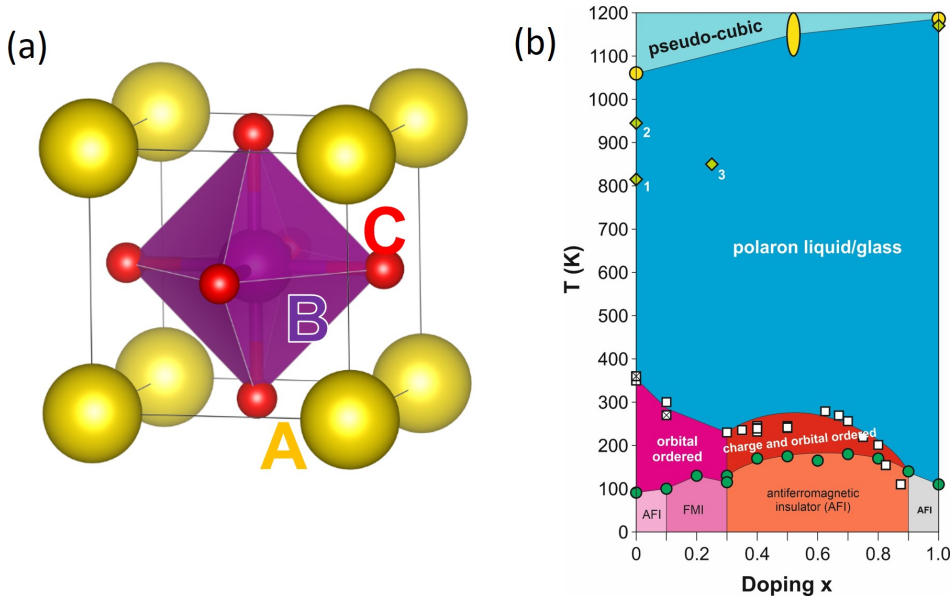


Figure 2.3: (a) In the ideal perovskite structure, the A site is occupied by a mix of  $Pr/Ca$ , the B site by  $Mn$  and C by oxygen. The purple structure represents the  $MnO_6$  octahedra (reprinted with permission [105]). (b) The electronic bulk phase diagram for the 3D  $Pr_{1-x}Ca_xMnO_3$  perovskite [106].

The 3D perovskite manganite shows an ideal structure of composition  $ABO_3$ . For the material system investigated within this thesis, the A site is occupied by a mixture of  $Pr$  and  $Ca$  and the B site is occupied by  $Mn$ . For these materials, the  $MnO_6$  octahedra with oxygen atoms positioned around the  $Mn$  on the B site is a prominent feature (see Fig. 2.3). Deviation from the ideal cubic structure occurs due to octahedral distortion and octahedral tilt. The system is characterized as an orthorhombic  $Pbnm$  space group [107]. For the ground state of an isolated  $Mn$  ion, the  $3d$  orbital is fivefold degenerated. Due to the  $MnO_6$  octahedral ligand field, i.e., crystal field splitting, the  $Mn$   $3d$  orbitals are split into three energetically reduced  $t_{2g}$  and two energetically increased  $e_g$  states. In a simplified ionic picture, the crystal field splitting results from the Coulomb repulsion as two  $e_g$  orbitals are aligned in direction of the negative charged oxygen ion [108]. In  $Mn^{4+}$ ,

there are three electrons in the  $3d$  orbital and thus, the three  $t_{2g}$  orbitals are filled with one electron each. For  $Mn^{3+}$  valence with  $4d$  electrons, the additional electron occupies one of the  $e_g$  orbitals. Due to Hund coupling, the spin is aligned parallel to the spins of the electrons within the  $t_{2g}$  orbital. For doping of  $x = 0$  in  $Pr_{1-x}Ca_xMnO_3$ , the valence of  $Mn$  is given as  $Mn^{3+}$ . Through doping with  $Ca^{2+}$ , the nominal  $Mn$  valence is reduced, simultaneously reducing the occupancy of the  $e_g$  state.

An additional splitting of the orbitals occurs through the Jahn–Teller distortion of the  $MnO_6$  octahedra, which depends on the doping [109]. For doping leading to predominantly  $Mn^{3+}$  ions, a cooperative static Jahn–Teller effect, i.e., distortion of the lattice structure, is observed. Since  $e_g$  orbitals are not occupied for  $Mn^{4+}$ , no static Jahn–Teller effect is observed for highly doped systems ( $x \rightarrow 1$ ). Within this thesis, a doping of PCMO  $x = 0.1$  is analyzed; thus, a strong static Jahn–Teller effect is present.

However, the overlap of the  $Mn$   $3d$  orbitals with  $O$   $2p$  states plays a major role for the electronic properties of the PCMO system. The  $e_g$  orbitals form  $\sigma$ -bonds with oxygen ligands with a strong orbital overlap. In contrast, the  $t_{2g}$  orbitals, with a weak orbital overlap, establish  $\pi$ -bonds [78].

In the manganites perovskite, the electron–phonon coupling results in the formation of polarons. A distinction is made between two types of polarons:

- Large polarons with a long interaction range over several neighboring lattice sites and weak electron–phonon coupling.
- Small polarons with short range interaction, which is localized on one site and strong electron coupling.

For PCMO, small polarons are observed as charge carriers, which demonstrate thermally activated hopping along a  $Mn-O-Mn$  bond over a wide doping range [110].

With varying doping values, PCMO displays various magnetic ground states, such as anti-ferromagnetic, ferromagnetic and canted structures [89]. Additionally, a number of ordered phases with periodic alignment of magnetic moments, charges and orbitals are observed for different doping levels (see Fig. 2.3). In the medium-doping regime, at higher temperatures, a two phase region with charge/orbital order and disorder is observed [111]. The volume fraction of the charge and orbital order phase increases with decreasing temperature. In the low-doping regime, orbital order is observed for temperatures above the magnetic phase transition. The phase diagram is shown in Fig. 2.3 and will be further discussed in Chapter 4.

Two exchange interactions are considered for these systems [76, 108, 112, 113]:

- On the one hand, **super exchange**, which is an indirect spin dependent exchange between two neighboring  $Mn$  sites with equal valence state through hopping. This is relevant for antiferromagnetic ground states, as the anti-parallel spins allow the transfer of electrons between two  $Mn$  sites of the same electronic configuration.
- On the other hand, the **double exchange**, in which the  $e_g$  electron can hop between  $Mn$  sites through enclosed  $O$  orbitals in ferromagnetic coupled states. Thus, this is predominantly found in hole-doped systems.

However, according to Millis et al., additional aspects, such as correlations and polarons, need to be included, as the double exchange alone does not adequately account for the experimentally observed conductivity in manganites [114]. The experimentally observed resistivity in  $La_{1-x}Sr_xMnO_3$   $x = 0.2 - x = 0.4$  is an order of magnitude higher than predicted by the double exchange model.

Two contrary models are discussed for the polaron charge carriers for the medium-doping range, in which, nominally, a similar quantity of  $Mn^{4+}$  and  $Mn^{3+}$  is present:

- The **Jahn–Teller polaron** is based on an ionic model, where atom positions with distinct integer valence values, i.e., Jahn–Teller distorted  $Mn^{3+}$  and undistorted  $Mn^{4+}$ , coexist. The polaron is then localized on the  $Mn$  site.
- A **Zener polaron** is characterized by an averaged  $Mn$  valence for all  $Mn$  sites. In particular, the deviations from the mean  $Mn$  valence between different sites are very small. For the Zener polaron, the doped hole charge is located in the  $Mn-O-Mn$  dimer.

The Zener polaron has been experimentally observed for PCMO doping values of  $x = 0.5$  as well as  $x = 0.34$  [111, 115, 116]. The orbital overlap with the  $O$   $2p$  orbital decreases with decreasing doping. However, even for low doping  $x = 0.1$ , the  $O$   $2p$  orbitals significantly contribute to the electronic state of the JT polaron.

### 2.2.2 2D Manganite RP System: $\text{Pr}_{0.5}\text{Ca}_{1.5}\text{MnO}_4$

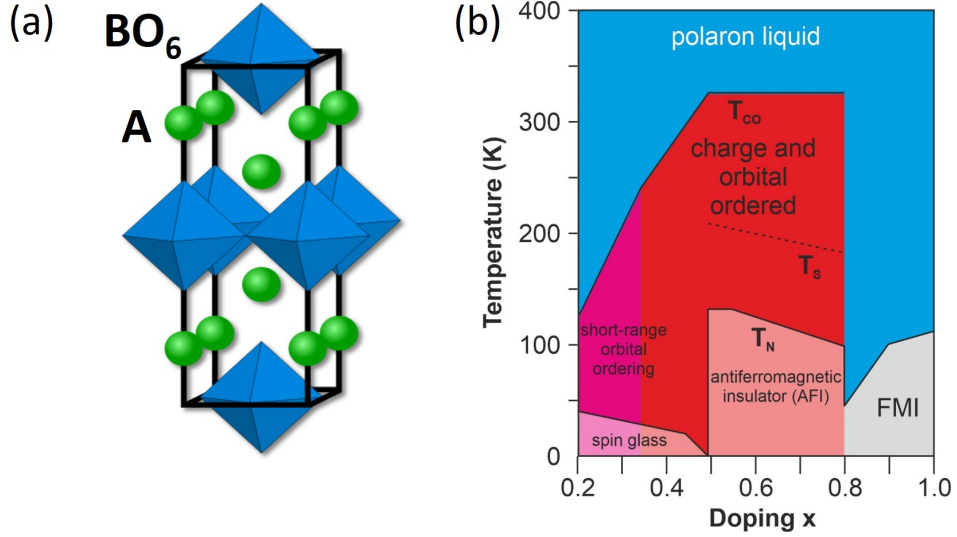


Figure 2.4: (a) Layered structure for an ideal 2D RP perovskite. (b) Schematic phase diagram of  $\text{Pr}_{1-x}\text{Ca}_{1+x}\text{MnO}_4$  according to [117, 118]

Further model system are the layered Ruddlesden–Popper (RP) manganites with their nearly 2-dimensional structure. For this,  $n$  layers of the 3D manganite perovskite and one rock-salt layer are alternately stacked on top of each other. Consequently, the layer number of  $n = \infty$  corresponds to the 3D perovskite. The structural formula and composition is given by  $A_{n+1}B_nO_{3n+1}$  or alternatively by  $(\text{ABO}_3)_n(\text{AO})_1$  (see Fig. 2.4).

The low-dimensional nature and the layer of rock salt, which separates the perovskite interlayers, affects, for example, the exchange interaction, coulomb repulsion and electron–phonon coupling and results in electronic state and phase diagrams that show strong deviations from the corresponding 3D perovskites [119–122]. This includes modified phase transitions and new aspects such as ground states with several different types of charge order, ferroelectricity and spin order. As an example, He et al. reported the coexistence of three different types of charge order in RP PCMO  $n = 2$  at room temperature [123].

Varying the number of consecutive perovskite layers thus provides a wide range of tuning possibilities. As the dimensionality plays a major role in defining the nature of the interaction within the material, a highly pronounced anisotropy exists and can, for example, be observed in magnetic susceptibility, as well as optical conductivity [124]. Another interesting topic in this context is the nature of the polaronic charge carrier, its

interactions and possible change of nature at phase transitions [125].

As a first model system, the layered RP structure with  $n = 1$  and a composition of  $Pr_{0.5}Ca_{1.5}MnO_4$  (RP PCMO) is investigated. Primarily of interest within this thesis is the remarkably high charge order transition temperature for the 2D layered system, which is significantly higher than its corresponding 3D perovskite counterpart [117]. Thus, this material offers itself as a candidate for room temperature photovoltaic energy conversion. In Fig. 2.4, the bulk material phase diagram is shown [117].  $Pr_{0.5}Ca_{1.5}MnO_4$  exhibits a phase transition into the charge and orbital order phase at  $T = 320$  K, an antiferromagnetic phase below 120 K and a short range and two-dimensional antiferromagnetic order at  $T = 200$  K. For higher doping values, similar phase transition temperatures are observed. At lower doping values, the transition temperature for the charge order phase is reduced and a spin-glass phase at low temperatures is given [117].

## 2.3 Tuning of Interface Properties in Manganite Heterojunctions

As introduced in the previous section, the highly correlated manganite perovskite material systems possess several complex and versatile electronic and structural phases, which change with respect to general composition, doping of specific sites and temperature [126, 127]. In addition, the introduction of external stimuli on the material itself can result in changes in the material properties, which includes the emergence of new phases, change in the balance between of competing phases within a phase coexistence region and can thus even result in phase transitions [128, 129]. These include, but are not limited to, photo irradiation, electron beams, voltage effects, current injection and magnetic fields [130–133]. This can be seen, for example, in the CMR, where large changes in electrical resistance are observed when an external magnetic field is applied [134]. Important factors that especially concern thin films are strain and oxygen vacancies, which, among other things, can affect the Curie and metal-to-insulator transition temperature [134–136]. As a further example, for PCMO, optical induced melting of charge order and remanent switching (i.e., the system can be switched between high and low resistance states when applying a high enough voltage) are reported [137–140].

For a heterojunction, such as the manganite/titanite solar cells investigated within this thesis, it gets even more complex, as not only the properties of the two compounds but the interface itself comes into play. Therefore, the interface will play a major role determining

the overall properties of the junction and can lead to electronic and magnetic properties of the junction that differ significantly from their bulk properties. In the case of photovoltaic energy conversion in PCMO/titanite heterojunctions, aspects such as the following need to be considered:

- I) the small space charge region and thus, the high electric fields at the interface;
- II) the interface itself, which includes factors such as strain, oxygen content, atomic and chemical structure of the first monolayers and structural symmetry;
- III) the transfer of charge carriers across the interface, which may even include a change of the nature of the charge carrier such as small to large polarons.

By applying external perturbations such as temperature, light, strain, electricity and magnetic fields, not only the bulk material but also the interface properties can be changed and tuned. The tuning of the photovoltaic energy conversion through electric fields in PCMO  $x = 0.36$  /STNO heterojunctions has been reported by Saucke et al. [77]. Additionally, the presence of charge order close to the interface is observed for this junction. In the charge and orbital ordered manganite a increase of the polaronic charge carrier mobility and a drop in the open circuit voltage at 100 K can be related to the colossal electroresistance effect, as the combination of high electric fields and electric current "melt" the charge and orbital order phase.

In this section, the ability to tune the interface properties in a manganite heterojunction is presented by the example of an external magnetic field and its effect on photovoltaic energy conversion. Depending on the electronic phase and ground state of the correlated material, the application of an external magnetic field can either enhance, suppress, or have no effect on the photovoltaic response. Therefore, it is possible to tune and find an optimum window for the photovoltaic response through an external magnetic field. Aspects that are presented include magnetic phases at the interface itself, phase transitions and change in balance for coexisting phases.

Under illumination, the generated minority carriers of electrons and holes are separated by the built in potential of the interface. For a conventional heterointerface, the interface properties are commonly considered within the framework of a rigid band model. However, the applicability of rigid bands is questionable for correlated interfaces. Thus, rigid bands can only be considered under conditions where correlations play a minor role for the properties. When applying an external magnetic field, the carrier density can be changed

and, therefore, the correlation effects will be dominant. Applying an external magnetic field on a heterojunction can influence the electron structure through the quasi-band profiles, which will affect the width of the depletion layer of the junction. This, in turn, changes the collection probability of minority carriers and the photovoltaic response.

The first aspect presented is the structural orientation of the material at the interface and its influence on the magnetic phase present at the interface and, accordingly, the impact of the type of magnetic interface phase on the tunability of the photovoltaic effect through magnetic fields. Sheng et al. investigated  $La_{0.7}Sr_{0.3}MnO_3$  junctions, which show a phase transition of paramagnetic isolating to ferromagnetic metallic around room temperature range for the bulk material [141]. Within this article, the temperature-dependent photovoltaic energy conversion under external magnetic fields was investigated in two  $La_{0.7}Sr_{0.3}MnO_3/STNO$  junctions with different growth orientations of (110) and (001). In the (110)  $La_{0.7}Sr_{0.3}MnO_3$  film, an increase of photocurrent by 30 % orientation for a magnetic field of 6 T is reported and the maximum increase is found in a temperature range of 150 K to 200 K, which follows magnetoresistance observation within this material. In contrast, the external magnetic field shows only a negligible influence for the (001)  $La_{0.7}Sr_{0.3}MnO_3$  junction.

As a result, the authors propose that for the (001)-oriented films, which exhibit no change of photocurrent under magnetic field, the width of the magnetic junctions stays constant, as this interface shows dominantly the metallic behavior of a Schottky junction. In comparison, the (110)-oriented films have a tilt-distorted insulating interfacial layer. For this interface magnetic state, as the temperature or magnetic field increase, the correlated insulating gap decreases and the effective carrier density is enhanced. Therefore, the correlated insulating gap and thus, the width of the depletion layer are dependent on temperature and magnetic field.

In  $La_{0.7}Ce_{0.3}MnO_3/STNO$  heterojunctions, the role of phase transition has been addressed [142]. In contrast with the previous example, the photovoltaic energy conversion represented by the open circuit voltage is suppressed within this heterojunction by introducing an external magnetic field. The open circuit voltage decreases linearly with increasing magnetic field [142]. In this system, the phase transition between the paramagnetic and ferromagnetic phase needs to be considered. Under an external magnetic field, the Fermi level decreases and, therefore, the depletion layer becomes smaller. Additional aspects of phase separation and coexistence of ferromagnetic insulating and ferromagnetic metallic phases in the interface region can have an effect, as the fraction can change through an applied field. As a third aspect, change of canting angles can influence the magnetic

domains.

The final aspect presented is the coexistence of different phases, where electronic phase separation and the change of balance between the phases are affected. Luo et al. observed temperature regions with no change, as well as temperature regions with a decrease of the photovoltaic effect, when applying a magnetic field in  $Pr_{0.65}(Ca_{0.75}Sr_{0.25})_{0.35}MnO_3/STNO$  junctions [143].

The authors proposed the coexistence of charge ordered insulating and ferromagnetic state and electronic phase separation as the main mechanism to consider. The ferromagnetic phase is spin ordered and the insulating phase is spin disordered. If the material is in a “deep” electronic phase-separation phase (in which the ferromagnetic phase is dominant) or the insulating phase, the magnetic field has no influence on the photovoltaic response. For the temperature range of a “prime” electronic phase separation with a coexisting ferromagnetic and charge ordered insulating phase, a decrease of about 63 % at 1 T at the phase transition temperature is reported. When applying an external field, spins align; therefore, transport of electrons across domains is easier. The charge order insulating phase will partially convert to ferromagnetic and, therefore, increase the conduction path. In turn, the accumulation of charge carriers is suppressed and the open circuit voltage decreases.





# Chapter 3

## Experimental Methods

This section will focus on the photovoltaic measurement, specifically dealing with the question of what types of measurements are possible in the current modified setup. In three subsections, the setup for the samples, the electrical measuring modes and the different types of illumination modes are introduced.

The thin-film preparation and experimental methods applied for structural analysis and physical properties, including transport, optical and magnetic properties, are described in the Methods sections of the publications in Chapter 4 – 6. The high-quality epitaxial thin films with layer-by-layer growth were prepared by ion beam sputtering and metalorganic aerosol deposition. Additional detailed information on the growth of RP PCMO thin-films can be found in the co-authored publication by Hoffmann-Urlaub et al. [87].

### Geometry and Setup

A schematic overview of the manganite/titanite heterojunction design for photovoltaic measurements is shown in Fig. 3.1. In the first step, a 100 nm manganite thin film is deposited on a conductive *Nb*-doped STO substrate with a size of 10 mm x 5 mm and a thickness  $d = 0.5$  mm. For films prepared by ion beam sputtering, a 9 mm x 4 mm shadow mask is applied in this process in order to avoid shortcuts via side-face coating. Back contacts composed of *Ti/Au* double layer are applied onto the back side of the substrate by ion beam sputtering again using a 9 mm x 4 mm shadow mask. For this process, the substrate is placed upside down in a holder with a 0.5 mm-wide raised-edge design. Therefore, only the outside edges of the substrate are in contact with the holder, ensuring that the deposited manganite thin film remains undamaged.

Thereafter, two front contacts composed of either *Pt* or *Au* with a size of 1 mm x 4 mm are deposited centered with the manganite film 2 mm apart. Four wires are connected to the contacts by silver paste, two on the back contact and two on the same front contact.

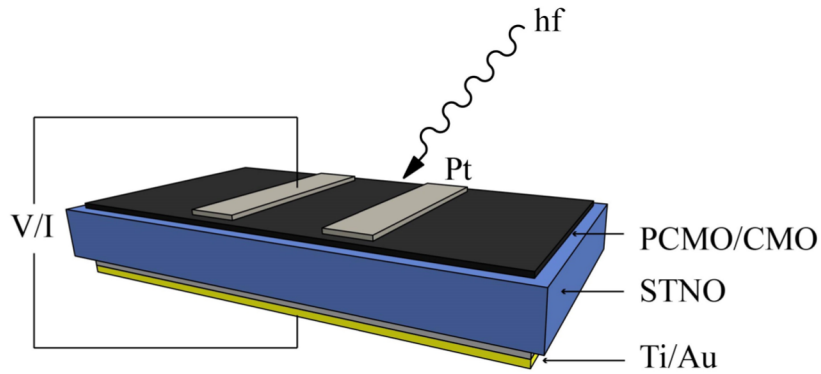


Figure 3.1: Schematic overview of the manganite/titanite heterojunction (reprinted with permission [86]). A thin manganite film (black) is deposited on a *Nb* doped STO substrate (blue). The back contacts are composed of *Ti/Au* double layer and the smaller top contacts are composed of either *Pt* or *Au*.

Next, the sample is glued flat onto a copper module of the same size of the substrate with an indentation in the middle, where the wires of the back contact are placed. The whole setup is mounted into an optical cryostat by CryoVac with double-sided adhesive tape to ensure electrical isolation as well as heat transport. The wires are connected to the inlets of the cryostat and after the lid is attached, a vacuum is created in the chamber.

For temperature-dependent measurements, helium is used as a cooling medium. Through a magnetic valve, a constant helium flow is achieved and the temperature is set by a heating wire regulated through a Tic-304 controller.

## Electrical Measuring Modes

The following two distinct measurement modes are available for temperature-dependent electrical measurement:

- I) current–voltage curves are recorded at a set, constant temperature;
- II) under open circuit conditions (no net current flow), the open circuit voltage is measured continuously.

For the first, a fixed temperature is set and measurements start when temperature fluctuations are below 0.1 K. Within this thesis, a temperature range of 80 to 300 K with a step width of 20 K is investigated. However, temperatures as low as 5 K are possible. In this measuring mode, a voltage is applied to the sample by a Keithley SourceMeter

2430 and current and voltage are recorded. The voltage drop is measured by a Keithley Nanovoltmeter 2182A.

The measuring procedure is controlled by a LabVIEW program. Current voltage cycles are measured and several measurement parameters, such as voltage range for a cycle, voltage step width/number of steps (limited by current resolution and at lower temperature by temperature fluctuations), number of cycles, waiting times for measurement and waiting time between pulses, are adjustable. The following parameters are typically applied for an overview cycle. One voltage cycle with a cycle process of 0 V to +1 V to -1 V to 0 V is set. A pulse mode is used for the voltage source with a waiting time of 500 ms until current and voltage values are recorded. Before the next voltage pulse is applied, there is a 200 ms voltage break.

The second measurement mode is a direct temperature dependent measurement of the open circuit voltage. In this case, a temperature sweep with a set cooling rate enables high temperature resolution for the data. Additionally, at a set temperature, the time dependence of the open circuit voltage on long time scales can be observed.

## **Illumination Modes for Photovoltaic Measurements**

For photovoltaic measurements, two beam paths with different illumination conditions are set up. For both setups, the illumination spot is positioned between the top contacts in such a way that the edge of the illumination spot partly covers the metallic top contact. The size of the illumination spot can be adjusted through a focus lens. The first beam path, with higher overall power density, is particularly suitable for varying the power density over a wide range of magnitude while still offering the option of spectral restrictions to a set range by filters. The second beam bath entails a monochromatic illumination source, which enables the user to vary transitions in a targeted manner while maintaining a relatively constant power density.

- I) The full incident spectrum of a 150 W Xe-lamp with an increased power density in the ultraviolet range, i.e., excitation in STNO with its band gap of about 3.2 eV, is included.

Typically, the spot size is adjusted to a diameter of around 3 mm and the overall illumination power is set at 175 mW. Within this beam path, additionally, two types of filters can be inserted into the setup in order to modify the incident spectrum.

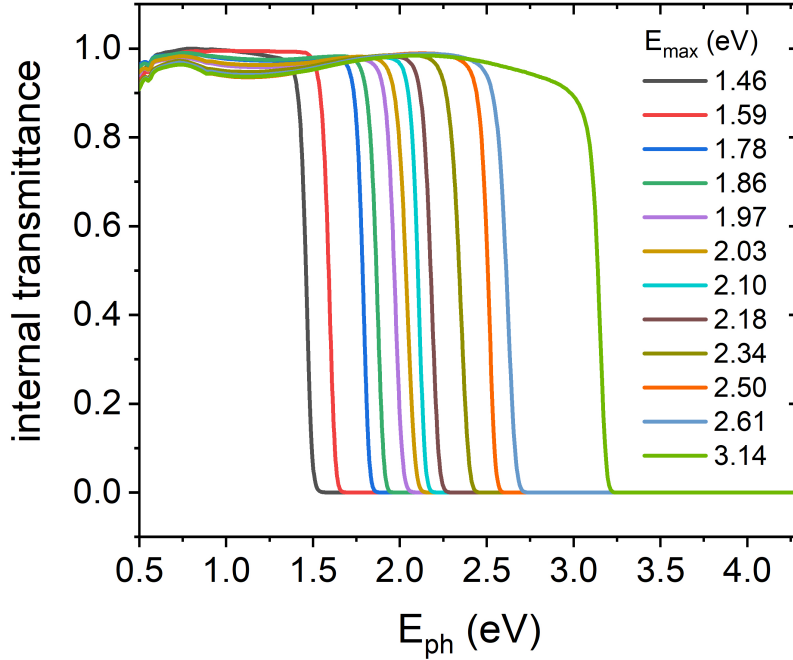


Figure 3.2: Spectral resolved internal transmittance for the spectral filters by Schott. These filters can be included into the illumination beam path and enable spectral limited measurements.

- Through cut-off filters, a spectral limited incident spectrum can be achieved. By using these filters, only incident photon energies below their respective  $E_{max}$  are transmitted. This allows a spectral limited investigation, in which, for example, the excitations in the STNO substrate can be to a high extent excluded or an energy-specific transition can be investigated. Several filters by Schott within a spectral range of  $E_{max} = 1.46\text{--}3.14$  eV are available. In Fig. 3.2, the transmission spectra are shown for all available cut-off filters.
- Neutral density filters enable the adjustment of power density over four orders of magnitude. The metallic neutral density filters by Quantum Design on fused silica substrates can be used for a spectral range of 0.6–5 eV. For the relevant spectral range of 1.5–3.5 eV investigated within this thesis, the deviation in spectral transmission is below 3 %. Seven filters are available with transmission values of around 80 %, 50 %, 30 %, 10 %, 1 %, 0.1 % and 0.01 %. Two or more filters can be combined, enabling a broad power density range.
- Both types of filters can be applied simultaneously.

II) For monochromatic illumination conditions, a LOT Quantum Design Monochromator Omni 300 is used. Three grids with adjustable slit width are available (Grid 1: 1200 gaps, Blaze angle of 300 nm; Grid 2: 1200 gaps, Blaze angle of 500 nm; Grid 3: 600 gaps, Blaze angle of 1000 nm). Here, lower power densities of 50–200  $\mu\text{W}$  are given. Typically, Grid 1 is used for measurements in a range of 1.5–3.1 eV with intervals of 40–150 eV. At 2.5 eV and slit width of 2 mm, the energy resolution of the monochromatic incident spectrum is 20 meV. The beam spot is adjusted to a diameter of around 3 mm and the overall power is set at 200  $\mu\text{W}$ .



## Chapter 4

# Room-temperature Hot-polaron Photovoltaics in the Charge-ordered State of a Layered Perovskite Oxide Heterojunction

In this Chapter, the article published in *Phys. Rev. Applied*, **14** 5, 054006 (2020) is presented.

doi: [10.1103/PhysRevApplied.14.054006](https://doi.org/10.1103/PhysRevApplied.14.054006)

The article is published in a peer-reviewed journal as an open-access article and is reprinted in its original format with permission. The corresponding Supplemental Material is included in Appendix A.



## Room-Temperature Hot-Polaron Photovoltaics in the Charge-Ordered State of a Layered Perovskite Oxide Heterojunction

B. Kressdorf,<sup>1</sup> T. Meyer<sup>1,2</sup>, A. Belenchuk<sup>1,3,4</sup>, O. Shapoval,<sup>3,4</sup> M. ten Brink,<sup>5</sup> S. Melles,<sup>1</sup> U. Ross,<sup>1</sup> J. Hoffmann<sup>1</sup>, V. Moshnyaga,<sup>3</sup> M. Seibt<sup>1,2</sup>, P. Blöchl,<sup>5,6</sup> and C. Jooss<sup>1,\*</sup>

<sup>1</sup>University of Goettingen, Institute of Materials Physics, Friedrich-Hund-Platz 1, 37077 Goettingen, Germany


<sup>2</sup>University of Goettingen, 4th Physical Institute – Solids and Nanostructures, Friedrich-Hund-Platz 1, 37077 Goettingen, Germany

<sup>3</sup>University of Goettingen, 1st Physical Institute, Friedrich-Hund-Platz 1, 37077 Goettingen, Germany

<sup>4</sup>IEN, Academy of Sciences in Moldova, str. Academiei 3/3, MD-2028, Chisinau, Moldova

<sup>5</sup>Institute for Theoretical Physics, University of Goettingen, Friedrich-Hund-Platz 1, 37077 Goettingen, Germany

<sup>6</sup>Institute for Theoretical Physics, Clausthal University of Technology, Leibnizstr. 10, D-38678 Clausthal-Zellerfeld, Germany

 (Received 5 June 2020; revised 25 September 2020; accepted 9 October 2020; published 4 November 2020)

Harvesting of solar energy by hot carriers from optically induced intraband transitions offers new perspectives for photovoltaic energy conversion. Clearly, mechanisms slowing down hot-carrier thermalization constitute a fundamental core of such pathways of third-generation photovoltaics. The intriguing concept of hot polarons stabilized by long-range phonon correlations in charge-ordered strongly correlated three-dimensional metal-oxide perovskite films has emerged and been demonstrated for  $\text{Pr}_{0.7}\text{Ca}_{0.3}\text{MnO}_3$  at low temperature. In this work, a tailored approach to extending such processes to room temperature is presented. It consists of a specially designed epitaxial growth of two-dimensional Ruddlesden-Popper  $\text{Pr}_{0.5}\text{Ca}_{1.5}\text{MnO}_4$  films on  $\text{Nb:SrTiO}_3$  with a charge-ordering transition at  $T_{\text{CO}} \sim 320$  K. This opens the route to a different *phonon-bottleneck* strategy of slowing down carrier relaxation by strong coupling of electrons to cooperative lattice modes.

DOI: [10.1103/PhysRevApplied.14.054006](https://doi.org/10.1103/PhysRevApplied.14.054006)

### I. INTRODUCTION

Establishing new mechanisms that overcome the constraints for photovoltaic energy conversion of conventional semiconductors due to transmission and thermalization losses is a high-priority goal of third-generation photovoltaics, for example, highly efficient solar cells that are based on thin films [1,2]. A primary goal to achieve higher efficiency is to overcome the Shockley-Queisser limit in semiconductors [3]. It arises from transmission losses of photons with energy below the bandgap as well as thermalization losses of hot carriers excited above the bandgap. The harvesting of *hot* carriers that normally undergo fast subpicosecond thermalization by scattering on optical phonons would be a major step into that direction. The

concept of a *phonon bottleneck* as a strategy to slow down the thermalization of hot carriers has been proposed [4,5], i.e., carriers that are excited above the lower edge of the valence band. The phonon-bottleneck strategy aims for a reduction of energy loss of hot carriers via scattering on optical phonons, and subsequent dissipation and transport of the energy. It was successfully established in semiconductor quantum-dot systems [6,7]. Surprisingly, in some of these systems the excited-state stabilization of hot carriers occurred via strong coupling of coherent electron and phonon states in a confined geometry [8] rather than by a simple reduction of the phonon scattering.

Such strong coupling can result in hot polarons with lifetimes of tenths of picoseconds [6]. The hot-polaron lifetime is limited only by the stability of the electron-phonon coupling in the excited state as well as the lifetime of the constituting particles, the electron, and the optical phonon. Therefore, in the absence of dipole relaxation that reduces the lifetime of the charge and anharmonicity that reduces the lifetime of the phonon, the hot-polaron state would be a long-lasting state that can be harvested by extraction of the hot carriers via an interface. It was recently shown that such a *phonon-bottleneck*

\*cjooss@gwdg.de

Published by the American Physical Society under the terms of the [Creative Commons Attribution 4.0 International](https://creativecommons.org/licenses/by/4.0/) license. Further distribution of this work must maintain attribution to the author(s) and the published article's title, journal citation, and DOI.

strategy via strong electron-phonon coupling can be generalized to other material systems such as high-performance halide-perovskite solar cells that show polaron quasiparticles with long lifetime of hundreds of picoseconds [9–11].

Perovskite oxide thin films are an emerging system for next-generation solar cells due to strong and broad-band infrared-to-visible photon absorption and high stability in photoelectrochemical applications [12]. However, the slowdown of Mn  $3d e_g$ -intra-band carrier cooling by formation of small polarons is typically restricted to low temperatures and defect trapping [13]. In doped manganite perovskites, small Jahn-Teller (JT) and Zener polarons can be formed in the strong coupling regime [14–16]. Here, a dipole-allowed polaron excitation suitable for light harvesting exists within the Mn  $3d e_g$ -O  $2p$  bands, which are split due to the JT polaron formation [17,18]. In an isolated MnO<sub>6</sub> octahedron, the excitation of an electron from the occupied lower to the unoccupied higher JT split state relaxes through a conical intersection of a *Mexican-hat-like* energy potential surface (EPS) in configuration space within the period of a JT mode, i.e., 70 fs [19]. This EPS represents the electron energy as a function of the displacement of the atoms. In contrast to the excitations in a single JT split MnO<sub>6</sub> octahedron, the JT excitations in a three-dimensional (3D) periodic lattice of MnO<sub>6</sub> octahedra exhibit a complex cooperative JT polaron and orbital dynamics, which can develop long-range correlations in the charge-ordered (CO) and orbital-ordered (OO) state [20]. We suggest that these long-range correlations of phonon modes involved in the polaron state represent an alternative type of *phonon bottleneck*. They can modify the EPS and thus can prevent the rapid structural relaxation through the conical intersection by local Jahn-Teller dynamics [19]. This enables polaron Mn  $3d e_g$ -intra-band photovoltaic response as demonstrated for Pr<sub>0.65</sub>Ca<sub>0.35</sub>MnO<sub>3</sub> with a charge- and orbital-order transition temperature  $T_{CO} \approx 240$  K [18,21].

In this work, we demonstrate that harvesting of hot-polaron excitations in a charge-ordered small polaron system can be extended to room temperature and thus could provide a general concept for future photovoltaics. Via advanced material design we succeed in the epitaxial growth of two-dimensional (2D) layered Ruddlesden-Popper manganite Pr<sub>0.5</sub>Ca<sub>1.5</sub>MnO<sub>4</sub> (RP PCMO) thin films with  $T_c$  well above room temperature. The high crystal quality and the coherence of the interface to the Nb-doped SrTiO<sub>3</sub> (STNO) single crystal is demonstrated using XRD and TEM. Optical spectroscopy and electrical transport reveal the expected polaron hopping, JT, and charge-transfer transitions at  $T_{CO} \approx 320$  K. The presence of a photovoltaic effect by hot-polaron excitations is demonstrated by the temperature-dependent measurement of current-voltage ( $I$ - $U$ ) characteristics in different spectral ranges.

## II. EXPERIMENTAL METHODS

### A. Film preparation by means of metalorganic aerosol deposition (MAD)

Films with thicknesses of 30 to 200 nm are grown on [011]-oriented STO and STNO substrates using the metalorganic aerosol deposition technique. It is based on the heterogeneous pyrolysis of sprayed liquid solution, which contains a mixture of metalorganic precursors taken in appropriate molar relations. The deposition setup is equipped with an optical pyrometer and ellipsometry for *in situ* growth monitoring. The precursors, acetylacetonates of Mn, Pr, and Ca, are dissolved in dimethylformamide to a concentration of 0.02 to 0.04 mol/l. The molar ratio between precursors in the solution as well as the growth conditions,  $T_{sub} = 800$  °C and deposition rate approximately equal to 0.5 nm/s are thoroughly optimized to allow the synthesis of material with a desired composition and structure.

### B. Film preparation by means of ion-beam sputtering (IBS)

For the optical characterization a thicker epitaxial film of 100 nm thickness is prepared by means of ion-beam sputtering from single target on a single-crystal double-side-polished STO [011] substrate. The deposition parameters for the film are set to  $p_{Ar} = 3 \times 10^{-4}$  mbar (beam neutralizer),  $p_{Xe} = 1 \times 10^{-4}$  mbar (sputter gas) and  $p_{O_2} = 1.4 \times 10^{-4}$  mbar (film oxidation). The temperature of the boron nitride heater is set to  $T = 790$  °C, which corresponds to a substrate surface temperature of approximately  $T_S = 700$  °C. The cooling rate after deposition is 10 °C/min with 20 min holding steps at 690, 490, 290 °C, respectively.

### C. Transmission electron microscopy

The TEM lamellae in cross-section geometry are prepared in an FEI Nova NanoLab Dual Beam focused ion-beam system and thinned to electron transparency using 5 kV during the final step. The subsequent TEM measurements are carried out in an FEI Titan 80–300 operated at 300 kV and equipped with a Gatan Quantum 965 ER image filter. For the acquisition of selective area electron diffraction (SAED) patterns, a 10- $\mu$ m aperture is used, which translates to approximately 170 nm in the image plane. STEM images are taken at 42 pA with an annular dark-field (ADF) detector having an inner and outer acceptance semi-angle of 46.8 and 200 mrad at the given camera length of 38 mm. For the electron energy-loss spectroscopy (EELS) data acquisition with a collection semiangle of 39 mrad, the beam current is increased to 150 pA and the resulting signals are analyzed using the power-law background subtraction routine of HyperSpy v1.4.2. [22].

#### D. Electric characterization

The four-probe in-plane electrical resistance of RP PCMO films is measured on insulating [011] STO substrates with silver-paste top contacts. The measurements are performed in a PPMS setup in the temperature range of  $T = 150\text{--}400$  K and applied magnetic fields  $B = 0\text{--}9$  T.

#### E. Optical characterization

Optical spectroscopy is performed in a transmission and reflection setup in a UV-vis range of wavelength,  $\lambda = 200\text{--}1100$  nm and in transmission in the NIR range,  $\lambda = 900\text{--}2500$  nm. In the UV-vis range the setup consists of an ‘‘OceanOptics DH-2000’’ Halogen light source, a fiberglass QP400-2-SR-BX, and Maya2000Pro spectrometer. The NIR setup includes a light source HL-2000-FHSA, a fiber QP400-2-SR-BX, and a NIR Quest512-2.5 spectrometer. For all measurements, a dark spectrum is subtracted by the equipment software. The transmittance is calculated by  $I = I_T/I_0$ , where  $I_0$  is the incident and  $I_T$  is the transmitted spectrally resolved intensity. This baseline correction eliminates contributions from the sample holder and mirror system. A fixed reflectance value of  $R_0 = 0.3$  is assumed over the entire spectral range (for additional details see the Supplemental Material [23]).

### III. RESULTS AND DISCUSSION

#### A. Epitaxial growth of Ruddleson-Popper PCMO

The orthorhombic crystal structure of RP PCMO is comprised of a perovskite layer  $AMnO_3$  ( $A = \text{Pr, Ca}$ ) separated by a rock-salt-layer  $AO$  (see inset Fig. 1), yielding a 2D network of  $MnO_6$  octahedra. The RP PCMO belongs to the space group  $Fmm2$  with  $a = 0.5365$  nm,  $b = 0.5354$  nm, and  $c = 1.1840$  nm [24]. We prepare high-quality epitaxial heterojunctions of RP PCMO/ $\text{SrTi}_{0.995}\text{Nb}_{0.005}\text{O}_3$  (STNO) with thicknesses between 30 and 200 nm grown by means of MAD [25,26] on (011) STNO substrates. In addition, a comparative study by ion-beam sputtering is pursued (for details see the Supplemental Material [23]). All films grown on (011) STNO substrates exhibit an orthorhombic structure with of  $[100]_{\text{RP}}$ , respectively,  $[010]_{\text{RP}} \parallel [011]_{\text{STO}}$  and in-plane alignment of their  $c$  axis  $[001]_{\text{RP}} \parallel [100]_{\text{STO}}$ .

The out-of-plane epitaxial relation is confirmed by XRD (Fig. 1). The experimentally observed  $(200)_{\text{RP}}/(020)_{\text{RP}}$  peak corresponds to a lattice spacing of  $d_{hkl} = 0.268$  nm, indicating a very small out-of-plane strain, despite the expected large tensile strain of 3% due to the lattice mismatch between RP PCMO and STNO. In addition, the Laue fringes around the  $(200)_{\text{RP}}/(020)_{\text{RP}}$  peak imply uniform lattice spacing within the whole film. Hence, the films are fully relaxed.

In order to get insight into the microstructure of the RP films, STEM is performed on cross-section lamellas prepared along the  $[01\bar{1}]$  and  $[100]$  directions of the STNO

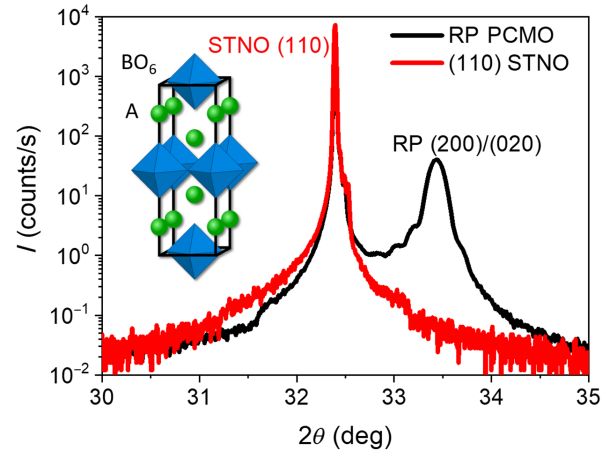


FIG. 1. XRD patterns of a 30-nm-thick MAD RP PCMO film on (011) STO and a blank substrate. Inset: pseudotetragonal representation of the RP  $(AA'BO_3)_1(AA'O)_1$  structure.

substrate, respectively. Figure 2(a) shows a high-resolution annular dark-field (ADF) STEM image of the lamella in the  $[01\bar{1}]$  zone axis, confirming the  $c$ -axis alignment along  $[100]_{\text{STO}}$  and the formation of a coherent manganite-titanite interface. Furthermore, a rather high density of planar defects aligned perpendicular to the substrate is visible, which appear at about 5 nm above the interface. High-resolution ADF imaging [Fig. 2(b)] provides evidence that the planar defects along the  $c$  axis are stacking faults, a typical defect in RP phases. Such planar defects are not visible perpendicular to the  $c$  axis, where misfit dislocations dominate.

Selective area electron diffraction confirms that the  $c$  axis of the RP PCMO is aligned along the  $[100]$  in-plane direction of STNO [Fig. 2(d)]. Note that the out-of-plane reflections of STNO and PCMO overlap. Furthermore, a discrimination between the RP PCMO  $[100]$  and RP PCMO  $[010]$  orientations along the growth direction cannot be made due to the small difference of the  $a$ - and  $b$ -lattice parameters. In the in-plane direction, the STNO (001) and RP PCMO (002) reflections can be distinguished. The blurring of the RP PCMO (002) diffraction spot indicates the presence of disorder in this direction. A high density of planar defects along the  $c$  direction is indeed clearly visible in the STEM image shown in Fig. 2(a).

Such planar defects are not observed perpendicular to the RP  $c$  axis. High-resolution ADF STEM imaging of the interface along the STO  $[01\bar{1}]$  direction shows a semicoherent interface with misfit dislocations (Fig. 3).

The bright contrast close to the interface in Fig. 2(a) suggests a deviation in chemical composition within the first 5 nm. In fact, high-resolution chemical analysis across the interface by means of electron energy-loss spectroscopy (EELS) reveals an increased Pr and a reduced Ca content in this region [Fig. 2(c)]. The Pr enrichment is associated with

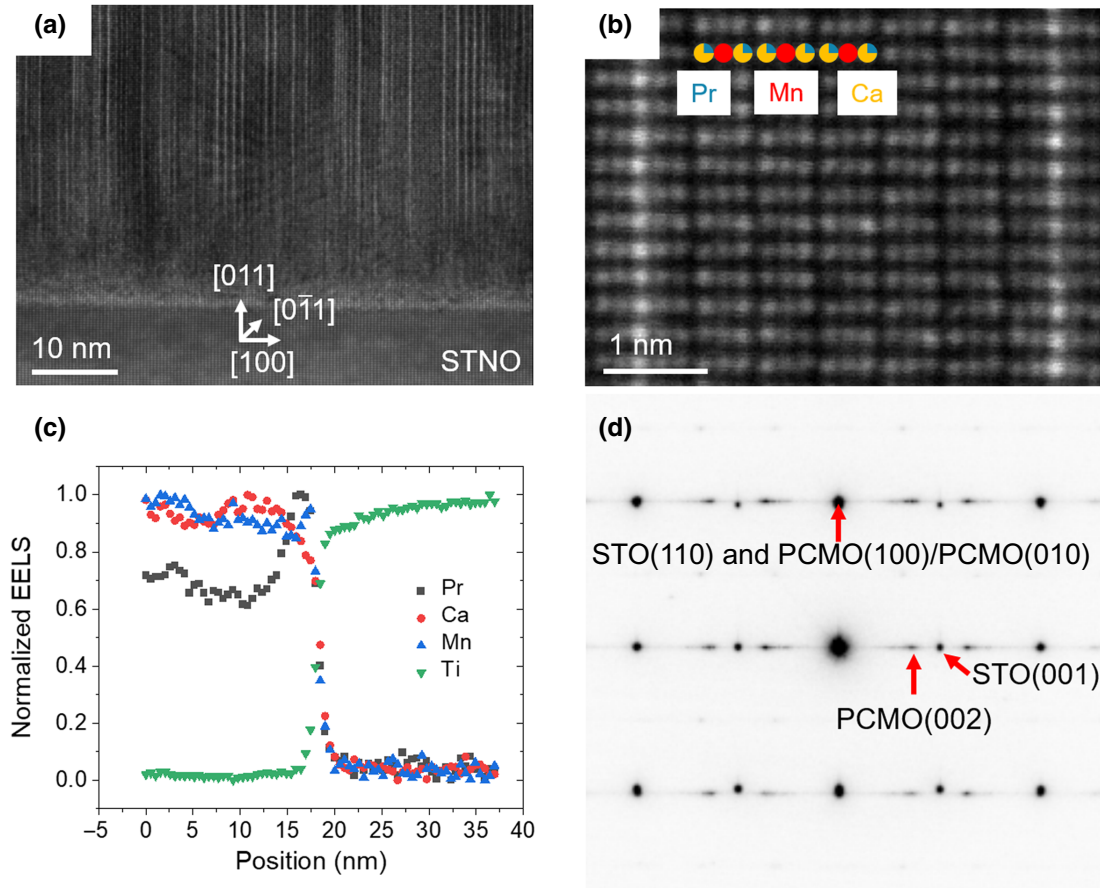


FIG. 2. Cross-section TEM imaging of RP PCMO on (011) STNO. The TEM lamella is prepared by focused ion-beam etching with the [011] zone axis of the STNO substrate. (a) High-resolution ADF STEM image of the film. (b) Enlarged picture of an area in (a). (c) Profile of the integrated EELS counts of the Ca, Ti, and Mn L as well as Pr M edge after power-law background subtractions normalized by the maximum. The concentration profiles across the interface between RP PCMO and STNO shows Pr segregation close to the interface. The RP layer sequence is visualized by the colored column markers. (d) Selective area electron diffraction pattern in the STO [011] zone axis shows reflections from the RP PCMO film and the STNO substrate due to the finite size of the SAED aperture.

an increase of the lattice parameters [27], suggesting that it represents an efficient misfit strain-relaxation mechanism that enables the growth of essentially strain-free films.

### B. Transport and optical properties

The epitaxial RP PCMO films exhibit a remarkably high charge-ordering transition temperature of  $T_{CO} = 320$  K well above room temperature that agrees well with the  $T_{CO}$  of single crystals [26]. The CO transition is deduced from the changes in the temperature dependence of the in-plane electric resistivity,  $\rho(T)$ , measured along the  $c$  axis of RP PCMO films grown on insulating STO (011) substrates. The exponential increase with decreasing temperature is consistent with thermally activated hopping mobility of small polarons [28] in the adiabatic limit:

$$\rho(T) = \rho_0 T e^{\frac{E_{act}}{kT}}. \quad (1)$$

Here,  $T$  denotes temperature and  $k$  the Boltzmann constant. In the disordered phase ( $T > T_{CO}$ ),  $\rho(T)/T$  obeys an Arrhenius-type behavior with constant prefactor  $\rho_0$  and activation energy  $E_{act}$ . The activation energy is modified in the charge-ordered phase, which allows for extracting  $T_{CO}$  from  $\rho(T)$ . Figure 4(a) shows the associated deviation of the measured resistance  $(R_{meas} - R_{DO})/R_{DO}$ , where  $R_{DO}$  represents the Arrhenius fit of Eq. (1) in the disordered (DO) phase, i.e., for  $T > T_{CO}$ . This yields a polaron activation energy  $E_{act,DO} \approx 163$  meV in the disordered phase. The inset of Fig. 4(a) depicts the changes in the temperature dependent activation energy by the phase transition obtained by differentiation of the data with respect to inverse temperature (see Ref. [29] for details). As expected, a pronounced increase of  $E_{act}(T)$  in the charge-ordered phase ( $T < T_{CO} \approx 320$  K) is observed in complete (and even quantitative) agreement to 3D bulk manganites [29]. As a noteworthy secondary result, Fig. 4(a) further

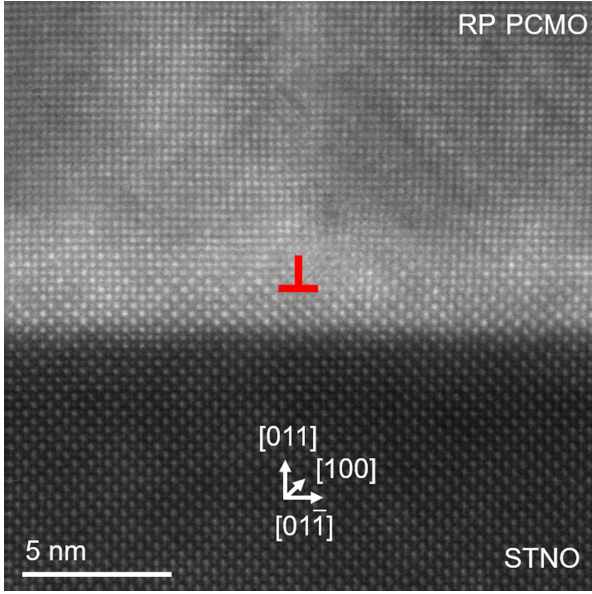


FIG. 3. High-resolution ADF STEM image of the interface of MAD grown RP PCMO on STO in the STO [100] zone axis. A misfit dislocation is marked by the red symbol.

shows that  $T_{CO}$  is independent of film thickness (compare data of the 200-nm-thick film), whereas the increase of  $E_{act}$  in the charge-ordered state is smaller for the smaller thickness. The latter is attributed to a higher amount of disorder and residual strain. Nevertheless, the observed increase of the activation energy by about 20–30 meV for the thin film is consistent with results obtained by Ibarra *et al.* in polycrystallite RP manganites ( $0.5 \leq x \leq 0.8$ ) [26].

Optical absorption measurements in Fig. 4(b) show the dominant contribution of small polaron absorption in the infrared and visible spectral range  $0.6 \text{ eV} \leq h\omega \leq 2.1 \text{ eV}$  and charge-transfer transitions for  $h\omega \geq 2.1 \text{ eV}$ , in qualitative agreement with spectra of single crystals [30]. The presented spectrum can be well approximated by three Gaussian peaks located at  $E_A = 0.76 \text{ eV}$ ,  $E_B = 1.3 \text{ eV}$ , and  $E_C = 3.5 \text{ eV}$ . An intensity decrease of the Gaussian peak *A* in the fitted absorption spectra below a limit value of  $1/e$  yields an estimated charge gap of  $E_g \approx 0.57 \text{ eV}$ .

In the following, processes related to the three absorption bands *A*, *B*, and *C* are identified, which is relevant for the interpretation of photovoltaic effects in the system (see Fig. 5). According to the detailed study of 3D PCMO by Mildner *et al.* [18], we assign peak *A* to an optically induced polaron hopping. As is well described by the theory of small polaron absorption [31], such an absorption band will occur at a photon energy  $h\omega$  double of the polaron formation energy  $E_p$  and thus  $E_p = \frac{1}{2}E_A \approx 380 \text{ meV}$ . A completely different route is to estimate  $E_p$  from the activation energy  $E_{act}$  of thermally assisted hopping based on the relation  $E_{act} = 1/2 E_P -$

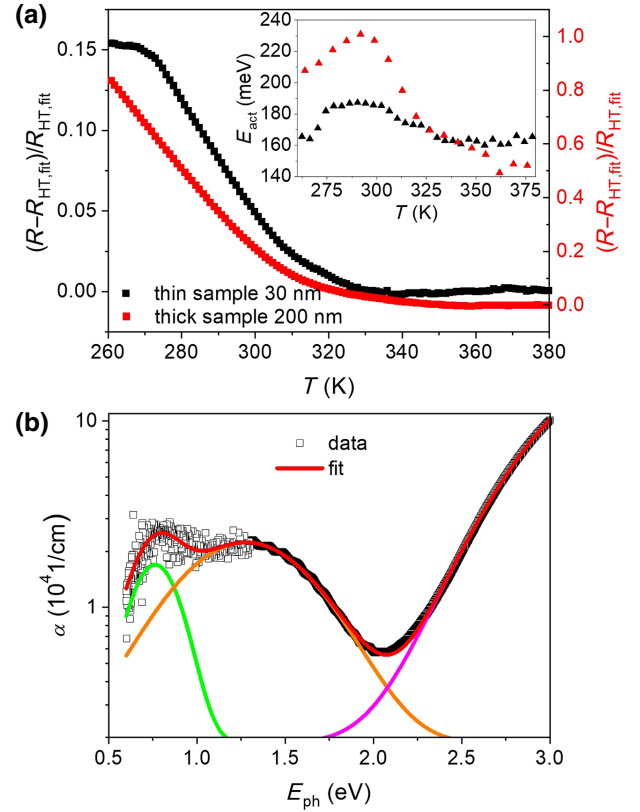


FIG. 4. Transport and optical properties of epitaxial [100]/[010] RP PCMO films on (011) STO. (a) Temperature-dependent deviation of resistance from the HT Arrhenius behavior and obtained temperature dependence of the activation energy (inset) for 30- and 200-nm-thick films. The change in slopes indicates the charge-ordering temperature of  $T_{CO} \approx 320 \text{ K}$ . (b) Spectrum of the absorption coefficient  $\alpha$ , measured for a 100-nm-thick RP PCMO film at room temperature. The experimental data is fitted by three Gaussian peaks, with  $E_A = 0.76 \text{ eV}$  (optical polaron hopping),  $E_B = 1.3 \text{ eV}$  (Jahn-Teller transition), and  $E_C = 3.5 \text{ eV}$  (charge-transfer transitions). The discontinuity in signal-to-noise ratio below 1.3 eV stems from different spectrometers used for the UV and NIR regimes.

*J*. It can, e.g., be derived within the two-site Holstein model [32] and reflects that elastic tunneling between next-neighbor sites requires an isoenergetic configuration of the occupied and unoccupied site. Neglecting the contribution from the transfer integral  $J$ ,  $E_{act} \approx 190 \text{ meV}$  in the charge-ordered phase implies  $E_p \approx 380 \text{ meV}$ . The striking agreement of  $E_p$  derived from electric transport and optical absorption strongly supports optically induced polaron hopping as the underlying microscopic process of absorption band *A*. We note here, that the rather small contributions of band *A* to the photovoltaic cannot be detected within the sensitivity of our photovoltaic setup. Nevertheless, these infrared excitations can induce pronounced

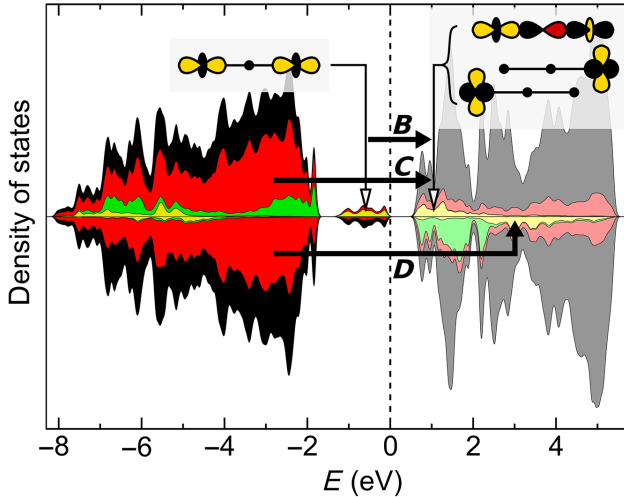


FIG. 5. Density of states of Ruddlesden-Popper  $\text{Pr}_{0.5}\text{Ca}_{1.5}\text{MnO}_4$  obtained from density-functional calculations (for details see Supplemental Material [23]). Majority and minority spin directions are shown with positive and negative sign. The colors correspond to the total density of states (black) and projections onto O  $p$  (red), as well as Mn  $t_{2g}$  (green) and Mn  $e_g$  (yellow) orbitals of the spin-up manganese atoms. The projected densities of states are shown stacked on top of each other; their values correspond to their colored areas. The JT splitting of the Mn  $e_g$  states leads to an occupied nonbonding and three unoccupied states of  $\sigma$  and  $\delta$  character. Small polaron absorption is due to the dipole-allowed optical transition within the Mn  $d$  shell (peak B) from the nonbonding to antibonding  $\sigma$  states. The dipole-allowed charge-transfer transitions (peaks C and D) take place from nonbonding O  $2p$  states to majority and minority spin Mn  $e_g$  states, respectively.

photoenhanced mobility of polarons [33] and thus reduce Ohmic losses.

The absorption band in the UV regime (peak C) has two contributions, i.e., interband transitions in STO (above 3.2 eV) and charge-transfer (CT) transitions in PCMO that are dipole-allowed transitions between nonbonding O  $2p$  states and majority-spin Mn  $3d e_g$  states (see Fig. 5). Also such transitions have polaronic character, since the generated O  $2p$  holes and excited Mn  $3d$  majority spin electrons strongly couple to Jahn-Teller phonons in addition to other phonon modes.

Finally, the key for the hot-polaron photovoltaics reported in this work is photon absorption by band B in the NIR regime. It originates from transitions between Mn  $3d e_g$ -O  $2p$  states that are split due to the Jahn-Teller polaron formation, i.e., they are Mn  $3d e_g$ -intra-band transitions. They are dipole allowed due to their different parity as a result of the hybridization with O  $2p$  orbitals (see Fig. 5). In agreement with 3D PCMO, these states consist of nonbonding and antibonding Jahn-Teller split  $e_g$  states of  $\sigma$ -bond character. Their origin is the hybridization of Mn  $3d e_g$  and O  $2p$  states at half doping that can be described

as a Zener polaron, i.e., two coupled  $\text{MnO}_6$  octahedra [19]. The 3D or 2D topology of the  $\text{MnO}_6$  network only has a minor effect on the resulting DOS. Interestingly, in comparison to 3D perovskites and to the results of Ref. [29], we observe a reduced spectral weight resulting in a larger absorption length of the order of  $\alpha(E_B)^{-1} \approx 400$  nm. This can be attributed to the anisotropic optical properties of the material and the epitaxial growth described above, which forces the  $c$  axis being perpendicular to the incoming light at normal incidence. Before proceeding to the photovoltaic results, it should be emphasized that in contrast to the CT interband transition (absorption band C) typically observed in metal oxides, the polaron transitions of peaks A and B are stemming from Mn  $3d e_g$ -intra-band excitations that establish a pathway of harvesting hot-polaron states.

### C. Temperature-dependent photovoltaic response

We show that charge ordering in the ground state is in fact a prerequisite for harvesting hot Jahn-Teller polarons from the Mn  $3d e_g$ -intra-band transitions of absorption B. In order to characterize the RP PCMO-STNO  $p$ - $n$  heterojunctions current density-voltage ( $J$ - $U$ ) measurements obtained in the dark at different temperature are summarized in Fig. 4(a). They exhibit rectifying characteristics with decreasing reverse-bias current and a shift of their exponential part to higher voltages by decreasing temperature. This behavior is completely in line with 3D PCMO and STNO junctions [6,21]. Within the one-diode model this behavior can be attributed to the increase of the diode ideality factor as well as of the shunt resistance, whereas contributions from series resistance to the total resistance is negligibly small.

Polychromatic illumination with a Xe-UV lamp leads to a photovoltaic effect with a downwards shift of the  $J(U)$  curve [Fig. 6(b)]. According to the absorption bands described above, two main spectral ranges are distinguished: (i) charge-transfer interband excitations at photon energies of 2.2–4 eV, and (ii) low-energy Mn  $3d e_g$ -intra-band excitations for 0.5–2.2 eV due to photoinduced hopping and Jahn-Teller-like excitations of small polarons. To separate these excitation processes, Fig. 6(b) shows the photovoltaic effect for a cut-off filter of 2.0 eV where the photocurrent results from A and B absorption bands of the polaron excitations.

For a concise presentation of the temperature dependence, we use the open-circuit voltage  $U_{OC}$  for different spectral ranges [22] as shown in Fig. 6(c) for the RP PCMO thin films and—for comparison—for 3D PCMO perovskites. In addition to a full polychromatic illumination by the Xe lamp, the maximum excitation energy is limited by introducing different cut-off filters. The contribution of excitations at  $\hbar\omega \leq 1.6$  eV is rather small at room temperature but it increases considerably below 230 K. These excitations involve the optical polaron hopping

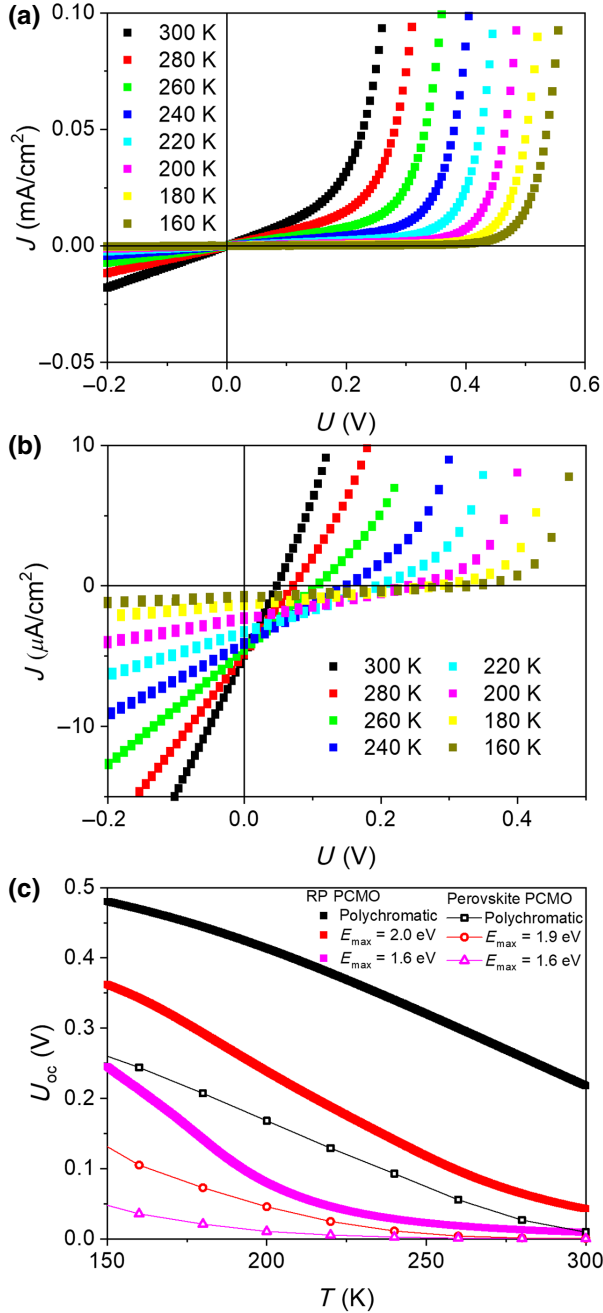


FIG. 6. Electric and photovoltaic characteristics of RP PCMO and STNO heterojunctions (a) Current density versus voltage as a function of temperature in the dark. (b) The same under illumination with low-pass filter for  $\hbar\omega \leq 2.0$  eV photon energy. (c) Open-circuit voltage  $U_{OC}$  versus temperature for limited spectral illumination ranges. For comparison, data for heterojunctions of the 3D perovskite  $\text{Pr}_{0.66}\text{Ca}_{0.34}\text{MnO}_3$  on STNO is also included.

(peak  $A$ ) as well as the major spectral weight of the Jahn-Teller transition (peak  $B$ ). Only photon energies above the peak- $B$  maximum are able to excite polarons into a long-living state. Increasing the spectral range from  $\hbar\omega \leq 1.6$  e

to  $\hbar\omega \leq 2.0$  eV strongly impacts the photovoltaic effect at room temperature. The open-circuit voltage  $U_{OC}$  increases from 9 to 42 mV due to the excitations of the upper shoulder of peak  $B$ . Above the peak maximum, the hot polaron forms a state where the Mn  $e_g$  population is inconsistent with its JT distortion and thus presumably underlies a long-range cooperative dynamics, similar to the one which has been observed in the 3D PCMO system [20] and is theoretically described by Rajpurohit *et al.* [34].

Under polychromatic illumination  $U_{OC}$  increases to 220 mV at 300 K mostly due to the charge-transfer transitions in peak  $C$ . Furthermore, at photon energies above 3.2 eV, one can expect a contribution of band-band excitations in STNO to the photovoltaic effect, with electron-hole pairs contributing both from the titanate and the manganite.

For comparison,  $U_{OC}(T)$  data of the 3D perovskite-based  $\text{Pr}_{0.66}\text{Ca}_{0.34}\text{MnO}_3/\text{STNO}$  heterojunctions is included in Fig. 6(c) [21]. In the 3D perovskites significant photovoltaic contributions due to polaronic electron-hole pair excitations only occur below the charge-order temperature  $T_{CO} \approx 240$  K, where such excitations reach sufficiently long lifetimes [19]. For the RP PCMO and STNO system,  $T_{CO} \approx 320$  K results in pronounced polaron contributions to the photovoltaic effect even at room temperature, as is shown in Fig. 6(c). Therefore, it can be concluded, that the underlying longer lifetime of Mn  $e_g$ -intra-band hot-polaron excitations with energies above the charge gap are emerging only in the charge- and orbital-ordered state.

#### IV. CONCLUSION

In summary, a room-temperature polaron photovoltaic effect is demonstrated in high-quality junctions of epitaxial RP PCMO on (011) STNO with charge-ordering temperature of  $T_{CO} = 320$  K. Although the individual properties of small polarons in the RP PCMO with formation energy of  $E_p = 0.38$  eV are more or less unchanged compared to the 3D PCMO ( $E_p = 0.36$ – $0.38$  eV [18]), the photovoltaic effect is remarkably enhanced. This result provides evidence that going from a 3D to a quasi-2D network of  $\text{MnO}_6$  octahedra changes the polaronic interactions and leaves their intrinsic properties virtually unaffected. That emphasizes again the key feature of cooperative hot-polaron behavior for photovoltaic energy conversion. In fact, the observation of Mn  $3d e_g$ -intra-band polaron photovoltaics being linked to the charge- and orbital-ordered state underlines the role of cooperative octahedral dynamics for the stabilization of long-living hot polarons. The polaron relaxation time in the CO and OO state may depend on both amplitude as well as long-range coherence of the involved lattice dynamics and, thus, depend on the excitation intensity [19–21]. Our result of polaron photovoltaic effect in the CO and OO state of the RP PCMO systems together with previous results of low-temperature polaron photovoltaics in ordered states of 3D manganites [21]

suggests a promising different type of “phonon-bottleneck” mechanism for slowing down the carrier thermalization. The emergence of a coherent lattice oscillation of the CO and OO superlattice reflections as observed by Beaud [35] may avoid the fast structural relaxation as expected for the incoherent dynamics of individual JT polarons. Our work demonstrates that room-temperature photovoltaic energy conversion in the visible to infrared spectral range in complex oxides with a small or vanishing band gap in the excitation spectrum by hot polarons is feasible. It moreover implies that material design along the route of improving excess carrier lifetime through involved phonon states that are strongly coupled to the charge carriers and display pronounced long-range coherence can serve as a blueprint to enhance the efficiency of hot-polaron photovoltaics.

### ACKNOWLEDGMENTS

The authors thank K. Stroh for the help in optical spectroscopy measurements and the authors are thankful for funding by the Deutsche Forschungsgemeinschaft (DFG, German Research Foundation-217133147/SFB 1073, projects A02, B02, B03, Z02). The use of equipment in the “Collaborative Laboratory and User Facility for Electron Microscopy” (CLUE) is gratefully acknowledged.

- 
- [1] M. Green, *Third Generation Photovoltaics* (Springer, Berlin Heidelberg, 2003).
- [2] M. A. Green and S. P. Bremner, Energy conversion approaches and materials for high-efficiency photovoltaics, *Nat. Mater.* **16**, 23 (2017).
- [3] W. Shockley and H. J. Queisser, Detailed balance limit of efficiency of p-n junction solar cells, *J. Appl. Phys.* **32**, 510 (1961).
- [4] H. Benisty, C. M. Sottomayor-Torres, and C. Weisbuch, Intrinsic mechanism for the poor luminescence properties of quantum-box systems, *Phys. Rev. B* **44**, 10 945 (1991).
- [5] G. Conibeer, S. Shrestha, S. Huang, R. Patterson, H. Xia, Y. Feng, P. Zhang, N. Gupta, M. Tayebjee, S. Smyth, *et al.*, Hot carrier solar cell absorber prerequisites and candidate material systems, *Sol. Energy Mater. Sol. C.* **135**, 124 (2015).
- [6] S. Sauvage, P. Boucaud, R. P. S. M. Lobo, F. Bras, G. Fishman, R. Prazeres, F. Glotin, J. M. Ortega, and J.-M. Gérard, Long Polaron Lifetime in InAs/GaAs Self-Assembled Quantum Dots, *Dots Phys. Rev. Lett.* **88**, 177402 (2002).
- [7] W. A. Tisdale, K. J. Williams, B. A. Timp, D. J. Norris, E. S. Aydil, and X.-Y. Zhu, Hot-Electron transfer from semiconductor nanocrystals, *Science* **328**, 1543 (2010).
- [8] S. Hameau, Y. Guldner, O. Verzellen, R. Ferreira, G. Bastard, J. Zeman, A. Lemaitre, and J. M. Gérard, Strong Electron-Phonon Coupling Regime in Quantum Dots: Evidence for Everlasting Resonant Polarons, *Phys. Rev. Lett.* **83**, 4152 (1999).
- [9] J. Moore Frost, L. D. Whalley, and A. Walsh, Slow cooling of Hot polarons in halide perovskite solar cells, *ACS Energy Lett.* **2**, 2647 (2017).
- [10] M. Park, A. J. Neukirch, S. E. Reyes-Lillo, M. Lai, S. R. Ellis, D. Dietze, J. B. Neaton, P. Yang, S. Tretiak, and R. A. Mathies, Excited-state vibrational dynamics toward the polaron in methylammonium lead iodide perovskite, *Nat. Commun.* **9**, 2525 (2018).
- [11] D. Ghosh, E. Welch, A. J. Neukirch, A. Zakhidov, and S. Tretiak, Polarons in halide perovskites: A perspective, *J. Phys. Chem. Lett.* **11**, 3271 (2020).
- [12] M. Lira-Cantu, *The Future of Semiconductor Oxides in Next-Generation Solar Cells* (Elsevier, Amsterdam, 2018).
- [13] O. Bidault, M. Maglione, M. Actis, M. Kchikech, and B. Salce, Polaronic relaxation in perovskites, *Phys. Rev. B* **52**, 4191 (1995).
- [14] G. Zhao, K. Conder, H. Keller, and K. A. Müller, Giant oxygen isotope shift in the magnetoresistive perovskite  $\text{La}_{1-x}\text{Ca}_x\text{MnO}_{3+y}$ , *Nature* **381**, 676 (1996).
- [15] G. Zhao, Y. S. Wang, D. J. Kang, W. Prellier, M. Rajeswari, H. Keller, T. Venkatesan, C. W. Chu, and R. L. Greene, Evidence for the immobile bipolaron formation in the paramagnetic state of the magnetoresistive manganites, *Phys. Rev. B* **62**, R11 949 (2000).
- [16] M. Sotoudeh, S. Rajpurohit, P. E. Blöchl, D. Mierwaldt, J. Norpoth, V. Roddatis, S. Mildner, B. Iffland, and C. Jooss, Electronic structure of  $\text{Pr}_{1-x}\text{Ca}_x\text{MnO}_3$ , *Phys. Rev. B* **95**, 235150 (2017).
- [17] J. H. Jung, K. H. Kim, D. J. Eom, T. W. Noh, E. J. Choi, J. Yu, Y. S. Kwon, and Y. Chung, Determination of electronic band structures of  $\text{CaMnO}_3$  and  $\text{LaMnO}_3$  using optical-conductivity analyses, *Phys. Rev. B* **55**, 15489 (1997).
- [18] S. Mildner, J. Hoffmann, C. Jooss, P. E. Bloechl, and S. Techert, Temperature- and doping-dependent optical absorption in the small-polaron system  $\text{Pr}_{1-x}\text{Ca}_x\text{MnO}_3$ , *Phys. Rev. B* **92**, 035145 (2015).
- [19] D. Raiser, S. Mildner, B. Iffland, M. Sotoudeh, P. Blöchl, S. Techert, and Ch. Jooss, Contribution of Jahn-Teller and charge transfer excitations to the photovoltaic effect of manganite/titanite heterojunctions, *Adv. Energy Mater.* **7**, 1602174 (2017).
- [20] P. Beaud, A. Caviezel, S. O. Mariager, L. Rettig, G. Ingold, C. Dornes, S.-W. Huang, J. A. Johnson, M. Radovic, T. Huber, *et al.*, A time-dependent order parameter for ultrafast photoinduced phase transitions, *Nat. Mater.* **13**, 923 (2014).
- [21] B. Iffland, J. Hoffmann, B. Kressdorf, V. Roddatis, M. Seibt, and Ch. Jooss, Contribution of Jahn-Teller and charge transfer excitations to the photovoltaic effect of manganite/titanite heterojunctions, *New J. Phys.* **19**, 063046 (2017).
- [22] F. de la Peña, E. Prestat, V. T. Fauske, *et al.*, 2019 hyperspy/hyperspy: v1.4.2.
- [23] See Supplemental Material at <http://link.aps.org/supplemental/10.1103/PhysRevApplied.14.054006> for a detailed description of electrical and optical characterization, density of state calculations, and additional x-ray diffraction and TEM studies of IBS-prepared thin films. Includes Refs. [16,36–40].
- [24] M. Ebrahimizadeh Abrishami, M. Risch, J. Scholz, V. Roddatis, N. Osterthun, and C. Jooss, Oxygen evolution at manganite perovskite ruddlesden-popper type particles: Trends of activity on structure, valence and covalence, *Materials* **9**, 921 (2016).



- [25] M. Jungbauer, S. Hühn, R. Egovail, H. Tan, J. Verbeeck, G. Tandeloo, and V. Moshnyaga, Atomic layer epitaxy of ruddlesden-popper  $\text{SrO}(\text{SrTiO}_3)_n$  films by means of metalorganic aerosol deposition, *APL* **105**, 251603 (2014).
- [26] A. Belenchuk, O. Shapoval, V. Roddatis, V. Bruchmann-Bamberg, K. Samwer, and V. Moshnyaga, Ruddlesden-Popper interface in correlated manganite heterostructures induces magnetic decoupling and dead layer reduction, *APL* **109**, 232405 (2016).
- [27] M. Ibarra, R. Retoux, M. Hervieu, C. Autret, A. Maignan, C. Martin, and B. Raveau, Charge-orbital ordering above room temperature in the 2D  $\text{Pr}_{1-x}\text{Ca}_{1+x}\text{MnO}_4$  manganites, *J. Solid State Chem.* **170**, 361 (2003).
- [28] V. V. Bryksin and H. Böttger, *Hopping Conduction in Solids*, 1st ed. (VCH, Weinheim, 1985).
- [29] J. Hoffmann, P. Moschkau, S. Mildner, J. Norpoth, Ch. Jooss, L. Wu, and Y. Zhu, Effects of interaction and disorder on polarons in colossal resistance manganite  $\text{Pr}_{0.68}\text{Ca}_{0.32}\text{MnO}_3$  thin films, *Mater. Res. Express* **1**, 046403 (2014).
- [30] M. A. Majidi, E. Thoeng, P. K. Gogoi, F. Wendt, S. H. Wang, I. Santoso, T. C. Asmara, I. P. Handayani, P. H. M. van Loosdrecht, A. A. Nugroho, *et al.*, Temperature-dependent and anisotropic optical response of layered  $\text{Pr}_{0.5}\text{Ca}_{1.5}\text{MnO}_4$  probed by spectroscopic ellipsometry, *Phys. Rev. B* **87**, 235135 (2013).
- [31] D. Emin, Optical properties of large and small polarons and bipolarons, *Phys. Rev. B* **48**, 13691 (1993).
- [32] T. Holstein, Studies of polaron motion, studies of polaron motion: Part I. The molecular-crystal model, *Ann. Phys.* **8**, 325 (1959).
- [33] J. F. Xi, K. Zhao, H. Ni, W. F. Xiang, X. Feng, Q. Sun, Z. Q. Lu, and L. Z. Xiao, Giant negative photoresistance of epitaxialmanganite  $\text{La}_{2/3}\text{Ca}_{1/3}\text{MnO}_{3-\delta}$  film, *Sci. China* **58**, 122402 (2015).
- [34] S. Rajpurohit, Ch. Jooss, and P. E. Blöchl, Evolution of the magnetic and polaronic order of  $\text{Pr}_{1/2}\text{Ca}_{1/2}\text{MnO}_3$  following an ultrashort light pulse, *Phys. Rev. B* **102**, 014302 (2020).
- [35] P. Beaud, S. L. Johnson, E. Vorobeva, U. Staub, R. A. De Souza, C. J. Milne, Q. X. Jia, and G. Ingold, Ultrafast Structural Phase Transition Driven by Photoinduced Melting of Charge and Orbital Order, *Phys. Rev. Lett.* **103**, 155702 (2009).
- [36] I. P. Handayani, A. A. Nugroho, S. Riyadi, G. R. Blake, N. Mufti, T. T. M. Palstra, and P. H. M. van Loosdrecht, Correlation between lattice vibrations with charge, orbital, and spin ordering in the layered manganite  $\text{Pr}_{0.5}\text{Ca}_{1.5}\text{MnO}_4$ , *Phys. Rev. B* **92**, 205101 (2015).
- [37] P. E. Blöchl, Projector augmented-wave method, *Phys. Rev. B* **50**, 17953 (1994).
- [38] Peter E. Blöchl and Clemens Först, „Node-less atomic wave functions, Pauli repulsion and systematic projector augmentation” arXiv:1210.5937 [physics.chem-ph].
- [39] O. K. Andersen and O. Jepsen, Explicit, First-Principles Tight-Binding Theory, *Phys. Rev. Lett.* **53**, 2571 (1984).
- [40] E. O. Wollan and W. C. Koehler, Neutron diffraction study of the magnetic properties of the series of perovskite-type compounds  $[(1-x)\text{La}_x\text{Ca}]\text{MnO}_3$ , *Phys. Rev.* **100**, 545 (1955).

## Chapter 5

# Orbital-order Phase Transition in $\text{Pr}_{1-x}\text{Ca}_x\text{MnO}_3$ probed by Photovoltaics

This Chapter contains an article published in Phys. Rev. B **103**, 235122 (2021).

doi: 10.1103/PhysRevB.103.235122

The article is reprinted in its original form in accordance with the obtained reuse and permissions license. The corresponding Supplemental Material is included in Appendix B.

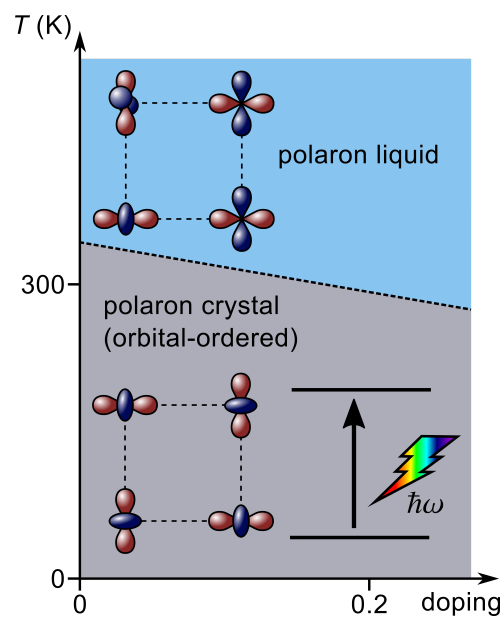


Figure 5.1: Teaser for the article (as published on Phys Rev B homepage): Schematic overview of the adjusted phase diagram and the low-temperature orbital order transition.

**Orbital-order phase transition in  $\text{Pr}_{1-x}\text{Ca}_x\text{MnO}_3$  probed by photovoltaics**B. Kressdorf<sup>1</sup>, T. Meyer<sup>2</sup>, M. ten Brink<sup>3,4</sup>, C. Seick<sup>5</sup>, S. Melles<sup>1</sup>, N. Ottinger<sup>1</sup>, T. Titze<sup>5</sup>, H. Meer<sup>5</sup>, A. Weisser<sup>5</sup>, J. Hoffmann<sup>1</sup>, S. Mathias<sup>5</sup>, H. Ulrichs<sup>5</sup>, D. Steil<sup>5</sup>, M. Seibt<sup>2</sup>, P. E. Blöchl<sup>3,4</sup> and C. Jooss<sup>1,\*</sup><sup>1</sup>University of Göttingen, Institute of Materials Physics, 37077 Göttingen, Germany<sup>2</sup>University of Göttingen, 4th Institute of Physics, 37077 Göttingen, Germany<sup>3</sup>Clausthal University of Technology, Institute of Theoretical Physics, 38678 Clausthal-Zellerfeld, Germany<sup>4</sup>University of Göttingen, Institute of Theoretical Physics, 37077 Göttingen, Germany<sup>5</sup>University of Göttingen, 1st Institute of Physics, 37077 Göttingen, Germany

(Received 15 January 2021; revised 31 March 2021; accepted 4 May 2021; published 11 June 2021)

The phase diagram of  $\text{Pr}_{1-x}\text{Ca}_x\text{MnO}_3$  (PCMO) is modified for  $x \leq 0.3$ , which suggests a reevaluation of the phase diagram of other manganites in that doping region. Rather than an orbital-ordered phase reaching up to high temperatures of  $\sim 800$ – $1100$  K, we propose a loss of spontaneous orbital order near room temperature. Above this temperature, the phase is characterized by a finite orbital polarization and octahedral tilt pattern. The tilt pattern couples to the Jahn-Teller distortion and thus induces a remaining orbital order, which persists up to high temperatures, where the tilt order is lost as well. This explains the experimental observation of orbital order up to high temperatures. The reevaluation of the orbital-order transition is based on observed anomalies of various physical properties at temperatures of  $220$ – $260$  K in epitaxial thin films of PCMO  $x = 0.1$ , i.e., in the photovoltaic effect, electric transport, magnetization, optical, and ultrafast transient pump probe studies. Finite-temperature simulations based on a tight-binding model with carefully adjusted parameters from first-principles calculations exhibit an orbital-order phase transition at  $T_{\text{OO}} \approx 300$  K for PCMO  $x = 0.1$ . This is consistent with the experimental observation of temperature-dependent changes in lattice parameter for bulk samples of the same doping at  $300$  K for  $x = 0.1$  and  $350$  K for  $x = 0$ , typical for second-order phase transitions. Since our reassignment of the orbital-order phase transition toward lower temperature challenges a well-established and long-accepted picture, we provide results of multiple complementary measurements as well as a detailed discussion.

DOI: [10.1103/PhysRevB.103.235122](https://doi.org/10.1103/PhysRevB.103.235122)**I. INTRODUCTION**

Perovskite manganites are a class of materials with strongly correlated electronic, spin, and phonon degrees of freedom. These correlations result in a complex phase diagram and a variety of exciting phenomena such as the colossal magnetoresistance [1–3] and photovoltaic [4,5] effects. Because of the Jahn-Teller effect,  $\text{Mn}^{3+}$  ions in manganites experience a strong electron-phonon coupling, which leads to the formation of polarons. The density of these polarons and their electronic coupling can be controlled by composition. Depending on the density, a variety of ordered and disordered polaron arrangements can be formed. Among the manganites, the class of  $\text{Pr}_{1-x}\text{Ca}_x\text{MnO}_3$  (PCMO) stands out because it allows us to explore the effect of doping while maintaining a similar electronic coupling (i.e., Mn-O-Mn hopping) [6]. Furthermore, the electron-phonon coupling in this class of manganites is strong compared to the electron hopping, which results in small, and thus stable, polarons and insulating ground states for the entire doping range [7].

At the heart of the manganite physics is the phase diagram and the nature of its individual phases. In this paper, we provide evidence that the phase diagram for PCMO accepted

so far [8] may need to be reconsidered (see Fig. 1). In the low-doping regime with PCMO  $x = 0$ – $0.2$ , phase transitions at  $900$  K for  $x = 0$  and at  $675$  K for  $x = 0.1$  [8] have been included, which are attributed to the order-disorder transition in the pattern of Jahn-Teller distortions. At higher doping, i.e., PCMO  $x = 0.3$ , orbital and charge orders exist only at a lower temperature up to  $T_{\text{CO}} = 240$  K. Our experimental and theoretical results indicate that, in the low-doping regime, spontaneous orbital order breaks down at temperatures much lower than previously believed. This finding at low temperatures requires a reinterpretation of the high-temperature regime of the phase diagram.

In the highly correlated PCMO, the onset of a photovoltaic effect in the visible-to-infrared spectral range can be linked to the emergence of long-living hot polarons [11,12]. Heterojunctions composed of Nb-doped  $\text{SrTiO}_3$  and PCMO with  $x = 0.34$  and  $0.95$  show such a photovoltaic effect only below their respective ordering temperatures, i.e., in the charge-, orbital-, and antiferromagnetically ordered phases [Fig. 1 (b)]. The connection of the photovoltaic effect to charge and orbital order has been recently demonstrated clearly by the observation of a pronounced photovoltaic effect at room temperature in the Ruddlesden-Popper manganite  $\text{Pr}_{0.5}\text{Ca}_{1.5}\text{MnO}_4$  [13], which has a charge-order transition temperature of  $T_{\text{CO}} \approx 320$  K. This raised the onset temperature of the photovoltaic effect above that of the parent compound PCMO at  $x = 0.34$ . To

\*cjooss@gwdg.de

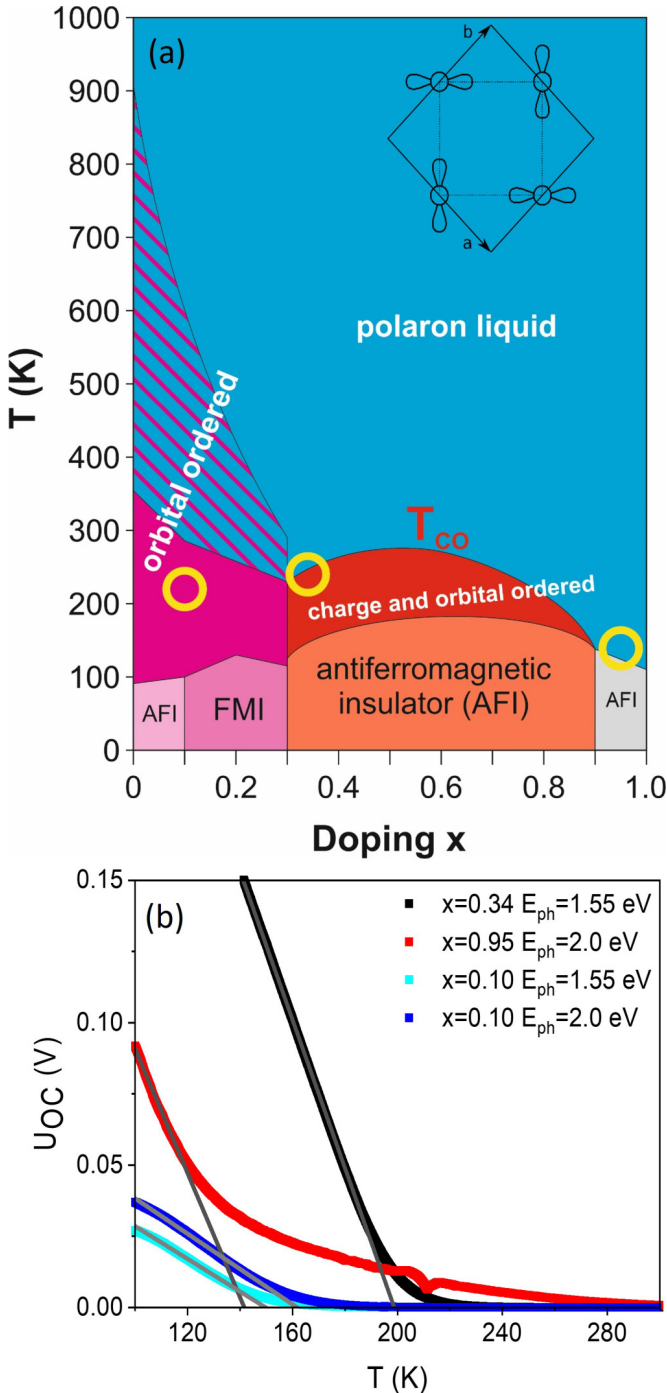


FIG. 1. Ordered states and onset of polaron photovoltaic effect in  $\text{Pr}_{1-x}\text{Ca}_x\text{MnO}_3$  (PCMO). (a) Phase diagram in zero magnetic field according to Refs. [8–10]. Our results on the onset of polaron photovoltaic effect are indicated by yellow circles. Inset: Schematic sketch of orbital-ordered structure of alternating orbitals for PMO. (b) Temperature dependence of the open circuit voltage  $U_{oc}(T)$  in  $\text{Pr}_{1-x}\text{Ca}_x\text{MnO}_3 - \text{SrTi}_{1-y}\text{Nb}_y\text{O}_3$  heterojunctions for  $x = 0.1, 0.34,$  and  $0.95$  for monochromatic photon excitation of lowest manganite transitions. The onset of linear increase coincides with the antiferromagnetic ( $x = 0.95$ ) and the charge-order/orbital-order phase transitions ( $x = 0.34$ ) [11]. As it is shown in this paper, the onset for PCMO  $x = 0.1$  reflects the onset of spontaneous orbital order which is at 220–260 K in thin films and at 300 K in the bulk.

extend the photovoltaic effect to even higher temperatures, we studied lightly doped PCMO with its high orbital-ordering temperature. However, for PCMO  $x = 0.1$ , we observe an onset of the photovoltaic effect only well below room temperature [Fig. 1(b)]. This discrepancy between the onset of the photovoltaic effect and the orbital-order temperature inspired a detailed study of the structural and electronic properties of the temperature-dependent orbital-ordered state at low doping presented in this paper.

Orbital-ordered phases evolve in transition metal oxides where the degeneracy of  $d$  orbitals is lifted by the Jahn-Teller effect. In manganite perovskites, the Mn  $3d$  orbitals are split into three states of  $t_{2g}$  symmetry ( $d_{xy}$ ,  $d_{xz}$ , and  $d_{yz}$ ) and two states of  $e_g$  symmetry ( $d_{x^2-y^2}$  and  $d_{3z^2-r^2}$ ) due to the octahedral ligand field of the  $\text{MnO}_6$  octahedra. At suitable doping with Mn valence close to  $\text{Mn}^{3+}$ , the degeneracy of these states is lifted by the Jahn-Teller distortion of the  $\text{MnO}_6$  octahedra that leads to a preferential occupation of  $d_{3x^2-r^2}$  or  $d_{3y^2-r^2}$  states with one electron [14]. In an orbital-ordered state, the two orbitals are alternately aligned, leading to an antiferro-type of orbital order with an order parameter  $C_Q$ . Such a type of ordering was discussed by Goodenough [15] in connection with experimental observations of structural distortions in  $\text{La}_{1-x}\text{Ca}_x\text{MnO}_3$  [16]. Since then, orbital order was found for many hole-doped manganites with small tolerance factor; the latter is an indicator for the stability and octahedral tilt distortion of the crystal structure based on the ratio of the ionic radii. In such manganites, orbital order is present in certain doping regions in correlation with charge ordering, such as in PCMO ( $x = 0.3-0.7$ ) [8,17] and  $\text{Nd}_{1-x}\text{Sr}_x\text{MnO}_3$  [18], in the undoped  $\text{LaMnO}_3$  [19] and  $\text{PrMnO}_3$  [10], as well as in other types of transition metal oxides [20]. The orbital-order ground state is well studied in theory [21,22].

To establish and study orbital-ordered states, different methods have been applied. In half-doped, low-bandwidth manganites, orbital ordering is accompanied by charge order. Here, the ordering of orbitals via ordering of formal  $\text{Mn}^{3+}/\text{Mn}^{4+}$  valence states generates a superlattice that can be detected by diffraction experiments [23,24]. In fact, because the charge disproportion is rather small and typically amounts to only  $\sim 0.1e$  [25,26], the observed charge-order/orbital-order superlattice reflections mainly correspond to periodically varying Jahn-Teller distortions of the  $\text{MnO}_6$  octahedra [24,27]. Powerful tools to directly study different occupation of the  $d_{3x^2-r^2}$  and  $d_{3y^2-r^2}$  orbitals are resonant scattering techniques at the Mn  $L$  and  $K$  edges with polarized x rays because they give direct access to the anisotropic charge density [28] and related orbital occupancy [29]. These resonant x-ray techniques are thus suitable to detect orbital-ordered states at low-doping levels, where charge order is absent. They have established ordering of  $e_g$  orbitals in  $\text{LaMnO}_3$  up to a temperature of 780 K, concomitant with a structural phase transition between the orthorhombic and pseudocubic phases [19]. In  $\text{PrMnO}_3$ , Sánchez *et al.* [30] showed evidence for the presence of orbital order via the structural refinement of distorted  $\text{MnO}_6$  octahedra with three different Mn-O bonding lengths. The neutron diffraction results showed the presence of some degree of orbital order up to the temperature of the orthorhombic-to-pseudocubic phase transition at 1050 K referred to by the authors as a “Jahn-Teller transition” [30].

The presence of some degree of ordering of Jahn-Teller distortions alone is, however, not sufficient to prove spontaneous orbital order. It is well known that, in structural phase transitions, secondary order parameters can appear that break symmetries of the high-temperature phase at the same transition temperature as the primary order parameter [31]. For example, in ferroelectric phase transitions in  $\text{BaTiO}_3$  or  $\text{SrTiO}_3$ , the ferroelectric polarization is associated with the appearance of a tetragonal distortion, although the symmetry of both order parameters is different. In  $\text{SrTiO}_3$ , the ferroelectric state can be also induced by external strains, e.g., misfit strain in epitaxial films grown on different substrates [32]. In the case of orbital-order transitions in  $\text{PrMnO}_3$  as well as  $\text{LaMnO}_3$ , the onset of ordering of Jahn-Teller distortions coincides with the tilting transition of  $\text{MnO}_6$  octahedra, which induces the transition between the cubic and orthorhombic phase. This phase transition is driven by the orthorhombic distortion that is related to the steric effect and is controlled by the tolerance factor [33,34]. As shown by Alonso *et al.* [35], the average tilt angle of  $\text{MnO}_6$  octahedra increases with decreasing tolerance factor. Furthermore, the increase of octahedral tilt angle also slightly increases the amplitude of the Jahn-Teller distortion. Since at higher doping levels, spontaneous orbital-ordering sets in at quite low transition temperatures of the charge-order/orbital-order phase transition (e.g., PCMO  $x = 0.5$ ,  $T_{\text{CO}} = 235$  K [36] and LCMO  $x = 0.5$ ,  $T_{\text{CO}} = 225$  K [37]) this raises the question about the nature of the orbital-order phase transition in the weakly doped phases with PCMO  $x < 0.3$ . The question needs to be considered whether the transition to spontaneous orbital order appears below the pseudocubic-to-orthorhombic phase transition and is partially hidden in the induced order of Jahn-Teller distortions driven by the tilting.

In this paper, we show that orbital ordering in lightly doped  $\text{PrMnO}_3$  much probably takes place near room temperature, i.e., at much lower temperatures than predicted by the phase diagram [Fig. 1(a)]. Notwithstanding the fact that structural data alone only provide a subtle signature of this phase transition, the presence of anomalies in electric transport, optical properties, magnetization, and transient behavior of optical excitations provides clear evidence for the presence of a phase transition. They point to the emergence of a spontaneous orbital order below  $T_{\text{OO}} \sim 220$  K in thin films, which differs from the induced order of Jahn-Teller distortions at higher temperatures. In their bulk material, detailed temperature-dependent x-ray diffraction (XRD) measurements reveal an ordering temperature of 350 K for PCMO  $x = 0$  and 300 K for PCMO  $x = 0.1$ . The finite-temperature simulations of the orbital-order phase transition based on a tight-binding model with carefully adjusted parameters from first-principles calculations confirm the presence of a spontaneous orbital ordering below  $T_{\text{OO}} \approx 300$  K for PCMO  $x = 0.1$ .

## II. EXPERIMENTAL AND THEORETICAL RESULTS

In the following subsection, we report experimental results on various physical properties that provide clear evidence for the presence of an electronic phase transition in  $\text{Pr}_{0.9}\text{Ca}_{0.1}\text{MnO}_3$  (PCMO  $x = 0.1$ ) thin films at a temperature of around  $T_{\text{OO}} \approx 220$  K. These physical properties include

(i) photovoltaic response (Sec. II A), (ii) transport properties (Sec. II B), (iii) magnetic ordering (Sec. II C), (iv) optical properties (Sec. II D), and (v) transient optical transmission (Sec. II E).

Preliminarily, we assign this phase transition in PCMO  $x = 0.1$  thin films as orbital-order transition and come back to a critical evaluation after presentation of our results of the theoretical simulations (Sec. II F) and experimental data on the structural aspects of the low-temperature phase transition (Sec. II G). To get access to the lattice constants and to exclude influence of strain effects commonly present in thin film samples, the latter investigations were performed on polycrystalline bulk PCMO prepared by conventional solid-state reaction.

The thin film samples were prepared by means of ion-beam sputtering on (100)  $\text{SrTiO}_3$  (STO), (100)  $\text{SrTi}_{0.995}\text{Nb}_{0.005}\text{O}_3$  (STNO), and (100) MgO (for details of preparation, see Appendix A). Conducting STNO substrates were used for cross-sectional electric and photovoltaic characterization (Sec. II A) and MgO substrates for transient optical transmission measurements (Sec. II E). On these substrates, the PCMO films reveal cube-on-cube epitaxial growth of the pseudocubic structure that possesses six different twin domains of the orthorhombic  $Pbnm$  structure, i.e., with [110] and [001] out-of-plane orientations. Here, films on STO/STNO and MgO mainly differ by the volume fraction of the different orientations: Films on STO/STNO predominately reveal the [001] and films on MgO the [110] orientations. The structural characterizations are summarized in the Supplemental Material [38] and in Ifland *et al.* [39]. Technical method details for all physical property measurements are given in the Appendix A.

### A. Photovoltaic properties of PCMO/STNO heterojunctions

Figure 2 shows the change of the photovoltaic properties of  $\text{Pr}_{0.9}\text{Ca}_{0.1}\text{MnO}_3$  (PCMO  $x = 0.1$ )- $\text{SrTi}_{0.995}\text{Nb}_{0.005}\text{O}_3$  (STNO) heterojunctions in the vicinity of the phase transition. The cross-plane current-voltage characteristics exhibit a diodelike rectifying behavior which is evident from the exponential current increase in forward voltage direction and a smaller current, with a weak voltage dependence, in backward direction [Fig. 2(a)]. This diodelike behavior is observed throughout the temperature range of room temperature down to 100 K, where the rectifying characteristics become more pronounced below the respective ordering temperature. Under illumination, the photovoltaic effect of these heterojunctions appears as an additional photocurrent. The photovoltaic response is characterized by the parameters of short-circuit current density  $J_{\text{sc}}$  (at  $U = 0$  V) and open-circuit voltage  $U_{\text{oc}}$  (at  $I = 0$  A). Their temperature dependences are displayed in Fig. 2(b).

The photovoltaic effect under polychromatic illumination is measured using an ultraviolet (UV)-enhanced Xe lamp which produces a nearly constant spectral irradiance in the range between 1.55 and 4.1 eV. Additionally, measurements with two cutoff filters that limit the maximum excitation energy  $E_{\text{max}}$  to 1.6 and 2.0 eV were realized. Both cutoff filters are well below the measured STNO bandgap of 3.3 eV [40], i.e., excess carrier excitations take place only in the manganite film.

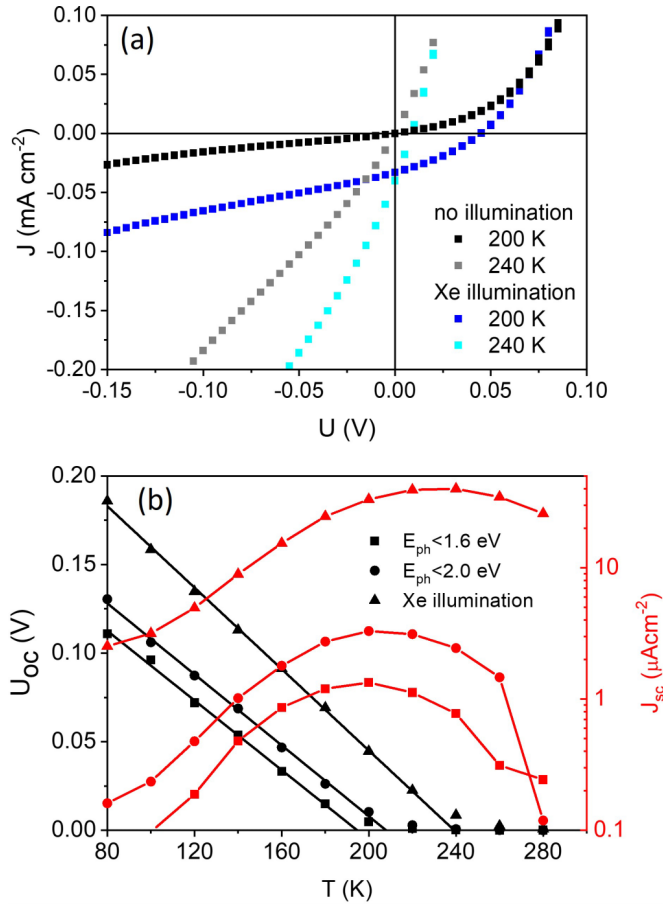


FIG. 2. Photovoltaic properties of the PCMO  $x = 0.1$ /STNO junction at the orbital-order phase transition. (a) Cross-plane current voltage characteristics above ( $T = 240$  K) and below ( $T = 200$  K) the phase transition in the dark and under polychromatic illumination. (b) Temperature dependence of open-circuit voltage  $U_{oc}$  and short-circuit current density  $J_{sc}$  measured under different spectral illumination ranges:  $E_{max} = 1.6$  eV,  $E_{max} = 2.0$  eV, and polychromatic illumination.

Regardless of the selected type of illumination, the open-circuit voltage  $U_{oc}$  and the short-circuit current density  $J_{sc}$  show characteristic temperature dependences with two distinct temperature regimes: At high temperatures,  $U_{oc}$  is small, whereas in the low-temperature regime, a significant open-circuit voltage is observed, which increases nearly linear with decreasing temperature. In contrast, the temperature dependence of  $J_{sc}$  exhibits a pronounced maximum at a temperature of  $\sim 200$  K [Fig. 2(b)].

Interestingly, with an increasing spectral range of incident photons,  $U_{oc}(T)$  is shifted to higher voltages. Since the open-circuit voltage reflects the splitting of the chemical potential of electrons and holes without carrier extraction, its increase with increasing  $E_{max}$  mainly reflects the contribution of electron-hole excitations at higher energy to  $U_{oc}(T)$ . Therefore, the “true” transition temperature  $T_{OO} \sim 220$  K is approximately presented by the  $U_{oc}(T)$  onset at highest photon irradiance.

In the temperature range of the ordering transition, the short-circuit current density  $J_{sc}(T)$  exhibits a pronounced maximum [Fig. 2(b)]. Since optical absorption is more or

less unchanged with temperature, the increase of  $J_{sc}(T)$  with decreasing  $T$  reflects an increase of the photo carrier lifetime when approaching the ordering transition. Below the phase transition, the carrier mobility decreases, as shown in the subsequent section. Like the shift of  $U_{oc}(T)$  with increasing spectral illumination, also the maximum of the  $J_{sc}(T)$  is shifted to higher  $T$  with an increase of the current density. The  $U_{oc}(T)$  onset and the maximum of  $J_{sc}(T)$  are at the same temperature. Such a behavior is unconventional and cannot be understood without the presence of changes in the electronic properties of the junction due to a phase transition in the temperature range between 190 and 240 K.

## B. Charge carrier mobility

The change of electronic properties at the ordering transition is additionally reflected in a change of DC carrier transport of PCMO. The charge carriers in Ca-doped PrMnO<sub>3</sub> are small polarons that reveal a thermally activated mobility above half of the Debye temperature  $\frac{1}{2}\theta_{Debye} \approx 160$  K [41]. In addition, a bandlike transport can appear at low temperatures in high magnetic fields [7] via a magnetic field-induced phase transition to a ferromagnetic metallic phase that evolves out of the charge-ordered state of small polarons [42]. In a broad doping range of PCMO, the temperature ( $T$ ) dependence of the resistivity can be described by thermally activated hopping of small polarons; that is in the adiabatic approximation given by [43]

$$\rho(T) = \rho_0 T \exp\left(\frac{E_A}{kT}\right). \quad (1a)$$

Electronic phase transitions commonly change the prefactor  $\rho_0$  as well as the activation energy  $E_A$ . It is, therefore, useful to consider the logarithmic derivative defined as

$$E_A = k \frac{d}{d\left(\frac{1}{T}\right)} \ln\left(\frac{\rho}{T}\right), \quad (1b)$$

as a temperature-dependent activation barrier. Within the adiabatic approximation, the logarithmic derivative is temperature independent well above half of the Debye temperature (for PCMO,  $\frac{1}{2}\theta_{Debye} \approx 160$  K) and significantly decreases below  $\frac{1}{2}\theta_{Debye}$  due to enhancement of tunnelling contributions [44].

Figure 3 shows the increase of in-plane resistivity with decreasing temperature. The measurement is performed on a PCMO  $x = 0.1$  film deposited on insulating STO substrate that was postannealed for 20 h at 900 °C to reduce growth-induced defects and strain (see Supplemental Material [38]). Above 220 K, the resistivity shows a thermally activated temperature dependence that is reflected in a logarithmic derivative value of about  $E_A \approx 160$  meV. In this temperature regime, the activation energy decreases slightly with decreasing temperature. Such deviations from the adiabatic approximation are frequently observed in thin film samples, most probably due to defect-related contributions to polaronic mobility [42]. Below the ordering transition at  $T_{OO} \approx 220$  K,  $E_A(T)$  shows a significant increase, reflecting a decrease of the hopping mobility of small polarons in the low-temperature state.

Interestingly, below the phase transition temperature, the resistivity shows a significant magnetoresistance effect. At an applied magnetic field of  $\mu_0 H = 9$  T, the logarithmic

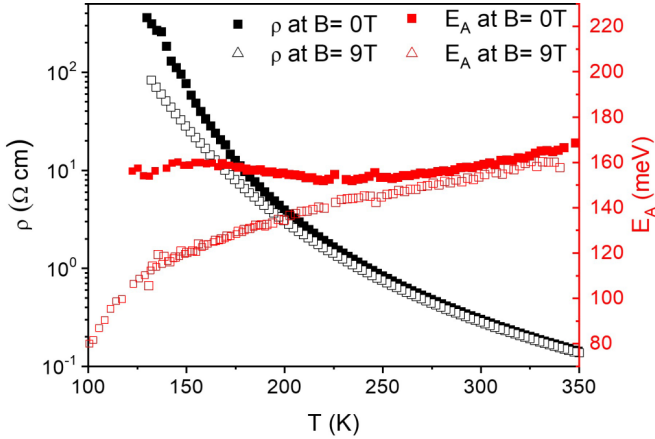


FIG. 3. Temperature dependence of in-plane resistivity and logarithmic derivative  $E_A$  in zero magnetic field as well as magnetic field of  $\mu_0 H = 9$  T for a PCMO  $x = 0.1$  film on (100) STO, postannealed for 20 h at 900 °C. The magnetic field was applied perpendicular to the substrate, i.e., parallel to the dominating [001] direction.

derivative  $E_A$  decreases almost linearly with decreasing temperatures down to  $\sim 150$  K. Furthermore, the increase of  $E_A$  below 220 K in zero-field is completely suppressed. The electric transport behavior supports the presence of orbital ordering below 220 K since an ordering of the underlying Jahn-Teller distortions obviously reduces the mobility of Jahn-Teller polarons. As worked out by Millis *et al.* [45], there is a strong mutual effect between the Jahn-Teller splitting of  $e_g$  orbitals and the electronic hopping via the magnetic double exchange interaction. Our results indicate that increase of magnetic double exchange by a magnetic field-induced spin alignment is more effective in the orbital-ordered state. This is reflected in the observed magnetoresistance below  $T_{OO}$ .

### C. Magnetic properties

The observed magnetoresistance below  $T_{OO}$  raises the question whether the magnetic properties are affected by the ordering transition as well. According to the established bulk phase diagram of lightly doped PCMO in Fig. 1(a), a magnetic phase transition takes place between a paramagnetic high-temperature phase and a magnetically ordered low-temperature phase. Its nature depends on the exact doping level since, at PCMO  $x = 0.1$ , there is a phase boundary between a canted antiferromagnetic and a ferromagnetic phase [9,10]. The Néel and Curie temperatures of both magnetic phases are at  $\sim 100$  K.

In thin film measurements by means of superconducting quantum interference device (SQUID)-magnetometer, the contribution of substrate to the magnetic moment is usually not negligible. To separate substrate and film contributions, we first measured the field and temperature-dependent moment  $m_{STO}$  of a pristine STO substrate. In the next step, a PCMO  $x = 0.1$  film was deposited on this substrate, and the same measurements of magnetic moment  $m_{tot}(H, T)$  for film and substrate under identical measurement parameters were performed. The film magnetic moment  $m_{film}$  was calculated by subtracting the substrate contribution from the total moment  $m_{tot}$ . The substrate correction procedure is described in Appendix A.

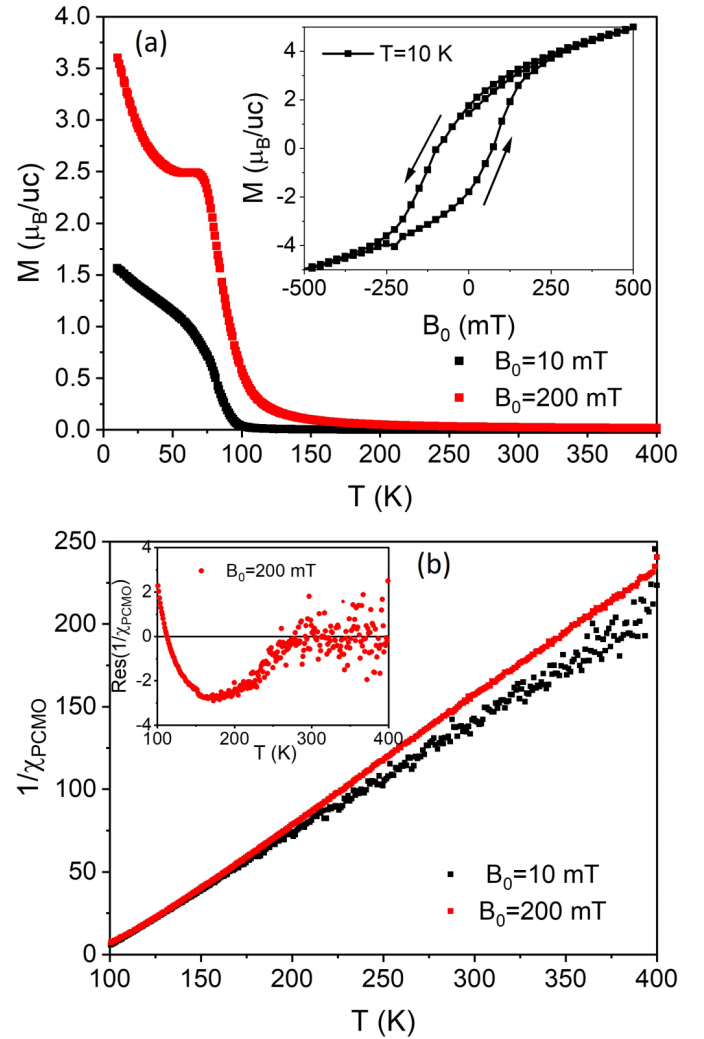


FIG. 4. Temperature dependence of magnetization and magnetic susceptibility of PCMO  $x = 0.1$  films on STO. The data are corrected with respect to substrate contributions, and the magnetic field is applied parallel to the substrate. (b) Temperature dependence of field-cooled magnetization in Bohr magnetons per unit cell for different applied fields. The inset shows the hysteric behavior of field-dependent magnetization at 10 K. Temperature dependence of the DC magnetic susceptibility at two different applied fields. The inset shows the residuum of the experimental data with respect to a linear fit of  $1/\chi_{PCMO}$  at temperatures  $T > 300$  K.

Figures 4(a) and 4(b) show the temperature-dependent magnetization and susceptibility of the PCMO  $x = 0.1$  thin film after the substrate correction. At low temperatures, the magnetization shows a distinct phase transition to a magnetically ordered state [Fig. 4(a)]. The strong increase of  $M$  at  $T_c = 80.3 \pm 1.0$  K is indicative of a transition into a phase with a ferromagnetic component, visible by the hysteretic behavior of  $M(H)$  at 10 K and the presence of a remanent magnetization [see inset Fig. 4(a)].

Well above the Curie temperature  $T_c$ , the susceptibility of PCMO  $x = 0.1$  reveals Curie-Weiss behavior [Fig. 4(b)]:

$$M_{film} = \frac{\chi_0 H}{(T - T_{CW})}, \quad (2)$$

Here,  $\chi_0$  represents the paramagnetic Curie constant and  $T_{CW}$  the Curie-Weiss temperature. Interestingly, the slopes in the Curie-Weiss plot reveal slight differences in the high-temperature ( $T > 280$  K) and in the low-temperature ( $T < 180$  K) ranges. At higher temperatures,  $\chi_{PCMO}(T)^{-1}$  in Fig. 4(b) reveals a weak magnetic field dependence, and the change in slope appears more pronounced for the smaller applied field of 10 mT than for 200 mT. Whereas the difference is close to noise for the measurement at 10 mT, the presence of two different temperature regimes is clearly visible in the residuum of the experimental data at 200 mT [inset Fig. 4(b)]. The deviation from the Curie-Weiss fit becomes significant below 260 K. This represents a probable magnetic fingerprint of a phase transition, in which the electronically ordered low-temperature phase has a higher susceptibility.

The error bars of  $\chi_{PCMO}(T)$  are too large for a quantitative determination of the different Curie constants and Curie-Weiss temperatures of the orbital-ordered and disordered phase. Therefore, we perform a linear fit of  $\chi_{PCMO}(T)$  in the entire temperature range of 120–400 K, i.e., including the ordered and disordered phases and only excluding the temperature range which contains ferromagnetic contributions. This yields an averaged Curie constant of both phases that corresponds to a magnetic moment of  $5.7 \pm 0.3 \mu_B$  and a Curie-Weiss temperature of  $T_{CW} = 93.4 \pm 0.2$  K. The magnetic moment is close to the expected one if the contribution of  $4f$  moments of Pr is considered [46]. The temperature-dependent deviations from this fit suggests qualitatively that, in the orbital-ordered phase, the Curie-Weiss temperature is lower, and the Curie constant is higher.

We can exclude that the change of  $\chi_{PCMO}(T)$  at 260 K is related to the transition into the ferromagnetically ordered state since the observed deviation from the Curie-Weiss fit is far above a possible onset of ferromagnetic fluctuations. This statement is supported by the additional change of the residuum [inset Fig. 4(c)] below a temperature of  $\sim 170$  K that represents a precursor of the ferromagnetic transition below 100 K due to ferromagnetic fluctuations. In addition, the temperature-dependent contribution  $\Delta m_s$  to the substrate correction is too small to explain the changes of  $\chi_{PCMO}(T)$  (see Appendix A and Fig. S5 in the Supplemental Material [38]).

#### D. Optical properties

Figure 5 shows the temperature dependence of the absorption coefficient  $\alpha(E_{ph}) = 1 - t$ , obtained through measurements of the transmission  $t$ , in the range of photon energies between 1.25 and 3.0 eV. It reveals four broad absorption bands at 1.8 eV (I), 2.4 eV (II), 2.7 eV (III), and  $> 3.2$  eV (IV). The band IV here overlaps with the onset of interband transitions in SrTiO<sub>3</sub> with a bandgap of 3.2 eV. For  $E_{ph} \leq 3$  eV, the absorption coefficient represents the manganese excitations only. The increase with decreasing temperature is most pronounced for the bands I and II, a behavior that is also observed for higher doping levels [6]. The reason is that peaks I and II stem from transitions between the Jahn-Teller split Mn  $3d e_g$  states, i.e., involving Mn intersite transitions. Here, note that the nominal Mn- $d e_g$  states contain a contribution from the “atomic” oxygen O  $2p$  states. In contrast, the absorption peaks  $> 2.2$  eV (peaks III and IV) are characterized as dipole-allowed charge transfer transitions between O $2p$

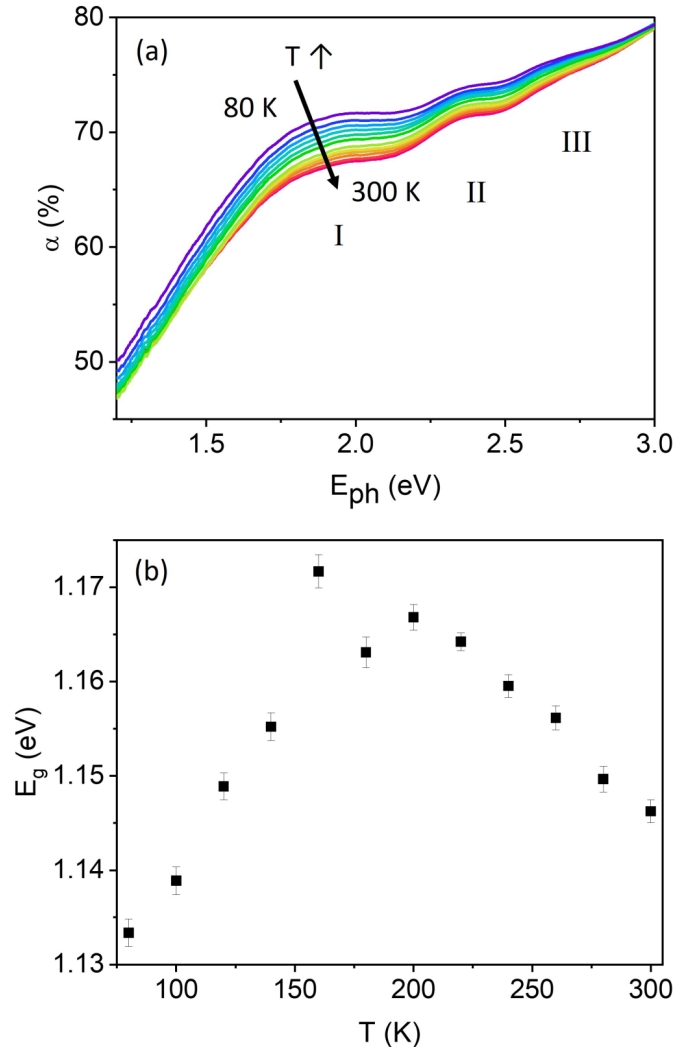


FIG. 5. Temperature dependence of optical absorption of a PCMO  $x = 0.1$  film on (100) STO under top-side illumination. (a) Spectral dependence of the absorption coefficient  $\alpha(E_{ph})$  at various temperatures. (b) Temperature dependence of the optical bandgap  $E_g$  deduced from Tauc plots.

states and minority-spin  $t_{2g}(\downarrow)$  and  $e_g(\downarrow)$  states that are less affected by the orbital-order phase transition [47].

To determine the bandgap, the temperature-dependent, reflection-corrected absorption coefficient  $\alpha_R(E_{ph})$  in the low-photon energy region of the absorption band I was then analyzed by means of Tauc’s relationship, which is used to determine bandgaps in semiconductors [48,49]. The best fits were observed for a Tauc exponent of  $\frac{3}{2}$  that corresponds to direct forbidden transitions (see Supplemental Material [38]). Since the transition I takes place between dipole-allowed Jahn-Teller split occupied and unoccupied Mn  $3d e_g$ -O  $2p$  bands with different symmetry [6], the fit allows for a precise analysis of the bandgap. Even though we use the semiconductor theory, which is based on rigid bands, it is to be noted that we have deviation of rigid bands due to the polaronic nature. The determined bandgap represents an upper limit to the real bandgap since the transmission will be underestimated and the reflectance overestimated due to substrate contributions, e.g., double reflection and interface contributions. However, this



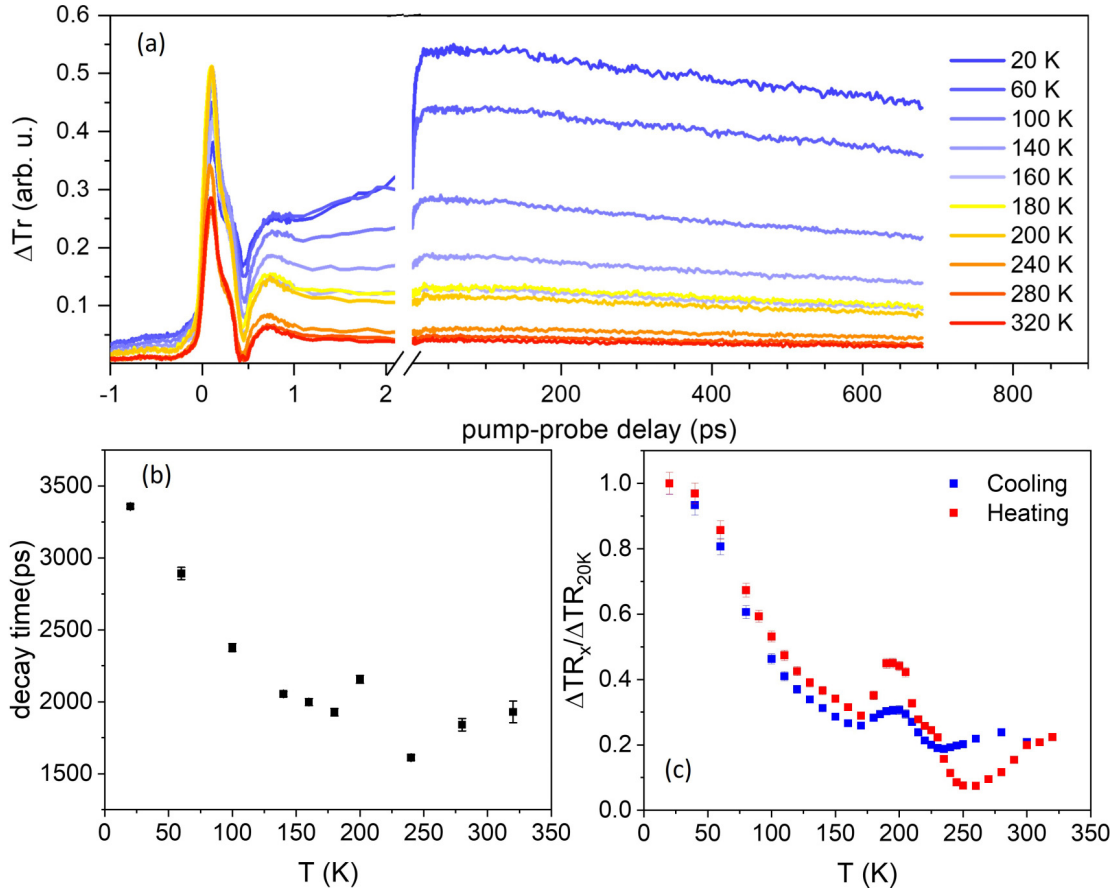


FIG. 6. Pump-probe transmission experiment for PCMO  $x = 0.1$  film on MgO (100). (a) Transient transmission at different sample temperatures between 20 and 300 K for an incident fluence of  $3.2 \text{ mJ/cm}^2$ . (b) Change in the signal decay time  $\tau$  back to the initial state with temperature showing a decrease with increasing temperature. A small anomaly is observed  $\sim 200 \text{ K}$ . (c) Transient transmission change at  $\sim 90 \text{ ps}$  delay for a combined cooling and heating temperature cycle with small temperature steps. The data are normalized to the value of the transient transmission change at 20 K. The strong anomaly observed for temperatures  $> 170 \text{ K}$  is due to a phase transition with hysteretic effects on temperature cycling.

does not modify the temperature-dependent relative changes as well as peak positions.

Figure 5(b) shows the temperature dependence of the deduced bandgap  $E_g$ . The temperature dependence changes at  $\sim 200 \text{ K}$ . At high temperatures, we observe a bandgap opening with decreasing temperature. Such an effect is, e.g., typically observed in semiconductors and has its origin in the thermal contraction as well as in the electron phonon interaction [50]. The latter smears out the bandgap at elevated temperatures. Remarkably, the bandgap decreases with decreasing temperature below the ordering transition. This is rather surprising since an ordering in the orbital system decreases the thermal fluctuations of the Jahn-Teller split state and thus should increase the bandgap. A possible explanation may be the anomalous thermal expansion of PCMO  $x = 0.1$ , where the  $c$  axis expands with decreasing temperature [51].

### E. Time-resolved optical transmission studies

Optical pump-probe transmission measurements allow study of the change of the nonequilibrium quantities of the system, e.g., the lifetime of excitations, but also access to equilibrium properties such as the specific heat, which are

otherwise difficult to measure in thin films. In our studies, a PCMO  $x = 0.1$  film (100 nm thick) was excited with a femtosecond laser pulse at fluences  $F$  of  $3\text{--}4 \text{ mJ/cm}^2$  with 1.2 eV pump photon energy, which is close to the bandgap. The time-dependent changes of the transmission were measured with a second pulse at 2.4 eV, which probes the band II, by dipole-allowed intersite transitions between Jahn-Teller split occupied and unoccupied Mn  $3d e_g$  states [47]. Figure 6(a) shows a series of transient transmission time traces measured at cryostat temperatures between 20 and 300 K. Three different timescales can be identified: an initial fast transient on the subpicosecond timescale, a second transient on a timescale of  $\sim 10 \text{ ps}$ , and long-term equilibration back to the ground state, which is not yet finished within the scan range of the pump-probe experiment. The transient transmission in Fig. 6(a) additionally shows a short-lived oscillatory behavior  $\Delta Tr$  in the first picosecond with a frequency of  $\sim 1.6 \text{ THz}$ , which likely corresponds to an optical phonon mode of the PCMO film.

Here, we are interested in signatures of phase transitions that manifest within transmission dynamics. We investigate two different quantities which may contain information about a possible phase transition: first, the signal decay  $\tau_{\text{Decay}}$  back

to the ground state and, secondly, the transmission change  $\Delta\text{Tr}$  with temperature.

A phase transition between different ground states of the system will change the relaxation channels for the decay of the optically excited electron-hole pairs, e.g., quasiparticle lifetimes and coupling constants between electrons, spins, and lattice may change, as well as the heat capacities or thermal conductivities [52–55]. From Fig. 6(a), we extracted the relaxation times  $\tau$  after optical excitation back to the ground state [depicted in Fig. 6(b)] by fitting a simple exponential decay of the form

$$\Delta\text{Tr}(t) = \Delta\text{Tr}(t < t_0) + Ae^{-t/\tau}, \quad (3)$$

to the data starting from a 90 ps delay. The extracted data in Fig. 6(b) shows an increase of the decay time from  $\sim 2$  ns at room temperature to  $\sim 3.5$  ns at low temperatures with a small maximum at  $\sim 200$  K. This behavior is in stark contrast to the values computed from a simple three-temperature model shown in the Supplemental Material [38]. Reflecting the strong increase of the thermal conductivity  $\kappa$  of the MgO substrate with decreasing temperature from 52 W/mK at 300 K to 1850 W/mK at 20 K, the modeling predicts a significant decrease of the lifetime of the long-term decay of transient transmission  $\Delta\text{Tr}$  from  $\sim 2$  ns at 300 K to  $\sim 0.7$  ns at 20 K. We note that this finding is very similar to results discussed in Ref. [12]. Like Ref. [12], this observation points toward the presence of electron-hole polaron excitations with rather long lifetime at low temperatures, which manifest as an additional signal contribution in the transmission change. This is supported by the observed photovoltaic response below the ordering transition.

Further information about a possible phase transition can be gained from inspecting an even simpler quantity from the data, the transmission change  $\Delta\text{Tr}$  after initial equilibration of the optically excited electrons [Fig. 6(c)]. In the experiment, we maintain a constant incident optical fluence or energy density

$$F = \frac{E_{\text{in}}}{A}, \quad (4a)$$

and vary the base temperatures  $T_0$  inside the cryostat. Assuming purely thermal effects, for different  $\Delta\text{Tr}(T_0)$ , the observed transmission change is proportional to the change of the temperature  $\Delta T$  caused by the transformation of the absorbed energy  $E_{ab} \approx \alpha_{\text{pump}}(T_0)E_{\text{in}}$  into heat, where  $\alpha_{\text{pump}}(T_0)$  is the absorption coefficient at the pump photon energy. For time scales larger than the initial relaxation time, the change in  $\Delta\text{Tr}$  should then be mostly given by the temperature rise. This contribution can be approximated by

$$\Delta\text{Tr} \sim \frac{d\alpha_{\text{probe}}}{dT}\Big|_{T=T_0} \Delta T = \frac{d\alpha_{\text{probe}}}{dT}\Big|_{T=T_0} C(T_0)^{-1} E_{ab}, \quad (4b)$$

where,

$$\alpha_{\text{probe}}(T_0 + \Delta T) \approx \alpha_{\text{probe}}(T_0) + \frac{d\alpha_{\text{probe}}}{dT}\Big|_{T=T_0} \Delta T, \quad (4c)$$

is the temperature dependence of the absorption coefficient at the probe photon energy, and  $C(T)$  is the specific heat. Due to the increase of  $C(T_0)$  with increasing  $T_0$ , a continuous decrease in  $\Delta\text{Tr}$  is expected for increasing the base temperature

$T_0$  at constant incident optical fluence  $F$ . In the presence of phase transitions, the related nonmonotonous change of  $C(T)$  or other system quantities would then result in additional features.

Figure 6(c) shows the temperature dependence of  $\Delta\text{Tr}$  for PCMO  $x = 0.1$  at  $\sim 90$  ps delay time, i.e., after internal equilibration of the system is assumed for a combined cooling and heating cycle of the cryostat. Each depicted data point is the average of 300 measurements in the range 88–91 ps, where the signal is nearly constant; error bars are the standard deviation. Below 170 K,  $\Delta\text{Tr}$  indeed decreases with increasing base temperature as expected, most pronounced in the vicinity of the ferromagnetic phase transition temperature  $\sim 80$  K. However, in the range starting from 170 K, strong, steplike changes of  $\Delta\text{Tr}$  are clearly visible, in addition to a significant hysteresis between the cooling and heating cycle. This is additional evidence for an orbital phase transition. Here, nonlinear behavior of material parameters like  $n$ ,  $C$ , and  $\kappa$  can give rise to a complex, nonmonotonous behavior of the transmission change. The hysteresis in the cooling and heating cycle especially may indicate the coexistence of different phases in the discussed temperature range. In the simulation, a similar decrease of the signal can be seen (see the Supplemental Material [38]), albeit it occurs significantly faster. This again shows that, in the experiment, additional physical processes—like a change of lifetime of polaronic excitations—are important. Note that the Supplemental Material [38] contains the time-dependent evaluation of  $\Delta\text{Tr}$  for all temperature steps in Fig. 6(a), showing the same kink in the data but at much worse temperature resolution for all times, showing that the result obtained here is not specific to a 90 ps delay.

## F. Theoretical simulation of the orbital-order transition

### 1. Model system

The experimental results shown in the previous subsections clearly hint at an electronic phase transition in PCMO  $x = 0.1$  that appears at  $\sim 220$  K in thin film samples. To identify the nature of the phase transition, we performed finite-temperature simulations of the orbital-order phase transition using a tight-binding model [56,57], which has been carefully adjusted to first-principles calculations [47].

The model captures the correlated motion of electrons, spins, and phonons. The Mn  $e_g$  electrons with two orbital degrees of freedom  $j \in \{d_{3z^2-r^2}, d_{x^2-y^2}\}$  and two spin degrees of freedom  $\sigma \in \{\uparrow, \downarrow\}$  per Mn site are described by a Slater determinant of one-particle wave functions  $|\Psi_n\rangle$ . The half-filled shell of Mn  $t_{2g}$  electrons is accounted for by a spin  $\vec{S}_R$  of length  $\frac{3}{2}\hbar$ . Two Jahn-Teller active octahedral distortions  $Q_{2,R}$ ,  $Q_{3,R}$  per Mn site and one octahedral breathing mode  $Q_{1,R}$  are considered [12,58]. The phonon amplitudes are extracted from the displacement of the oxygen ions along the Mn-O-Mn bridge, which accounts for their strongly cooperative nature. The oxygen atoms are limited to a one-dimensional motion along the oxygen bridge. We allow the lattice constants to adjust dynamically.

The Hamiltonian considers the intersite hopping of Mn  $e_g$  electrons and their onsite Coulomb interaction. The hopping parameters have been obtained by down folding the O- $p$  orbitals of the oxygen bridge considering only  $\sigma$ -type matrix

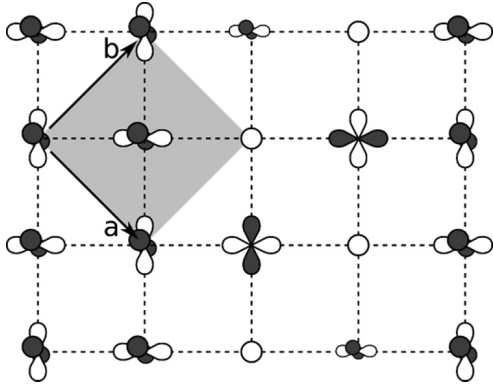


FIG. 7. Sketch of the orbital structures occurring in the low-temperature phase at  $x \approx 0.1$ . We mainly observe the  $\text{PrMnO}_3$ -like alternating orbitals  $d_{z^2-x^2}/d_{z^2-y^2}$ , together with clusters combining alternating hole and  $d_{x^2-y^2}$  orbitals. Orbitals drawn with a smaller scale indicate a reduced orbital polarization, which can occur on sites between the two types of orbital ordering.

elements of the Mn-O axes. The spins of Mn  $e_g$  electrons experience a strong but finite Hund's coupling with the spins  $\vec{S}_R$  of the  $t_{2g}$  electrons. The latter experience an antiferromagnetic Heisenberg coupling between sites. A linear electron-phonon coupling [59] correlates the  $e_g$  electrons with the Jahn-Teller active phonons  $Q_2$  and  $Q_3$  and the breathing mode  $Q_1$ . The Jahn-Teller active phonons lift the degeneracy of the  $e_g$  electrons, and the outward breathing mode  $Q_1$  stabilizes all  $e_g$  electrons on this site. A detailed description of the model and its parameters can be found in an earlier publication [47].

The dynamics of the model is simulated in a Car-Parrinello framework [60]: The oxygen atoms are treated as classical particles that evolve according to Newton's equation of motion with forces obtained from the partial derivatives of the instantaneous total energy. Electrons and spins follow the atomic motion quasi-adiabatically in their instantaneous ground state. This quasi-adiabatic motion of electrons and spins is implemented by a fictitious Lagrangian. The temperature of the oxygen atoms is controlled by a Nosé-Hoover thermostat [61,62], which establishes a canonical (constant temperature) ensemble. More details of our simulations are given in Appendix B.

## 2. Ground state

Below the orbital-order transition temperature, PCMO  $x = 0.1$  exhibits an orbital order like  $\text{PrMnO}_3$ , which is broken by the presence of hole polarons, as sketched in Fig. 7. The PCMO  $x = 0$  orbital order consists of a checkerboardlike arrangement of alternating  $d_{z^2-x^2}$  and  $d_{z^2-y^2}$  orbitals in the  $ab$  plane [63]. The hole polarons are Mn ions in the formal 4+ oxidation state, i.e., they show a small charge deficiency and the absence of orbital polarization toward a certain  $e_g$  orbital. The neighboring orbitals arrange preferentially with their lobes pointing toward the hole polarons. This leads to cluster formation of hole polarons and Mn sites with in-plane  $d_{x^2-y^2}$  orbitals. The formation of such clusters in neighboring  $ab$  planes is unfavorable. At very low temperatures, the hole polaron clusters are concentrated in single  $ab$  planes. We

found no influence of this ordering on the orbital-order phase transition investigated in this paper. More disordered states with the hole polaron clusters scattered in many of the  $ab$  planes have an only slightly increased ground state energy by a few millielectronvolts.

The PMO-like orbital order prefers an antiferromagnetic order along the  $c$  axis, while the hole polarons favor a ferromagnetic alignment in that direction. The competition of these effects can lead to spin canting. A common problem of model Hamiltonians of the type used here is that they yield a  $c/a$  ratio  $> 1$ , which differs from experiment [8]. We are not aware of a nontrivial cure for this problem.

## 3. The order parameter

The orbital order of the system is described by the structure factor

$$C_Q(\vec{q}) = \frac{1}{N_R} \sum_{j \in \{2,3\}} \left| \sum_R e^{-i\vec{q}\vec{R}_R} Q_{j,R} \right|^2, \quad (5)$$

of the Jahn-Teller distortions  $Q_{2,R}$ ,  $Q_{3,R}$ . Here,  $N_R$  is the number of Mn sites in the sum. Due to the finite supercell size in our calculations, this correlation function has contributions only at discrete points in reciprocal space. We define the order parameter for the orbital-order phase transition as the structure factor summed along the  $q_c$  direction:

$$C_Q^{\text{av}}(q_a, q_b) = \sum_{q_c} C_Q(q_a, q_b, q_c) \quad \text{at} \quad (q_a, q_b) = \left( \frac{2\pi}{a}, 0 \right), \quad (6)$$

in  $Pbnm$  notation. This order parameter quantifies the checkerboardlike alternating orbital order in the  $ab$  plane. In our simulations, the orbital order of the Mn  $e_g$  electrons appears simultaneous with the ordering of the Jahn-Teller distortions. A correlation function of the Mn  $e_g$  electrons yields the same transition temperature as the Jahn-Teller order parameter used here.

## 4. Simulations

In finite-temperature simulations for PCMO  $x = 0.1$ , the orbital order melts at 270 K. Figure 8(a) shows the order parameter  $C_Q^{\text{av}}(\frac{2\pi}{a}, 0)$  for the orbital order as a function of temperature. Both the heating (red) and the cooling (blue and magenta) curves are shown to ensure that the hysteresis due to the finite simulation time is negligible. As a result of the finite supercell used in the calculations, the transition is not abrupt. The sharpest drop of the order parameter occurs  $\sim 270$  K, where it passes its half maximum value. Above 400 K, the Jahn-Teller correlation function becomes nearly independent of the wave vector, as seen in Fig. 8(b). The correlation length of the antiferrodistortive order reduces to nearest neighbors only at high temperatures.

The Jahn-Teller distortions are present over the entire temperature range investigated, i.e.,  $T < 800$  K, but the correlation

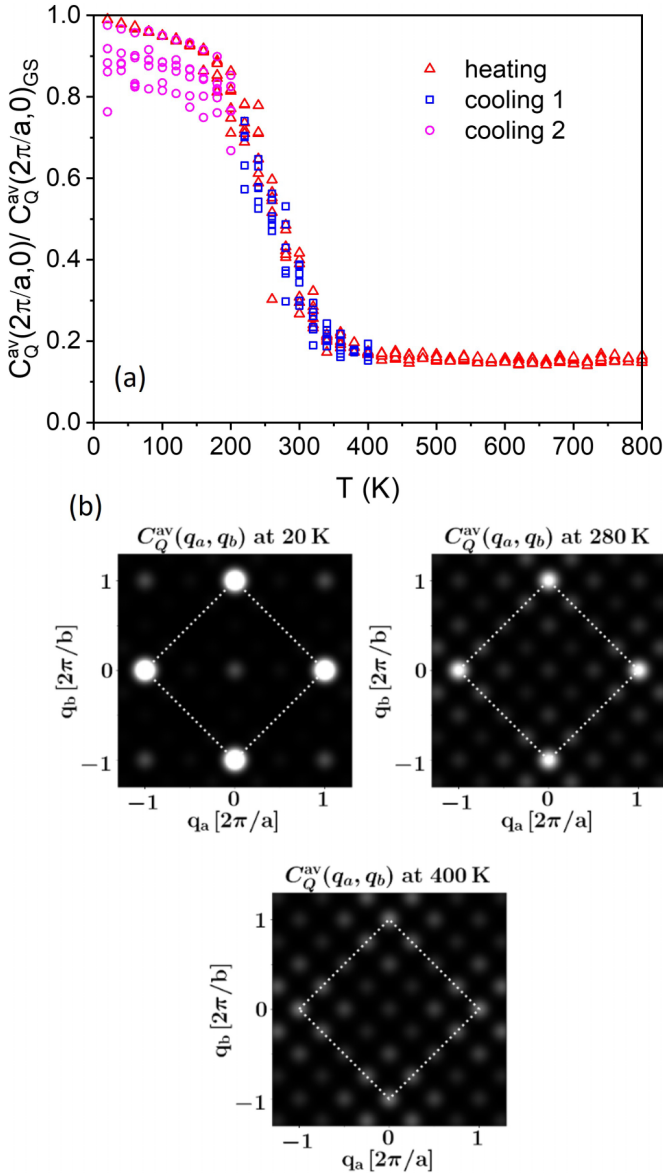


FIG. 8. (a) Order parameter  $C_Q^{\text{av}}(\frac{2\pi}{a}, 0)$  for the orbital-order transition in PCMO  $x = 0.1$  as a function of temperature obtained in our simulations, scaled to its ground state value. Six simulation runs are shown for each temperature. The system was first heated from the ground state to nonzero temperatures, shown with red crosses. The system was subsequently cooled from the 400 K heating calculations to lower target temperatures (cooling 1), and in a second step from the 200 K cooling calculations back to 20 K (cooling 2), shown with blue squares and magenta circles, respectively. More details on the heating and cooling cycles are provided in the Supplemental Material [38]. (b) In-plane Jahn-Teller correlation function  $C_Q^{\text{av}}(q_a, q_b)$  of a typical heating simulation close to the ground state (20 K), during the transition (280 K), and above the transition (400 K). The white dotted line marks the shape of the reciprocal unit cell. The peaks have been broadened by a Gaussian. Near the ground state, we clearly see the  $\text{PrMnO}_3$ -like alternating orbital structure at  $(q_a, q_b) = (\frac{2\pi}{a}, 0)$ , respectively,  $(q_a, q_b) = (0, \frac{2\pi}{b})$ . At 400 K, nearly all possible diffraction spots of our unit cell have the same weight.

of the distortions at different sites vanishes above the transition temperature due to the breakdown of orbital order.

In Fig. 8(b), the  $ab$ -plane Jahn-Teller correlation function  $C_Q^{\text{av}}(q_a, q_b)$  is shown for a typical heating cycle at 20, 280, and 400 K. The 20 and 400 K correlation functions are fully reproducible for all simulation runs. In the 280 K calculations, we observed a few runs that have a more pronounced (0,0) peak. The correlation function for the finite supercell has contributions only at discrete points in reciprocal space, which have been broadened by a Gaussian in Fig. 7(b). The mean intensity is the measure for the expectation value of the Jahn-Teller distortion.

These model simulations indicate the presence of an orbital-order phase transition at  $\sim 270$  K, close to the experimental values presented in this paper. A comment on the magnetic phase transition is provided in the Supplemental Material [38].

## G. Temperature-dependent structural changes in bulk PCMO

### 1. Temperature-dependent changes of lattice constants

The theoretical simulations give clear evidence for the presence of the orbital-ordering phase transition in the vicinity of room temperature. This temperature is somewhat higher than the experiments in PCMO  $x = 0.1$  thin films, where relevant physical properties change in the vicinity of temperature of 220–280 K. A reduced ordering temperature in the thin films compared with bulk is expected due to growth-induced defects and substrate-induced epitaxial strain.

After observing small changes or anomalies in various physical properties, the question is obvious whether such a phase transition might be visible in a change of the lattice parameters as well. Therefore, we have performed temperature-dependent XRD measurements on polycrystalline PCMO  $x = 0$  and PCMO  $x = 0.1$  powder samples to avoid substrate-induced strain effects in the thin films and to get access to a higher number of different crystal orientations. The lattice parameters  $a$ ,  $b$ , and  $c$  were deduced from the (200), (020), and (004) reflections, respectively, and their temperature dependences are shown in Fig. 9. A careful inspection of the intensity distributions shows that the XRD reflections reveal a double-peak structure [Fig. 9(a)] for both systems PCMO  $x = 0$  and PCMO  $x = 0.1$ . The shape of the doubled reflection peaks does not change with temperature. The double-peak structure originates from  $K\alpha_1$  and  $K\alpha_2$  irradiation contribution. With respect to temperature dependence, the lattice constants deduced from the  $K\alpha_1$  peak may include a systematic but temperature-independent error. The room temperature lattice parameters are in good agreement with experimental data from Refs. [8,30,65].

The temperature dependence of the lattice parameters [Figs. 9(b)–9(d)] exhibits a contraction in the  $c$  direction and an expansion in the  $b$  direction while cooling. The  $a$  lattice parameter decreases as well, but the change is very small in comparison with the changes in  $b$  and  $c$ . These trends are typical for the orthorhombic  $Pbnm$  structure of PCMO and are fully consistent with the results of Refs. [10,30] for PMO. However, our detailed temperature scan reveals the presence of two regimes with distinctly different behavior of the lattice parameters  $a(T)$ ,  $b(T)$ , and  $c(T)$ . We observe a significantly reduced temperature dependence below 350 K for  $x = 0$  and 300 K for  $x = 0.1$ . For the  $a$  lattice parameter, this reduction

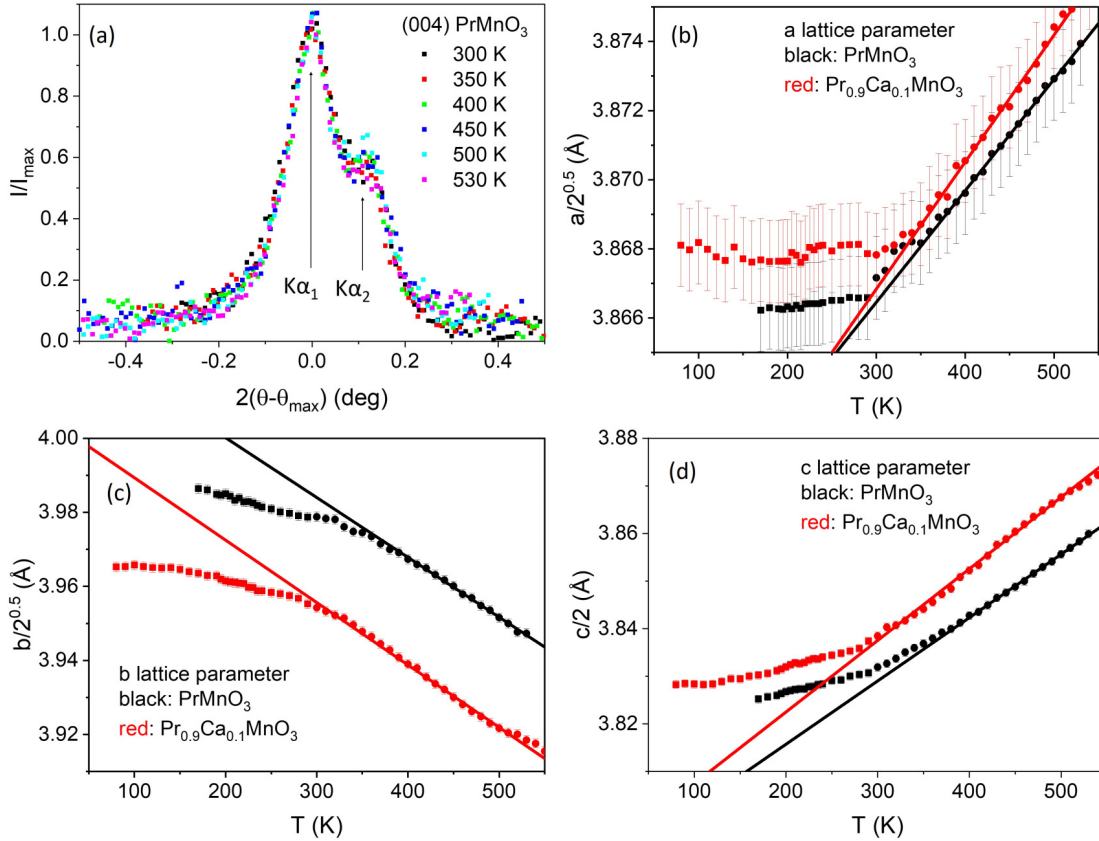


FIG. 9. Temperature-dependent x-ray diffraction (XRD) analysis of polycrystalline bulk  $\text{Pr}_{1-x}\text{Ca}_x\text{MnO}_3$  samples with  $x = 0$  and  $0.1$ . (a) Intensity distributions of (004) PCMO  $x = 0$  reflections at different temperatures. The data are normalized to the position and the height of the intensity maximum. (b)–(d) Temperature dependence of lattice parameters of PCMO  $x = 0$  and PCMO  $x = 0.1$ . The lattice parameters correspond to  $Pbnm$  notation and are converted into a pseudocubic setting to facilitate the quantitative comparison.

even results in a temperature-independent value within the experimental errors. The comparison of PCMO  $x = 0$  and PCMO  $x = 0.1$  as seen in Fig. 9 reveals a similar temperature dependence with comparable temperature slopes but a lower transition temperature for the lightly doped system. The shift of  $a$  and  $c$  to higher and of  $b$  to lower values for the doped system is as expected for a reduced orthorhombicity in the Ca-doped system compared with PMO.

In the temperature region below 150 K, the lattice parameters for PCMO  $x = 0.1$  exhibit a second change in slope, where they tend to become temperature independent. This happens at temperatures far below the Debye temperature, where a saturation of thermal expansion is expected. The appearance of temperature-independent lattice parameters may reflect the well-established second phase transition into magnetic ordered state [51].

Usually, thermal expansion coefficients reveal a similar temperature dependence as the specific heat [66]; thus, they strongly change below the Debye temperature, where the specific heat of materials is typically strongly temperature dependent. To the best of our knowledge, no measurements of the specific heat of PCMO  $x = 0$  and PCMO  $x = 0.1$  near room temperature are published. The decrease of the thermal expansion at 350 K, not far below the Debye temperature of  $\sim 460$  K [67], thus represents an anomalous thermal expansion behavior and implies an anomaly of the thermal properties in this temperature regime.

The available data on temperature dependence of the specific heat of lightly Ag-doped  $\text{PrMnO}_3$  ( $\text{Pr}_{1-x}\text{Ag}_x\text{MnO}_3$ ,  $x \leq 0.2$ ) do not show any anomaly that would indicate a phase transition in the temperature range between 200 and 320 K [68]. This raises the question whether the orbital-order transition, if present at lightly Ag-doped  $\text{PrMnO}_3$ , is a continuous transition since the structural changes between a tilt-induced order and spontaneous order are rather small.

## 2. Change in lattice parameters for Jahn-Teller modes

In the following, we want to consider whether the changes of the lattice parameter can be interpreted as a structural fingerprint of Jahn-Teller distortions with respect to the Jahn-Teller modes  $\Delta Q_2$  and  $\Delta Q_3$ . Therefore, we study the influence of Jahn-Teller distortions as well as octahedral tilt on the orthorhombic lattice parameters [69]. The atomic positions in bulk PCMO  $x = 0$  and PCMO  $x = 0.1$ , obtained in Rietveld refinement by Jiráček *et al.* [8,69] at room temperature, provide our starting point. In accordance with Tamazyan and Van Smaalen [70], the lattice parameters of a corner-shared network of  $\text{MnO}_6$  octahedra can be expressed as a function of the tilt angle  $\theta$  and the Jahn-Teller modes  $\Delta Q_2$  and  $\Delta Q_3$  as follows:

$$a = \sqrt{2}(d_1 + d_s)[\cos\theta + n_1^2(1 - \cos\theta)] + \sqrt{2}(d_1 - d_s)[n_1n_2(1 - \cos\theta) - n_3 \sin\theta], \quad (7a)$$

$$b = \sqrt{2}(d_1 + d_s)[\cos \theta + n_2^2(1 - \cos \theta)] + \sqrt{2}(d_1 - d_s)[n_2 n_1(1 - \cos \theta) + n_3 \sin \theta], \quad (7b)$$

$$c = 4 d_m[\cos \theta + n_3^2(1 - \cos \theta)]. \quad (7c)$$

Here,  $(n_1, n_2, n_3)$  is the normal vector along the tilt axis, and  $d_l, d_m,$  and  $d_s$  the long, medium, and short Mn-O distances of the  $\text{MnO}_6$  octahedra. The octahedra are assumed to be ideal, i.e., no distortion of the right angles appears as justified by the work of Zhou and Goodenough [71]. Combined with values obtained by Jiráček *et al.* [8,69] at room temperature, the changes in Mn-O bonding lengths can be parametrized by the relative changes of the amplitude of the two Jahn-Teller modes  $\Delta Q_1, \Delta Q_2,$  and  $\Delta Q_3$  compared with their room temperature values:

$$d_l = d_l^{\text{RT}} + \frac{1}{\sqrt{3}\Delta Q_1} + \frac{1}{\sqrt{2}\Delta Q_2} - \frac{1}{\sqrt{6}\Delta Q_3}, \quad (7d)$$

$$d_m = d_m^{\text{RT}} + \frac{1}{\sqrt{3}\Delta Q_1} + \frac{2}{\sqrt{6}\Delta Q_3}, \quad (7e)$$

$$d_s = d_s^{\text{RT}} + \frac{1}{\sqrt{3}\Delta Q_1} - \frac{1}{\sqrt{2}\Delta Q_2} - \frac{1}{\sqrt{6}\Delta Q_3}, \quad (7f)$$

Here, we assume that the average Mn-O distance remains unchanged, i.e., no temperature dependent breathing of the octahedra are accounted for, and thus,  $\Delta Q_1 = 0$ . In a next step, the direction of the rotation axis is set to the values given by the refinements [8,69], and it is assumed that the direction of the axis remains temperature independent. Subsequently, the root mean square difference between modeled and experimental lattice parameters is minimized by varying  $\Delta Q_2, \Delta Q_3,$  and tilt angle  $\theta$ . This yields temperature-dependent values for the Jahn-Teller modes  $\Delta Q_2, \Delta Q_3,$  as well as the tilt angle, which are presented in Fig. 10(a). While the tilt angle remains relatively unchanged, the increased anisotropy in lattice parameters can be described with enhanced Jahn-Teller distortions toward low temperatures. The comparison between modeled and experimental lattice parameters is shown in Fig. 10(b) and shows a very good quality of the fit.

Noteworthy, the fixation of the rotation axis as well as the mean Mn-O distance to the literature values at room temperature is a model assumption chosen to avoid an underdetermined minimization problem, possibly affecting the quantitative values of the extracted parameters. However, while the rotation axis is known to be rather insensitive to doping and temperature changes [8,30,69], a change in the mean Mn-O distance affects all lattice parameters equally. A uniform outward-inward breathing distortion  $\Delta Q_1$  is thus unsuitable to explain the increased anisotropy at low temperatures. Consequently, the experimentally found data can be described by changes in the Jahn-Teller modes  $\Delta Q_2$  and  $\Delta Q_3$  only. The parallel trends of  $\Delta Q_2$  and  $\Delta Q_3$  indicate that a very similar type of continuous change of the amplitudes of the Jahn-Teller distortions takes place in PCMO  $x = 0$  and PCMO  $x = 0.1$  that mainly increases the antiferrodistortive in-plane ordering  $\Delta Q_2$  with decreasing temperature.

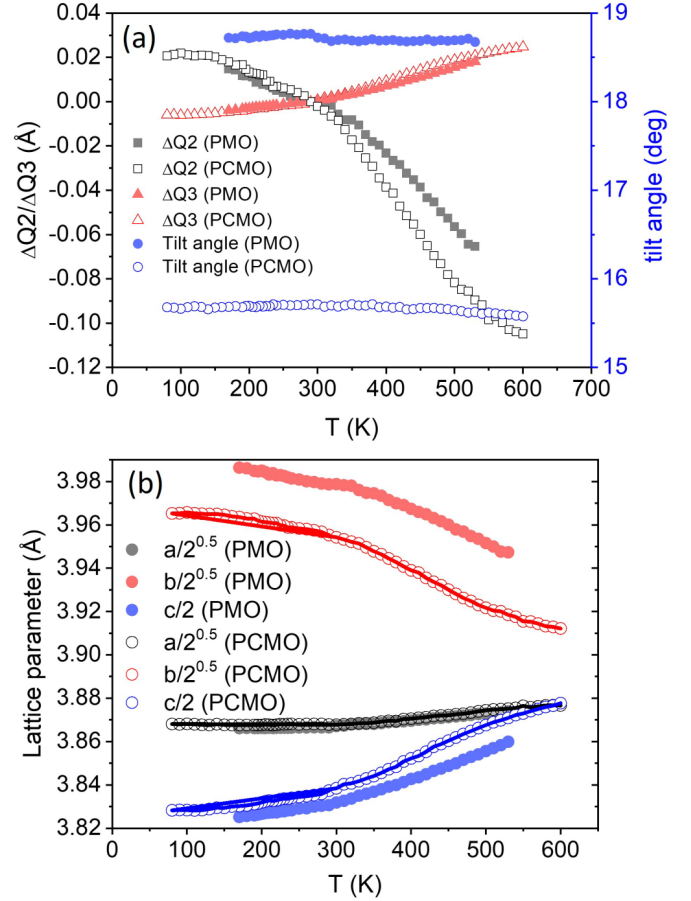


FIG. 10. (a) Change of Jahn-Teller modes  $\Delta Q_3$  and  $\Delta Q_2$  relative to the room temperature values as well as octahedral tilt angle for PCMO  $x = 0$  (closed symbols) and PCMO  $x = 0.1$  (open symbols). (b) Pseudocubic lattice parameters corresponding to the  $\Delta Q_2, \Delta Q_3,$  and tilt angle  $\theta$  shown in (a) (symbols) as well as the experimentally obtained values replotted from Fig. 8 (lines).

### III. DISCUSSION

The comprehensive temperature-dependent study of physical and structural properties of PCMO  $x = 0.1$  presented above indicates the presence of an additional low-temperature phase transition in the phase diagram of PCMO. The main changes of the physical properties of the films observed at the orbital-order phase transition at  $T_{\text{OO}} \approx 220\text{--}250$  K can be summarized as follows:

(1) The hot-polaron photovoltaic effect sets in at  $T_{\text{OO}}$  (Fig. 2) and therefore depends on orbital order (for PCMO  $x = 0.1$ ), respectively, on orbital and charge order (for PCMO  $x = 0.34$ ) [11]. An increased hot-polaron lifetime below  $T_{\text{OO}}$  has been identified by optical pump-probe experiments in (Fig. 6).

(2) A subtle but reliable change of the activation barrier for thermally activated hopping of hole-type polarons is observed at  $T_{\text{OO}}$  (Fig. 3). Such an increase of the activation barrier with decreasing temperatures can be explained through the formation energy of orbital defects in an orbital-ordered structure. Such an excess energy is not required in an orbital-disordered structure or is lower in a structure with a lower degree of order.

(3) Another fingerprint of the phase transition is the observed onset of a pronounced magnetoresistance effect below  $T_{OO}$ . Furthermore, a slight change in the temperature dependence of the magnetic susceptibility  $\chi(T)$  is visible. The onset of this change in  $\chi(T)$  is observed at 260 K, which is above but close to  $T_{OO}$ . Typically, phase transitions that affect spin properties manifest themselves at higher temperatures in the magnetic susceptibility through a change in spin fluctuations. The physical origin might be a change in the double exchange coupling between Mn ions due to an increase in orbital order, as, e.g., described in the model of Millis *et al.* [45].

(4) The temperature dependence of the optical bandgap shows a transition from a normal behavior with an increase with decreasing temperature due to thermal contraction to an anomalous behavior below  $T_{OO}$  (Fig. 5), where the bandgap decreases during cooling. This may reflect the anomalous thermal expansion behavior below the transition temperature, where the thermal expansion coefficients change due to the ordering. The change in optical properties is also reflected in a change of the transient optical response after pumping polaron excitations at the bandgap: Polaronic excitations do not only show an increase in the lifetime below  $T_{OO}$ , but the transient absorption also exhibits nonmonotonous and hysteretic features, pointing to an anomaly in the specific heat in this temperature range.

(5) The lattice parameters of two bulk powder PCMO samples with doping of  $x = 0$  and 0.1 exhibit a change in thermal expansion at  $\sim 350$  and 300 K, respectively, which we attribute to the orbital-order transition. This gives us access to the orbital-order temperature in the bulk as opposed to films, for which the orbital-order transition temperature is lower due to misfit strain and growth-induced defects.

### A. Orbital order and orbital polarization

Our theoretical calculation of the orbital-order phase transition exhibits an onset of spontaneous orbital order near 270 K for PCMO  $x = 0.1$ , and preliminary results for PCMO  $x = 0$  yield a transition temperature of 360 K. At the transition temperature, the calculated order parameter for orbital order  $C_Q^{\text{av}}$  for  $\vec{q} = (\frac{2\pi}{a}, 0)$  falls off rapidly with increasing temperature. The orbital polarization, on the other hand, is not affected by the orbital-order transition and remains intact up to high temperatures. While the orbital polarization is a measure of the size of the distortion in a single octahedron, the orbital order describes the correlation of distortions on different octahedra.

The orbital polarization is quantified by the corresponding structural parameter, the relative distortion  $D = \frac{1}{6} \sum_{j=1\dots 6} [(d_j - \langle d \rangle) / \langle d \rangle]^2$  with the Mn-O distances  $d_j$  in the octahedron and their mean value  $\langle d \rangle = \frac{1}{6} \sum_{j=1\dots 6} d_j$ . The relative distortion is directly related to the integral  $D = \frac{1}{12\langle d \rangle^2} \int d^3q C_Q(\vec{q})$  of the correlation function  $C_Q$ , when only the Jahn-Teller active distortions  $Q_2$  and  $Q_3$  are considered.

Specifically, the correlation functions exhibit peaks which broaden as the system loses the orbital order [72]. The broadening lowers the peak intensity at the wave vectors of the lattice but not its integrated weight. The width is a measure of the (inverse) correlation length and thus of orbital disorder.

The total weight of the peaks, on the other hand, is a measure of orbital polarization.

We note that our simulations do not incorporate the tilt order of the material. Therefore, the remaining induced orbital order observed experimentally [19] above the orbital-order transition, which we attribute to an orbital order induced by the octahedral tilt, is absent.

### B. The nature of nonmagnetic thermal phase transitions at low doping

Our results indicate that the orbital-order transition in the low-doped region occurs at considerably lower temperatures than previously believed. For bulk PCMO  $x = 0$ , our results indicate the transition to be near 360 K, which is consistent with the simulations. This conclusion also affects the assignment of the high-temperature phase transition above 800 K [10,30,73] for PCMO  $x = 0$ , previously assigned to be due to orbital order. At this point, however, we can only speculate about the nature of the phases in the high-temperature part of the phase diagram:

At high temperatures, Pollert *et al.* [10] determined two phase transitions in PCMO  $x = 0$ , namely, an orthorhombic-to-orthorhombic O/O' transition at 815 K and an orthorhombic-to-pseudocubic O'/C transition at 945 K. Sánchez *et al.* obtained a similar pattern, albeit with transitions shifted to higher temperatures, namely, with the O/O' transition at 948 K and the O'/C transition at  $T_{JT} = 1050$  K [74]. The O'/C transition is related to a strong increase of the electric conductivity with increasing temperature [73,75]. In the orthorhombic low-temperature phase, conductivity is restricted due to thermally activated polarons, while metallic band conduction dominates in the high-temperature phase. Zhou and Goodenough [73] also describe a transition temperature  $T^* < T_{JT}$  which is characterized by a slope discontinuity in the thermoelectric power. It must remain open at this point whether  $T^*$  can be identified with the O/O' transition observed by Pollert *et al.* [10].

The loss of orbital order alone does not explain the transition to metallic conduction because it preserves the Jahn-Teller splitting between the  $e_g$  orbitals. This notion is supported by our finding in the simulations, which exhibit a finite bandgap also above the orbital-order transition.

A possible mechanism for the metal-insulator transition is as follows: A reduction of the mean Mn-O-Mn bond angle increases the band width, which in turn may close the bandgap between upper and lower Jahn-Teller bands. The resulting redistribution of electrons from the lower to the upper Jahn-Teller band could eventually lead to a collapse of the orbital polarization. Loss of orbital polarization lowers the Jahn-Teller splitting, and this eventually causes the metal-insulator transition.

Hence, we tend to attribute the orthorhombic-to-pseudocubic transition at  $T_{JT}$  to the loss of orbital polarization rather than that of orbital order. With this reassignment, there is no contradiction with an orbital-order transition near room temperature consistent with our findings.

Both transitions O/O' and O/C have a strong tilt component, as indicated by the strong dependence of the transition

temperatures on the tolerance factor [73]. The thermodynamics of the octahedral tilt pattern, which strongly determines the ordering at high temperatures, is expected to be similar for  $\text{PrMnO}_3$  and  $\text{CaMnO}_3$ . The latter exhibits two tilt transitions close to  $900^\circ\text{C}$  [76]. It is conceivable, although not guaranteed, that the phase transitions  $T^*$  and  $T_{\text{JT}}$  are connected to the two tilt transitions observed for  $\text{CaMnO}_3$ .

A direct experimental probe of the orbital order is the resonant x-ray scattering experiments by Murakami *et al.* [19] on  $\text{LaMnO}_3$ . The orbital-order reflection (3,0,0) exhibits a clear drop near 200 K, which the authors relate to the Néel transition at 140 K. Our finding offers the orbital-order transition as an alternate explanation for the drop in the orbital-order reflection. However, the work by Murakami *et al.* [19] also shows a high-temperature tail of the reflection. A possible explanation for this tail is a remaining orbital polarization induced by the tilt pattern, which persists up to the orthorhombic-to-orthorhombic transition of  $\text{LaMnO}_3$  at 780 K. Furthermore, Zimmermann *et al.* [17] observed an orbital-order (0,3,0) reflection at the Mn  $K$  edge in polarized x ray for  $\text{Pr}_{0.75}\text{Ca}_{0.25}\text{MnO}_3$  which exhibits a steplike reduction above 220 K and a high-temperature tail up to 850 K, where it vanishes. Also, Raman studies of  $\text{PrMnO}_3$  thin films on  $\text{LaAlO}_3$  and  $\text{SrTiO}_3$  substrates indicate possible structural phase transitions by the significant softening of the JT active modes at 412 and  $690\text{ cm}^{-1}$  above a temperature of 220 K [77].

This apparent contradiction can be resolved within a model in the spirit of the Landau theory of phase transitions for two coupled order parameters. As reviewed by Cowley [31], there are several types of Landau free energies that describe the impact of a primary order parameter, e.g., due to a structural phase transition, on a secondary order parameter, such as an induced physical property. Here, we start from the free energy of two independent second-order phase transitions at different temperatures, one for the orbital-order parameter and another one for the tilt angle. The saturation of the order parameters further away from the transition temperature is accounted for by replacing the linear prefactor  $\frac{T-T_c}{\Delta}$  by  $\tanh(\frac{T-T_c}{\Delta})$ . Finally, the two order parameters  $x$  and  $y$  are coupled by a bilinear term.

Let us consider a free energy of the form

$$F_T(x, y) = \frac{1}{4}x^4 + \tanh\left(\frac{T - T_x}{\Delta_x}\right)\frac{1}{2}x^2 + \frac{1}{4}y^4 + \tanh\left(\frac{T - T_y}{\Delta_y}\right)\frac{1}{2}y^2 - \alpha xy, \quad (8)$$

which describes the free energy for two order parameters  $x$  and  $y$  as a function of temperature  $T$ . For  $\alpha = 0$ , the free energy describes two systems that each undergo a second-order phase transition at, respectively,  $T_y$ . The parameters  $\Delta_x$  and  $\Delta_y$  control the sharpness of the corresponding transition. The last term with the coupling parameter  $\alpha$  describes the coupling of the two systems. For  $\alpha > 0$ , it favors states with order parameters having equal signs over those with opposite signs. The parameters ( $T_x = 300\text{ K}$ ,  $\Delta_x = 50\text{ K}$ ,  $T_y = 700\text{ K}$ ,  $\Delta_y = 100\text{ K}$ , and  $\alpha = 0.9$ ) have been adjusted so that the orbital-order parameter resembles the data for the orbital reflection of Murakami *et al.* [19]. The variable  $x$  represents the order

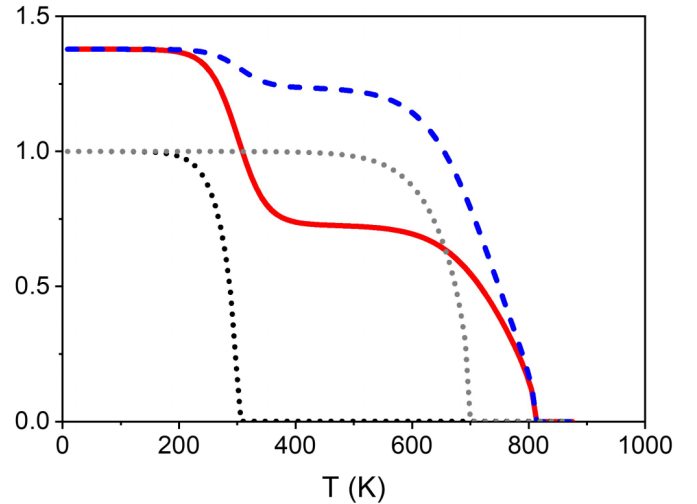


FIG. 11. Order parameters for the free energy of Eq. (8) as a function of temperature. The full line describes the orbital-order parameter  $x$ , and the dashed line represents the tilt angle. Both are scaled to their low-temperature value without coupling. The dotted lines show the order parameters in the absence of coupling.

parameter for the orbital order, while the variable  $y$  represents the tilt angle. For the sake of simplicity, we consider only one tilt angle. Both order parameters are given in units of their uncoupled low-temperature values.

As shown in Fig. 11, in the presence of a coupling, the order parameter  $x$  for orbital order has two nonzero plateaus. At low temperatures, the orbital order is spontaneous, while being enhanced in size due to the cooperative effect of the tilt angle. At the temperature of the orbital-order transition of the uncoupled system, the order parameter does not fall off to zero, but it exhibits a drop to a lower value, which is due to orbital order induced by the tilt pattern. Consequently,  $T_x = 300\text{ K}$  marks the temperature for which the orbital order is largely lost, i.e., the transition temperature for spontaneous orbital ordering. While the order parameter  $x$  for the orbital order goes to zero at  $T_y = 800\text{ K}$  simultaneously with that for the tilt pattern, one would characterize the region of the induced orbital order by the tilt pattern rather than by the orbital order.

Interesting are the changes upon doping, which reduce the weight of the checkerboard pattern of the orbital order by inserting hole polarons. Hole polarons in the background of the checkerboard orbital order are shown in Fig. 1. This reduces the magnitude of the induced orbital order, as opposed to shifting the transition temperature from  $T_y = 800\text{ K}$  to  $T_x = 300\text{ K}$ , as one might expect [78].

When the hole polarons order themselves in a pattern that cannot couple to the tilt pattern, the two transitions at  $T_x$  and  $T_y$  become decoupled, and two independent second-order transitions are obtained. This is clearly seen by comparing the temperature dependence of Zimmermann *et al.* [17]: The orbital (0,3,0) reflection for doping PCMO  $x = 0.25$  exhibits an induced orbital order, while that for doping PCMO  $x = 0.4$  in the charge-ordered regime undergoes an abrupt transition to zero at 240 K.



The distinction between induced and spontaneous order in the experimental studies has an impact on the classification of the phase transition. Figure 9 shows continuous changes of the lattice parameter across the phase transition, indicative for a continuous, e.g., second-order phase transition. This is also reflected in the fit of the lattice parameter by the structure model including tilt and Jahn-Teller distortion. Only the amplitudes of the  $Q_2$  and  $Q_3$  modes are changing across the phase transition, whereas the symmetry of the distortions is the same above and below the phase transition. As a result, the lattice possesses  $Pbnm$  symmetry above and below the orbital-order transition. In contrast, the high-temperature tilt phase transition is of first order since both the lattice symmetry is changing as well as the lattice parameters, and the cell volume shows a step at the transition temperature.

#### IV. CONCLUSIONS

A previously unknown phase transition has been detected in the low-doping region of PCMO at  $T_{OO} = 350$  K for  $x = 0$ ,  $T_{OO} = 300$  K for  $x = 0.1$ , and at  $\sim T_{OO} = 220$ – $250$  K in thin films with  $x = 0.1$ . The experimental fingerprints are an anomalous thermal expansion behavior in the bulk materials and changes in the physical properties of the thin films. Remarkable is the increase of lifetime of polaron excitations below  $T_{OO}$  that corresponds to an onset of the polaron photo-voltaic effect.

Our theoretical simulations provide evidence that this transition is the orbital-order phase transition with the appearance of spontaneous orbital ordering. In the theoretical simulations, the orbital order vanishes during the transition, while the orbital polarization remains intact up to high temperatures. Our findings indicate that the orbital-order transition in the low-doped region occurs in a similar temperature range for the whole doping regime.

A remaining induced orbital order above the orbital-ordering temperature observed in resonant XRD [19] for  $\text{LaMnO}_3$  and PCMO for  $x = 0.25$  [17] is attributed to an induced orbital order caused by an octahedral tilt pattern. The tilt pattern couples to the Jahn-Teller distortion and thus induces an orbital order via displacements of the A-type (Pr, Ca) ions. The resonant x-ray scattering studies at PCMO  $x = 0.25$  exhibit a strong decay of the orbital-order reflection above 220 K with a tail extending to high temperatures of 850 K.

Our reassignment of the orbital-order transition to appear at temperatures close or below room temperature has an impact on the interpretation of the high-temperature phase transition at 950 K, previously assigned to the orbital-order transition [10] and taken up by Refs. [17,64]. We attribute it to a combination of a tilt transition with a metal-insulator transition, which explains the increased metallic conductivity above the phase transition. The altered phase diagram is shown in Fig. 12.

Other studies of orbital order in the charge- and orbital-ordered range of the phase diagram of PCMO using resonant XRD never found an orbital-ordered state at temperature close to the melting temperature and thus support our conclusion that spontaneous orbital ordering driven by electronic correlations only emerges at low and moderate temperatures.

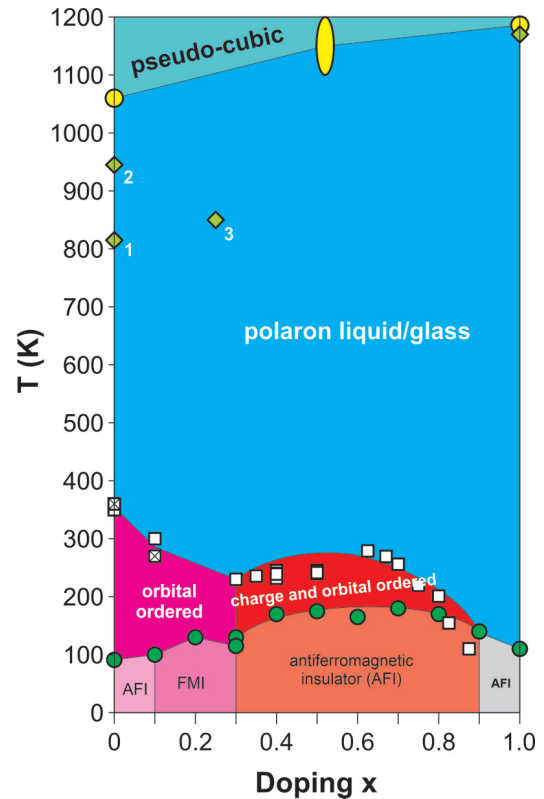


FIG. 12. Proposed modified bulk phase diagram of PCMO: Data points included in the phase diagram are based on the following published results [7–9,16,17,76,79–81] and are listed in Appendix C. For undoped  $x = 0$  and low-doped  $x = 0.1$ , our experimental results based on temperature anomaly of lattice parameters are shown (squares). In addition, the results from theoretical simulations (crossed out squares) redefine the low-doped region. The data points for the high-temperature phase transition are included: For undoped PCMO  $x = 0$  (1) is an observed change in the thermoelectric power [30], (2) an O/O' transition [73], and (3) the disappearance of residual orbital order measured by resonant x-ray spectroscopy for PCMO  $x = 0.25$  [64]. Note that various magnetic subphases are not indicated; see Refs. [8,9,37] as well as possible changes in properties of the polaron liquid/glass phases as a function of doping found in other manganites [82]. Since induced orbital order is different from spontaneous orbital order, it is not indicated as a true phase, as discussed in the text.

Our results also suggest reevaluating the orbital-ordered corner of the phase diagrams of other orthorhombic manganites such as  $\text{LaMnO}_3$  and  $\text{NdMnO}_3$ .

#### ACKNOWLEDGMENTS

This paper is funded by the Deutsche Forschungsgemeinschaft (DFG, German Research Foundation) 217133147/SFB 1073, projects B02, B03, A06, and B07. The authors thank K. Stroh for supporting the absorption experiments. M.t.B. and P.E.B. are grateful to Dr. Sangeeta Rajpurohit for fruitful discussions on the dynamical and thermodynamical properties of manganites.

B.K., T.M., and M.t.B. contributed equally to this paper.

## APPENDIX A: EXPERIMENTS

### 1. Sputter deposition of epitaxial films

Epitaxial  $\text{Pr}_{0.9}\text{Ca}_{0.1}\text{MnO}_3$  (PCMO) thin films were deposited on (100)  $\text{SrTiO}_3$  (STO) and (100)  $\text{SrTi}_{0.995}\text{Nb}_{0.005}\text{O}_3$  (STNO) substrates by ion-beam sputtering with a thickness of 100 nm. STNO serves as the  $n$ -doped part of the heterojunctions. For optical and pump-probe spectroscopy, epitaxial PCMO films on MgO substrates were used because of the larger bandgap and higher thermal conductivity of this substrate.

During deposition, the total gas pressure amounted to  $5.4 \times 10^{-4}$  mbar. Argon was used for beam neutralization ( $P_{\text{Ar}} = 3 \times 10^{-4}$  mbar) and xenon for sputtering ( $P_{\text{Xe}} = 1 \times 10^{-4}$  mbar). An oxygen partial pressure of  $P_{\text{O}_2} = 1.4 \times 10^{-4}$  mbar is sufficient for a correct oxygen stoichiometry of the perovskite phase. The deposition temperature of the substrate surface was  $\sim 720$  °C (the temperature of the heater was fixed at 820 °C). To reduce strain and growth-induced defects that affect resistivity, the samples for electric transport measurements were postannealed in air at 900 °C up to 20 h. The heating and cooling rates were fixed to 100 K/h.

### 2. XRD

To characterize the out-of-plane growth directions and the strain states of the thin film samples, XRD in  $\Theta$ -2 $\Theta$  Bragg-Brentano geometry and at room temperature was performed with a Bruker D8 Discover system with monochromatic  $\text{Cu } K\alpha_1$  radiation  $\lambda = 1.5406$  Å.

For temperature-dependent characterization in the range between 540 and 90 K, polycrystalline bulk powders prepared by conventional solid-state reaction were investigated using a Bruker D8 Advance Powder X-Ray system with  $\text{Cu } K\alpha$  radiation. To avoid oxygen losses, measurements above room temperature were performed in air. For low-temperature measurements, the sample holder was cooled with liquid nitrogen, and the sample chamber was evacuated down to  $P = 10^{-2}$  mbar. The lattice parameters were deduced from measurements with an angular resolution of 0.01°.

### 3. Photovoltaic characterization

For photovoltaic characterization, previously reported sample geometry was used [11]. On the rear side of the STNO substrate, ohmic back contacts were realized by Ti layers with protective Au coatings. Using a shadow mask, Pt top contacts with a thickness of 200 nm and a size of  $4 \times 1$  mm were deposited onto the PCMO  $x = 0.1$  films. All current densities are normalized to this top contact area. The deposition of the contact layers was also performed by ion-beam sputtering (IBS).

The samples were set up in a Cryostat (Cryovac) with a suprasil entry window and analyzed in a temperature range from 80 to 300 K. Excluding resistance contributions of the supply cables, top and back contacts were connected to a Keithley 2430 serving as voltage source and ammeter. Additionally, the voltage drop was measured by a Keithley 2182A Nanovoltmeter (internal resistance  $> 10\text{G } \Omega$ ).

A LOT 150W Xe-UV lamp served for polychromatic illumination and, by introducing cutoff filters characterized by

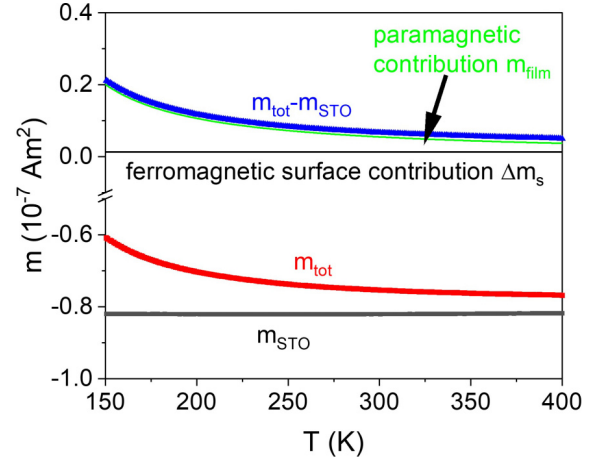


FIG. 13. Temperature dependence of different contributions to the magnetic moment at  $B_0 = 200$  mT.  $m_{\text{STO}}$ : blank STO substrate (black symbols).  $m_{\text{tot}}$ : PCMO  $x = 0.1$  on STO (red symbols). Difference  $m_{\text{tot}} - m_{\text{STO}}$  (blue symbols).  $m_{\text{film}}$ : paramagnetic PCMO  $x = 0.1$  contribution (green line).  $\Delta m_s$ : temperature-independent contribution due to STO surface ferromagnetism (black line).

a maximum photon excitation energy  $E_{\text{max}}$ , for illuminations with  $E_{\text{ph}} \leq E_{\text{max}}$ . The output power of the source was set to 175 mW.

### 4. Temperature-dependent resistivity

Temperature-dependent four-point resistance measurements in zero magnetic field and at 9 T at a constant voltage of 75 mV were performed in a Physical Properties Measurement System from Quantum Design. The investigated PCMO  $x = 0.1$  films on insulating STO substrates were prepared with ion-beam sputtered  $4 \times 1$  mm Pt top contacts with a spacing of 2 mm by using a shadow mask. The magnetic field was aligned perpendicular to the substrate.

### 5. Magnetic properties

The field- and temperature-dependent magnetic moment of PCMO  $x = 0.1$  films on STO was measured with a Quantum Design SQUID-magnetometer in the DC measurement mode. The magnetic field was aligned in-plane, i.e., parallel to the substrate. Diamagnetic background contributions of the sample holder and the STO substrate contributions were deduced from the blank (100) STO substrate. This background signal was then subtracted from the experimentally observed moment of coated substrates.

For STO substrates, three relevant contributions to the magnetic moment need to be considered [83]: the intrinsic diamagnetic moment, a paramagnetic contribution due to impurities, and a ferromagnetic surface magnetism  $m_0$  that is closely related to the formation of oxygen vacancies.

As shown in Fig. 13, the contributions of film and substrate are comparable in magnitude, and the extraction of the film contribution needs careful consideration. The blank substrate measurement  $m_{\text{STO}}$  mainly exhibits a diamagnetic contribution. However, it weakly depends on temperature and applied field, indicating an additional magnetic contribution that is most probably due to magnetic impurities. The ferromagnetic

surface contribution of STO substrates may change while heating to the PCMO  $x = 0.1$  deposition temperature under deposition conditions due to the surface formation of oxygen vacancies. Therefore, the paramagnetic moment  $m_{\text{film}}$  of the PCMO  $x = 0.1$  film cannot be directly related to the difference between the total moment  $m_{\text{tot}}$  of film and the substrate moment  $m_{\text{STO}}$ .

To consider these changes of the substrate, we have fitted the difference of the two experimental datasets  $m_{\text{tot}}(H, T) - m_{\text{STO}}(H, T)$  in the high-temperature range ( $T > 300$  K) by including a temperature-independent substrate contribution  $\Delta m_S(H)$ . Within this model, the magnetic moment  $m_{\text{film}}$  of the film is then given by

$$\begin{aligned} m_{\text{film}} &= m_{\text{tot}}(H, T) - m_{\text{STO}}(H, T) - \Delta m_S(H) \\ &= \frac{\chi_0 H}{(T - T_{\text{CW}})} V_{\text{film}}, \end{aligned} \quad (\text{A1})$$

Here,  $\Delta m_S$  is treated as a temperature-independent constant that corresponds to changes during heating. This seems to be reasonable because the surface contribution  $m_0(H)$  is temperature independent and saturates at external field of  $\sim 200$  mT [46]. The temperature dependence of  $\Delta m_S$  is very small; see Fig. S5 of the Supplementary Material [38]. From the fit, we observed that the correction  $\Delta m_S$  is negligibly small ( $3 \times 10^{-12}$  Am<sup>2</sup>) for small fields of 10 mT but significant ( $1.6 \times 10^{-9}$  Am<sup>2</sup>) at 200 mT.

## 6. Optical spectroscopy

The overview of the spectral- and temperature-dependent absorption coefficient was measured in a transmission setup and is not corrected by reflection. In the UV-Vis range ( $E_{\text{ph}} = 1.13\text{--}6.2$  eV), the setup consists of an OceanOptics DH-2000 Halogen light source, a fiberglass QP400-2-SR-BX, and a Maya2000Pro spectrometer. For the determination of the band gap, additional spectral- and temperature-dependent reflection measurements in the range  $E_{\text{ph}} = 1.2\text{--}1.6$  eV were included to calculate a reflection-corrected absorption coefficient. For the reflectance measurements, enhanced AU mirror (Thorlabs) was included in the setup, which provides a reference spectrum.

The transmittance was calculated by  $I = I_T/I_0$ , where  $I_0$  is the incident, and  $I_T$  is the transmitted spectrally resolved intensity. A baseline correction was applied to the detectors by subtracting a dark spectrum.

## 7. Pump-probe experiments

Experimental data on transient transmission were recorded with a bichromatic pump-probe setup making use of a femtosecond fiber amplifier system from Active Fiber Systems running at 50 kHz repetition rate. The pump beam has a central wavelength of 1030 nm (1.2 eV photon energy); the frequency-doubled probe beam has a central wavelength of 515 nm (2.4 eV photon energy). Both pump and probe beams have a pulse duration of  $< 40$  fs, as checked by autocorrelation in front of the sample. The measurements were performed in nearly collinear beam geometry inside a liquid helium flow cryostat from Janis with optical access. To obtain high signal-to-noise ratio, the pump beam was additionally modulated

with an external chopper at a frequency of 534 Hz to allow direct detection of the transmission change  $\Delta \text{Tr}$  using lock-in detection at the chopper frequency. Probe signal detection itself was performed using a silicon photodiode with an added bandpass filter to block residual pump light. The measurements were performed on an PCMO  $x = 0.1$  sample on MgO [39].

## APPENDIX B: DETAILS OF THE SIMULATION

### 1. Model parameters

The parameters for the model Hamiltonian are extracted from density functional calculations of PCMO with  $x \in \{0, \frac{1}{2}, 1\}$ . The energy terms and the parameters of the model Hamiltonian are provided in an earlier publication [47].

We modified this Hamiltonian in the following ways: (1) We allow the lattice constants to adjust dynamically, as mentioned above, but we constrain the lattice constants in the  $ab$  plane to be equal. (2) Following Rajpurohit *et al.* [84], the resting force constant of the breathing mode is reduced slightly from  $k_{br} = 10.346$  to  $9.04$  eV/Å<sup>2</sup> to reproduce the ratio of the amplitudes of Jahn-Teller vs breathing mode of the *ab initio* calculations for PrMnO<sub>3</sub>.

### 2. Computational details

The Car-Parrinello dynamics [60] used in our simulations introduces fictitious kinetic energy terms for all dynamic degrees of freedom. The degrees of freedom are described by wave functions  $\Psi_{\sigma,j,R,n}$  for the  $e_g$  electrons, occupations  $f_n$ , positions  $R_{R,R'}$  connecting manganese site  $R$  to the neighbor  $R'$ , spins  $\vec{S}_R$  and lattice constants  $T_{x/y/z}$ . Here,  $n$  refers to the band index, index  $R$  to manganese sites, and  $\sigma$  and  $j$  to spin and orbital degrees of freedom of the wave functions. This yields the Lagrangian

$$\begin{aligned} \mathcal{L} &= \sum_{\sigma,j,R,n} f_n \langle \dot{\Psi}_{\sigma,j,R,n} | m_{\Psi} | \dot{\Psi}_{\sigma,j,R,n} \rangle + \frac{n}{2} \sum_{R,R'} M_R \dot{R}_{R,R'}^2 \\ &+ \frac{1}{2} \sum_R m_S \dot{S}_R^2 + \frac{1}{2} \sum_{k \in \{x,y,z\}} M_T \dot{T}_k^2 - E_{\text{pot}}[\Psi, f, R, S, T] \\ &- \mathcal{L}_{\text{constr}}. \end{aligned}$$

Here, the dot refers to the time derivative,  $E_{\text{pot}}$  summarizes all energy terms introduced before and described in Ref. [47], and the last term  $\mathcal{L}_{\text{constr}}$  describes additional constraints, such as orthogonality of the wave functions. Friction terms have been added to the Euler-Lagrange equations.

In the finite-temperature calculation, the Nosé-Hoover thermostat [61,62] drives the thermal fluctuations via a (positive and negative) friction acting on the oxygen atoms. The electrons and spins follow the atoms quasi-adiabatically when they have a sufficiently small mass and a small constant friction. The values of the thermostat masses, frictions, and the period of the Nosé-Hoover thermostat are given in Table I. The lattice constants are kept fixed during the finite-temperature calculations. For the ground state calculation, the masses and frictions are adjusted for a rapid convergence, and the lattice constants are optimized.

TABLE I. Masses and friction values used in the Lagrangian equation.  $m_\psi$  and  $m_S$  are the fictitious masses of electron wave functions and spins.  $M_R$  is the oxygen mass.  $P_{TS}$  is the quasiperiod of the Nosé-Hoover thermostat. The friction forces are  $-f_\psi m_\psi \dot{\Psi}_{\sigma,\alpha,R,n}$  for the wave functions and  $-f_S m_S \dot{S}_R$  for the spins.

$m_\psi$	$m_S$	$M_R$	$P_{TS}$	$f_\psi$	$f_S$
$1.0 m_e a_0^2$	$1.0 m_e \cdot (\frac{a_0}{3/2\hbar})^2$	$15.999 u$	$100 fs$	$0.41 \frac{1}{fs}$	$0.41 \frac{1}{fs}$

The finite-temperature calculations are performed in a  $4 \times 4 \times 4$  manganese sites unit cell. We use a doping of  $x = \frac{6}{43} = 0.09375$ , close to the nominal experimental doping of  $x = 0.1$ . Calculations in a  $6 \times 6 \times 4$  sites unit cell at doping  $x = \frac{14}{144}$  confirmed the ground state and the transition temperature obtained in the smaller unit cell.

### APPENDIX C: PHASE DIAGRAM FOR PCMO

Data points included in the phase diagram in Fig. 10 are based on data in this publication and the following previously published results.

#### 1. Low-temperature magnetic transitions

Summary of the magnetic transitions documented by Jiráček *et al.* [8,9] for doping levels PCMO  $x = 0-0.9$  and Wollan and Koehler [16] for PCMO  $x = 1$  in a combination of x-ray and neutron diffraction measurements as well as additional transport measurements:

- (1)  $x = 0$ :  $T_N = 91$  K antiferromagnetic type A order.
- (2)  $x = 0.1$ :  $T_N = 100$  K ferromagnetic order with easy axis [010], below  $T_2 = 70$  K canted antiferromagnetic order.
- (3)  $x = 0.2$ :  $T_C = 130$  K ferromagnetic order.
- (4)  $x = 0.3$ : ferromagnetic and antiferromagnetic contributions  $T_C = 115$  K and  $T_N = 130$  K, respectively.
- (5)  $x = 0.4$ :  $T_N = 170$  K antiferromagnetic CE type.
- (6)  $x = 0.5$ :  $T_N = 175$  K antiferromagnetic CE type.
- (7)  $x = 0.6$ :  $T_N = 165$  K antiferromagnetic CE type.
- (8)  $x = 0.7$ :  $T_N = 180$  K antiferromagnetic and noncommensurate spiral magnetic ordering.
- (9)  $x = 0.8$ :  $T_N = 170$  K antiferromagnetic type C.
- (10)  $x = 0.9$ :  $T_N = 140$  K antiferromagnetic type C and  $T = 110$  K antiferromagnetic type G.
- (11)  $x = 1.0$ :  $T_N = 110$  K antiferromagnetic type G.

#### 2. Charge and orbital-order transitions at medium temperature

Our bulk analysis of the lattice constant determined by temperature-dependent XRD suggests an orbital-order transition temperature of 350 and 300 K for PCMO doping levels of  $x = 0$  and 0.1, respectively. For higher doping levels between PCMO  $x = 0.3$  and PCMO  $x = 0.5$ , a simultaneous transition of orbital and charge ordering has been experimentally observed in a variety of the following publica-

tions and measuring techniques resulting in similar transition temperature values. For example, Zimmermann *et al.* [17] performed resonant x-ray spectroscopy measurements to determine a simultaneous charge- and orbital-ordering transition at  $T_{CO/OO} = 245$  K for doping of PCMO  $x = 0.4$  and PCMO  $x = 0.5$ . The structural analysis and transport measurements performed by Jiráček *et al.* [8,9] determined the charge-order/orbital-order transition at  $T_{CO/OO} = 230$  K for PCMO  $x = 0.3$  and  $T_{CO/OO} = 232$  K for PCMO  $x = 0.4$ , whereas Yoshizawa *et al.* [79] gave a transition temperature of  $T_{CO/OO} = 200$  K based on changes in lattice parameters determined from neutron diffraction studies for PCMO  $x = 0.3$ . In temperature-dependent resistivity measurements, the onset of charge order is visible in a pronounced step in resistivity. Based on such measurements, Tomioka *et al.* [7] determined  $T_{CO/OO} = 220-230$  K for PCMO  $x = 0.35/0.4/0.5$  and  $T = 200$  K for PCMO  $x = 0.3$ .

The charge-order materials are generally considered to show a broad two-phase region of order and disorder domains. Jooss *et al.* [24] and Wu *et al.* [27] showed for PCMO  $x = 0.32$  and 0.5 a two-phase region of charge-order/orbital-order domains visible from room temperature until 70 K.

For higher doped region PCMO  $x = 0.5$  to 0.875, Zheng *et al.* [81] measured transport, ultrasound, and powder XRD. In this paper, samples with the following doping have been investigated PCMO  $x = 0.5, 0.55, 0.6, 0.625, 0.67, 0.7, 0.75, 0.8, 0.825, 0.85, \text{ and } 0.875$ .

#### 3. Structural phase transitions at high temperature

As previously mentioned for PCMO  $x = 0$ , a variety of publications on the high-temperature phase transition exist. The exact transition temperatures and the statement whether there are one or two transitions varies. Pollert *et al.* [10] published neutron diffraction measurements indicating an O-to-O'-to-pseudocubic transition for  $T_{OO'} = 815$  K and  $T_{OC} = 945$  K, respectively, whereas Sánchez *et al.* [30] published considerably higher  $T_{TT}$  at 1050 K and a possible second transition at 948 K, and Zhou and Goodenough [73] identified two phase transitions using a combination of resistivity and thermoelectric power measurements. They yielded  $T_{TT}$  and  $T^*$  at  $\sim 1050$  and 750 K [73]. Even though the absolute temperatures vary, we suggest that all three publications observe the same two transitions, although their assignment differs.

For doping PCMO  $x = 0.52$ , Carpenter *et al.* [80] published a symmetry and strain analysis of structural phase transitions using powder neutron diffraction. At high temperatures, a first-order transition of orthorhombic  $Pbmn$  structure to  $R\bar{3}c$  is reported in a temperature region between 1100 and 1200 K, which has a significant hysteresis [80]. Zimmermann *et al.* [17] analyzed resonant x-ray scattering for PCMO  $x = 0.25$  and found that the orbital-ordered (030) peak has a residual intensity until 850 K. In the case of PCMO  $x = 1.0$ , Taguchi *et al.* [76] found an orthorhombic phase with a transition into tetragonal phase at 1170 K and a subsequent cubic transition at 1186 K.

[1] M. R. Lees, J. Barratt, G. Balakrishnan, D. McK. Paul, and M. Yethiraj, Influence of charge and magnetic ordering on the

insulator-metal transition in  $\text{Pr}_{1-x}\text{Ca}_x\text{MnO}_3$ , *Phys. Rev. B* **52**, R14303(R) (1995).

- [2] R. von Helmolt, J. Wecker, B. Holzapfel, L. Schultz, and K. Samwer, Giant Negative Magnetoresistance in Perovskite like  $\text{La}_{2/3}\text{Ba}_{1/3}\text{MnO}_x$  Ferromagnetic Films, *Phys. Rev. Lett.* **71**, 2331 (1993).
- [3] Y. Tomioka, A. Asamitsu, Y. Moritomo, and Y. Tokura, Anomalous magnetotransport properties of  $\text{Pr}_{1-x}\text{Ca}_x\text{MnO}_3$ , *J. Phys. Soc. Japan* **64**, 3626 (1995).
- [4] J. Dho, Electrode size dependent IV characteristics and photovoltaic effect in the oxide Pn junctions  $\text{Pr}_{0.7}\text{Ca}_{0.3}\text{MnO}_3/\text{Nb} : \text{SrTiO}_3$  and  $\text{La}_{0.7}\text{Ca}_{0.3}\text{MnO}_3/\text{Nb} : \text{SrTiO}_3$ , *Solid State Commun.* **150**, 2243 (2010).
- [5] G. Saucke, J. Norpoth, C. Jooss, D. Su, and Y. Zhu, Polaron absorption for photovoltaic energy conversion in a manganite-titanate *pn* heterojunction, *Phys. Rev. B* **85**, 165315 (2012).
- [6] S. Mildner, J. Hoffmann, P. E. Blöchl, S. Teichert, and C. Jooss, Temperature- and doping-dependent optical absorption in the small-polaron system  $\text{Pr}_{1-x}\text{Ca}_x\text{MnO}_3$ , *Phys. Rev. B* **92**, 035145 (2015).
- [7] Y. Tomioka, A. Asamitsu, H. Kuwahara, Y. Moritomo, and Y. Tokura, Magnetic-field-induced metal-insulator phenomena in with controlled charge-ordering instability, *Phys. Rev. B* **53**, R1689 (1996).
- [8] Z. Jiráček, S. Krupička, Z. Šimša, M. Dlouhá, and S. Vratislav, Neutron diffraction study of  $\text{Pr}_{1-x}\text{Ca}_x\text{MnO}_3$  perovskites, *J. Magn. Magn. Mater.* **53**, 153 (1985).
- [9] Z. Jiráček, S. Krupička, V. Nekvasil, E. Pollert, G. Villeneuve, and F. Zounová, Structural and magnetization study of  $\text{Pr}_{1-x}\text{Ca}_x\text{MnO}_3$ , *J. Magn. Magn. Mater.* **15-18**, 519 (1980).
- [10] E. Pollert, S. Krupička, and E. Kuzmičová, Structural study of  $\text{Pr}_{1-x}\text{Ca}_x\text{MnO}_3$  and  $\text{Y}_{1-x}\text{Ca}_x\text{MnO}_3$  perovskites, *J. Phys. Chem. Solids* **43**, 1137 (1982).
- [11] B. Ifland, J. Hoffmann, B. Kressdorf, V. Roddatis, M. Seibt, and C. Jooss, Contribution of Jahn-Teller and charge transfer excitations to the photovoltaic effect of manganite/titanite heterojunctions, *New J. Phys.* **19**, 063046 (2017).
- [12] D. Räiser, S. Mildner, B. Ifland, M. Sotoudeh, P. Blöchl, S. Teichert, and C. Jooss, Evolution of hot polaron states with a nanosecond lifetime in a manganite perovskite, *Adv. Energy Mater.* **7**, 1602174 (2017).
- [13] B. Kressdorf, T. Meyer, A. Belenchuk, O. Shapoval, M. ten Brink, S. Melles, U. Ross, J. Hoffmann, V. Moshnyaga, M. Seibt, P. Blöchl, and C. Jooss, Room Temperature Hot Polaron Photovoltaics in the Charge Ordered State of a Layered Perovskite Oxide Heterojunction, *Phys. Rev. Appl.* **14**, 054006 (2020).
- [14] H. A. Jahn and E. Teller, Stability of polyatomic molecules in degenerate electronic states. I—Orbital Degeneracy, *Proc. R. Soc. Lond. A* **161**, 220 (1937).
- [15] J. B. Goodenough, Theory of the Role of Covalence in the Perovskite-Type Manganites [ $\text{La}, \text{M}(\text{II})\text{MnO}_3$ ], *Phys. Rev.* **100**, 564 (1955).
- [16] E. O. Wollan and W. C. Koehler, Neutron Diffraction Study of the Magnetic Properties of the Series of Perovskite-Type Compounds [ $(1-x)\text{La}, x\text{Ca}\text{MnO}_3$ ], *Phys. Rev.* **100**, 545 (1955).
- [17] M. v. Zimmermann, C. S. Nelson, J. P. Hill, D. Gibbs, M. Blume, D. Casa, B. Keimer, Y. Murakami, C.-C. Kao, C. Venkataraman, T. Gog, Y. Tomioka, and Y. Tokura, X-ray resonant scattering studies of orbital and charge ordering in  $\text{Pr}_{1-x}\text{Ca}_x\text{MnO}_3$ , *Phys. Rev. B* **64**, 195133 (2001).
- [18] H. Kuwahara, Y. Tomioka, A. Asamitsu, Y. Moritomo, and Y. Tokura, A first-order phase transition induced by a magnetic field, *Science* **270**, 961 (1995).
- [19] Y. Murakami, J. P. Hill, D. Gibbs, M. Blume, I. Koyama, M. Tanaka, H. Kawata, T. Arima, Y. Tokura, K. Hirota, and Y. Endoh, Resonant X-Ray Scattering from Orbital Ordering in  $\text{LaMnO}_3$ , *Phys. Rev. Lett.* **81**, 582 (1998).
- [20] T. Katsufuji, T. Kajita, S. Yano, Y. Katayama, and K. Ueno, Nucleation and growth of orbital ordering, *Nat. Commun.* **11**, 2324 (2020).
- [21] S. Okamoto, S. Ishihara, and S. Maekawa, Orbital ordering in  $(\text{LaMnO}_3)$  electron-electron and electron-lattice interactions, *Phys. Rev. B* **65**, 144403 (2002).
- [22] V. Anisimov, I. Elfimov, M. Korotin, and K. Terakura, Orbital and charge ordering in  $\text{Pr}_{1-x}\text{Ca}_x\text{MnO}_3$  ( $x = 0$  and  $0.5$ ) from the *ab initio* calculations, *Phys. Rev. B* **55**, 15494 (1997).
- [23] A. Daoud-Aladine, J. Rodríguez-Carvajal, L. Pinsard-Gaudart, M. T. Fernández-Díaz, and A. Revcolevschi, Zener Polaron Ordering in Half-Doped Manganites, *Phys. Rev. Lett.* **89**, 097205 (2002).
- [24] C. Jooss, L. Wu, T. Beetz, R. F. Klie, M. Beleggia, M. A. Schofield, S. Schramm, J. Hoffmann, and Y. Zhu, Polaron melting and ordering as key mechanisms for colossal resistance effects in manganites, *Proc. Natl. Acad. Sci. U. S. A.* **104**, 13597 (2007).
- [25] J. Herrero-Martín, J. García, G. Subías, J. Blasco, and M. Concepción Sánchez, Structural origin of dipole x-ray resonant scattering in the low-temperature phase of  $\text{Nd}_{0.5}\text{Sr}_{0.5}\text{MnO}_3$ , *Phys. Rev. B* **70**, 024408 (2004).
- [26] S. Grenier, J. P. Hill, D. Gibbs, K. J. Thomas, M. v. Zimmermann, C. S. Nelson, V. Kiryukhin, Y. Tokura, Y. Tomioka, D. Casa, T. Gog, and C. Venkataraman, Resonant x-ray diffraction of the magnetoresistant perovskite  $\text{Pr}_{0.6}\text{Ca}_{0.4}\text{MnO}_3$ , *Phys. Rev. B* **69**, 134419 (2004).
- [27] L. Wu, R. F. Klie, Y. Zhu, and C. Jooss, Experimental confirmation of Zener-polaron-type charge and orbital ordering in  $\text{Pr}_{1-x}\text{Ca}_x\text{MnO}_3$ , *Phys. Rev. B* **76**, 174210 (2007).
- [28] V. E. Dmitrienko, Forbidden reflections due to anisotropic x-ray susceptibility of crystals, *Acta Crystallogr. Sect. A* **39**, 29 (1983).
- [29] S. B. Wilkins, T. A. W. Beale, P. D. Hatton, J. A. Purton, P. Bencok, D. Prabhakaran, and A. T. Boothroyd, Probing orbital order with soft x-rays: the case of the manganites, *New J. Phys.* **7**, 80 (2005).
- [30] D. Sánchez, J. A. Alonso, and M. J. Martínez-Lope, Neutron-diffraction study of the Jahn-Teller transition in  $\text{PrMnO}_3$ , *J. Chem. Soc. Dalt. Trans.* **2002**, 4422 (2002).
- [31] R. A. Cowley, Structural phase transitions. I. Landau theory, *Adv. Phys.* **29**, 1 (1980).
- [32] N. A. Pertsev, A. K. Tagantsev, and N. Setter, Phase transitions and strain-induced ferroelectricity in  $\text{SrTiO}_3$  epitaxial thin films, *Phys. Rev. B* **61**, R825(R) (2000).
- [33] A. M. Glazer, The classification of tilted octahedra in perovskites, *Acta Cryst. B* **28**, 3384 (1972).
- [34] P. M. Woodward, T. Vogt, D. E. Cox, A. Arulraj, C. N. R. Rao, P. Karen, and A. K. Cheetham, Influence of cation size on the structural features of  $\text{Ln}_{1/2}\text{A}_{1/2}\text{MnO}_3$  perovskites at room temperature, *Chem. Mater.* **10**, 3652 (1998).
- [35] J. A. Alonso, M. J. Martínez-Lope, M. T. Casais, and M. T. Fernández-Díaz, Evolution of the Jahn-Teller distortion of

- MnO<sub>6</sub> octahedra in RMnO<sub>3</sub> perovskites ( $R = \text{Pr, Nd, Dy, Tb, Ho, Er, Y}$ ): A neutron diffraction study, *Inorg. Chem.* **39**, 917 (2000).
- [36] J. J. Turner, K. J. Thomas, J. P. Hill, M. A. Pfelfer, K. Chesnel, Y. Tomioka, Y. Tokura, and S. D. Kevan, Orbital domain dynamics in a doped manganite, *New J. Phys.* **10**, 053023 (2008).
- [37] P. G. Radaelli, D. E. Cox, M. Marezio, and S.-W. Cheong, Charge, orbital, and magnetic ordering in La<sub>0.5</sub>Ca<sub>0.5</sub>MnO<sub>3</sub>, *Phys. Rev. B* **55**, 3015 (1997).
- [38] See Supplemental Material at <http://link.aps.org/supplemental/10.1103/PhysRevB.103.235122> for additional microstructural characterization, transport, optical and magnetic properties, simulations of pump probe dynamics and theoretical simulation, and includes Refs. [8,30,42,49,51,64,80,82–89].
- [39] B. Ifland, J. Hoffmann, T. Kramer, M. Scherff, S. Mildner, and C. Jooss, Strain driven phase decomposition in ion-beam sputtered Pr<sub>1-x</sub>Ca<sub>x</sub>MnO<sub>3</sub> films, *J. Nanomater.* **2015**, 935167 (2015).
- [40] M. Takizawa, K. Maekawa, H. Wadati, T. Yoshida, A. Fujimori, H. Kumigashira, and M. Oshima, Angle-resolved photoemission study of Nb-doped SrTiO<sub>3</sub>, *Phys. Rev. B* **79**, 113103 (2009).
- [41] A. Wahl, V. Hardy, C. Martin, and C. Simon, Magnetic contributions to the low-temperature specific heat of the ferromagnetic insulator Pr<sub>0.8</sub>Ca<sub>0.2</sub>MnO<sub>3</sub>, *Eur. Phys. J. B* **26**, 135 (2002).
- [42] J. Hoffmann, P. Moschkau, S. Mildner, J. Norpoth, C. Jooss, L. Wu, and Y. Zhu, Effects of interaction and disorder on polarons in colossal resistance manganite Pr<sub>0.68</sub>Ca<sub>0.32</sub>MnO<sub>3</sub> thin films, *Mater. Res. Express* **1**, 046403 (2014).
- [43] V. V. Bryksin and H. Böttger, *Hopping Conduction in Solids*, 1st ed. (VCH-Verlagsgesellschaft, Weinheim, 1985).
- [44] T. Holstein, Studies of polaron motion: Part I. The molecular-crystal model, *Ann. Phys. (N. Y.)* **8**, 325 (1959).
- [45] A. J. Millis, P. B. Littlewood, and B. I. Shraiman, Double Exchange Alone Does Not Explain the Resistivity of La<sub>1-x</sub>Sr<sub>x</sub>MnO<sub>3</sub>, *Phys. Rev. Lett.* **74**, 5144 (1995).
- [46] J. Hemberger, M. Brando, R. Wehn, V. Yu. Ivanov, A. A. Mukhin, A. M. Balbashov, and A. Loidl, Magnetic properties and specific heat of RMnO<sub>3</sub> ( $R = \text{Pr, Nd}$ ), *Phys. Rev. B* **69**, 064418 (2004).
- [47] M. Sotoudeh, S. Rajpurohit, P. Blöchl, D. Mierwaldt, J. Norpoth, V. Roddatis, S. Mildner, B. Kressdorf, B. Ifland, and C. Jooss, Electronic structure of Pr<sub>1-x</sub>Ca<sub>x</sub>MnO<sub>3</sub>, *Phys. Rev. B* **95**, 235150 (2017).
- [48] J. Tauc, Optical properties and electronic structure of amorphous Ge and Si, *Mat. Res. Bull.* **3**, 37 (1968).
- [49] A. S. Hassanien, and A. A. Akl, Effect of Se addition on optical and electrical properties of chalcogenide CdSSe thin films, *Superlattices Microstruct.* **89**, 153 (2016).
- [50] C. Rincón, S. M. Wasim, G. Marín, and I. Molina, Temperature dependence of the optical energy band gap in CuIn<sub>3</sub>Se<sub>5</sub> and CuGa<sub>3</sub>Se<sub>5</sub>, *J. Appl. Phys.* **93**, 780 (2003).
- [51] J. Tikkanen, S. Kauhala, H. Huhtinen, and P. Paturi, Anomalous thermal expansion in (Pr, Ca)MnO<sub>3</sub> due to orbital ordering, *Phys. Procedia* **75**, 475 (2015).
- [52] W. Liang, H. Hou, Y. Lin, and S. N. Luo, Ultrafast electron and spin dynamics of strongly correlated NdNiO<sub>3</sub>, *J. Phys. D: Appl. Phys.* **52**, 075303 (2019).
- [53] P. Ruello, S. Zhang, P. Laffez, B. Perrin, and V. Gusev, Ultrafast electronic dynamics in the metal-insulator transition compound NdNiO<sub>3</sub>, *Phys. Rev. B* **76**, 165107 (2007).
- [54] J. L. Cohn, J. J. Neumeier, C. P. Popoviciu, K. J. McClellan, and Th. Leventouri, Local lattice distortions and thermal transport in perovskite manganites, *Phys. Rev. B* **56**, R8495(R) (1997).
- [55] A. I. Lobad, R. D. Averitt, C. Kwon, and A. J. Taylor, Spin-lattice interaction in colossal magnetoresistance manganites, *Appl. Phys. Lett.* **77**, 4025 (2000).
- [56] T. Hotta, Orbital ordering phenomena in d- and f-electron systems, *Reports Prog. Phys.* **69**, 2061 (2006).
- [57] E. Dagotto, T. Hotta, and A. Moreo, Colossal magnetoresistant materials: The key role of phase separation, *Phys. Rep.* **344**, 1 (2001).
- [58] J. H. Van Vleck, The Jahn-Teller effect and crystalline Stark splitting for clusters of the form XY<sub>6</sub>, *J. Chem. Phys.* **7**, 72 (1939).
- [59] J. Kanamori, Crystal distortion in magnetic compounds, *J. Appl. Phys.* **31**, S14 (1960).
- [60] R. Car and M. Parrinello, Unified Approach for Molecular Dynamics and Density-Functional Theory, *Phys. Rev. Lett.* **55**, 2471 (1985).
- [61] S. Nosé, A unified formulation of the constant temperature molecular dynamics methods, *J. Chem. Phys.* **81**, 511 (1984).
- [62] W. G. Hoover, Canonical dynamics: equilibrium phase-space distributions, *Phys. Rev. A* **31**, 1695 (1985).
- [63] The orbital shape in the calculations differs slightly from  $d_{3x^2-r^2}$  and  $d_{3y^2-r^2}$  proposed on experimental grounds [64].
- [64] J. P. Hill, C. S. Nelson, M. V. Zimmermann, Y. J. Kim, D. Gibbs, D. Casa, B. Keimer, Y. Murakami, C. Venkataraman, T. Gog, Y. Tomioka, Y. Tokura, V. Kiryukhin, T. Y. Koo, and S. W. Cheong, Orbital correlations in doped manganites, *Appl. Phys. A* **73**, 723 (2001).
- [65] B. Christopher, A. Rao, B. S. Nagaraja, K. Shyam Prasad, G. S. Okram, G. Sanjeev, V. C. Petwal, V. P. Verma, J. Dwivedi, and P. Poornesh, Correlation between structural and transport properties of electron beam irradiated PrMnO<sub>3</sub> compounds, *Solid State Commun.* **270**, 30 (2018).
- [66] J. Garai, Correlation between thermal expansion and heat capacity, *CALPHAD* **30**, 354 (2006).
- [67] J. G. Cheng, Y. Sui, X. J. Wang, Z. G. Liu, J. P. Miao, X. Q. Huang, Z. Lü, Z. N. Qian, and W. H. Su, Specific heat of single-crystal PrMnO<sub>3</sub>, *J. Phys. Condens. Matter* **17**, 5869 (2005).
- [68] A. G. Gamzatov, A. M. Aliev, A. B. Batdalov, H. Ahmadvand, H. Salamati, and P. Kameli, Specific heat and magnetocaloric effect of Pr<sub>1-x</sub>Ag<sub>x</sub>MnO<sub>3</sub> Manganites, *J. Mater. Sci.* **49**, 294 (2014).
- [69] Z. Jirák, J. Hejtmánek, E. Pollert, M. Maryško, M. Dlouhá, and S. Vratilav, Canted structures in the Mn<sup>3+</sup>/Mn<sup>4+</sup> Perovskites, *J. Appl. Phys.* **81**, 5790 (1997).
- [70] R. Tamazyan and S. Van Smaalen, Quantitative description of the tilt of distorted octahedra in ABX<sub>3</sub> structures, *Acta Cryst. B* **63**, 190 (2007).
- [71] J.-S. Zhou and J. B. Goodenough, Universal Octahedral-Site Distortion in Orthorhombic Perovskite Oxides, *Phys. Rev. Lett.* **94**, 065501 (2005).
- [72] In our simulations, this broadening happens at discrete points due to the finite supercell size.

- [73] J.-S. Zhou and B. Goodenough, Orbital order-disorder transition in single-valent manganites, *Phys. Rev. B* **68**, 144406 (2003).
- [74] Sánchez *et al.* [30] emphasized that the pseudocubic phase is still actually orthorhombic and named it O\* rather than C. We assigned the O/O' transition based on the similar data of Sánchez *et al.* [30] and Pollert *et al.* [10].
- [75] J.-S. Zhou and J. B. Goodenough, Paramagnetic phase in single-crystal LaMnO<sub>3</sub>, *Phys. Rev. B* **60**, R15002(R) (1999).
- [76] H. Taguchi, M. Nagao, T. Sato, and M. Shimada, High-temperature phase transition of CaMnO<sub>3-δ</sub>, *J. Solid State Chem.* **78**, 312 (1989).
- [77] A. Chaturvedi and V. G. Sathe, Raman spectroscopy and x-ray diffraction study of PrMnO<sub>3</sub> oriented thin films deposited on LaAlO<sub>3</sub> and SrTiO<sub>3</sub> substrates, *J. Magn. Magn. Mater.* **344**, 230 (2013).
- [78] The hole polarons have a destabilizing effect, which lowers the orbital-order transition temperature, but this effect, which is also present in our simulations, shifts the transition temperature by a much smaller amount, and it is independent of the tilt pattern.
- [79] H. Yoshizawa, H. Kawano, Y. Tomioka, and Y. Tokura, Neutron-diffraction study of the magnetic-field-induced metal-insulator transition in Pr<sub>0.7</sub>Ca<sub>0.3</sub>MnO<sub>3</sub>, *Phys. Rev. B* **52**, R13145(R) (1995).
- [80] M. A. Carpenter, R. E. A. McKnight, C. J. Howard, and K. S. Knight, Symmetry and strain analysis of structural phase transitions in Pr<sub>0.48</sub>Ca<sub>0.52</sub>MnO<sub>3</sub>, *Phys. Rev. B* **82**, 094101 (2010).
- [81] R. K. Zheng, G. Li, Y. Yang, A. N. Tang, W. Wang, T. Qian, and X. G. Li, Transport, ultrasound, and structural properties for the charge-ordered Pr<sub>1-x</sub>Ca<sub>x</sub>MnO<sub>3</sub> ( $0.5 \leq x \leq 0.875$ ) manganites, *Phys. Rev. B* **70**, 014408 (2004).
- [82] D. N. Argyriou, J. W. Lynn, R. Osborn, B. Campbell, J. F. Mitchell, U. Ruett, H. N. Bordallo, A. Wildes, and C. D. Ling, Glass Transition in the Polaron Dynamics of Colossal Magnetoresistive Manganites, *Phys. Rev. Lett.* **89**, 036401 (2002).
- [83] J. M. D. Coey, M. Venkatesan, and P. Stamenov, Surface magnetism of strontium titanate, *J. Phys. Condens. Matter* **28**, 485001 (2016).
- [84] S. Rajpurohit, C. Jooss, and P. E. Blöchl, Evolution of the magnetic and polaronic order of Pr<sub>1/2</sub>Ca<sub>1/2</sub>MnO<sub>3</sub> following an ultrashort light pulse, *Phys. Rev. B* **102**, 014302 (2020).
- [85] T. Meyer, B. Kressdorf, V. Roddatis, J. Hoffmann, C. Jooss, and M. Seibt, Phase transitions in a perovskite thin film studied by environmental in-situ heating nano-beam electron diffraction, [arXiv:2007.14882](https://arxiv.org/abs/2007.14882) [cond-mat.mtrl-sci].
- [86] H. Ulrichs, D. Meyer, M. Müller, M. Mansurova, and F. Döring, Numerical calculation of laser-induced thermal diffusion and elastic dynamics, in *Proceedings of the 2nd International Symposium on Frontiers in Materials Science (FMS2015)*, edited by T. Yamamoto, M. Yoshiya, H. N. Nhat, and M. Mnzenberg, AIP Conf. Proc. No. 1763 (AIP, New York, 2016), p. 040004.
- [87] S. Adachi, *Magnesium Oxide (MgO) in Handbook on Physical Properties of Semiconductors* (Springer, Boston, 2004).
- [88] P. Thiessen, V. Roddatis, F. Rieger, A. Belenchuk, M. Keuncke, V. Moshnyaga, and C. Jooss, Effect of charge ordering on crossplane thermal conductivity in correlated perovskite oxide superlattices, *Phys. Rev. B* **98**, 195114 (2018).
- [89] A. K. Raychaudhuri, A. Guha, I. Das, R. Rawat, and C. N. R. Rao, Specific heat of single-crystalline (formula presented) in the presence of a magnetic field, *Phys. Rev. B* **64**, 165111 (2001).

## **Chapter 6**

# **Power Density and Spectral Photovoltaic Response in a Hot Polaron Solar Cell**

This Chapter considers the energy and intensity dependence of short circuit current density and open circuit voltage in PCMO  $x=0.1$ . The experimental results are discussed in the framework of applicability of the SQ theory and modifications caused by the hot polaron contributions as well as the role of orbital order. Results and discussions are presented as a manuscript draft that is not published yet.

The corresponding Supplemental Material is included in Appendix C.



# Power density and spectral photovoltaic response in a hot polaron solar cell.

*B. Kressdorf, J. Hoffmann, M. Seibt, C. Jooss*

## 1. Introduction

Solar cells based on semiconductor junctions possess an upper theoretical limit of photovoltaic energy conversion efficiency as given by the Shockley-Queisser (SQ) theory [1]. It is based on the application of the detailed balance principle, where at equilibrium, i.e., without power extraction, electron hole pair generation by photon absorption is balanced by radiative recombination. For conventional semiconductors, the excess carrier recombination in general and radiative recombination in particular is dominated by the excited carriers that have thermalized to the band edges after relaxation / carrier cooling. Thus, photon energy input with a thermal solar spectrum of temperature  $T_s$  is entirely compensated by emission of thermal radiation at the temperature of the device  $T_d$ , however at different solid angles  $\omega$ . This type of radiative equilibrium is disturbed by electric power extraction. In the absence of any other type of recombination a theoretical upper efficiency limit is obtained that depends only on the bandgap  $E_g$ . For Si homojunctions with  $E_g = 1.1$  eV at room temperature the efficiency limit is 32% [1].

A specific characteristic of the SQ theory is that it describes conventional semiconductors, where the quantum efficiency  $Q(E_{ph})$  that accounts for the number of electron-hole pairs generated by an absorbed photon at energy  $E_{ph}$  shows a step-like spectral response with  $Q = 1$  for photon energy  $E_{ph} > E_g$  and  $Q = 0$  for  $E_{ph} < E_g$ . Since relaxation and thermalization of hot carriers is much faster than carrier extraction, all generated electrons and holes are extracted with the same energy-independent collection efficiency.

In real solar cells, a deviation from the ideal SQ limit can of course occur through many different processes. Different types of recombination mechanisms, ohmic transport losses and absorption losses must be taken into consideration [2–5]. Indeed, the SQ limit considers a solar cell in the limit of ideal absorption and ideal collection, neglecting spatial dependency of absorption and carrier extraction. In organic solar cells the large energy for separation of excitons at interfaces must be taken into account [6]. Impact ionisation, where more than one exciton or charge carrier pair is generated from a single high energy photon lead to deviations in the photon spectral and power dependence compared to prediction from the SQ model [7,8]. Often, the SQ theory serves as a starting point, where deviations and non-ideal behaviour can be taken into consideration by incorporating additional semi-empirical quantities [9–12].

In order to overcome the SQ limit, an important strategy within third generation photovoltaics is the development of hot carrier solar cells, which aims to reduce thermalization losses by harvesting the hot carriers before they relax to the band edges. At present such cells are mainly subject of fundamental research [13–15]. The two main directions studied are the increase of the lifetime and a faster extraction process of hot carriers. Increase of hot carrier lifetime can be realized via a so-called phonon bottleneck strategy, aiming at reduction of hot carrier scattering at phonons, which represent the main relaxation channel. Moreover, the transfer of the energy of non-equilibrium phonon populations back to the charge carriers can be enhanced by restricting phonon thermal transport. Such processes are studied in a number of systems such as quantum dots [16,17], quantum wells, Halide-perovskites [18,19] and nanowires [20]. Faster extraction of hot carrier can be achieved by well-designed contacts which however typically work only in a narrow allowed energy range [21]. The key advancement of hot carrier extraction is to reduce the voltage losses  $\Delta U = (kT_s - E_g)/e$  through hot carrier relaxation towards the

band edges. Here,  $Q(E_{ph})$  can strongly deviate from a step-like spectral function since carrier extraction now becomes a non-trivial function of photon energy.

The theoretical upper limit of an ideal hot carrier solar cell is given by the Carnot efficiency  $\eta = (T_s - T_d)/T_s$  [22,23]. In principle, this result can also be derived from the SQ theory for a system with  $E_g = 0$  and taking into account hot carrier collection. This would then require concentrator solar cell photovoltaics to achieve  $f_\omega = 1$ .

The applicability of the ideal SQ theory to hot carrier devices thus needs careful evaluation and possible adjustments. Relaxing the SQ assumption of a step-like quantum efficiency  $Q(E_{ph})$  due to harvesting of hot carriers is of course a very natural extension. Changing the assumption of ideal carrier collection to an excitation energy dependent hot carrier collection efficiency is, however, a greater modification. It requires the analysis of the competition between energy loss via relaxation and energy dependent carrier extraction. Furthermore, a deviation of power density dependence of the photovoltaic response from the SQ theory is expected. In conventional semiconductor junctions, the open circuit voltage, which represents the splitting of Fermi level by excited electrons and holes, is logarithmic in power density. It exhibits an upper limit given by the bandgap in the non-degenerate case. In contrast, the Fermi level splitting in hot carrier materials can show a much stronger power dependence since it is only limited by the temperature of excited carriers.

In this article, we present a study of the photon power density and spectral dependence of hot polaron solar cells and show that the photo-voltaic response strongly deviates from that expected from SQ theory. Such solar cells were recently demonstrated in junctions based on p-doped manganite perovskites, where intraband optical excitations of Jahn-Teller polarons can be stabilized, enabling photovoltaic energy conversion [24–27]. The manganite perovskites consist of a  $3d$  or  $2d$  network of  $MnO_6$  octahedra that undergo Jahn-Teller distortion and form small polaron charge carriers in doped systems [28,29]. The absorption of photons generates hot carriers in an excited  $Mn 3d$  state that is incompatible with the remaining Jahn-Teller deformation in the ground state, see Fig. 1. Thus, the excited polaron state must undergo a structural relaxation until the electronic structure and the Jahn-Teller distortion becomes self-consistent. In contrast to the fast relaxation dynamics of isolated  $MnO_6$  octahedra, where the structural relaxation happens on the timescale of a Jahn-Teller vibrational mode (70 fs), the lifetime of hot carriers can reach ns systems [26,27,30,31].

The required slowdown of hot carrier relaxation is observed in the charge- and orbital-order states of manganites, where excited carrier stabilization results from cooperative electron-phonon dynamics. Whereas, the transition to the ground state is dipole forbidden [31], the remaining structural relaxation of the excited Jahn-Teller polarons is damped by the strong cooperative electron-phonon interaction. This is called a new type of phonon bottleneck strategy [27], where the strong electron phonon interaction can be turned into an advantage. Therefore, the structural recombination via a conical intersection dominates over radiative recombination [31]. As we will show in this article, in addition to a non SQ-like spectral and power dependent photovoltaic response, the temperature dependent order parameter of charge- and orbital-order needs to be taken into account. Due to the nature of the phase transition as of second order [26], the continuous change of order parameter with temperature across the orbital order phase transition at  $T_c \approx 200$ -240 K must be considered.

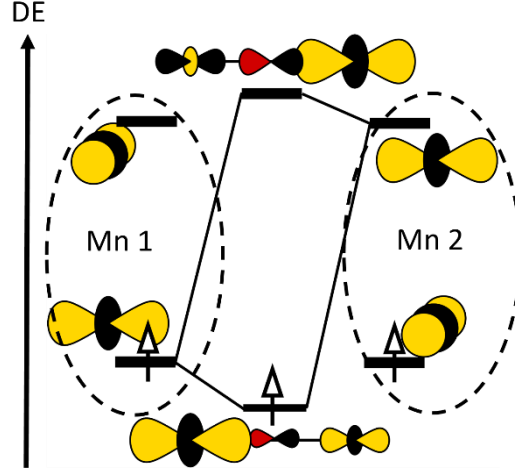


FIG. 1: Molecular orbital scheme of ground and excited state of Jahn-Teller polarons in low doped manganites based on a dimer of two  $MnO_6$  octahedra. It possesses a dipole-allowed excitation from non-bonding to antibonding Jahn-Teller split  $\sigma d$  states. Sign of the wave function is indicated by yellow/black for Mn 3d and red/black colour for oxygen 2p.

The paper is structured as follows: Chapter 2 presents a brief summary of a spectral extension of concepts and governing equations based in SQ theory. In Chapter 3 we present the temperature and illumination dependent photovoltaic properties and an analysis of the observed trends of short circuit current density  $J_{sc}$  and open circuit voltage  $U_{oc}$  in comparison to the SQ theory. We show that strong deviations of the qualitative trends of these parameters occur. In Chapter 4 we extend our analysis of  $U_{oc}$  and  $J_{sc}$  dependent on power density  $p$  and photon energy  $E_{ph}$  at a fixed temperature of 150 K. Here, we introduce as a new parameter the characteristic temperature  $T^*$ , which includes the effect of order phenomena on photovoltaics. The paper ends in Chapter 5 with a general discussion of the observed illumination dependent photovoltaic response and discuss the deviation from the SQ predictions in terms of hot carrier spectral and power dependent response that is strongly impacted by the temperature dependent order parameter.

## 2. Photovoltaic characteristics derived from Shockley-Queisser theory

The SQ theory is based on the detailed balance principle, i.e., equilibrium between the absorbed and emitted photon flux density. Within this idealized model each absorbed photon generates exactly one electron-hole-pair [1]. Without charge extraction, each generated is finally removed by radiative recombination as long as other recombination channels can be ignored. If electric energy is extracted out of the device, the electric current density  $J$  is then given by the difference between total generation rate  $G$  and total recombination rate  $R$  as  $J=q(G-R)$ .

In the case of an ideal collection of charge carriers, where all generated electron hole pairs are extracted, the maximum short circuit current  $J_{sc}$  is then given by only the generation rate  $J_{sc}=qG$ .

Shockley and Queisser applied this powerful general approach to conventional semiconductors, where the rate of thermalization of excitation above the bandgap  $E_g$  is much higher than the rate of charge extraction. Thus, all extracted charges that contribute to  $J_{sc}$  stem from electronic states close to the band edges. Furthermore, taken into account that only charges within the distance of the diffusion length  $L$  to the junction interface are collected, one can derive an equation, where the short circuit current is expressed via a spatially homogeneous mean generation rate  $G(T,p,E_{ph})$  in the areas of distance  $L$  from the interface [32]:

$$(eq. 1) \quad J_{sc} \approx q G(L_h + L_e) \approx q G(\sqrt{D_h\tau_h} + \sqrt{D_e\tau_e}).$$

The diffusion length can be expressed through the diffusion coefficient  $D$  and effective lifetime  $\tau$  of thermalized carriers close to the band edges.

Thus, in accordance with equation (1), the SQ models predicts for conventional semiconductors that the energy as well as the power dependence of the photocurrent only arises from the carrier generation  $G(T,p,E_{ph})$ . Therefore,  $J_{sc}$  depends linearly on power density [33–36]. Since all minority carriers thermalize to the band edges, the collection of charge carriers is independent of  $E_{ph}$ . Therefore,  $J_{sc}$  is independent of photon energy if  $E_{ph} > E_g$  is met. This is reflected in a step-like spectral dependence of the quantum efficiency  $Q(E_{ph})$  with  $Q = 1$  for photon energy  $E_{ph} > E_g$  and  $Q = 0$  for  $E_{ph} < E_g$  for an ideal device [37].

The current voltage characteristics of a solar cell is then comprised by the balance of generation and recombination currents in the dark, which is modified by the photocurrent. For an ideal homojunction under an applied external voltage  $U$  the total current is given by the Shockley's ideal diode equation [38], originally derived by Davydov [39]:

$$(eq. 2) \quad J = J_0 \left( \exp\left(\frac{eU}{kT}\right) - 1 \right) - J_{sc}$$

$J_0$  represents the dark saturation current density. The equation holds for voltages that are small compared to the energy of the emitted thermal radiation of the device, i.e., the distortion of the radiative equilibrium is small.

Under open circuit conditions the carrier generation and recombination balances out. The open circuit voltage corresponds to the splitting of hole and electron quasi-Fermi levels in a semiconductor according to [40]

$$(eq. 3a) \quad qU_{oc} = E_{f,e} - E_{f,h}.$$

The open circuit voltage can be derived from equation (1) for  $J = 0$ , yielding

$$(eq. 3b) \quad qU_{oc} = kT \ln(J_{sc}/J_0 + 1).$$

For the purpose of our analysis, it is more convenient to express the open circuit voltage via ratio of excited charge carriers  $n_e$  resp.  $n_h$  to intrinsic carrier concentration  $n_i$  [41].

$$(eq. 3c) \quad qU_{oc} = kT \ln\left(\frac{n_e n_h}{n_i^2}\right) = \Delta E - k_B T \ln\left(\frac{N_c N_v}{n_e n_h}\right).$$

It represents the point of operation where the total generation current is entirely balanced by the recombination current. For a conventional semiconductor homojunction, the recombination current is limited by the intrinsic bulk carrier concentration (in the depletion region), i.e.

$$(eq. 4) \quad n_i^2 = N_c N_v \exp(E_g/kT),$$

where  $N_c$  and  $N_v$  represent the effective density-of-states of the conduction and valence band close to the band edges, respectively, and  $\Delta E = E_g$ . More general,  $\Delta E$  represents the limiting barrier for the recombination current [42]. In a heterojunction, this can be either given by the bulk bandgap or by interface band offsets.

Since the concentration of excited carriers,  $n_e$  and  $n_h$ , is proportional to  $G(T,p,E_{ph})$ , equation (3c) yields a logarithmic dependence of  $U_{oc}(T)$  on power density [33,36,43]. Furthermore, since all charge carriers thermalize to the band gap,  $U_{oc}(T)$  is independent of photon energy for  $E_{ph} >$

$E_g$ . If one neglects the temperature dependence of the logarithmic term, the open circuit voltage thus decreases linearly with increasing temperature. A power law correction to this linear temperature dependence enters equation (3c) via the temperature dependence of the effective density of states, where the effect of thermal broadening of carrier occupation must be considered via an appropriate spectral integration of the states.

In contrast, hot carrier solar cells may show deviations for both the spectral as the power dependence of  $U_{oc}(p, E_{ph})$  and  $J_{sc}(p, E_{ph})$ , since hot carriers can be directly extracted.

### 3. Results and discussion within the framework of SQ carrier kinetics

In this chapter we give an overview on the photovoltaic response as function of power density and photon energy and analyse the characteristics in the light of SQ theory.

#### 3.1. Overview on photovoltaic response

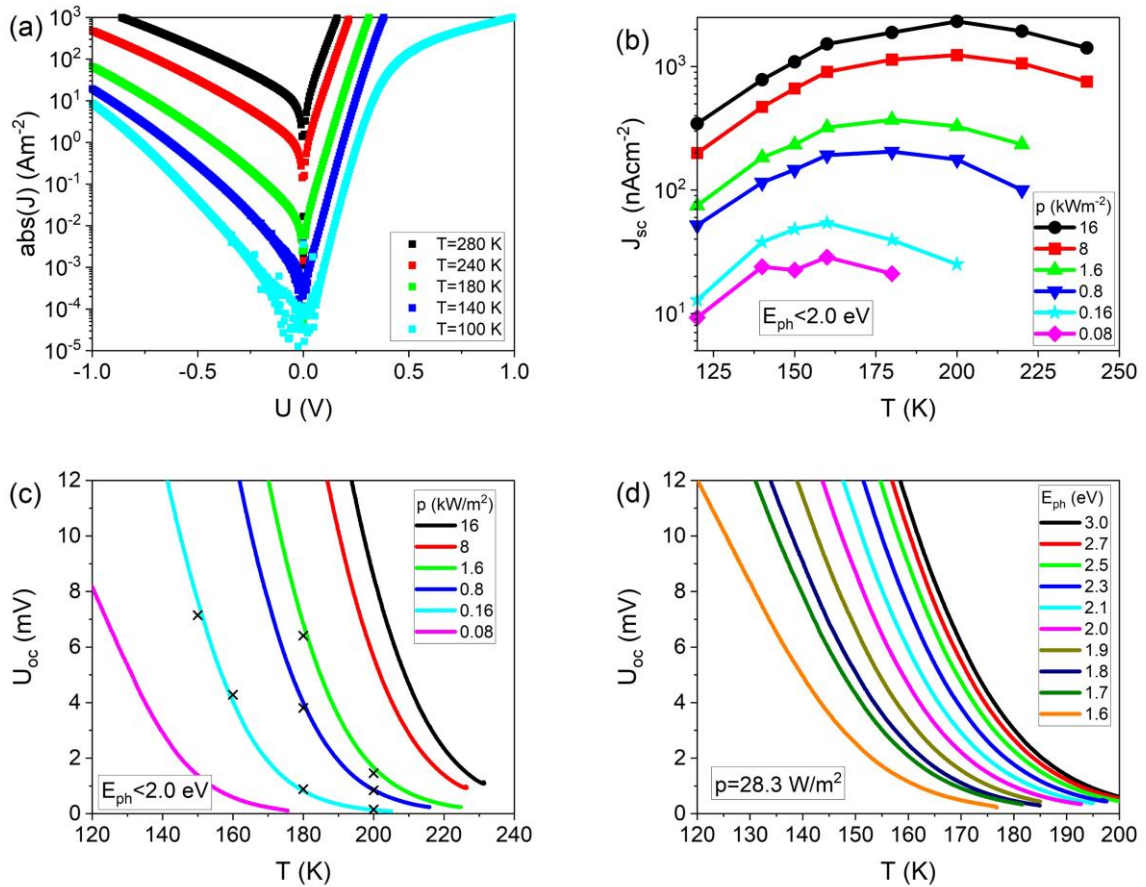


FIG. 2: a) Absolute current-density-voltage curves without illumination at different temperatures. b)  $J_{sc}$  vs.  $T$  for different power densities and c)  $U_{oc}$  vs  $T$  for different power densities (the black X marks the isothermal measurement values), both at fixed spectral range  $E_{ph} < 2.0 \text{ eV}$  (cut-off filter). d)  $U_{oc}$  vs  $T$  for monochromatic illumination at indicated photon energies and an energy width of  $60 \text{ meV}$ . The power density was fixed to  $p = 28.3 \text{ W/m}^2$ .

As expected from SQ theory, the current-voltage of PCMO/STNO junction characteristic  $J(U)$  exhibits diode-like rectifying behaviour (Fig. 2(a)), i.e., exponential increase of the current in forward direction and small current in reverse direction, see equation (2). Similar as observed for PCMO junctions with higher doping [30], the reverse saturation current deviates from the

SQ theory characteristics by a much stronger voltage dependence due to an electric field dependent polaron pair dissociation rate.

Illumination results in a pronounced photovoltaic response only well below room temperature. In order to investigate the photovoltaic response in dependence of the incident photons flux, i.e., photon power density  $p$  and photon energy  $E_{ph}$ , two characteristic parameters are determined from isothermal  $J(U)$  measurements: Short circuit current-density  $J_{sc}$  (at  $U=0V$ ) and open circuit voltage  $U_{oc}$  (at  $I=0$  A). Additionally,  $U_{oc}$  is measured under open circuit conditions during continuous cooling. Both methods yield the same values of  $U_{oc}$ . (see fig 2(c)) This proves self-consistency of the measurements and excludes cooling rate dependent effects on the direct  $U_{oc}(T)$  data. The power density dependent measurements span 3 orders of magnitude. Here, polychromatic illumination with a cut-off filter at  $E_{max}= 2.0$  eV was used that generates a constant spectral range energy distribution. Therefore, these measurements scale only with the flux of incoming photons. The maximum excitation energy of  $E_{max}= 2.0$  eV excludes photovoltaic contributions in STNO, with its band gap of 3.2 eV. To analyse the spectral dependent photovoltaic response,  $J_{sc}(E_{ph})$  and  $U_{oc}(E_{ph})$  are measured through monochromatic illumination in the spectral range between 1.6 eV and 3.0 eV with a spectral width of about 60 meV. Here, the power density was fixed to  $p= 28.3$  W/m<sup>2</sup>.

Let us first consider the temperature dependence of the characteristic parameters (Figs. 2(b), (c), (d)). For all illumination conditions regardless of  $p$  and  $E_{ph}$ , the following general temperature dependencies are observed:

- The short circuit current-density  $J_{SC}(T)$  reveals a dome-shaped temperature dependence. With decreasing temperature  $J_{SC}(T)$  first increases and, after approaching a maximum value then decreases. This temperature dependence is, therefore, characterized by a maximum  $J_{max}(T_{max})$ .
- The open circuit voltage  $U_{OC}(T)$  increases monotonously with decreasing temperature, as expected qualitatively from equation (3c). With increasing temperature, it vanishes at a characteristic temperature which depends on  $p$  and  $E_{ph}$ . This temperature will be discussed in detail in section 4.
- In addition to the illumination dependence of the characteristic temperature, there is a pronounced change of the slope of  $U_{OC}(T)$  with temperature with curves getting steeper with increasing power density and photon energy.

Since the monochromatic illumination experiments are performed at a fixed overall power density  $p$ , the flux of incident photons changes with photon energy  $E_{ph}$  according to  $\phi=p/E_{ph}$ . Therefore, the photon flux is increased by a factor of 2 while decreasing the photon energy from 3.0 to 1.6 eV. However, Fig. 2(d) reveals a reverse and significantly larger shift in the characteristic temperature where  $U_{OC}(T) \approx 0$  than expected by a change of photon flux alone. This shows that both, power density and photon energy strongly affect the photovoltaic response but changes in photon energy have a greater impact.

A qualitative comparison within the SQ theory reveals that the photovoltaic response in the manganite junction exhibits several general dependencies which agree with the expected behavior: Diode-like rectifying behavior with and without illumination (eq. 2), increase of  $U_{OC}$  with decreasing temperatures (eq. 3c) and the existence of a characteristic onset temperature,

$$(eq. 5) \quad T_{onset} \approx \frac{\Delta E}{k_B \ln\left(\frac{N_C N_V}{n_e n_h}\right)}$$

where  $U_{oc}(T)$  approaches zero, depending on power density. In conventional semiconductor or organic heterojunctions the linear extrapolation of  $U_{oc}(T)$  shown in [44–46] would result in an onset temperature very far above room temperature. This is in contrast to our study of the manganite junctions, where the onset temperature is below the order phase transition. Before we analyze the effect of the temperature dependent order parameter in section 4, in the following we give an analysis of the power dependence of  $J_{sc}(T,p)$  and  $U_{oc}(T, p)$  in the framework of the SQ theory.

### 3.2. Analysis of $J_{sc}$ within the SQ theory

As shown in Fig. 2(b), the temperature dependence of the short circuit current density  $J_{sc}$  shows a pronounced maximum at  $T=T_{max}$  that depends on the incident power density  $p$ . According to equation (1),  $J_{sc}$  is governed by the mean generation rate  $G$  in the diffusion region, the diffusion coefficient of the minority charge carriers and the lifetime of excitations. Since we only consider excitation energies below the band gap of SrTiO<sub>3</sub>, we can restrict the analysis to the electron-type minority charges in the manganite. Using the Einstein relation to express the diffusion constant by the mobility  $\mu_e$  of the polarons, equation (1) simplifies to

$$(eq. 6) \quad J_{sc} \approx q G L_e \approx q G \sqrt{\frac{k \cdot T}{q}} \mu_e \tau_e$$

The mean generation rate is given by

$$(eq. 7) \quad G = \frac{1}{L} \int_{d-L}^d \int_{E_{min}}^{E_{max}} \frac{f(E_{ph})}{E_{ph}} \alpha e^{-\alpha x} dE_{ph} dx$$

where  $f(E_{ph})$  is the spectral power density distribution of the incident radiation,  $\alpha$  is the absorption coefficient,  $L$  is the diffusion length and  $d=100$  nm is the absorber layer thickness. Here, we have assumed that only excitations with photon energies  $E_{ph}$  between  $E_{min} \approx 1$ eV and  $E_{max}=2$ eV (Fig. 5). The spatial integration is performed over diffusion region with  $d \gg L$ . For details see section S1 in the supplementary information.

Due to a negligible small temperature dependence of the absorption coefficient [26], the small temperature dependence of  $G$  can be disregarded and thus  $J_{sc}(T)$  is mainly governed by the temperature dependence of the carrier mobility and the polaron lifetime. As seen in Fig. 2(b), the short circuit current  $J_{sc}(T)$  first increases with decreasing temperature. Since electronic order is a prerequisite of photovoltaic energy conversion in manganite-based junctions [26], we expect, that the increase of hot polaron lifetime  $\tau_e$  due to the appearance of orbital order governs  $J_{sc}(T)$  in this temperature range. This would imply that  $\tau_e$  may scale with the order parameter  $S$ .

In the lower temperature range, where the slope of  $J_{sc}(T)$  reverses, we propose that the temperature dependence is influenced by the reduced mobility. If the mobility of the excited polaron charge carrier's scales with the thermally activated mobility of the small polaron in the ground state,  $J_{sc}(T)$  should almost exponentially decrease with decreasing temperature as it is observed in Fig. 2(b).

While the temperature dependence of  $J_{sc}(T)$  can be qualitatively explained by a competition of increasing lifetime and decreasing mobility, it fails to explain the shift of position of the maximum with power density. In SQ theory it is commonly assumed that mobility and lifetime are power density independent and thus no shift of the  $J_{sc}(T)$  maximum is expected. In addition, equation (6) fails to predict the right order of magnitude of  $J_{sc}(T)$ , as will be shown in the following:

With a spectrally constant reflection of  $R \approx 0.3$  as well as absorption coefficient  $\alpha \approx 6 \cdot 10^6 \text{ m}^{-1}$  and assuming a constant power density distribution  $f(E_{ph})$  in the energy range of  $E_{min}$  to  $E_{max}$ , the generation rate amounts to about  $G \approx 6 \cdot 10^{27} \text{ m}^{-3}\text{s}^{-1} \approx 0.4/(\text{u.c. s})$  for an incident power density of  $p=1.6 \text{ kW/m}^2$  ([26], supplemental information [47]).

Table 1 summarizes the calculated generation rate  $G$ , the maximum short circuit current density  $J_{max}$  at  $T_{max}$  and the calculated effective diffusion length  $L_{eff}=J_{sc}/qG$ . The order of magnitude of the obtained  $L_{eff}$  does not dependent on the details of calculation, which yields extremely small values of  $L_{eff}$  in the pm range.

In comparison, the diffusion length  $L_e$  can be also estimated from the experimentally observed hot polaron lifetime and the ground state mobility of the polarons. Using a lifetime of a ns [26,31] and a ground state mobility deduced from the temperature dependent resistivity, yielding an order of magnitude of  $\mu_e \approx 10^{-3} \text{ cm}^2/\text{Vs}$  (see supplemental information [47]), we obtain a diffusion length  $L_e$  of the order of a few nm. Despite the ground state  $\mu_e$  representing most probably only a lower limit to the excited state mobility, this result is consistent to measured diffusion lengths of PCMO ( $x=0.34$ ) using electron beam induced current (EBIC) [30].

The contradiction that  $L_{eff}$  is three orders of magnitude smaller than  $L_e$  determined from mobility and lifetime cannot be resolved by experimental errors in determining  $J_{sc}$ . By scaling the current to the contact area, we underestimate the absolute value of the current density, since the true photovoltaic active volume is significantly smaller. However, this cannot explain three to four orders of magnitude of difference. This points to a strong suppression of the measured  $J_{sc}$  in PCMO/STNO heterojunctions either due to a very low quantum efficiency or collection efficiency, since a quite high fraction of generated hot carriers are not extracted. The obtained increase of  $L_{eff}$  with  $G$  indicates a power dependent quantum efficiency or collection efficiency.

p (kW/m <sup>2</sup> )	G (10 <sup>27</sup> /m <sup>3</sup> s)	T <sub>max</sub> (K)	J <sub>max</sub> (mA/m <sup>2</sup> )	L <sub>eff</sub> (nm)
16.1	62.3	200.1	23.2	2.3·10 <sup>-3</sup>
8.1	31.1	195.7	12.1	2.4·10 <sup>-3</sup>
1.61	6.23	183.8	3.74	3.8·10 <sup>-3</sup>
0.81	3.11	178.9	2.08	4.2·10 <sup>-3</sup>
0.16	0.62	160.8	0.542	5.4·10 <sup>-3</sup>

Table 1: incident power density  $p$ , generation rate  $G$  and experimentally observed  $J_{max}(T_{max})$  data. The effective diffusion length  $L_{eff} = J_{max} / (e G)$  was calculated according to equation (6) and (7).

### 3.3. Analysis of $U_{oc}$ within the SQ theory

The open circuit voltage as a function of temperature and power density is now analyzed within the SQ theory using Eq. (3c). In a homojunction, the splitting of the chemical potential is determined by the total electron and hole density  $n_e$  and  $n_h$ , respectively. Since we consider only excitations in the manganite,  $n_h$  is the intrinsic hole density due to doping and  $n_e$  the excess electron density due to optical excitations.

Equation 3(c) predicts a nearly linear decrease with temperature because the temperature dependence of  $N_e$  and  $n_e$  contribute only logarithmically. The experimental  $U_{oc}(T)$  data (Fig. 2(c), (d)) of the hot polaron solar cell show such a linear decrease with increasing temperature only in a narrow temperature range. For this temperature range, a linear fit of the experimental data is performed and exemplarily shown in Fig. 3(a). The obtained power dependence of the



energy barrier  $\Delta E = e U_{oc}(T \rightarrow 0)$  and slope  $b = -1/k dU_{oc}/dT$  are shown as black symbols in Fig. 3(c) and (d), respectively, showing an increase with  $p$ .

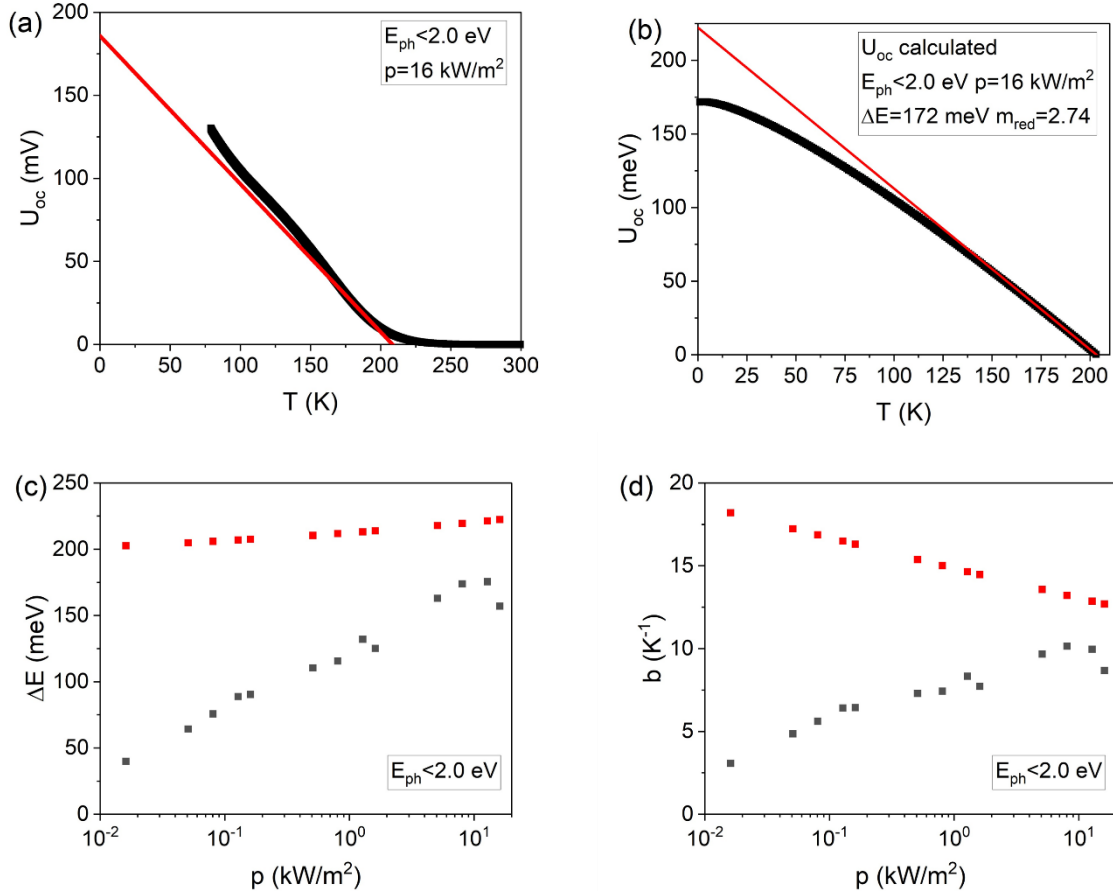


FIG. 3: Analysis of the power density dependence of  $U_{oc}(T)$  in linear approximation. a) Exemplary result for experimental  $U_{oc}(T)$  at  $E_{ph} < 2$  eV and  $p = 1.6 \cdot 10^4$  W/m<sup>2</sup> (black) with a linear fit in the temperature range between 200 K and 160 K (red). b) Exemplary result for a calculated  $U_{oc}(T)$  at  $p = 1.6 \cdot 10^4$  W/m<sup>2</sup> using Eq. (3c) with barrier  $\Delta E = 172$  meV and reduced polaron mass  $m_{red} = 2.74$  (black). The red line again shows the linear approximation. The power density dependence of the obtained barrier  $\Delta E$  (c) and slope  $b$  (d) from the fit of the data (black squares) and calculated trends using Eq. (3c) of the Shockley Queisser model. For details see text.

The experimental data can be compared with prediction of  $\Delta E$  and  $b = -1/k \ln((N_c N_v)/(n_e n_h))$  within the SQ model. The minority charge carrier density  $n_e$  is estimated by

$$(Eq. 8) \quad n_e \approx R_{eff} \tau_{eff} \approx G \tau_{eff},$$

using the equality of recombination rate  $R_{eff}$  and generation rate  $G$  under open circuit conditions. For the generation rate, the same approximations as in chapter 3.2. are used and the effective lifetime of excitations is estimated to  $\tau_{eff} \approx 2$  ns [26]. The hole carrier density  $n_h = 1.87 \cdot 10^{27}$  m<sup>-3</sup> is calculated from heterovalent Ca doping.

A precise expression for the effective density of states for manganites is not accessible until now. One can approximate the  $Mn3d_{eg} - O2p$  conduction band by a parabolic structure that allows an effective mass approach. If the thermal population of the conduction band is taken into account by a Boltzmann distribution, the effective density of states  $N_c$  as well as  $N_v$  can be expressed via the effective mass  $m^*$  through [48]

$$(Eq. 9) \quad N_c = N_v = 2 \left( \frac{2 \pi m^* k T}{h^2} \right)^{\frac{3}{2}} M,$$

where  $M$  is the number of equivalent band minima and is set to  $M = 1$ .

Within these approximations,  $U_{oc}$  can be written as

$$(Eq. 10) \quad e \cdot U_{oc} \approx \Delta E - C_1(p) T - 3k \ln \left( m_{red} \frac{T}{T_{ref}} \right) T,$$

where the prefactor  $C_1$  depends on the power density via  $n_e$ ,  $m_{red}=m^*/m_e$  is the reduced effective mass and  $T_{ref}$  is an arbitrary reference temperature.

Fitting the experimental data of Fig. 3(a) over the whole temperature range yields reasonable values of  $\Delta E = 0.172$  eV and  $m^* = 2.74 m_e$ . The conduction band offset between the *Mn 3d e<sub>g</sub>* and *Ti 3d* bands gives an upper limit to  $\Delta E$  that can be estimated from the work functions of the hole and electron doped semiconductors (see [24] for higher doping levels). Using  $W_{STO} = 4.1$  eV for Nb-doped SrTiO<sub>3</sub> [49] and  $W_{PCMO} \approx 4.4$  eV for  $x=0$  [50] yields  $\Delta E = W_h - W_e \leq 0.3$  eV. For the effective mass a range between 1.8 and 5  $m_e$  can be estimated [51].

Assuming that  $\Delta E$  and  $m^*$  do not depend on  $p$ ,  $U_{oc}(T,p)$  can be calculated for the various power densities. To compare experimental and calculated data we have applied a linear approximation to the calculated  $U_{oc}(T,p)$  high temperature data (Figure 3(b)). The extrapolated barriers  $eU_{oc}(T \rightarrow 0)$  and the slopes  $b$  are plotted as red symbols in Figures 3(c) and (d).

In Fig. 3(c), the extrapolated barriers  $eU_{oc}(T \rightarrow 0)$  do not coincide with the estimated barrier  $\Delta E = 0.172$  eV. This difference originates from the temperature dependence of the effective density of states resulting in a weak increase of the experimentally determined barrier with increasing power density. In addition to the difference in absolute value, there is a remarkable difference between the power dependence of  $\Delta E(p)$  expected from the SQ model, where it is almost constant, and the experimental trend.

Furthermore, absolute values and  $p$  dependence of the slope  $b$  expected from the SQ model and obtained from experiment show drastic differences as shown in Fig. 3(d). Experimentally, the slope  $b(p)$  increases with increasing power density. This trend is opposite to what is expected from SQ theory (see Eq. (8b)) which predicts that  $b$  decreases with increasing  $p$  due to the increasing concentration of photocarriers.

#### 4. Impact of order, power density and energy dependence on $J_{sc}$ and $U_{oc}$

In this section, the impact of the temperature dependent order parameter of the orbital order phase transition is discussed. Such a transition can change several material properties such as the density of states, and most importantly, the hot polaron lifetime [26,31]. We introduce a new characteristic parameter, the crossover temperature  $T^*$  as the temperature where  $U_{oc}(T)$  drops towards zero. Since  $U_{oc}(T)$  in Fig. 2(c) and (d) shows a nonlinear-temperature dependence, a well-suited quantitative definition for  $T^*$  is required. Clearly,  $T^*$  does not represent the equilibrium transition temperature of the phase transition since it is a non-equilibrium property that depends on illumination conditions. However, a connection to the orbital order transition is implied by the similar range of values of  $T^* \lesssim T_0$ .

We thus define  $T^*$  as the temperature, where a pronounced change in the first derivative  $dU_{oc}/dT$  occurs. More precisely,  $T^*$  is defined as the temperature where the deviation to the linear slope of the first derivative exceeds 5% (see S3 in the supplemental information [47]). We find that  $T^*$  undergoes huge changes as a function of energy and power density and thus has an enormous effect on the power dependency of  $J_{sc}$  and  $U_{oc}$ . In order to analyze this effect, we exemplarily

show an analysis of  $U_{oc}(p, E_{ph})$  and  $J_{sc}(p, E_{ph})$  at a fixed temperature of 150 K, i.e., close to the minimum value of  $T^*$ . In addition, we have selected this temperature because we expect that the temperature dependent order parameter for orbital order is approaching a value close to its maximum [26]. The same qualitative behavior of photovoltaic properties as at 150 K are also observed at other temperatures (see S4 in the supplemental information [47]).

#### 4.1. Power density dependencies of $U_{oc}$ , $J_{sc}$ and $T^*$

Figure 4 shows the power density dependence of the photovoltaic parameters  $U_{oc}(p)$  and  $J_{sc}(p)$  at a temperature of  $T = 150$  K as well as the onset temperature  $T^*$ . For  $U_{oc}(p)$  and  $J_{sc}(p)$  logarithmic and linear dependencies on power density are expected from the SQ theory.

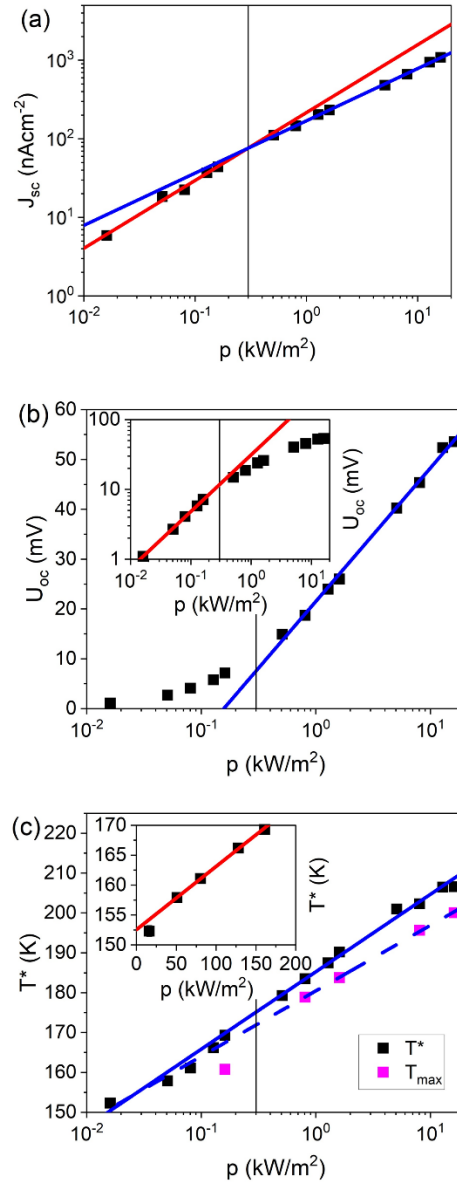


FIG. 4: Power density dependencies of (a) short circuit current  $J_{sc}$  (b) open circuit voltage  $U_{oc}$  (c) crossover temperature  $T^*$  at 150 K with illumination  $E_{ph} < 2$  eV.

Red lines correspond to low-power and blue lines to the high-power regime. In the inset the scale is adjusted to emphasize the different trends. For comparison, Fig. (c) shows the temperature  $T_{max}$  of maximum  $J_{sc}$  (see Fig. 2(b)). The critical power density of  $p_c \approx 300 \text{ W/m}^2$  is marked in each figure.

Two distinct power density regimes are a common feature for the two parameters  $U_{oc}$  and  $J_{sc}$  (Fig. 4(a), (b) which are indicated by a significant change in slope at the same critical power density of  $p_c \approx 300 \text{ W/m}^2$ . More specifically, the short circuit current  $J_{sc}$  exhibits a power law dependency of  $J_{sc} \propto p^n$  with  $n \approx 1$  below and  $n \approx 0.64$  above the critical power density. The strong deviation from a linear  $J_{sc}(p)$  dependence shows an excess loss for charge carriers that can be harvested at higher power density. In contrast, open circuit voltage  $U_{oc}(p)$  exhibits an approximately logarithmic dependence on the power density (Fig. 4(b)) for power densities above the critical power density. However, it turns into a power law dependence below the critical power density.

The cross over temperature  $T^*$  as analyzed in Fig. 4(c) reveals a huge change of more than 50 K for a change of  $p$  by four orders of magnitude. The observed range of  $T^*(p)$  variation in Fig. 4(c) remains below the transition temperature for the appearance of spontaneous orbital order in the films at  $T_O \approx 200\text{-}240 \text{ K}$ . Only  $T^*$  at the highest applied power density is approaching the equilibrium transition temperature of the orbital order transition.

It is quite remarkable, that  $T_{max}$  as determined from the maximum of the short circuit current density follows a similar trend as  $T^*$  determined from  $U_{oc}$ . The change in power dependence at a critical power of  $p \approx 300 \text{ W/m}^2$  observed for  $J_{sc}(p)$  and  $U_{oc}(p)$  is also visible in the  $T^*(p)$ .  $T^*$  increases linearly at low power densities (inset Fig. 4(c)) and the minimum value  $T^*(p \rightarrow 0)$  amounts to about 150 K. At high power densities the dependence is almost logarithmic and the crossover between the two regimes also takes place at about  $300 \text{ W/m}^2$ .

In summary, the photovoltaic parameter  $J_{sc}$ ,  $U_{oc}$  and  $T^*$  reveal a crossover from low to high power density regime that is accompanied by a reduction of the overall photovoltaic response compared to the values extrapolated from the lower power density regime.

#### 4.2. Photon energy dependencies of $U_{oc}$ , $J_{sc}$ and $T^*$

As visible in Fig. 5 for  $T=150 \text{ K}$ , the photon energy greatly impacts the photovoltaic response in the studied hot polaron junctions. The photon energy is varied under monochromatic illumination in the range between 1.6 to 3.2 eV. Therefore, two types of optical transitions are involved: the intraband  $e_g$  to  $e_g$  transition of the Jahn-Teller polaron at low photon energy as well as a charge transfer (CT) transition at higher photon energy. All three quantities  $J_{sc}$ ,  $U_{oc}$  and  $T^*$  significantly increase with photon energy.

Figure 5(a) shows the increase of  $U_{oc}$  with photon energy  $E_{ph}$  without any sign of saturation. This is a strong deviation from the spectral response of a conventional bandgap semiconductor. As already mentioned above, the monochromatic measurements include a weak change of incident photon flux because of fixed incident power density. Fitting the low-energy branch (below 2.2 eV) according to

$$(eq. 11) \quad U_{oc}(T, E) = C_U(T) (E - E_{ou}(T))$$

yields a temperature dependent slope  $C_U(T)$  and a minimum required excitation energy  $E_{ou}$  that are summarized in table 2.

To take power dependence into account, we replaced the short circuit current density by effective internal quantum efficiency defined as the number of generated charge carriers per absorbed photon

$$(eq. 12) \quad Q_{IQE}(E_{ph}, T) = \frac{J_{SC}(E_{ph}, T)}{q(1-R)\Phi(E_{ph})\alpha(E_{ph}, T)},$$

where  $J_{SC}$  is the short circuit current density under monochromatic in with photons of energy  $E_{ph}$ ,  $\Phi$  is number of photons per area and unit time incident on the absorber,  $R$  the reflectance and  $\alpha$  is the absorption coefficient deduced from reflection-corrected transmission measurements [26].

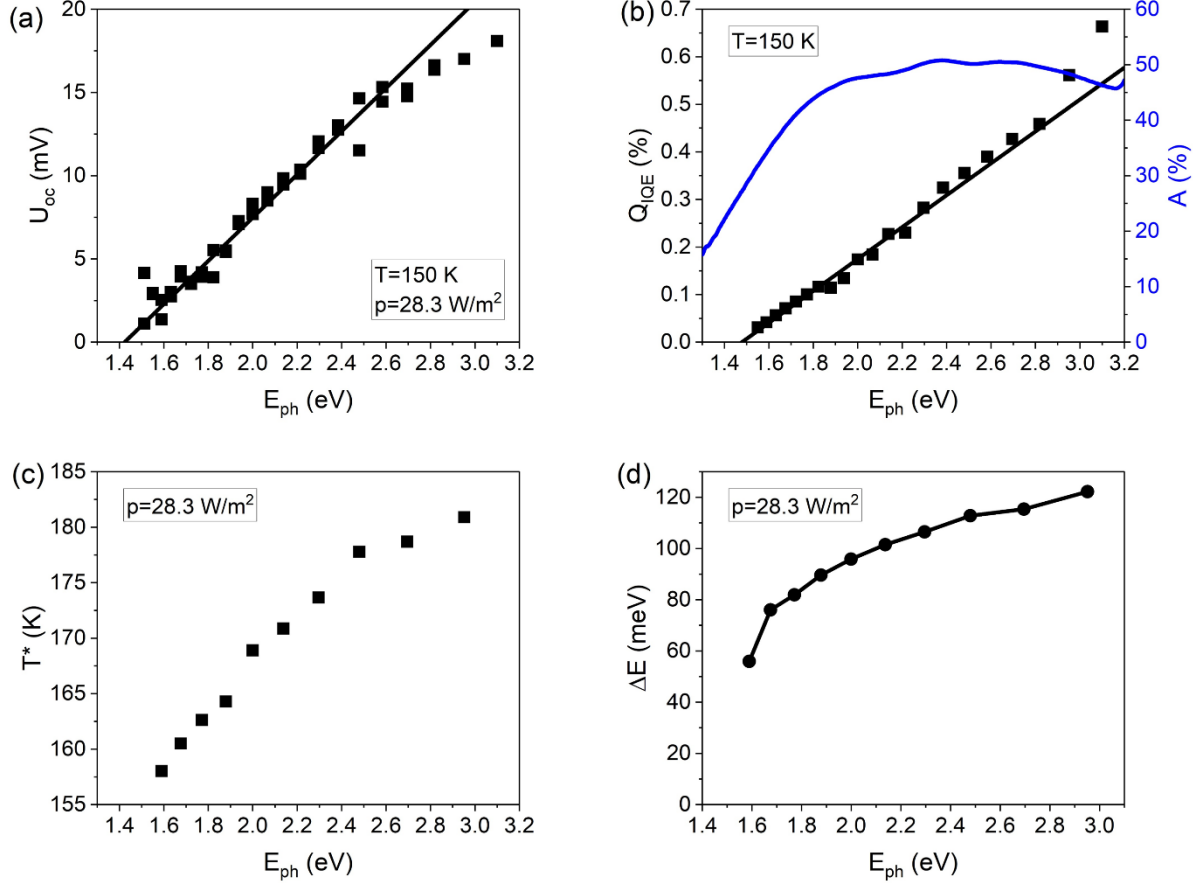


FIG. 5: Photon energy dependencies at fixed power density  $p = 28.3 \text{ W/m}^2$  of (a) open circuit voltage  $U_{oc}$ , and (b) internal quantum efficiency  $Q_{IQE}$  at 150 K, as well as (c) crossover temperature  $T^*$  and (d) the intrinsic barrier  $\Delta E$ . For comparison, the spectral dependent absorption  $A$  is shown in b).

Figure 5(b) gives the spectral dependence of absorption  $A(E_{ph})$  and effective quantum efficiency  $Q_{IQE}(E_{ph})$ . The absolute values of  $Q_{IQE}$  are well below the 1% level, indicating that only a very small fraction of electron hole polaron pairs are extracted. The main origin of the small values is the small diffusion length  $L_e$  which is 2 orders of magnitude smaller than the photon absorption length of the order of  $\alpha^{-1} \approx 70 \text{ nm}$  [26]. For the qualitative  $Q_{IQE}(E_{ph})$  trend, we observe a significant deviation from conventional semiconductor photovoltaics, where a step function of  $Q_{IQE}(E_{ph})$  with a value of zero for energies below the band gap and quantum efficiency close to 100% for excitations above the band gap is observed. Remarkably,  $Q_{IQE}(E_{ph})$  shows an almost linear increase with photon energy over the entire temperature range (125 and 200 K in supplemental information [47]). Thus, for the quantum efficiency more charge carriers are harvested for higher photon energies. The small deviations from a monotonous increase at about 1.8 and 2.5 eV reflects that different transitions are involved in generating long living charge carriers. A linear fit according to

$$(eq. 13) \quad Q_{IQE}(T, E) = C_Q(T) \left( E - E_{0Q}(T) \right),$$

yields the parameters as shown in Table 2, too.

Both prefactors  $C_u$  and  $C_Q$  reflect the temperature dependence of  $U_{oc}$  and  $J_{sc}$  (Fig. 2). The minimum required excitation energies  $E_{0u}$  and  $E_{0Q}$  strongly decrease with decreasing temperature. Since  $E_{0u}$  is underestimated compared to  $E_{0Q}$  due to the change of photon flux with spectral variation, the onset energies of photovoltaic response do not seem to be very different for  $J_{sc}$  and  $U_{oc}$ . Such a temperature dependence cannot be associated with temperature dependence of the orbital order ‘band gap’ since this dependence is very small. The orbital order band gap is at about 1 to 1.2 eV and thus represents the ultimate lower limit of Jahn Teller polaron excitations in the orbital order state.

T (K)	U <sub>oc</sub> (T)		Q <sub>IQE</sub>	
	C <sub>U</sub> (V/eV)	E <sub>0u</sub> (eV)	C <sub>Q</sub> (1/eV)	E <sub>0Q</sub> (eV)
200	0.50	1.63	0.0176	1.72
150	12.57	1.41	0.3353	1.48
125	17.09	0.89	0.0046	1.34

Table 2: Fit parameters of the low-energy part of the energy-dependent open circuit voltage and internal quantum efficiency. The parameters are defined in equations (11) and (13).

Figure 5(c,d) shows the spectral dependencies of cross over temperature  $T^*(E_{ph})$  and energy barrier  $\Delta E(E_{ph})$  derived from the linear part of  $U_{oc}(T)$  as  $\Delta E(E_{ph}) = U_{oc}(T > 0)$ . Remarkably, both show a strong spectral change. Clearly,  $\Delta E(E_{ph})$  should be constant in a bandgap semiconductor as described by in SQ theory. The strong increase of  $\Delta E(E_{ph})$  with photon energy without any sign of saturation is expected in a hot carrier solar cell and confirms that it is not an intrinsic electronic property, e.g. determined by band offset. It rather reflects that polarons with different excitation energy can overcome the interface barrier.

#### 4.3. Scaling behavior of $U_{oc}(T, p, E_{ph})$ – impact of the phase transition

In order to analyse the effect of the phase transition, we consider a scaling of the equilibrium order parameter with temperature in accordance to  $S = S_0 (1 - T/T_c)^y$  with a critical exponent  $y$ . Such a critical behaviour is typically found for second order phase transitions as it is observed for PCMO  $x=0.1$  [26]. In order to take into consideration, the non-equilibrium properties measured in photovoltaic response, we replace the intrinsic equilibrium order-transition temperature  $T_c$  with a parameter  $T_0(p, E_{ph})$ , which depends on photon energy and power density. Indeed, although the absolute value of  $T_0(p, E_{ph})$  is above that of the experimentally determined parameter  $T^*(p, E_{ph})$ , the trend of both parameters in  $p$  and  $E_{ph}$  are similar.

We replace equation (3) by the empirical relation

$$(eq. 14a) \quad U_{oc}(T, p, E_{ph}) \approx U_o(p, E_{ph}) \cdot \left( 1 - \frac{T}{T_0(p, E_{ph})} \right)^y$$

where, the temperature dependence is expressed by a scaling law typical for the temperature dependence of an order parameters for a second order phase transition, however, with an order temperature  $T_0$  that depends on the illumination conditions.

In addition, the maximum open circuit voltage  $U_0$  also depends on both, power density and photon energy. This is justified from our analysis described above that  $U_{oc}$  does not possess an intrinsic barrier and strongly deviates from the close to linear temperature dependence expected from the SQ theory.

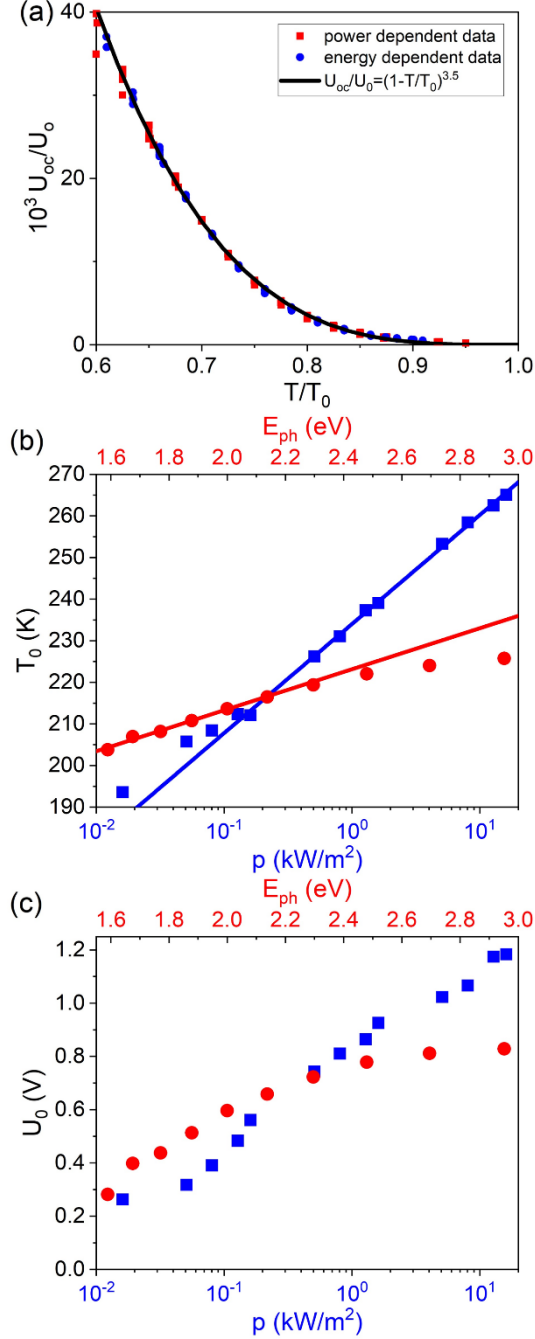


FIG. 6: Fit results for  $U_{oc}$  with empirical relation according to equation (14a), which includes an order parameter and  $\gamma=3.5$ . (a) Selection of power density (green) and photon energy (blue) data points in comparison to the fit. (b)  $T_0$  and (c)  $U_0$  for both power density and photon energy.

Fitting the experimental data of  $U_{oc}(T,p,E_{ph})$  (Fig. 2(c) and (d)) with respect to  $U_0$  and  $T_0$  indeed gives a good approximation. Although the energy dependence of both parameters is much stronger than the almost logarithmic dependence on power density (Fig. 6(b,c)), the same exponent of  $\gamma=3.5$  describes the temperature dependence rather well. Figure 6(a) reveals the experimental data, normalized according to  $U_{oc}(T,p,E_{ph})/U_0(p,E_{ph})$  and  $T/T_0(p,E_{ph})$ . For clarity,

only data at selected values of  $T/T_0$  are shown. Despite of good overall agreement, spreading of data points as well as small deviations to the slope, e.g., with regards to power density and energy dependence are visible.

## 5. Discussion

Summarizing the experimental results in this section, we discuss the physical origin of the deviations in  $U_{oc}(T, p, E_{ph})$ ,  $J_{sc}(T, p, E_{ph})$  of the manganite solar cell from the SQ theory, due to stabilisation of hot polarons by correlations and the impact of the temperature dependent order. This includes an interpretation of  $T^*$ .

### Open circuit voltage

The SQ theory predicts that the Fermi-level splitting and, therefore, the open circuit voltage depends logarithmically on the power density and has an intrinsic upper limit  $\Delta E$  that corresponds, e.g., for homojunctions, to the band gap. Due to the accumulation of the generated excess carriers at the band edges, no dependence on  $E_{ph}$  is expected.

Clearly, the hot polaron junction deviates from this behaviour:  $U_{oc}(p)$  exhibits a power law dependence below a critical power density and undergoes to an approximately logarithmic  $p$  dependence only above that threshold (Fig. 4(b)). We observe a strong dependence  $U_{oc}(E_{ph})$  on photon energy. Remarkably, the internal quantum efficiency does not follow the absorption coefficient  $A(E_{ph})$ . Since the open circuit voltage reflects the Fermi-level splitting, these observations imply that the splitting is neither governed by the effective density of states at band edges, as in semiconductors, nor by the energy dependent density of states, reflected in  $A(E_{ph})$ . Since the spectral dependence of the dipole matrix element is low in the studied energy range (see e.g. [52]), this implies a pronounced spectral dependence of the collection efficiency of hot polarons.

Furthermore, an intrinsic upper limit of the open circuit limit is not observed.  $\Delta E(p, E_{ph})$  does not saturate in the studied photon power and spectral range. These results may imply a modification of equation (3c) according to:

$$(eq. 15) \quad q \cdot U_{oc}(p, E_{ph}) = \Delta E(p, E_{ph}) - k_B T \ln \left( \frac{N_c(p, E_{ph})}{n(p, E_{ph})} \right)$$

It is important to note that even in a non-degenerate conventional semiconductor,  $N_c$  represents an effective density of states that is integrated over the thermal energy distribution of carriers at the band edges. In addition, for manganites, the approximation of rigid bands, where the density of states is independent of their population is not valid. Due to the Jahn-Teller splitting, the removal of an electron from the lower  $e_g$  bands leads to a shift of this empty state to the upper non-occupied  $e_g$  states. Vice versa, the occupation of a former unoccupied state by an excited charge leads to a structural relaxation of this state to the occupied  $e_g$  levels. The rate of such a Jahn-Teller structural dynamics strongly depends on the orbital order. This has the consequence that the correction to the linear temperature dependence given in equation (15) becomes strong due to the ordering phase transition.

Indeed, the remarkably good fit of  $U_{oc}(T, p, E_{ph})$  by an empirical scaling law equation (14a) with an exponent of  $y=3.5$  from fit of the data shows a strong deviation from the linear behaviour. Comparing equation (15) with the SQ theory by rewriting equation (3c) as



$$(eq. 14b) \quad U_{oc} = \Delta E \left(1 - \frac{T}{T_0}\right), T_0 \equiv \frac{\Delta E}{k \ln\left(\frac{N_c}{n}\right)}.$$

would predict a critical exponent  $y = 1$  in strong contrast to the fit. This indicates that the temperature dependent order parameter is reflected in the  $U_{oc}(T, p, E_{ph})$  behaviour as evidenced from the nice scaling behaviour using eq. (14a).

### Order parameter and $T^*$

A significant Fermi level splitting reflected in the open circuit voltage is only present below the crossover temperature  $T^*$  that characterizes turning point from a very small  $U_{oc}$  value to a significant increase of  $U_{oc}$  with decreasing  $T$ . Therefore,  $T^*$  reflects the onset of Fermi level splitting as a function of both power density and photon energy. The increase of  $T^*$  with power density (Fig. 4(c)) and with  $E_{ph}$  (Fig. 5c) reflects an increase of Fermi level splitting due to a higher density and higher energy of excited carriers. On the other hand, at constant  $p$  and  $E_{ph}$ , a higher fermi level splitting can be reached by increasing order parameter. Since these change of  $T^*(p, E_{ph})$  reflect the change in Fermi level splitting, it only indirectly reflects the equilibrium transition temperature of the phase transition. We suggest that the temperature dependent order parameter  $s(T)$  determines the change of the lifetime of hot polaron excitations from very fast structural relaxation in the range of ps in the disordered state to stabilized hot polarons on a ns timescale in the ordered state.

### Short circuit current density

The short circuit current density  $J_{sc}$  is orders of magnitude smaller than predicted from lifetime and polaron mobility (see section 3.2). Since our analysis considers that only electron-hole pair generation in the diffusion zone contributes to  $J_{sc}$ , the huge difference points to additional loss channels that affect the collection probability of hot polarons. This might be related to the polaron transfer process across the interface of the junction. As discussed above, the temperature dependence of  $J_{sc}$  is governed by two counteracting effects, i.e., increase of lifetime when approaching the ordered state and decrease of mobility at decreasing temperature. This results in maximum  $J_{sc}$  at characteristic temperature  $T_{max}$  (Fig. 2(b)). The shift of  $T_{max}$  with increasing power density to higher temperatures may thus reflect a charge mobility of excited carriers above the mobility in the dark state, e.g., due to a change of the activation barrier for polaron hopping. Remarkably, the temperature of maximum  $J_{sc}$  almost coincides with  $T^*$  deduced from onset of the open circuit voltage. This confirms that an increase of  $T^*$  and thus of Fermi level splitting with increasing power density is due to a higher concentration of long living electron hole pairs.

In summary, the Shockley Queisser theory fails to explain several significant aspects observed for the hot polaron photovoltaic system. The characteristic parameters  $J_{sc}$  and  $U_{oc}$  exhibit a dependence on power density and photon energy that is qualitatively different and reflect stronger the spectral distribution of excited carrier concentration. For the power dependence, even two different regimes are observed, where the p-dependent response is reduced at higher power densities. This might indicate an onset of excitation induced disordering, although the concentration of excited carriers is still very much below that of predicted optically induced phase transitions [53]. Additionally, the barrier for the recombination current  $\Delta E$  varies with photon energy and power density and is therefore no longer an intrinsic quantity that is fixed by interfacial band offset. This suggests, that hot polarons can contribute to the recombination current across the junction.

We identified two main origins of the still low efficiency of the hot polaron solar cells: The small diffusion length compared to the photon absorption length that results in a small quantum efficiency below 1 % and a low collection efficiency of hot polarons at the interface or at contacts that further reduces the short circuit current density. Since hot polaron stabilization requires the ordered phase, the theoretical description of such solar cells requires the analysis of the interplay of temperature dependent order and hot polaron carrier kinetics. Accordingly, we introduce the crossover temperature  $T^*$  for  $U_{oc}$  and  $T_{max}$  for  $J_{sc}$ .  $T^*$  marks an increase of hot electron hole polaron pair lifetime at lower temperatures. The structural relaxation of excited Jahn-Teller polarons slows down significantly at  $T^*(p)$  which is thus governed by both the order transition as well as the hot carrier concentration. It might be interesting to study photovoltaic response at much higher photon power where optically induced phase transitions are expected, as predicted e.g. in [53,54] for higher doped systems.

## Appendix A: Experimental Methods

### 1. Photovoltaic junctions

The photovoltaic PCMO/STNO heterojunctions studied here, consist of a 100 nm thin epitaxial  $\text{Pr}_{1-x}\text{Ca}_x\text{MnO}_3$  (PCMO) film with doping of  $x=0.1$  on single-crystalline Nb doped (100)  $\text{SrTiO}_3$  (STNO) substrate (Appendix A1). The thin film shows orbital order (OO) below a transition temperature of  $T_c=220\text{-}240$  K. The sample characteristics is studied in detail elsewhere [26]. There, we reported the presence of a 2<sup>nd</sup> order orbital order-transition which is at much lower temperatures than proposed by former phase diagram [55]. The optical hot polaron excitations occur in an energy range of 1.2-2.0 eV by intraband  $e_g$  transitions which are split by the formation of Jahn-Teller polarons. Other transitions set in at higher energy, i.e., transitions to  $Mn-3d t_{2g}$  states above 2 eV and charge transfer transitions above 2.6 eV. The onset of polaron absorption at about 1.2 eV is due to the polaron formation in the orbital ordered state and therefore fundamentally different from the intrinsic band gaps in conventional semiconductor systems. The optical excitations in Nb doped  $\text{SrTiO}_3$  are excluded in our experiments by using a cut-off filter (Appendix A2).

### 2. Sputter deposition

Epitaxial thin films of  $\text{Pr}_{0.09}\text{Ca}_{0.1}\text{MnO}_3$  are deposited on  $\text{SrTiO}_3$ : Nb0.5wt% substrates by means of ion-beam deposition. During deposition Argon beam as neutralizer was set to a pressure of  $P_{Ar}=3 \cdot 10^{-4}$  mbar and Xenon gas for sputtering was set at  $P_{Xe}=1 \cdot 10^{-4}$  mbar. In order to avoid significant oxygen depletion additional oxygen was inserted into the chamber at  $P_{O_2}=1.4 \cdot 10^{-4}$  mbar. The heater was fixed to a set temperature of  $T=820^\circ\text{C}$ . Additional information on sample preparation and characteristic film properties such as Xray diffraction, resistivity, magnetic properties are published in [26].

### 3. Photovoltaic property measurements

For the measurements the previously reported sample geometry was applied [26] and the current densities are normalized to the  $4 \times 1 \text{ mm}^2$  top Pt contact.

The electric characterization was performed through two-point geometry and exclusion of contribution to the resistance by the connecting cables. The voltage source and ammeter was a Keithley 2430, while the voltage drop across the sample was measured by Keithley 2182A Nanovoltmeter. The sample was set up in a Cryostat by Cryovac with a suprasil window and measured in a temperature range of 80 K to 300 K.

For illumination two different light sources were applied. For the spectrally resolved measurements the light source was a 300W Xe lamp with LOT Omni 300 monochromator. The power density was calibrated to 200  $\mu\text{W}$  using a calibrated Laserpoint Silicon diode. As a second light source a LOT 150W Xe-UV lamp was fixed to a power source output fixed at 175 mW and focused on a 3 mm diameter light spot. For the spectral limited measurements cut-off filters by Schott with  $E_{max}$  of 1.8, 2.0, 2.2 eV were added to the beam bath. For power density measurements additional metallic coated neutral density filters by Quantum Design were included.

#### 4. Absorption

The optical property measured in transmission was set up in a photon energy range of  $E_{ph}=1.13-6.2\text{eV}$ . As a light source an OceanOptics DH-2000 Halogen light coupled into a fiberglass QP400-2-SR-BX was used. The Maya2000Pro served as the spectrometer and a dark spectrum baseline subtraction was performed. For reflection correction a fixed baseline value of  $R=30\%$  was applied.

#### References:

- [1] W. Shockley and H. J. Queisser, *Detailed Balance Limit of Efficiency of P-n Junction Solar Cells*, J. Appl. Phys. **32**, 510 (1961).
- [2] W. Shockley and W. T. Read, *Statistics of the Recombinations of Holes and Electrons*, Phys. Rev. **87**, 835 (1952).
- [3] R. A. Sinton and R. M. Swanson, *Recombination in Highly Injected Silicon*, IEEE Trans. Electron Devices **34**, 1380 (1987).
- [4] S. Liu, X. H. Zhao, C. M. Campbell, M. B. Lassise, Y. Zhao, and Y. H. Zhang, *Carrier Lifetimes and Interface Recombination Velocities in CdTe/MgxCd1-XTe Double Heterostructures with Different Mg Compositions Grown by Molecular Beam Epitaxy*, Appl. Phys. Lett. **107**, 2 (2015).
- [5] A. W. Bett, F. Dimroth, R. Lockenhoff, E. Oliva, and J. Schubert, *III-V Solar Cells under Monochromatic Illumination*, in *2008 33rd IEEE Photovoltaic Specialists Conference* (IEEE, 2008), pp. 1–5.
- [6] J. C. Blakesley and D. Neher, *Relationship between Energetic Disorder and Open-Circuit Voltage in Bulk Heterojunction Organic Solar Cells*, Phys. Rev. B - Condens. Matter Mater. Phys. **84**, (2011).
- [7] S. Maiti, M. van der Laan, D. Poonia, P. Schall, S. Kinge, and L. D. A. Siebbeles, *Emergence of New Materials for Exploiting Highly Efficient Carrier Multiplication in Photovoltaics*, Chem. Phys. Rev. **1**, 011302 (2020).
- [8] H. Goodwin, T. C. Jellicoe, N. J. L. K. Davis, and M. L. Böhm, *Multiple Exciton Generation in Quantum Dot-Based Solar Cells*, Nanophotonics **7**, 111 (2018).
- [9] U. Rau, B. Blank, and T. Kirchartz, *Detailed Balance Analysis of Photovoltaic Materials and Devices*, 2017 IEEE 44th Photovolt. Spec. Conf. PVSC 2017 1 (2017).
- [10] T. Kirchartz, J. Mattheis, and U. Rau, *Detailed Balance Theory of Excitonic and Bulk Heterojunction Solar Cells*, Phys. Rev. B - Condens. Matter Mater. Phys. **78**, 1 (2008).
- [11] T. Kirchartz and U. Rau, *Detailed Balance and Reciprocity in Solar Cells*, Phys. Status Solidi Appl. Mater. Sci. **205**, 2737 (2008).

- [12] S. N. Agbo, T. Merdzhanova, U. Rau, and O. Astakhov, *Illumination Intensity and Spectrum-Dependent Performance of Thin-Film Silicon Single and Multijunction Solar Cells*, Sol. Energy Mater. Sol. Cells **159**, 427 (2017).
- [13] D. König, Y. Yao, B. Puthen-Veetil, and S. C. Smith, *Non-Equilibrium Dynamics, Materials and Structures for Hot Carrier Solar Cells: A Detailed Review*, Semicond. Sci. Technol. **35**, 073002 (2020).
- [14] I. Ahmed, L. Shi, H. Pasanen, P. Vivo, P. Maity, M. Hatamvand, and Y. Zhan, *There Is Plenty of Room at the Top: Generation of Hot Charge Carriers and Their Applications in Perovskite and Other Semiconductor-Based Optoelectronic Devices*, Light Sci. Appl. **10**, 174 (2021).
- [15] D. K. Ferry, S. M. Goodnick, V. R. Whiteside, and I. R. Sellers, *Challenges, Myths, and Opportunities in Hot Carrier Solar Cells*, J. Appl. Phys. **128**, 220903 (2020).
- [16] Y. Harada, N. Iwata, S. Asahi, and T. Kita, *Hot-Carrier Generation and Extraction in InAs/GaAs Quantum Dot Superlattice Solar Cells*, Semicond. Sci. Technol. **34**, 4003 (2019).
- [17] P. Singhal and H. N. Ghosh, *Hot Charge Carrier Extraction from Semiconductor Quantum Dots*, J. Phys. Chem. C **122**, 17586 (2018).
- [18] Q. Lin, Z. Wang, H. J. Snaith, M. B. Johnston, and L. M. Herz, *Hybrid Perovskites: Prospects for Concentrator Solar Cells*, Adv. Sci. **5**, 1 (2018).
- [19] S. Kahmann and M. A. Loi, *Hot Carrier Solar Cells and the Potential of Perovskites for Breaking the Shockley–Queisser Limit*, J. Mater. Chem. C **7**, 2471 (2019).
- [20] I. J. Chen, S. Limpert, W. Metaferia, C. Thelander, L. Samuelson, F. Capasso, A. M. Burke, and H. Linke, *Hot-Carrier Extraction in Nanowire-Nanoantenna Photovoltaic Devices*, Nano Lett. **20**, 4064 (2020).
- [21] S. C. Limpert and S. P. Bremner, *Hot Carrier Extraction Using Energy Selective Contacts and Its Impact on the Limiting Efficiency of a Hot Carrier Solar Cell*, Appl. Phys. Lett. **107**, (2015).
- [22] T. Markvart, *Can Thermodynamics Guide Us to Make Better Solar Cells?*, IEEE J. Photovoltaics **9**, 1614 (2019).
- [23] I. Konovalov and V. Emelianov, *Hot Carrier Solar Cell as Thermoelectric Device*, Energy Sci. Eng. **5**, 113 (2017).
- [24] G. Saucke, J. Norpoth, C. Jooss, D. Su, and Y. Zhu, *Polaron Absorption for Photovoltaic Energy Conversion in a Manganite-Titanate p-n Heterojunction*, Phys. Rev. B **85**, 165315 (2012).
- [25] B. Iffland, J. Hoffmann, B. Kressdorf, V. Roddatis, M. Seibt, and C. Jooss, *Contribution of Jahn-Teller and Charge Transfer Excitations to the Photovoltaic Effect of Manganite/Titanite Heterojunctions*, New J. Phys. **19**, 063046 (2017).
- [26] B. Kressdorf, T. Meyer, M. Ten Brink, C. Seick, S. Melles, N. Ottinger, T. Titze, H. Meer, A. Weisser, J. Hoffmann, S. Mathias, H. Ulrichs, D. Steil, M. Seibt, P. E. Blöchl, and C. Jooss, *Orbital-Order Phase Transition in Pr<sub>1-x</sub>Ca<sub>x</sub>MnO<sub>3</sub> Probed by Photovoltaics*, Phys. Rev. B **103**, 1 (2021).
- [27] B. Kressdorf, T. Meyer, A. Belenchuk, O. Shapoval, M. ten Brink, S. Melles, U. Ross, J. Hoffmann, V. Moshnyaga, M. Seibt, P. Blöchl, and C. Jooss, *Room-Temperature*

- Hot-Polaron Photovoltaics in the Charge-Ordered State of a Layered Perovskite Oxide Heterojunction*, Phys. Rev. Appl. **14**, 054006 (2020).
- [28] S. Mildner, J. Hoffmann, P. E. Blöchl, S. Techert, and C. Jooss, *Temperature- and Doping-Dependent Optical Absorption in the Small-Polaron System  $Pr_{1-x}Ca_xMnO_3$* , Phys. Rev. B **92**, 035145 (2015).
- [29] H. A. Jahn and E. Teller, *Stability of Polyatomic Molecules in Degenerate Electronic States - I—Orbital Degeneracy*, Proc. R. Soc. Lond. **A161**, 220 (1937).
- [30] B. Ifland, P. Peretzki, B. Kressdorf, P. Saring, A. Kelling, M. Seibt, and C. Jooss, *Current-Voltage Characteristics of Manganite-Titanite Perovskite Junctions*, Beilstein J. Nanotechnol. **6**, 1467 (2015).
- [31] D. Raiser, S. Mildner, B. Ifland, M. Sotoudeh, P. Blöchl, S. Techert, and C. Jooss, *Evolution of Hot Polaron States with a Nanosecond Lifetime in a Manganite Perovskite*, Adv. Energy Mater. **7**, 1602174 (2017).
- [32] A. Rose, *Concepts in Photoconductivity and Allied Problems* (Interscience, 1963).
- [33] E. Cuce, P. M. Cuce, and T. Bali, *An Experimental Analysis of Illumination Intensity and Temperature Dependency of Photovoltaic Cell Parameters*, Appl. Energy **111**, 374 (2013).
- [34] F. Khan, S. N. Singh, and M. Husain, *Effect of Illumination Intensity on Cell Parameters of a Silicon Solar Cell*, Sol. Energy Mater. Sol. Cells **94**, 1473 (2010).
- [35] M. Chegaar, A. Hamzaoui, A. Namoda, P. Petit, M. Aillerie, and A. Herguth, *Effect of Illumination Intensity on Solar Cells Parameters*, Energy Procedia **36**, 722 (2013).
- [36] S. N. Agbo, T. Merdzhanova, U. Rau, and O. Astakhov, *Illumination Intensity and Spectrum-Dependent Performance of Thin-Film Silicon Single and Multijunction Solar Cells*, Sol. Energy Mater. Sol. Cells **159**, 427 (2017).
- [37] W. Shockley and H. J. Queisser, *Detailed Balance Limit of Efficiency of P-n Junction Solar Cells*, J. Appl. Phys. **32**, 510 (1961).
- [38] W. Shockley, *The Theory of p-n Junctions in Semiconductors and p-n Junction Transistors*, Bell Syst. Tech. J. **28**, 435 (1949).
- [39] B. Davydov, *The Rectifying Action in Semiconductors*, J. Tech. Phys. USSR **5**, 87 (1938).
- [40] P. Wurfel, *The Chemical Potential of Radiation*, J. Phys. C Solid State Phys. **15**, 3967 (1982).
- [41] W. Tress, *Perovskite Solar Cells on the Way to Their Radiative Efficiency Limit - Insights Into a Success Story of High Open-Circuit Voltage and Low Recombination*, Adv. Energy Mater. **7**, 1602358 (2017).
- [42] R. E. Brandt, N. M. Mangan, J. V. Li, Y. S. Lee, and T. Buonassisi, *Determining Interface Properties Limiting Open-Circuit Voltage in Heterojunction Solar Cells*, J. Appl. Phys. **121**, (2017).
- [43] F. Khan, S. H. Baek, and J. H. Kim, *Intensity Dependency of Photovoltaic Cell Parameters under High Illumination Conditions: An Analysis*, Appl. Energy **133**, 356 (2014).

- [44] M. Asaduzzaman, A. N. Bahar, M. M. Rahman Bhuiyan, and M. A. Habib, *Impacts of Temperature on the Performance of Cdte Based Thin-Film Solar Cell*, IOP Conf. Ser. Mater. Sci. Eng. **225**, (2017).
- [45] A. Javed, *The Effect of Temperatures on the Silicon Solar Cell*, Int. J. Emerg. Technol. Comput. Appl. Sci. **9**, 305 (2014).
- [46] P. Löper, D. Pysch, A. Richter, M. Hermle, S. Janz, M. Zacharias, and S. W. Glunz, *Analysis of the Temperature Dependence of the Open-Circuit Voltage*, Energy Procedia **27**, 135 (2012).
- [47] *Supplemental Information [URL Will Be Inserted by Publisher]*, (n.d.).
- [48] Y. Zhou and G. Long, *Low Density of Conduction and Valence Band States Contribute to the High Open-Circuit Voltage in Perovskite Solar Cells*, J. Phys. Chem. C **121**, 1455 (2017).
- [49] L. F. Zagonel, M. Bäurer, A. Bailly, O. Renault, M. Hoffmann, S. J. Shih, D. Cockayne, and N. Barrett, *Orientation-Dependent Work Function of Insitu Annealed Strontium Titanate*, J. Phys. Condens. Matter **21**, (2009).
- [50] S. Asanuma, H. Akoh, H. Yamada, and A. Sawa, *Relationship between Resistive Switching Characteristics and Band Diagrams of Ti/Pr<sub>1-x</sub>Ca<sub>x</sub>MnO<sub>3</sub> Junctions*, Phys. Rev. B - Condens. Matter Mater. Phys. **80**, 1 (2009).
- [51] P. E. B. M. ten Brink, Personal Communication January 17, 2022, n.d.
- [52] M. Sotoudeh, S. Rajpurohit, P. Blöchl, D. Mierwaldt, J. Norpoth, V. Roddatis, S. Mildner, B. Kressdorf, B. Ifland, and C. Jooss, *Electronic Structure of Pr<sub>1-x</sub>Ca<sub>x</sub>MnO<sub>3</sub>*, Phys. Rev. B **95**, 235150 (2017).
- [53] S. Rajpurohit, L. Z. Tan, C. Jooss, and P. E. Blöchl, *Ultrafast Spin-Nematic and Ferroelectric Phase Transitions Induced by Femtosecond Light Pulses*, Phys. Rev. B **102**, 174430 (2020).
- [54] S. Rajpurohit, C. Jooss, and P. E. Blöchl, *Evolution of the Magnetic and Polaronic Order of Pr<sub>1/2</sub>Ca<sub>1/2</sub>MnO<sub>3</sub> Following an Ultrashort Light Pulse*, Phys. Rev. B **102**, 1 (2020).
- [55] Z. Jiráček, S. Krupička, Z. Šimša, M. Dlouhá, and S. Vratislav, *Neutron Diffraction Study of Pr<sub>1-x</sub>Ca<sub>x</sub>MnO<sub>3</sub> Perovskites*, J. Magn. Magn. Mater. **53**, 153 (1985).



# Chapter 7

## General Discussion and Summary

In this thesis the conversion of photon to electrical energy in highly correlated materials in the model system of manganite perovskite/titanite heterojunction is explored. The focus is placed on investigating the fundamental mechanisms of photovoltaic energy conversion, in particular the impact of correlation effects, on this process within these hot polaron solar cells.

The presented junctions are composed of thin films of  $Pr_{0.5}Ca_{1.5}MnO_4$  (RP PCMO) and  $Pr_{1-x}Ca_xMnO_3$   $x = 0.1$  and *Nb*-doped  $SrTiO_3$  (STNO) substrates. Central topics are the photovoltaic characterization and investigation of material properties, specifically with regards to order phenomena. The photovoltaic properties are investigated as a function of temperature  $T$ , power density  $p$  and photon energy  $E_{ph}$ . Hereby, high quality and well characterized thin films prepared on different substrates are required.

A key result is that cooperative long-range order is required for photovoltaic energy conversion in hot polaron solar cells. Ifland et al. first proposed this hypothesis based on the photovoltaic studies of charge and orbital ordered PCMO  $x = 0.34$  [86]. Within the scope of this thesis the investigation is extended to two additional materials with different ordered ground states. The concept is verified, because hot polaron photovoltaics is established in the purely orbital order phase of PCMO  $x = 0.1$  and in the charge and orbital order phase of RP PCMO. A pronounced open circuit voltage, which increases nearly linear with decreasing temperature, is only observed in the order phase, whereas  $U_{oc}$  is exponentially small in the disorder phase. A characteristic temperature for vanishing  $U_{oc}$  can be defined and for a power density of  $p=16$  kW/m<sup>2</sup> this characteristic temperature coincides with the onset of order phenomena.

Within the framework of this thesis a generalized concept for a new type of phonon bottleneck for the photovoltaic energy conversion in hot polaron solar cells is proposed. Thereby, hot charge carriers are stabilized through cooperative long-range order and these now long-living hot carriers can be harvested for photovoltaic energy conversion. These



long-living states with lifetimes of the order of nanoseconds have been experimentally observed for charge and orbital ordered PCMO  $x = 0.34$  and for purely orbital ordered PCMO  $x = 0.1$  by transient pump probe measurements [79, 106]. For the intraband excitation between occupied and unoccupied  $e_g$  states (Jahn–Teller transition) and relevant relaxation process of the Jahn–Teller  $Mn-O-Mn$  dimer, a model along the following lines is proposed. The rapid structural relaxation through a conical intersection of the potential energy surfaces for a single isolated  $MnO_6$  octahedra can be suppressed by placing the octahedra into a cooperative environment [79]. This results in a shift of the conical intersection between potential surfaces and establishes states with sufficiently long lifetimes [79].

Additionally, hot polaron photovoltaics is observed in the magnetic ordered phase of PCMO  $x = 0.95$  [86]. As the manganese valence is mainly  $Mn^{4+}$ , this material has no static Jahn–Teller effect and thus, the charge transfer excitation result in the observed photovoltaic effect. In the materials investigated within this thesis both Jahn–Teller transition and charge transfer transition are explored.

The verification of the new phonon bottleneck principle is carried out in two model systems: charge and orbital order  $Pr_{0.5}Ca_{1.5}MnO_4$  (RP PCMO) and purely orbital order  $Pr_{1-x}Ca_xMnO_3$   $x = 0.1$ .

In Chapter 4 proof of principle for the design of a room temperature RP PCMO hot polaron solar cell is demonstrated. Epitaxial thin RP PCMO films with an in plane alignment of the c-axis and a high quality interface were prepared by means of MAD (by A. Belenchuk, O. Shapoval and V. Moshnyaga) and as well as IBS [87, 88]. The quasi 2D layered Ruddlesden Popper structure in combination with small out-of-plane strains of the prepared thin films yielded a charge and orbital order transition temperature of 320 K. Consequently, an order transition temperature not only significantly higher than the typical transition temperatures observed in their 3D counterparts, but also well above room temperature, has been achieved. Illumination with photon energies well below the band gap of STNO yields a pronounced photovoltaic effect that is only caused by excitations in the manganite. Due to the charge order at room temperature, it was possible to achieve room temperature hot polaron photovoltaics for the first time.

Chapter 5 demonstrates the close correlation between electronic phase diagram and photovoltaic effect for the purely orbital order PCMO  $x = 0.1$  (see Fig. 7.1). According to the commonly accepted phase diagram by Jirak et al. the orbital order transition temperature amounts to about 600 K for  $x = 0.1$  [89]. The photon bottleneck model therefore predicts a characteristic temperature for the pronounced increase of the open

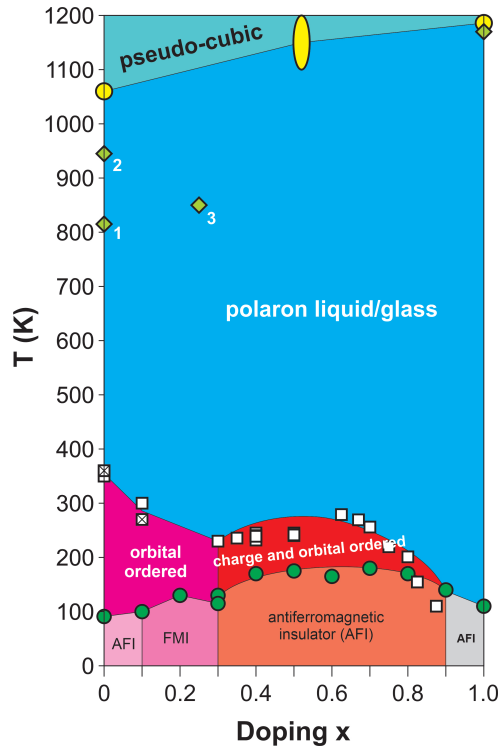


Figure 7.1: Phase diagram for the 3D  $Pr_{1-x}Ca_xMnO_3$  perovskite according to [106] (see Chapter 5) shows the purely orbital order phase for doping  $x < 0.28$  and the charge and orbital order phase for  $0.28 < x < 0.9$ . At low temperatures different magnetic ground states such as antiferromagnetic insulating (AFI) and ferromagnetic insulating (FMI) emerge.

circuit voltage at similar temperatures. However, experimentally a pronounced open circuit voltage is only present well below room temperature, as the characteristic temperature for vanishing is observed at about  $T = 220$  K.

This apparent contradiction prompted a closer investigation of the orbital order phase of  $x = 0.1$ . Since the orbital order cannot be measured directly, several complementary properties were investigated within the relevant temperature range. Here, changes and anomalies well below room temperature were found in optical absorption, electric transport, magnetization, and ultra-fast transient pump probe studies. For bulk material changes in the temperature dependence of lattice parameters and thermal expansion are evident. This is additionally strengthened by theoretical finite-temperature simulations performed by M. ten Brink using a tight-binding model, which reveals an orbital order transition at 300 K [106]. When considered together, these results collectively indicate a second order phase transition in a temperature regime of 200 – 240 K.

As the phase diagram indicates, PCMO undergoes a structural transition from pseudo-cubic

to orthorhombic at high temperatures, which results in tilt and distortion of the  $Mn - O$  octahedra and the emergence of static Jahn–Teller effect. Therefore, this phase transition was equated with the orbital order transition in the original phase diagram by Jirak. This structural high temperature transition was also observed in a PCMO  $x = 0.1$  thin film by T. Meyer by environmental in-situ heating nano-beam electron diffraction, demonstrating a slightly reduced transition temperature [144]. Two aspects for orbital order must be considered separately: At the high temperature orthorhombic phase transition, orbital polarization is induced by the octahedral tilt pattern, which couples to the Jahn–Teller distortion. However, at lower temperatures, a second phase transition to spontaneous orbital order, driven by electronic correlations, occurs. Thus, only the low temperature, orbital ordered phase fulfills the required cooperative phenomena in order to stabilize the long living hot polaron states for photovoltaic energy conversion.

In Chapter 6 the dependence of the open circuit  $U_{oc}$  and the short circuit voltage on temperature  $T$ , power density  $p$  and photon energy  $E_{ph}$  is investigated. Due to the different nature of the mechanism for photovoltaic energy conversion in hot polaron systems and conventional solar cells, major deviations to the Shockley–Queisser theory for conventional semiconductors are observed. The dependence of the internal quantum efficiency on photon energy is quite different. Because all charge carriers relax to the band edge in the conventional semiconductor model, they are extracted at the same energy and thus, the internal quantum efficiency is independent of the photon energy for excitation energies above the band gap. In contrast, in hot carrier systems, electron–hole pairs generated by a variety of different photon energies can be harvested. Experimentally, the internal quantum efficiency for monochromatic illumination in the PCMO  $x = 0.1$  junction increases linearly with increasing photon energy.

In contrast to the prediction of the SQ model, the short circuit current density and the open circuit voltage exhibit two distinct regimes with respect to dependence on incident power density and in the higher power densities regime the response of both parameters is reduced. Additionally, the short circuit current density  $J_{sc}$  is orders of magnitude smaller than the lifetime and polaron mobility would lead one to expect. This indicates additional loss channels in the hot polaron solar cells, which significantly reduce the collection of hot polarons.

A new characteristic photovoltaic parameter  $T^*$  is introduced.  $T^*$  is defined as the characteristic turning point from a very small  $U_{oc}$  value to a significant increase of  $U_{oc}$  with decreasing  $T$ . Remarkably  $T^*$  can be tuned through power density and photon energy as  $T^*$  decreases with increasing  $p$  and  $E_{ph}$ . The temperature  $T^*$  is governed by the hot

carrier concentration and the order transition, as carrier lifetime increases towards lower temperatures.

As hot polaron solar cells, the investigated materials belong to third generation solar cells. They fall within the concept of slowing down of hot carrier thermalization and the corresponding harvest of such hot charge carriers. However, the new type of phonon bottleneck differs in approach and mechanism compared to the typical phonon bottleneck observed in for example Halides and Quantum dots. For the latter, the phonon interactions are suppressed. With this new type of phonon bottleneck, the strong electron-phonon interaction is turned into an advantage and utilized, because the cooperative correlations stabilize the hot polaron state.

However, very small overall efficiencies are observed for the hot polaron solar cells. This can be traced back to several different reasons and fundamental mechanisms. Only charge carriers generated in the material volume, which is composed of the space charge region and the diffusion length distance from the space charge region, contribute to the photovoltaic effect. The number of charge carriers generated within this volume depends among other things on the absorption of the materials. The intrinsic material variable of absorption length is defined as the distance, in which the fraction  $1/e$  (or 63 %) of the incident photons has been absorbed. The excited charges are separated within the space charge region and transported through the material to the contacts, through which they finally are extracted as current. These loss processes, that affect the collection of charges, are summarized in the collection probability. As indicated in Chapter 6, the hot polaron solar cells exhibit small quantum efficiency and small collection probability, which are influenced by different factors:

- With a space charge region of approximately 1 nm and a diffusion length of the excited charge carriers in the order of 2 nm, the active material volume for charge carriers generation, which can be utilized the photovoltaic effect, is small. Additionally, space charge region and diffusion length are significantly smaller than the length scale of absorption, which is in the order of 70 nm. Therefore, only a small fraction of the generated electron-hole-pairs can be utilized for photovoltaic energy conversion.
- The transfer of the charges across the interface is accompanied by a change in nature of the polaron, as the excited electron polarons in the PCMO component converts into a large polaron in the STNO component. Additionally, the currently applied contacts are not electronically optimized for hot carrier extraction. Accordingly, significant losses are expected for this process.

Strategies to overcome these limits are given by, but not limited to:

- The number of charge carriers generated within the active volume relevant for the photovoltaics can be significantly increased by decreasing the absorption length, while simultaneously reducing the manganese film thickness. For this design concept a 5 – 10 nm thick film with almost full absorption on this length scale is proposed. The absorption of the film could be increased through plasmonic concept, where high electric fields lead to higher absorption [145, 146].
- By increasing the diffusion length and thus increasing the active generation volume, the number of charge carriers, which can be utilized for photovoltaic energy conversion, can also be increased. As the diffusion length is determined by mobility and lifetime of charge carrier, increasing either of these factors would increase the volume.
- The collection probability can be increased through electrical and structural interface design e. g. increase the width of the space charge region, increase the transfer probability across the interface, as well as the integration of energy-selective or energy specific contacts.

The mobility and lifetime of the hot charge carriers and their interplay are possible parameters for tuning the photovoltaic energy conversion in hot polaron solar cells. One question raised, is, if the mobility and diffusion length can be modified separately. Within the non-rigid band of the manganite, the excitation of charge carriers impacts and modifies the density of states and additionally induces localized disruption. Open questions remain, how the excited state influences the mobility of the charge carrier and can the mobility be tuned. Additionally, the impact of correlation and different order ground states on the life time of the hot polaron states can be further explored.

The RP PCMO room temperature hot polaron solar cell now enables investigations at room temperature. In the context of material development, the Ruddlesden-Popper  $n = 2$  phase is an additional model system for the systematically study the correlation between charge and orbital order transition temperature and photovoltaic energy conversion. As the order transition temperature is shifted to higher temperatures, the question is raised whether short circuit current density and open circuit voltage at room temperature simultaneously increase. With access to additional types of order states, such as additional short range charge order, the impact of correlation and order on the lifetime of hot polarons can be further extended. For illumination conditions applied in this thesis, the mean distance between two simultaneous excitation events is large and thus, no interaction is expected.

Accordingly, the global order parameter is not changed, i.e., reduced. Under high excitation density, where correspondingly significant proportion of distorted areas are introduced into the material, the global order parameter could be reduced. Implementing laser light sources will give access to very high incident power density, thus, aspects such as collective distortion, interaction between excitation events and even optically induced phase transitions come into play [147–149].

Further research is needed to determine the respective role of the charge order compared to the orbital order in the stabilization of the hot polaron state. One could cautiously hypothesise that orbital order is the fundamental requirement and that the charge order further improves the stabilization of the long-living state. Strong correlation between order and pronounced open circuit voltage is demonstrated for orbital as well as orbital and charge ordered systems. However, the questions arises which other types of order besides orbital/charge order contribute to long-living states.



## **Appendix A**

### **Supplemental Material for Room-temperature Hot-polaron Photovoltaics in the Charge-ordered State of a Layered Perovskite Oxide Heterojunction**



## Room-temperature hot-polaron photovoltaics in the charge-ordered state of a layered perovskite oxide heterojunction

B. Kressdorf<sup>1</sup>, T. Meyer<sup>2</sup>, A. Belenchuk<sup>3,4</sup>, O. Shapoval<sup>3,4</sup>, M. ten Brink<sup>5</sup>, S. Melles<sup>1</sup>,  
U. Ross<sup>1</sup>, J. Hoffmann<sup>1</sup>, V. Moshnyaga<sup>3</sup>, M. Seibt<sup>2</sup>, P. Blöchl<sup>5,6</sup>, C. Jooss<sup>1</sup>

<sup>1</sup>University of Goettingen, Institute of Materials Physics, Friedrich-Hund-Platz 1, 37077 Goettingen, Germany

<sup>2</sup>University of Goettingen, 4th Physical Institute – Solids and Nanostructures, Friedrich-Hund-Platz 1, 37077 Goettingen, Germany

<sup>3</sup>University of Goettingen, 1st Physical Institute, Friedrich-Hund-Platz 1, 37077 Goettingen, Germany

<sup>4</sup>IEN, Academy of Sciences in Moldova, str. Academiei 3/3, MD-2028, Chisinau, Moldova

<sup>5</sup>Institute for Theoretical Physics, University of Goettingen, Friedrich-Hund-Platz 1, 37077 Goettingen Germany

<sup>6</sup>Institute for Theoretical Physics, Clausthal University of Technology, Leibnizstr. 10. D-38678 Clausthal-Zellerfeld, Germany

(Dated: October 15, 2020)

### I. X-ray diffraction (XRD)

XRD in  $\Theta-2\Theta$  Bragg-Brentano geometry was performed with a Bruker D8 Discover system with monochromatic Cu  $K\alpha_1$  radiation.

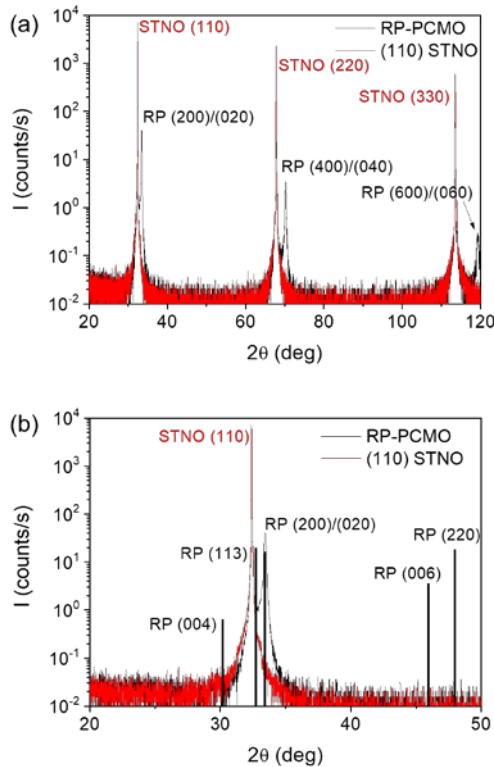


FIG S1. a) XRD patterns of the MAD grown [100]/[010] oriented RP-PCMO films on a (011) STNO substrate. Beside reflections of the substrate only the RP-PCMO [200]/[020] peak and higher orders are visible. b) Detail of the diffractogram showing angular position and relative height of possible misorientation reflections (black bars) which are however not detected within detection limit.

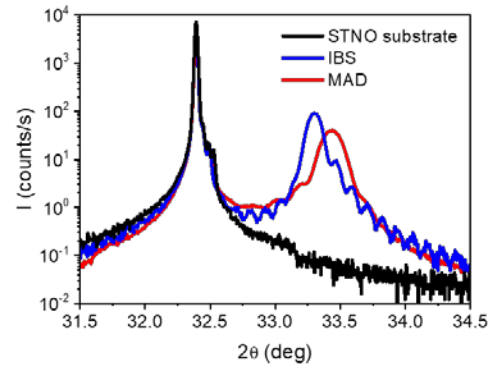


FIG S2. A comparison of XRD patterns of MAD- and IBS-prepared RP-PCMO films on [011] STO.

The diffractogram of the PR-PCMO film only reveals reflections corresponding to a [100]/[010] growth direction. No peaks of possible misorientations are visible (Fig. S1a, b). Figure S2 shows the comparison of [100]/[010] films on (011) STNO, grown by metalorganic aerosol deposition (MAD) and ion beam sputtering (IBS).

### II. Film grown by means of IBS

The thin film epitaxial growth was checked by XRD (Fig. S2) and annular dark field (ADF) scanning transmission electron microscopy (STEM) (Fig. S3) and reveals the same [100]/[010] growth orientation as films prepared by MAD. Furthermore, the IBS grown films reveal a similar out-of-plane strain state, as well as a comparable photovoltaic response compared to the MAD prepared film. Therefore, MAD and IBS result in films with same epitaxial relationships as well as comparable bulk properties.

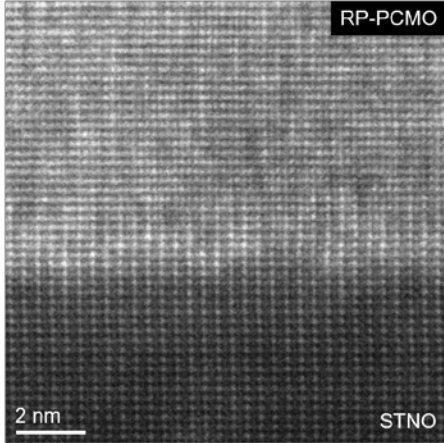


FIG. S3. High-resolution ADF-STEM image of the interface of MAD grown RP-PCMO on STNO in STO [100] zone axis. A misfit dislocation is marked by the red symbol.

### III. Electric characterization

Using film thickness of 30 nm, film width of 4 mm and a distance between the contacts of 2 mm, the resistance at room temperature and at zero magnetic field corresponds to a resistivity parallel to the c-axis of  $0.46 \Omega\text{cm}$ .

After cooling down the sample to 150 K in zero field, a magnetic field of 9 T was applied and the sample was heated up to room temperature. The resistance at room temperature and 9 T corresponds to a resistivity of  $0.6 \Omega\text{cm}$ . We expect that the small increase in resistivity reflects hysteretic behavior in the charge ordering phase transition.

In order to investigate the cross-plane electric transport of RP-PCMO/STNO heterojunctions in the dark and under illumination, Pt contacts were deposited on top of the RP-PCMO film and Ti/Au layers on the rear side of the STNO substrates. Here, the Ti layer is used to avoid formation of a Schottky-barrier at the metal/STNO interface and the Au layer serves as a protection layer. Top and bottom contact were connected to a Keithley 2430, which served as voltage source and ammeter.

At room temperature, the resistivity is of the order of  $30 \text{ m}\Omega\text{cm}$  for STNO and of the order of  $1 \Omega\text{cm}$  for RP-PCMO in the charge ordered phase [1], respectively. In cross-section measurements, this would lead to a resistance contribution of the manganite film of approx.  $10^{-3} \Omega$ . However, the two-point cross-plane resistance between the top and bottom contacts ( $2.8 \times 10^5 \Omega$ ) is orders of magnitude larger than that expected from the bulk resistivity. Therefore, the interface resistances Pt/RP-PCMO and RP-PCMO/STNO dominate the total cross-plane resistance  $R_{cp}$ . For a contact area of  $A = 4 \text{ mm}^2$ ,  $R_{cp}$  corresponds to a contact resistance of  $R_c = R_{cp} \times A = 1.1 \times 10^4 \Omega\text{cm}^2$ . Within the equivalent circuit

model of a solar cell, the interface contact resistance corresponds to the shunt resistance.

Fig. S4a shows temperature-dependent resistances normalized to the room temperature values; in-plane in zero magnetic field and 9 T and cross-plane in zero field. The different data points almost follow the same master curve (especially above 200 K), indicating that the activation barrier of polaronic mobility is only weakly affected by magnetic fields and quite similar in in-plane and cross-plane direction.

Fig S4b shows Arrhenius-type analysis for two films of different thicknesses. At high temperature range of constant slope is visible, where a fit is performed to deduce the activation energy in the charge-disordered HT-phase. At lower temperatures, the dependence is non-linear and the change in slope indicates the charge-ordering temperature  $T_{CO}$ . Due to higher volume of material the change in resistance and slope is more pronounced for the 200 nm film but  $T_{CO}$  is almost unaffected by the film thickness.

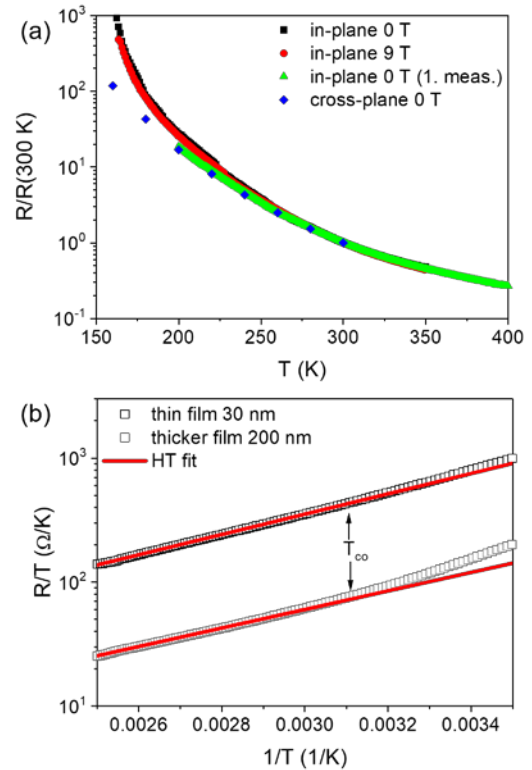


FIG. S4. a) Temperature dependence of resistance normalized to room temperature value. In-plane resistance in zero-field (black squares) and at 9 T (red circles) of a 30 nm thick RP-PCMO film on insulating (110) STO. The sample was analyzed twice at an interval of 3 months (green triangles). Cross-plane resistance was measured for a 60 nm thick sample on STNO (blue diamonds). b) Temperature dependence of the Arrhenius-type representation  $R/T$  vs.  $1/T$  of a 30 nm and 200 nm thick film. The change in slopes in the Arrhenius plot indicate the charge ordering temperature of  $T_{CO} \approx 320 \text{ K}$ .

## IV. Optical characterization

The reflectance is measured with the addition of a UV-enhanced AU mirror (Thorlabs) which provides a reference spectrum. The measured transmittance and reflectance are shown in Fig. S5 a. Measurements of reflectance in the NIR regime were not possible in our current setup due to low signal-to-noise ratio. In such a measurement setup transmission will be underestimated due to, e.g., additional contributions from the substrate, whereas the reflection is overestimated due to contributions of double reflections, interface and substrate contributions. Therefore, a fixed reflectance value of  $R_0=0.3$  was assumed over the entire spectral range for the calculation of the absorption coefficient in the main text. Note, that the exact value of  $R_0$  shifts the absolute value of the absorption coefficient but the peak positions of the absorption bands remain fixed. In Fig S5 b) the comparison between two different RP samples shows similar transmission spectra. The absolute value of transmittance in sample 2 is higher than in sample 1. Since the reflectance of samples strongly depend on surface, which in turn changes due to contamination during measurements, sample age, a variation in absolute transmittance for different samples is expected. Even though the absolute value of the transmittance differs, the general shape of 3 observed peaks and their energetic positions does not change. In sample 2 the C peak intensity is stronger whereas the B peak intensity is diminished in comparison to sample 1.

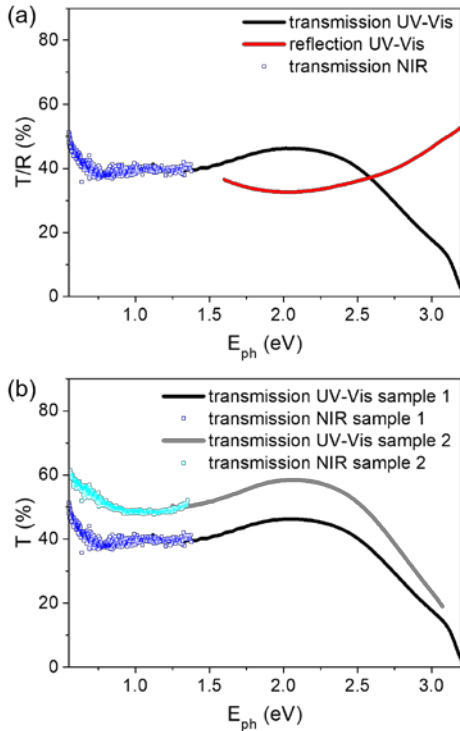


FIG. S5. a) Spectra of reflectance and transmittance at room temperature of an RP-PCMO film with thickness  $d=100\text{nm}$ . b) Comparison of the transmittance spectra for two  $d=100\text{nm}$  samples.

## V. Density of states

The density functional calculations for the density of states were performed analogous to a previous publication [2]. The calculations based on the projector augmented wave method (PAW) [3] using the PBE0r hybrid functional introduced in Ref [2]. The PBE0r exchange and double-counting correction terms are expressed in terms of a set of local orbitals.

The augmentation of the orbital shells, the construction and radii of the nodeless partial waves, the plane-wave cutoffs, the hybrid mixing factors and the PBE0r local orbitals are chosen similar as in Ref. [2], and summarized in table T1.

orbital shells of augmentation	
Pr	5s,6s,5p,6p,5d,4f
Ca	3s,4s,3p,4p,3d
Mn	4s,4p,3d
O	2s,2p,3d
partial waves for augmentation	
construction method	nodeless partial waves [4]
matching radii for Pr	s: 0.84, p: 0.77, d: 0.8, f:0.7
matching radii for Ca	all angular momenta: 0.6
matching radii for Mn	all angular momenta: 1
matching radii for O	all angular momenta: 0.85
plane-wave cutoffs	
auxiliary wave function	40 Ry
auxiliary density	80 Ry
hybrid mixing factors	
Pr	0.15
Ca	0.1
Mn	0.07
O	0.1
PBE0r local orbitals	
construction method	tight-binding linear muffin tin orbitals [5] with nodeless partial waves
orbital sets for Pr	5s,5p,5d,4f
orbital sets for Ca	3s,3p
orbital sets for Mn	4s,3d
orbital sets for O	2s,2p

TAB. T1. Parameters of the density functional calculations. All parameters listed here are chosen similar as in [2] and described in more detail there.

The calculations were performed in a 2x2x1 supercell of the original Fmm2 unit cell, with total lattice parameters  $a=10.730 \text{ \AA}$ ,  $b=10.709 \text{ \AA}$  and  $c=11.840 \text{ \AA}$ , corresponding to two manganese planes with eight manganese atoms each. A k-point integration grid of (4x4x4) reciprocal lattice vectors was used. Starting from an initial magnetic structure corresponding to CE-type magnetic chains (see [6]), both electronic and atomic degrees of freedom were relaxed.

## References

- [1] I. P. Handayani, A. A. Nugroho, S. Riyadi, G. R. Blake, N. Mufti, T. T. M. Palstra and P. H. M. van Loosdrecht, Correlation between lattice vibrations with charge, orbital, and spin ordering in the layered manganite  $\text{Pr}_{0.5}\text{Ca}_{1.5}\text{MnO}_4$ , *Phys. Rev. B* **92**, 205101 (2015).
- [2] M. Sotoudeh, S. Rajpurohit, P.E. Blöchl, D. Mierwaldt, J. Norpoth, V. Roddatis, S. Mildner, B. Iffland, C. Jooss, Electronic structure of  $\text{Pr}_{1-x}\text{Ca}_x\text{MnO}_3$ , *Phys. Rev. B* **95**, 235150 (2017).
- [3] P. E. Blöchl, Projector augmented-wave method, *Phys. Rev. B* **50**, 17953 (1994).
- [4] Peter E. Blöchl and Clemens Först, „Node-less atomic wave functions, Pauli repulsion and systematic projector augmentation” [arXiv:1210.5937](https://arxiv.org/abs/1210.5937) [physics.chem-ph]
- [5] O. K. Andersen and O. Jepsen, Explicit, First-Principles Tight-Binding Theory, *Phys. Rev. Lett.* **53**, 2571 (1984).
- [6] E. O. Wollan and W. C. Koehler, Neutron Diffraction Study of the Magnetic Properties of the Series of Perovskite-Type Compounds  $[(1-x) \text{La}, x \text{Ca}]\text{MnO}_3$ , *Phys. Rev.* **100**, 545 (1955).



## **Appendix B**

### **Supplemental Material for Orbital-order Phase Transition in $\text{Pr}_{1-x}\text{Ca}_x\text{MnO}_3$ probed by Photovoltaics**

## Orbital order phase transition in $\text{Pr}_{1-x}\text{Ca}_x\text{MnO}_3$ probed by photovoltaics

B. Kressdorf<sup>1</sup>, T. Meyer<sup>2</sup>, M. ten Brink<sup>3,4</sup>, C. Seick<sup>5</sup>, S. Melles<sup>1</sup>, N. Ottinger<sup>1</sup>, T. Titze<sup>5</sup>, H. Meer<sup>5</sup>, A. Weisser<sup>5</sup>, J. Hoffmann<sup>1</sup>, S. Mathias<sup>5</sup>, H. Ulrichs<sup>5</sup>, D. Steil<sup>5</sup>, M. Seibt<sup>2</sup>, P.E. Blöchl<sup>3,4</sup>, C. Jooss<sup>1</sup>

<sup>1</sup> University of Göttingen, Institute of Materials Physics,

<sup>2</sup> University of Göttingen, 4th Institute of Physics,

<sup>3</sup> Clausthal University of Technology, Institute of Theoretical,

<sup>4</sup> University of Göttingen, Institute of Theoretical Physics,

<sup>5</sup> University of Göttingen, 1st Institute of Physics

### I. Microstructural characterization of epitaxial thin film junctions

Figure S1 shows the structural characterization of a typical  $\text{Pr}_{0.9}\text{Ca}_{0.1}\text{MnO}_3$  (PCMO  $x=0.1$ ) on STO/STNO substrates by x-ray diffraction (XRD) measurements and transmission electron (TEM) studies. In the Pbnm notation, epitaxial relations typically observed for PCMO films on (100) STO are

$[001]_{\text{oop}} \text{STO} \parallel [001]_{\text{oop}} \text{PCMO}$  with  $[110]_{\text{ip}} \text{STO} \parallel [100]_{\text{ip}} \text{PCMO}$  or  $[110]_{\text{ip}} \text{STO} \parallel [010]_{\text{ip}} \text{PCMO}$

and

$[001]_{\text{oop}} \text{STO} \parallel [110]_{\text{oop}} \text{PCMO}$  with  $[100]_{\text{ip}} \text{STO} \parallel [001]_{\text{ip}} \text{PCMO}$  or  $[010]_{\text{ip}} \text{STO} \parallel [001]_{\text{ip}} \text{PCMO}$

Here, oop corresponds to the epitaxial relation perpendicular to the substrate and ip to the in-plane configuration. Additional exchange of the  $a$  and  $b$  directions of PCMO leads to six different twin domains.

The XRD scan in Fig. S1 (a) reveals that PCMO  $x=0.1$  on STO has two out-of-plane growth orientations,  $[110]$  and  $[001]$ , that corresponds to the usually observed twinning. No additional orientations are visible. By considering the different structure factors of  $[220]$  and  $[004]$  reflections, the intensity ratio of the experimentally observed peaks implies predominantly  $[001]$  growth with a volume fraction of about 85%. This has been confirmed by TEM annular dark-field (ADF) imaging of cross plane lamellas.

Electron-transparent lamellae in cross-section geometry were prepared by means of focused ion-beam etching (FEI Nova NanoLab Dual Beam system) using an acceleration voltage of 5 kV during the final thinning step. The TEM measurements were carried out in an FEI Titan 80-300 operated at 300kV and equipped with a Gatan Quantum 965 ER image filter. Selective area electron diffraction (SAED) was performed with a 10  $\mu\text{m}$  aperture that approximately corresponds to a lateral size of about 170 nm in the image plane. Scanning TEM (STEM) images with an annular dark field (ADF) detector were taken at an electron current of 42 pA with an inner and outer acceptance semi-angle of 46.8 mrad and 200 mrad, respectively (camera length 38 mm). Electron energy loss spectroscopy (EELS) data acquisition was performed at a beam current of 150 pA and at a collection semi-angle of 39 mrad.

Fig. S1 (b) shows a typical columnar pattern of (001) oriented quite regularly arranged domains with a size of 100-150 nm. Remarkably, the interface between STO and PCMO  $x=0.1$  is almost coherent with a very low density of dislocations (Fig. S1 (c)), although the nominal lattice mismatch is rather large. EELS analysis confirms a chemically sharp interface with no interdiffusion (Fig S1 (d)).

The formation of  $[110]$  and  $[001]$  orientational twin domains is a result of the local symmetry breaking in the cubic to orthorhombic phase transition above 600 K [1]. In addition to the (minor) contribution of (220) orientations they are visible by subsequent alternation of PCMO  $x=0.1$  in-plane  $[100]$  and  $[010]$  orientations within the (001) oriented domains. Post-annealing of the sample at 900° C gives rise to a quite strong relaxation of the small volume fraction of (110) oriented domains and a pronounced reduction of the out-of-plane strain  $\epsilon_{\text{oop}}$  (Fig. S1 (a)).

The strain stress state in our thin films can be determined through the XRD measurement. According to [2], the lattice parameters of PCMO  $x=0.1$  are  $a=0.5442$  nm,  $b=0.5617$  nm and  $c=0.7635$  nm. Using the lattice constant of STO of  $0.3905$  nm, the lattice mismatches for [001] growth correspond to  $\varepsilon_{ip}(a) = 1.48\%$  ( $[110]_{ip}$  STO  $\parallel$   $[100]_{ip}$  PCMO) and  $\varepsilon_{ip}(b) = -1.68\%$  ( $[110]_{ip}$  STO  $\parallel$   $[010]_{ip}$  PCMO).

From simple isotropic elastic consideration, the out-of-plane strain  $\varepsilon_{oop}$  should be of the order of

$$(1) \quad \varepsilon_{oop} \approx -\frac{\nu}{1-\nu} (\varepsilon_{ip}(a) + \varepsilon_{ip}(b)),$$

where Poisson's ratio of PCMO is about 0.3. Therefore, one would expect an out-of-plane strain of the order of 0.1% which is considerably smaller than the experimentally observed  $\varepsilon_{oop} = 0.8\%$  deduced from the plane spacing of the [004] reflection. This suggests an additional compressive in-plane strain component. Since this additional component almost vanished after post-annealing (see main text), preparation-induced defects are the most likely source of this strain.

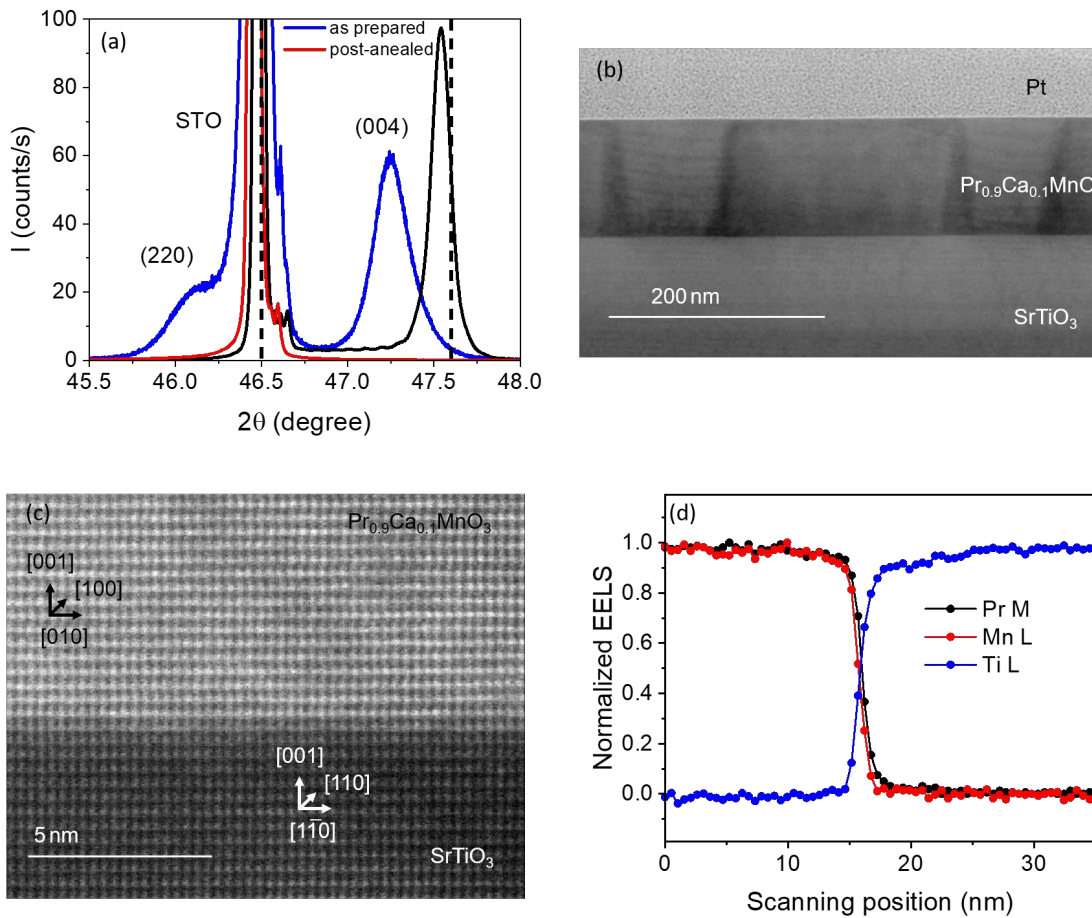


**FIG. S1:** Structural characterization of PCMO  $x=0.1$  thin films on STO substrates. Because of nearly identical lattice constant, the same structure is observed on Nb-doped STO. (a) XRD of the PCMO  $x=0.1$  film on (100) STO, as-prepared and post-annealed for 4h at  $900^\circ\text{C}$  in air. The black lines indicate the angular peak positions of (220) and (004) for bulk PCMO  $x=0.1$  [2]. (b) Annular dark field (ADF)-STEM image showing the nano twinned microstructure of PCMO  $x=0.1$  films on STO. (c) ADF-HRSTEM of a [001] twin domain showing a coherent interface between film and substrate. (d) Normalized EELS profile reveals no chemical segregation or interdiffusion at the interface.

In Fig. S2 the complementary structural characterization of an as-prepared PCMO  $x=0.1$  film on (100) MgO by XRD and TEM studies is shown. Similar to the films grown on STO the XRD scan (Fig. S2 (a)) reveals epitaxial growth with the twinning of [110] and [001] out-of plane directions. In contrast to STO, the film growth on MgO is dominated by the [110] orientation and only the asymmetric, shoulder-like intensity distribution of the substrate peak hints to a small [001] contribution. No additional miss<sub>109</sub>



orientations are observed. Similar to films of STO the reduced angle of both orientations indicates a compressive in plane strain. For [220] reflection the strain arises to  $\epsilon_{oop} = 1.1\%$ . TEM studies in Fig. S2 (b)-(d) confirm the epitaxial growth with preferred [110] orientation and the absence of interfacial chemical interdiffusion between the MgO substrate and the PCMO film.

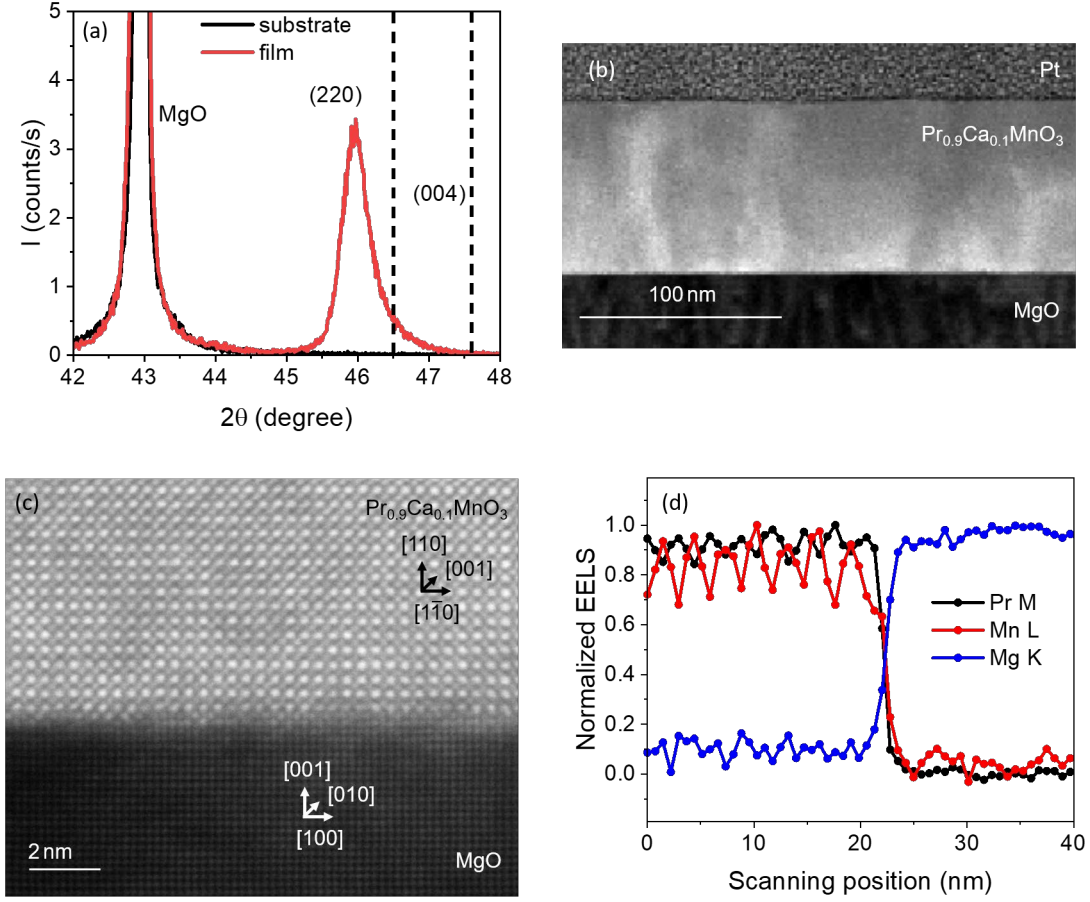


**FIG. S2:** Structural characterization of an as-prepared PCMO  $x=0.1$  film on MgO. (a) XRD scan, where the peak positions of (220) and (004) for bulk PCMO  $x=0.1$  have been included [2]. (b) ADF-STEM image showing a flat film with a columnar structure of (110) oriented domains. Electron diffraction indicates that the c-axis is in-plane and alternates between the [100] and [010] directions of the MgO substrate (not shown). (c) The ADF-HRSTEM of a [110] oriented twin domain reveals a semicoherent interface with some misfit dislocations. (d) Normalized EELS profile reveals no chemical segregation or interdiffusion at the interface.

## II. Resistivity and logarithmic derivative

Post-annealing, i.e. annihilation of preparation-caused defects, strongly affects the temperature dependent resistivity of weakly doped PCMO  $x=0.1$ . Fig. S3 (a) shows the changes of resistivity  $\rho$  due to post-annealing for  $t_a$  hours at  $900^\circ\text{C}$ . The heat treatment causes a reduction of resistivity by roughly one order of magnitude. The magneto-resistance effect

$$(2a) \quad \frac{\Delta\rho}{\rho} \equiv \frac{\rho(0) - \rho(9T)}{\rho(0)}$$

at room temperature amounts to about 6% but strongly increases to about 30% at 180 K. The effect of post-annealing is small but an increase with increasing annealing time is observed.

Fig. S3 (b) shows the influence of different annealing times on the logarithmic derivative

$$(2b) \quad E_A = k \frac{d}{d(1/T)} \ln\left(\frac{\rho}{T}\right)$$

that equals the small polaron hopping energy in the adiabatic approach. In [3], the interplay of preparation-caused defects, charge- and orbital ordering and melting in strong magnetic fields is discussed.

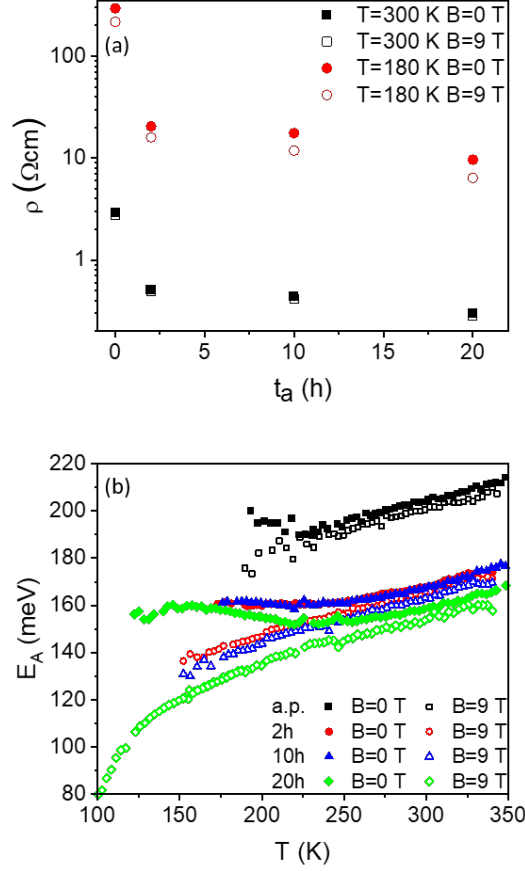


**FIG. S3:** (a) Resistivity of the PCMO  $x=0.1$  film on (100) STO at 300/180 K in zero field and  $B=9\text{ T}$  vs. annealing time  $t_a$ . Post-annealing was performed at  $900^\circ\text{ C}$  with a heating and cooling rate of  $100\text{ K/min}$ . (b) Logarithmic derivative  $E_A$  vs. temperature in zero field and  $B=9\text{ T}$  after different annealing time  $t_a$ .

### III. Reflection correction of the absorption coefficient

Using Tauc's relationship, the reflection-corrected absorption coefficient  $\alpha$  and the optical band gap  $E_g$  can be deduced from the transmittance  $T$ , the reflectance  $R$  and the film thickness  $d$  [4 and references within]:

$$(3a) \quad \alpha = \frac{1}{d} \ln \left[ \frac{(1-R)^2}{2T} + \sqrt{\frac{(1-R)^4}{4T^2} + R^2} \right]$$

$$(3b) \quad \alpha h\nu = \alpha_0 (h\nu - E_g)^n$$

$\alpha_0$  is the band tailing parameter and  $n$  is a characteristic exponent depending on the character of transition. Fig. S4 (a) shows the absorption coefficient according to equation (3a) for various temperatures in the photon energy regime of  $E_{ph}=1.2\text{ eV}$  to  $E_{ph}=1.6\text{ eV}$ . The reflection data for the samples were measured and scaled down by 7% to match a reference mirror sample. In order to determine the band gap, we compare the measured  $\alpha h\nu$  vs  $h\nu$  with Eq.3b for various trial values of the band gap  $E_g$  and for the characteristic exponents of  $n=1/2$  for direct allowed transitions,  $n=2$  for indirect allowed,  $n=3/2$  for direct forbidden and  $n=3$  for indirect forbidden transitions. The exponent  $n=3/2$  gave the best fit. In figure S4 (b) the phonon energy  $E_{ph}$  is plotted for this exponent and a linear fit is applied for the shown energy regime to determine the band gap in accordance with equation (3b). A detailed analysis of this method for determining the band gap using Tauc's relation can be found in [4].

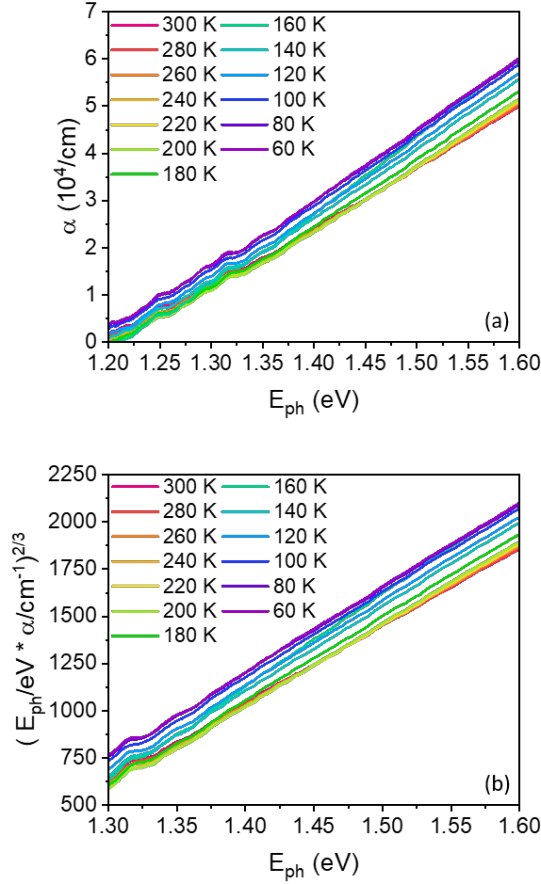


**FIG. S4:** (a) Temperature and spectral dependence of the absorption coefficient for PCMO  $x=0.1$  film on (001) STO deduced from eq. 3a. (b) Linearized plot according to eq. 3b with characteristic exponent  $n=3/2$ .

#### IV. Magnetic measurements: Substrate correction

Due to the small magnetic signal of the thin film the substrate contributions need to be considered very carefully in the orbital ordering temperature range. Therefore, we took a closer look at temperature dependent substrate contribution and its change at thin film deposition conditions. This is required, since the treatment of the STO-substrate during the sputtering process – strong heating under low pressure conditions – can cause a loss of oxygen and therefore, a higher ferromagnetic moment can be generated in the STO-substrate [5]. We take this additional moment  $\Delta m_s(H)$  into account in equation (A1) in the main text as a temperature-independent contribution.

Therefore, we heated a STO-substrate, from the same batch of substrates as the sample shown in the main text, in two different ways: (i) under sputter conditions, and (ii) under vacuum conditions. After both steps, we measured  $m(T)$  at an external magnetic field of 200mT as well as  $m(H)$  of the substrate.

Case (i) represents the conditions during the sputtering process. We heated the substrate to deposition temperature of about 720° C for the duration of film deposition of  $t=33$  min under a partial oxygen pressure of  $p_{O_x} = 1.4 * 10^{-4}$  mbar. Since the ion bombardment of the STO surface in the initial growth stages can result in additional vacancies, we increased the oxygen vacancy density of the substrate surface in case (ii) by an additional heating process to 720 °C in high vacuum, i.e.  $p = 1 * 10^{-6}$  mbar for 45 min.

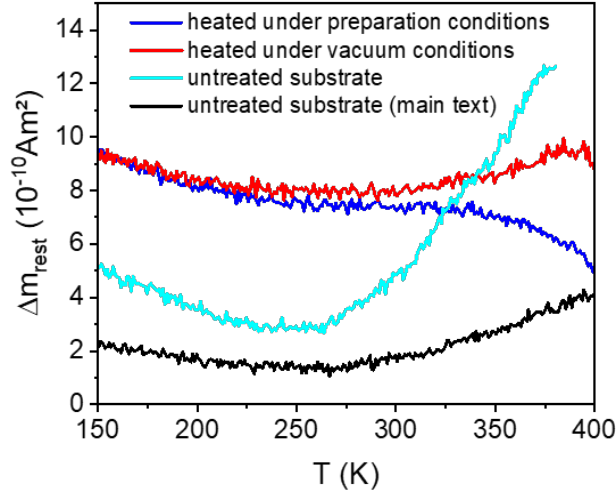


**FIG. S5:** Temperature dependence magnetic moment  $\Delta m_{rest}(T)$  of STO-substrates at 200mT applied field after subtraction of the diamagnetic contribution. The black curve shows the pristine state of the substrate used for the study of the magnetic properties of the PCMO  $x=0.1$  film in the main text. Furthermore, an additional substrate is shown before (cyan) and after heating at sputtering conditions (blue) and in high vacuum (red).

We subtracted a temperature independent diamagnetic contribution obtained from  $m(H)$  curves from the measured total substrate moment in order to separate the possible paramagnetic impurity and temperature depended diamagnetic contributions as well as ferromagnetic surface contributions  $\Delta m_{rest}(T)$ . The diamagnetic correction was determined through linear fits to  $m(H)$  in the high-field region at 250 K. The resulting magnetic properties of the substrate before and after the two heating procedures are shown in the Fig. S5. Data of the original substrate with the PCMO  $x=0.1$  film shown in the main text is shown. It exhibits a comparable magnetic behavior.

The para- and ferromagnetic contributions  $\Delta m_{rest}(T)$  after annealing show only a small temperature variation which is most pronounced above 300 K and thus well above the orbital ordering transition observed in the PCMO 0.1 films. This  $T$ -dependent deviation from a constant average magnetization is of the order of  $10^{-10}$  Am<sup>2</sup> and therefore much too small to affect the change in slope  $\chi_{PCMO}(T)$  at the orbital order transition. Thus, the assumption of a temperature independent offset  $\Delta m_S(H)$  after thin film growth is justified. It can be excluded that the change in the slope of the magnetic susceptibility  $\chi_{PCMO}(T)$  is caused by preparation-induced changes.

## V. Simulation of pump probe dynamics

Finite-Difference Time Domain (FDTD) simulations of a one dimensional three-temperature model [6] were carried out in order to interpret the pump-probe experiments. In this model, the PCMO film (100 nm) on a MgO substrate (1000 nm) is divided into three subsystems, conventionally associated with electrons, lattice and spins. To each subsystem, a temperature is assigned, which evolves in time and space according to a simple diffusion equation. Differential coupling terms  $\sim(T_i - T_j)$  assure equilibration of the subsystems.

Note that free electrons are likely not present in the PCMO film. We here include them, representing an energy reservoir which a) takes up the optically deposited energy, and b) rapidly (faster than a few picoseconds) equilibrates with the lattice. These simulations explore a counter argument to the explanations given in the main text, namely, the outcome from our pump-probe experiments on time scales above 10 ps, when only thermal diffusion inside the manganite and into the substrate are considered.

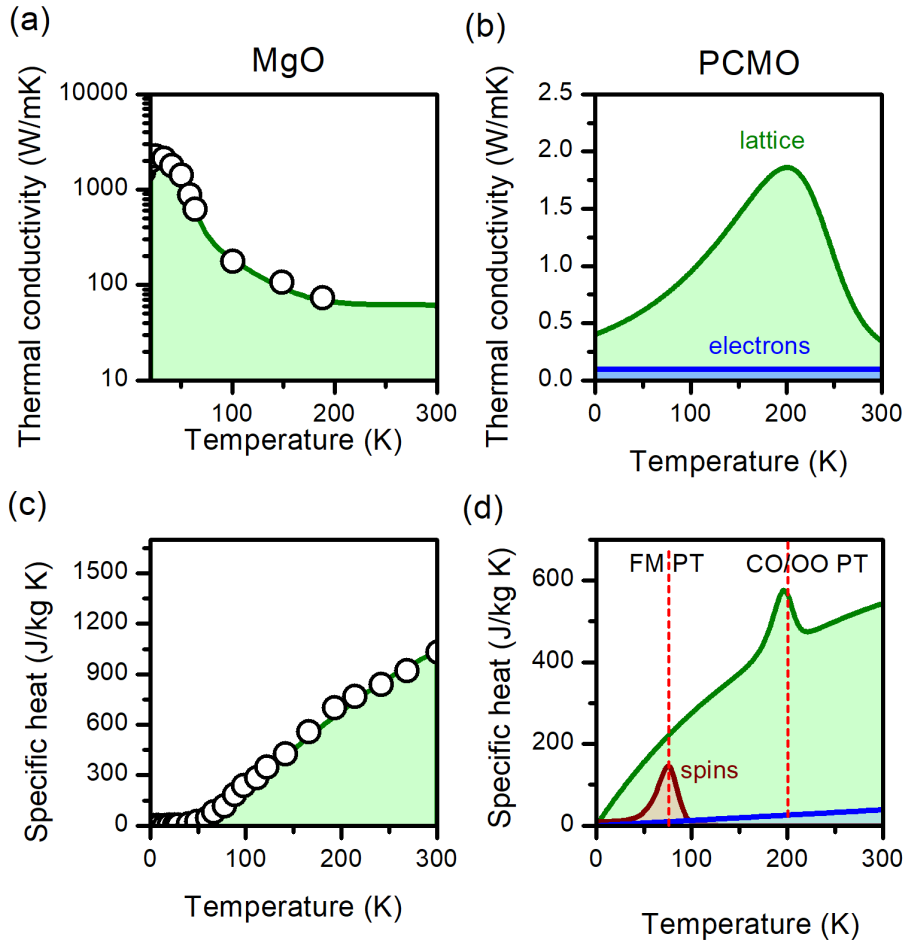


**FIG. S6:** Temperature dependencies of modelling parameters used for the FDTD simulation. (a) and (c) refer to MgO. The green curves interpolated between the experimental data points from [...] and [...] is used for simulation. For the non-magnetic insulator MgO only the lattice temperature is defined. (b) and (d) refer to PCMO, for which below the FM PT at 80 K three temperature reservoir (electrons, lattice, spin) are distinguished. The CO or OO PT at 200 K is modelled by a corresponding local maximum in the lattice specific heat.

When only thermal diffusion is considered, thermal relaxation is governed by the thermal conductivity and the specific heats of the manganite film and of the MgO substrate, including their temperature dependencies. Figure S6 shows these temperature dependencies entering the coupled diffusion equations. For MgO (see Fig. S5 (a) and (c)), tabulated data from literature were taken and interpolated [7] or the special PCMO  $x=0.1$  composition investigated in this work, such data do not yet exist. Therefore, the generic behavior of the thermal material properties (see Fig. S6 (b) and (d)) compatible with typical experimental findings obtained from different manganite films was assumed. [8,9] During the simulation, the parameters are adjusted in each time step to the local temperature. Note that, our FDTD model [6] was initially developed to describe pump-probe reflectivity experiments. In contrast, the experiments discussed in the main article are concerned with pump-probe transmission. The physical processes sampled by these two measurement schemes are nevertheless almost identical, in particular regarding transient thermal properties.

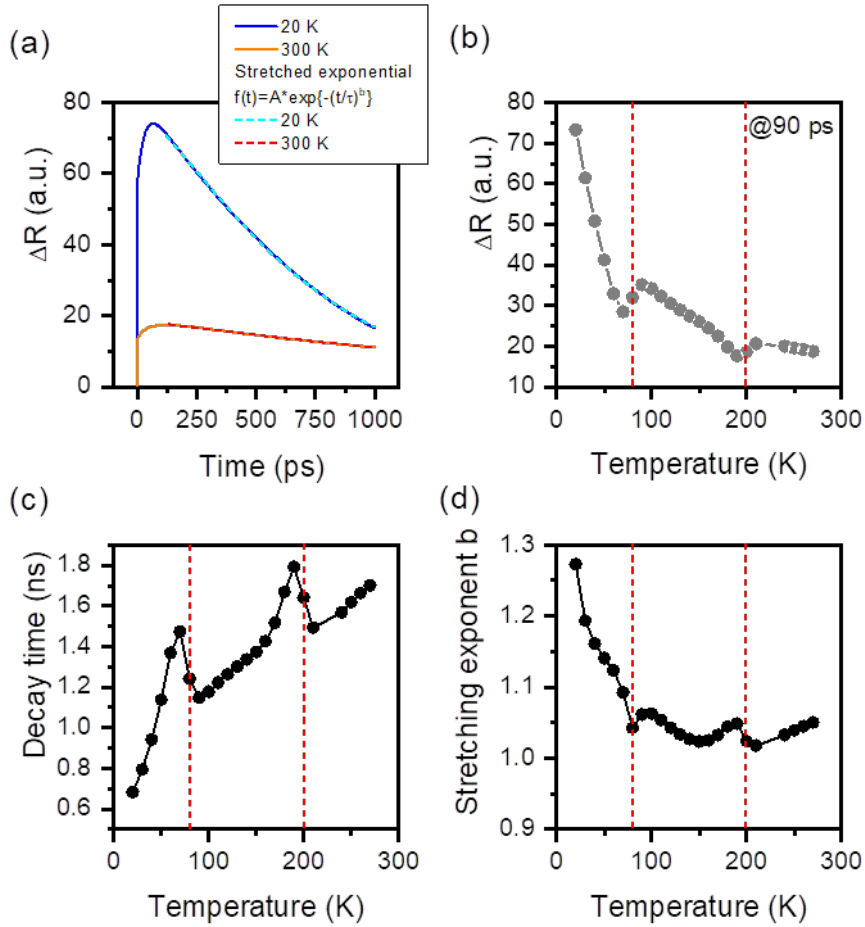


**FIG. S7:** Simulated pump probe reflectivity dynamics. (a) Emulated reflectivity signals  $\Delta R(t)$  for two different base temperatures as indicated (solid lines), overlaid a fit of a stretched exponential function (dashed line). (b) Temperature dependence of  $\Delta R(90 \text{ ps})$ . (c) and (d) depict the temperature dependence of the thermal decay time and of the stretching exponent  $b$ . Red vertical dashed lines indicate the phase transition temperatures.

Fig. S7 summarizes the results from the simulations. Typical reflectivity curves, emulated from simulations at base temperatures of 20 K and 300 K are shown in Fig. S7 (a). One can clearly see that, the relaxation towards equilibrium is much faster at low temperatures than at 300 K. Also, the maximum amplitudes are much larger, reflecting the much smaller specific heat of both the film and the substrate at low temperature. In Fig. S7 (b), the reflectivity signal 90 ps after the initial excitation is depicted as a function of the base temperature. Similar to the experimental findings, one sees an overall decrease of the reflectivity with increasing temperature. Around the phase transition temperature, anomalies appear, as explained in the main article.

Furthermore, the emulated reflectivity curves were fitted by a stretched exponential function  $f(t) \sim e^{-\left(\frac{t}{\tau}\right)^b}$ , yielding the temperature dependence of the decay time  $\tau$  and of the stretching parameter  $b$  shown in Fig S7 (c) and (d). Both show a monotonous behavior for temperatures away from phase transitions, and anomalies at the critical temperatures. Note that, quantitatively similar results can be obtained from an even simpler one-temperature model, because all subsystems are equilibrated anyway on the time scales of interest (100 ps to 1 ns). In such a one-temperature model, all contributions to the specific heat and the thermal conductivity are summed up.

In contrast to the real experiments, the simulations show an increase of the decay time from about 0.7 ns to 1.7 ns between 20 K and 300 K. We infer that, in particular at low temperatures, a long-living excitation is present in the experiments, whose live time exceeds the thermal decay time. A more realistic modelling of the manganite should incorporate this non-thermal process. Simply decreasing the electron-phonon and electron-spin coupling constant is not sufficient. Instead of electrons, a polaronic subsystem should be considered. The spatio-temporal diffusion of polarons and decay into phonons can maybe be described within the framework of a two-temperature model as derived for semiconductors.

## VI. Details on the theoretical simulation of the orbital ordering transition

### A. Heating and cooling protocol

The heating simulations started from the ground state described in the main text. The oxygen atoms received an initial random velocity distribution according to the target temperature of each simulation, followed by 2.4 ps of equilibration (24 thermostat cycles) with the thermostat at that temperature. Afterwards the Jahn-Teller structure factor was averaged for the next 12 ps. Starting from the 400 K heating simulation, the first set of cooling simulations reduced the target temperature of the thermostat to values between 20 K and 400 K. Again 2.4 ps of equilibration and 12 ps of averaging was used. A direct cooling from 400 K to low temperatures freezes the system in metastable states, as the cooling happens within one cycle of the thermostat of  $P_{TS}=100$  fs. Therefore, a second set of cooling simulations continued from the 200 K cooling calculations, again with the same equilibration and averaging times. The simulations recovered the initial orbital order of the ground state, although, in some cases, with the hole-polaron clusters distributed over several planes and thus with a slightly reduced order parameter. These more disordered metastable states are close in energy to the ground state, as explained in the main text. Heating simulations starting from such a metastable state led to the same transition temperature as the calculations shown in this paper.

### B. Orbital-order transition and Néel transition

In our simulation, the dominant *A*-type antiferromagnetic order breaks down simultaneously with the orbital order. In some simulation runs, we observe a small increase in the ferromagnetic moment during the transition. Above the orbital-order transition the system is paramagnetic. This is inconsistent with experiment where the Néel transition occurs at around 70 K and the system becomes paramagnetic around 80-130 K [2,10]. Both temperatures are substantially lower than in our simulations. This failure might originate from the adiabatic description of the spin dynamics in our simulation. In our current framework, we cannot yet verify whether the ferromagnetic moment is related to another magnetic phase transition.

## VII. Temperature dependent XRD studies: double-peak structure

The temperature dependence of the lattice parameters was deduced from the peak positions of the (200), (020) and (004) reflections. Fig. S8 shows the shift of these peaks with temperature for PCMO  $x=0$  ((a), (b), (c)). For comparison, the shift of (004) PCMO  $x=0.1$  peak is also shown (d).

For both compositions, the reflections reveal a double-peak shape, clearly visible in the shoulder-like feature of the (220) and (004) reflections ((c), (d)). For a coarse estimation of the volume fractions, the (004) reflections were fitted by two Gaussian peaks. Figure S8 shows such fits for the PCMO  $x=0.1$  data in two different temperature ranges (230 – 300 K and 83 – 150 K). The data points at different temperatures were normalized to position and maximum height of the (004) reflection. The Gaussian peaks are practically unaffected by the temperature range and the peak areas correspond to a volume fraction of about 10% of the right-handed peak.

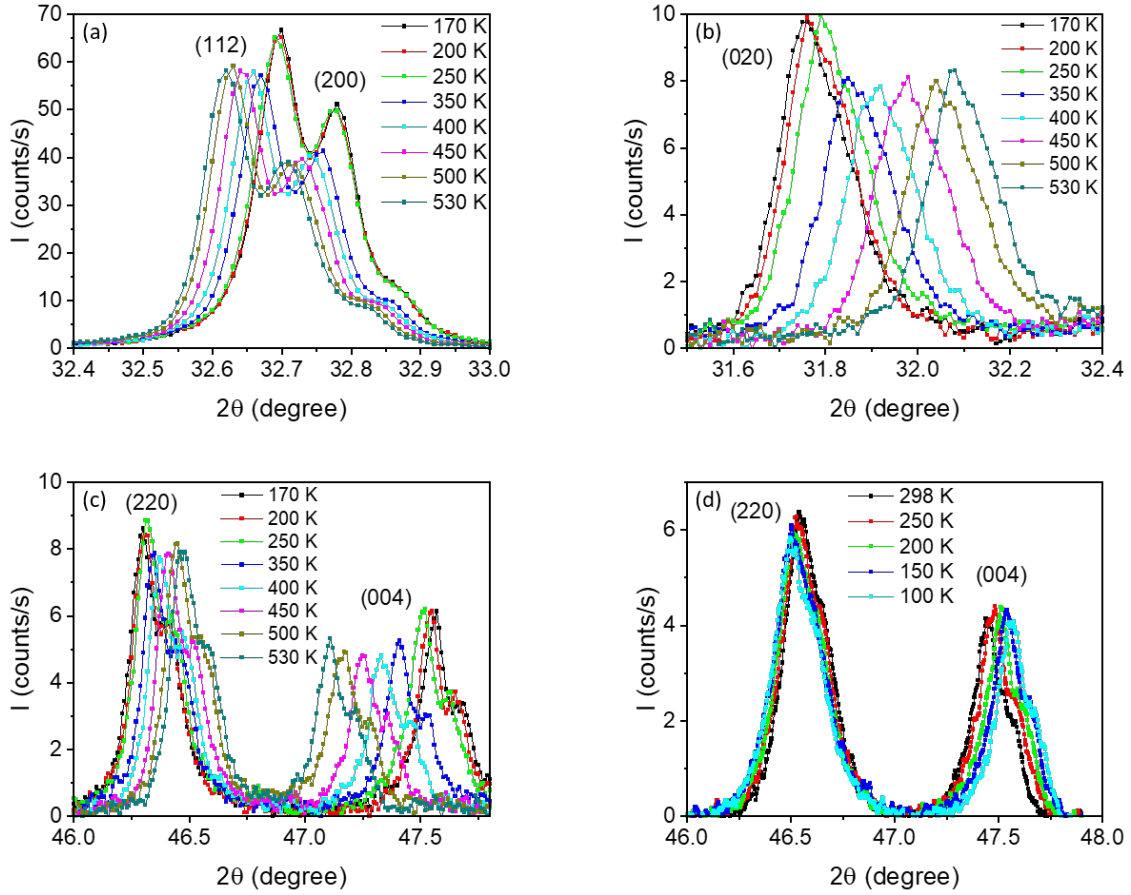


**FIG. S8:** (a), (b), (c) poly-crystalline PCMO  $x=0$  bulk sample: Temperature dependence of angular position and shape of (a) (200) reflection, (b) (020) reflection and (c) (004) reflection. d) PCMO  $x=0.1$  bulk sample, angular position and shape of (004) reflection.

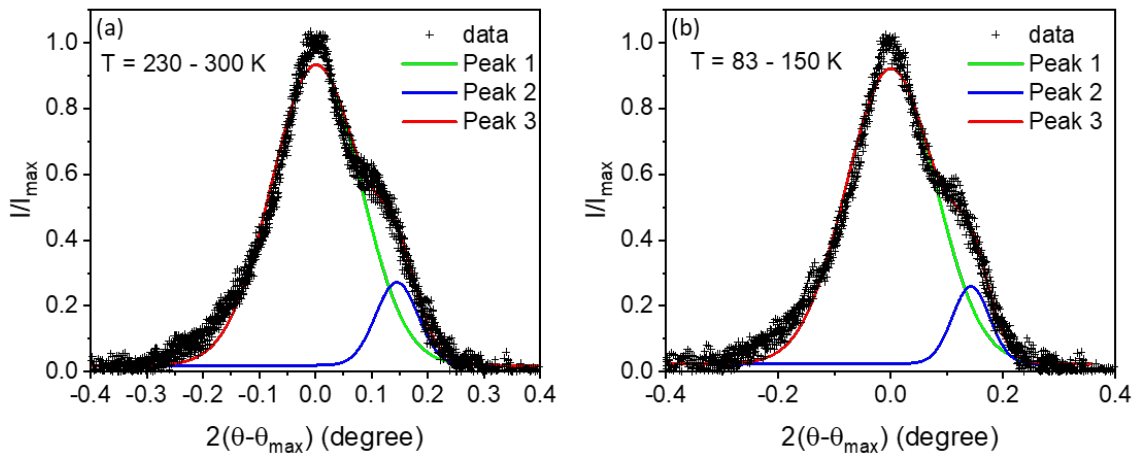


**FIG. S9:** (004) reflection PCMO  $x=0.1$  bulk sample. The experimental data points are normalized to angular position and maximum intensity of the reflections at the respective temperature. (a) Data points in the temperature range from 230 to 300 K. (b) Data points in the temperature range from 83 to 150 K. The solid green and blue lines correspond to fit with two gaussian distributions (peak 1 and 2). The red line is the sum of both peaks.



### VIII. Extraction of the octahedral rotation axis from Rietveld refined data

As Rietveld refined positions due to experimental noise do not necessarily satisfy the condition of ideal  $\text{MnO}_6$  octahedra, i.e. no distortion of the right angles, the rotation axis  $(n_1, n_2, n_3)$  resp. angle  $\theta$  are defined as minima of

$$(5) \quad \min_{n_1, n_2, n_3, \theta} \sum_{i=1}^6 \|d_i \cdot \mathbf{R}(n_1, n_2, n_3, \theta) \vec{e}_i - \vec{o}_i\|^2 \quad \text{subject to } n_1^2 + n_2^2 + n_3^2 = 1$$

Here,  $\vec{o}_i$  are the refined positions of the six oxygen atoms with respect to Mn,  $d_i$  the experimentally found bonding lengths, and  $\vec{e}_i$  unit vectors pointing to the position of the corresponding oxygen atom prior any rotation, i.e. along the Cartesian axes.  $\mathbf{R}(n_1, n_2, n_3, \theta)$  denotes a three-dimensional rotation matrix with rotation axis  $(n_1, n_2, n_3)$  and angle  $\theta$ . Noteworthy, the extracted values from [2,11] show little variations with doping and temperature justifying their fixation. In detail, solely  $n_2 = 0.78$  is fixed, as the same geometrical consideration of a corner-shared octahedral network with Pbnm symmetry leading to eq.s (7a)-(7c) in the main text yields the following condition:

$$(6) \quad 0 = (d_l + d_s) \cdot (n_3 n_2 (1 - \cos \theta) + n_1 \sin \theta) + (d_l - d_s) \cdot (n_3 n_1 (1 - \cos \theta) - n_2 \sin \theta)$$

Combined with the normalization condition of  $(n_1, n_2, n_3)$ , fixing  $n_2$  determines the rotation axis fully for given values  $(d_l, d_s, \theta)$ .

- [1] T. Meyer, B. Kressdorf, V. Roddatis, J. Hoffmann, C. Jooss, and M. Seibt, *Phase Transitions in a Perovskite Thin Film Studied by Environmental In-Situ Heating Nano-Beam Electron Diffraction*, (2020).
- [2] Z. Jirák, S. Krupička, Z. Šimša, M. Dlouhá, and S. Vratislav, *Neutron Diffraction Study of  $\text{Pr}_{1-x}\text{Ca}_x\text{MnO}_3$  Perovskites*, *J. Magn. Magn. Mater.* **53**, 153 (1985).
- [3] J. Hoffmann, P. Moschkau, S. Mildner, J. Norpoth, C. Jooss, L. Wu, and Y. Zhu, *Effects of Interaction and Disorder on Polarons in Colossal Resistance Manganite  $\text{Pr}_{0.68}\text{Ca}_{0.32}\text{MnO}_3$  Thin Films*, *Mater. Res. Express* **1**, (2015).
- [4] A. S. Hassanien and A. A. Akl, *Effect of Se Addition on Optical and Electrical Properties of Chalcogenide  $\text{CdSse}$  Thin Films*, *Superlattices Microstruct.* **89**, 153 (2016).
- [5] J. M. D. Coey, M. Venkatesan, and P. Stamenov, *Surface Magnetism of Strontium Titanate*, *J. Phys. Condens. Matter* **28**, (2016).
- [6] H. Ulrichs, D. Meyer, M. Müller, M. Mansurova, and F. Döring, *Numerical Calculation of Laser-Induced Thermal Diffusion and Elastic Dynamics*, *AIP Conf. Proc.* **1763**, (2016).
- [7] S. Adachi, *Magnesium Oxide (MgO) in Handbook on Physical Properties of Semiconductors* (Springer, Boston, MA, 2004).
- [8] P. Thiessen, V. Roddatis, F. Rieger, A. Belenchuk, M. Keunecke, V. Moshnyaga, and C. Jooss, *Effect of Charge Ordering on Crossplane Thermal Conductivity in Correlated Perovskite Oxide Superlattices*, *Phys. Rev. B* **98**, 1 (2018).
- [9] A. K. Raychaudhuri, A. Guha, I. Das, R. Rawat, and C. N. R. Rao, *Specific Heat of Single-Crystalline (Formula Presented) in the Presence of a Magnetic Field*, *Phys. Rev. B - Condens. Matter Mater. Phys.* **64**, 1 (2001).
- [10] J. Tikkanen, M. Geilhufe, M. Frontzek, W. Hergert, A. Ernst, P. Paturi, and L. Udby, *The Low-Temperature Magnetostructure and Magnetic Field Response of  $\text{Pr}_{0.9}\text{Ca}_{0.1}\text{MnO}_3$ : The Roles of Pr Spins and Magnetic Phase Separation*, *J. Phys. Condens. Matter* **28**, 36001 (2016).
- [11] D. Sánchez, J. A. Alonso, and M. J. Martínez-Lope, *Neutron-Diffraction Study of the Jahn-Teller Transition in  $\text{PrMnO}_3$* , *J. Chem. Soc. Dalton Trans.* 4422 (2002).

## **Appendix C**

### **Supplemental Material for Power Density and Spectral Photovoltaic Response in a Hot Polaron Solar Cell**

**Supplemental Information for:  
Power density and spectral photovoltaic response in a hot polaron solar cell**

*B. Kressdorf, J. Hoffmann, M. Seibt, C. Jooss*

**S1. Estimation of the generation rate**

As mentioned in the main text (eq. 7) the mean generation rate can be estimated from

$$(eq. S1.1) \quad G = \frac{1}{L} \int_{d-L}^d \int_{E_{min}}^{E_{max}} \frac{f}{E_{ph}} \alpha e^{-\alpha x} dE_{ph} dx$$

where  $f$  is the spectral power density distribution of the incident radiation,  $\alpha$  is the absorption coefficient,  $L$  is the diffusion length and  $d=100$  nm is the absorber layer thickness. Here, it is assumed that the absorption is governed by Lambert-Beer law and that only photons in the energy range  $E_{min}$  to  $E_{max}$  absorbed near the interface contribute to the photovoltaic effect.

To relate the incident power density  $p$  and the absorbed power density two approximations can be used:

- i) The temperature and spectral dependence of reflectance  $R$  and absorption coefficient  $\alpha$  can be neglected. We have used  $R=0.3$  and  $\alpha=6 \cdot 10^6/\text{m}$  [1].
- ii) The spectral power density distribution  $f$  is constant within the spectral range between  $E_{min}$  to  $E_{max}$ .

The fraction  $(1-a) \approx 0.4$  of absorbed power that corresponds to the spectral range between  $E_{min}$  to  $E_{max}$  was deduced from intensities passing different cut-of filters.

$$(eq. S1.2) \quad f = \frac{(1-a)p}{E_{max}-E_{min}}$$

Since the diffusion length  $L$  is small compared to absorber thickness  $d$ , the integration finally yields

$$(eq. S1.3) \quad G = \frac{(1-a)(1-R)}{E_{max}-E_{min}} \ln\left(\frac{E_{max}}{E_{min}}\right) \alpha e^{-\alpha d} p \approx 3.9 \cdot 10^{27} \left(\frac{p}{\text{kWm}^2}\right) \text{m}^{-3} \text{s}^{-1}$$

**S2. Estimation of charge carrier mobility**

The charge carriers in PCMO ( $x=0.1$ ) are small polarons. Within the adiabatic model the temperature dependence of the resistivity is given by [2]

$$(eq. S2.1) \quad \rho(T) = \rho_0 T e^{\frac{E_A}{kT}}$$

where  $E_A$  is the activation barrier of thermally activated hopping steps and  $k$  is the Boltzmann constant.

The mobility  $\mu$  of these hole polarons can be calculated from the resistivity and the charge carrier density  $n_{dop}$  that is given by the Ca doping level:  $n_{dop} \approx 1.9 \cdot 10^{27} \text{m}^{-3}$ .

$$(eq. S2.2) \quad \mu(T) = \frac{1}{e \rho(T) n_{dop}}$$

Figure S2 shows the temperature dependence of mobility calculated from experimental resistivity data in [1].

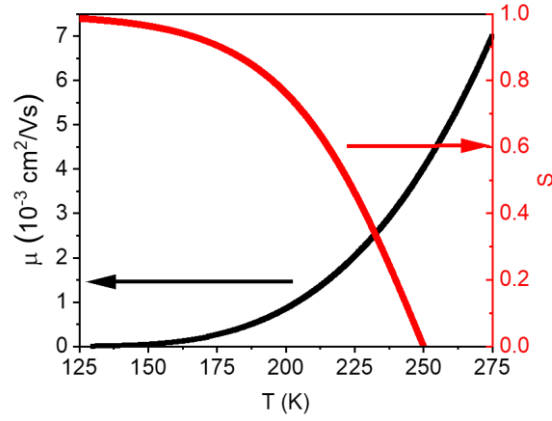


Fig. S2: Temperature dependence of mobility (black symbols) and Landau (orbital) order parameter (red line). The latter was calculated for an ordering temperature  $T_{OO}=250$  K and a transition width  $\Delta_{OO}=50$  K.

For comparison, the temperature dependence of a Landau order parameter  $S$

$$(eq. S2.3) \quad S(T) = -\tanh\left(\frac{T-T_{OO}}{\Delta_{OO}}\right)$$

is included in Fig. S2 (see also [1]). Here,  $T_{OO}$  is the orbital ordering temperature and  $\Delta_{OO}$  is the transition width.

### S3. Determination of $T^*$ through temperature dependent $U_{oc}$

We determine the crossover temperature  $T^*$  -the onset of photovoltaic response- for the experimental data of  $U_{oc}(T)$  through the change in slope  $dU_{oc}/dT$  behavior as follows.

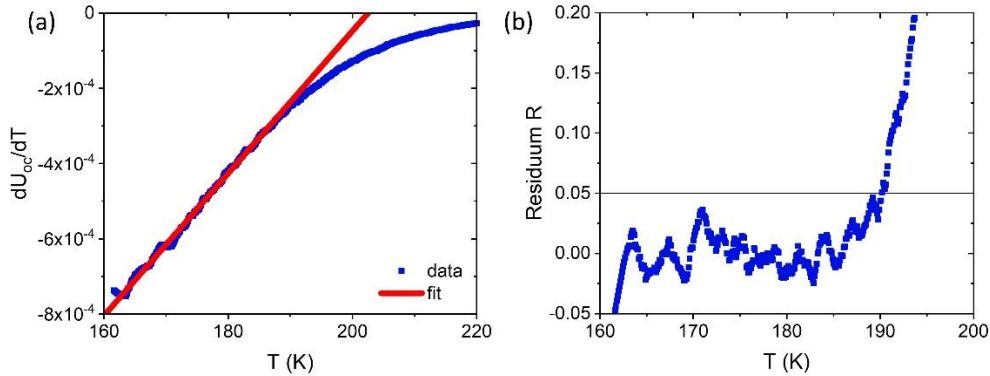


Fig. S3: Exemplary determination of  $T^*$  from  $U_{oc}(T)$  experimental data  $E_{max}=2$  eV and  $p=16$  kW/cm<sup>2</sup>: (a) first derivative of  $U_{oc}(T)$  with a linear low temperature fit and (b) residuum  $R$

In Figure S3 the different analysis steps are shown exemplary for cut-off filter data set of  $E_{max}=2$  eV and highest incident power density of  $p=16$  kW/cm<sup>2</sup>. As a first step we calculate the first derivative for  $U_{oc}(T)$  (Fig. S3(a)). For all data sets a region of linear increase of  $dU_{oc}/dT$  at lower temperatures and a significant change of the slope at higher temperatures is observed. Additional features at even further decreased temperatures can be found. Note that we do not obtain a constant slope at lower temperatures, therefore the dependence of the open-circuit voltage on the temperatures is not linear but a more complicated dependence.

As a second step we perform a linear fit in the regime at low temperatures. The Residuum  $R$  between experimental data and fit is shown in Figure S3(b), where a clear turning point in slope behavior can be seen. Finally, we define  $T^*$  as the temperature value, where 5% change in slope

is achieved. The 5% change in slope is chosen since this value exceeds the error bars of the linear fit.

#### S4: Power density dependence of $J_{sc}$ and $U_{oc}$ at different $T$ and cut-off filters

In the main text, we have focused our analysis of the power dependent data on a fixed temperature of  $T=150$  K and a cut-off filter of  $E_{max} = 2.0$  eV showing that the power dependence of  $J_{sc}$  and  $U_{oc}$  changes at a critical power density  $p_c$ . Here, we present data for additional temperatures and cut-off filter settings.

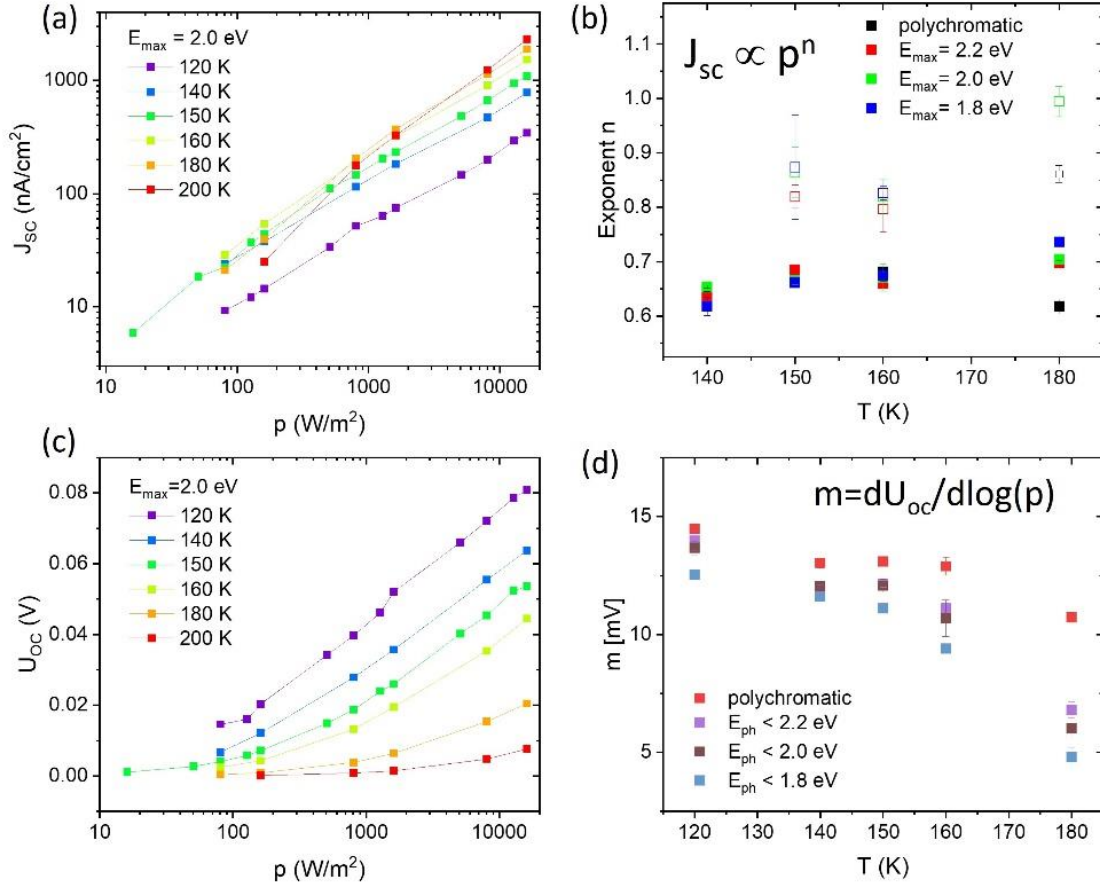


Fig. S4: Power density dependence for different temperatures and cut-off filter settings. (a) Change of  $J_{sc}(p)$  with temperature for  $E_{max} = 2.0$  eV and (b) exponent  $n$  of power law dependence  $J_{sc} \propto p^n$  at different temperatures and filter settings. Open symbols correspond to the low-power and solid symbols to the high-power regime. (c) Change of  $U_{oc}(p)$  with temperature for  $E_{max} = 2.0$  eV. (d) Change of slope  $m = dU_{oc}/d\log(p)$  with temperature and filter setting.

Figure S4 (a) and (c) shows power density dependence of  $U_{oc}$  and  $J_{sc}$  for  $E_{max} = 2.0$  eV in 20 K steps for a temperature range of 120 to 200 K. The temperature dependence is in accordance with results discussed in chapter 3 of the main text i.e.  $J_{sc}$  decreases with decreasing  $T$  as  $U_{oc}$  increases. Note that the crossover between the two power density regimes (see Fig. 4, main text), i.e., the critical power density  $p_c$ , increases to higher power densities for increased temperatures.

As shown in the main text for  $T=150$  K and  $E_{max}=2$  eV, the short-circuit current density exhibits power law dependence on power density, i.e.,  $J_{sc} \propto p^n$  with exponent  $n$  that changes from  $n \approx 1$  to  $n \approx 0.64$  at the critical power density. Although the number of data points is smaller and,

therefore, the accuracy of fits is greatly reduced, similar exponents  $n$  are observed at other temperatures and other filter settings (Fig. S4(b)).

In the high-power regime the open-circuit voltage increases with power according to  $U_{oc} \propto \ln(p)$ . This dependence is observed in a broad temperature range (Fig. S4(c)) but with a slope  $dU_{oc}/d\log(p)$  that dependent on temperature and filter setting (Fig. S4(d)).

### S5: Photon energy dependence of $Q_{IQE}$ and $U_{oc}$ at different T (125 K, 200 K)

Analog to the irradiance dependent measurements, the main text shown the experimental photon energy dependent data for fixed temperature of 150 K.

Fig. S4 shows additional experimental results for the photon energy dependence of  $Q_{IQE}$  and  $U_{oc}$  at two additional temperatures of 125 K and 200 K. The general slope behavior of the decrease of  $Q_{IQE}$  and  $U_{oc}$  with decreasing photon energy does not change with temperature. But the absolute values change in accordance with the temperature dependence of  $J_{sc}$  and  $U_{oc}$  as discussed in the main text in chapter 3. A decrease of temperature from 200 K to 150 K leads to an increase of  $U_{oc}$  at fixed photon energy of 3 eV of 0.68 mV to 17 mV by 2 orders of magnitude. The current  $J_{sc}$  increases from 0.14  $\mu\text{A}/\text{cm}^2$  to 3.2  $\mu\text{A}/\text{cm}^2$  by one order of magnitude.

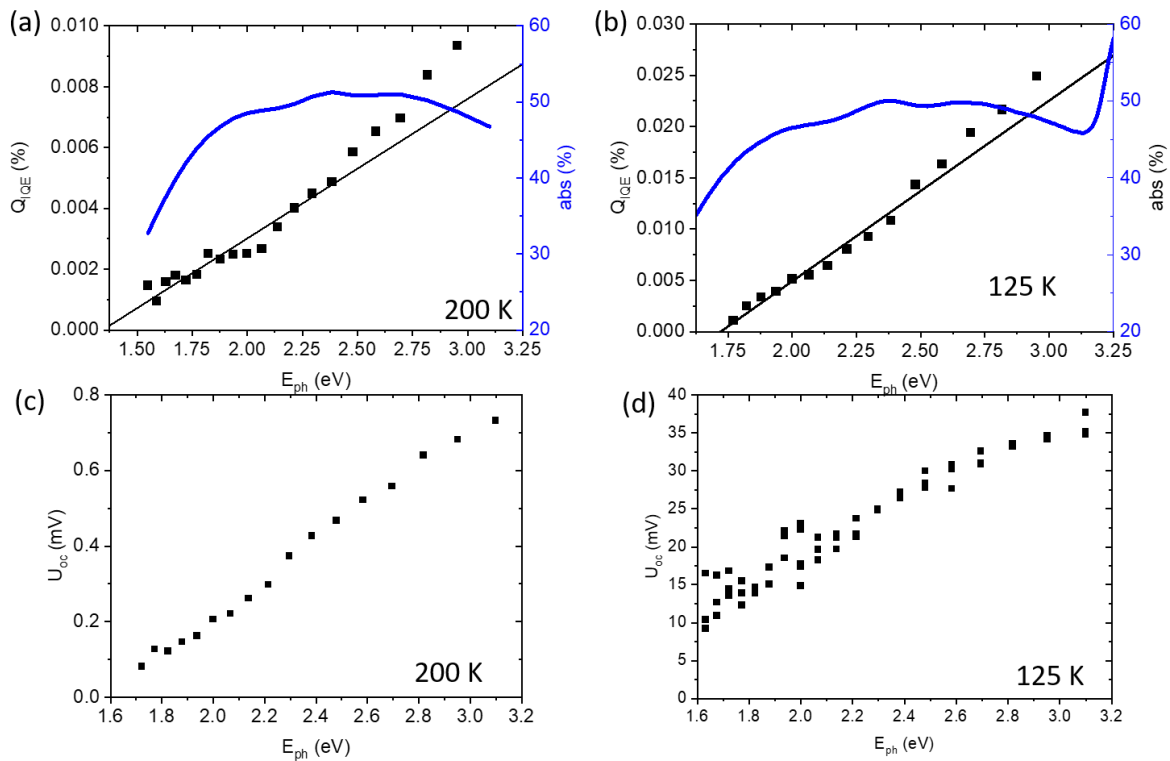


Fig. S5: Photon dependent  $Q_{IQE}$  and  $U_{oc}$  for  $T=200$  K (a)+(c) and  $T=125$  K for (b)+(d)

### References:

- [1] B. Kressdorf, T. Meyer, M. ten Brink, C. Seick, S. Melles, N. Ottinger, T. Titze, H. Meer, A. Weisser, J. Hoffmann, S. Mathias, H. Ulrichs, D. Steil, M. Seibt, P.E. Blöchl, and C. Jooss, Phys. Rev. B 103, 235122 (2021)
- [2] V.V. Bryksin and H. Böttger, Hopping Conduction in Solids, 1st ed. (Weinheim, 1985)



## Bibliography

- [1] E. Becquerel, Comptes Rendus **9** (1839).
- [2] C. E. Fritts, American Journal of Science **s3-26**, 465 (1883).
- [3] D. M. Chapin, C. S. Fuller, and G. L. Pearson, Journal of Applied Physics **25**, 676 (1954).
- [4] A. J. Nozik and J. Miller, Chemical Reviews **110**, 6443 (2010).
- [5] P. B. H. Bahar, IEA (2020) <https://www.iea.org/reports/tracking-solar-pv-2020> (accessed 26/12/2021) (2020).
- [6] M. A. Green, Progress in Photovoltaics: Research and Applications **9**, 123 (2001).
- [7] A. Shah, P. Torres, R. Tscharnner, N. Wyrsh, and H. Keppner, Science **285**, 692 (1999).
- [8] W. H. Bloss, F. Pfisterer, M. Schubert, and T. Walter, Progress in Photovoltaics: Research and Applications **3**, 3 (1995).
- [9] M. A. Green, Physica E: Low-dimensional Systems and Nanostructures **14**, 65 (2002).
- [10] B. G. Akinoglu, B. Tuncel, and V. Badescu, Sustainable Energy Technologies and Assessments **46**, 101287 (2021).
- [11] T. Kirchartz and U. Rau, Advanced Energy Materials **8**, 1703385 (2018).
- [12] R. T. Ross and A. J. Nozik, Journal of Applied Physics **53**, 3813 (1982).
- [13] Y. Takeda, T. Motohiro, D. König, P. Aliberti, Y. Feng, S. Shrestha, and G. J. Conibeer, Applied Physics Express **3**, 104301 (2010).
- [14] B. K. Ridley, Journal of Physics C: Solid State Physics **15**, 5899 (1982).
- [15] J. Shah and R. C. C. Leite, Physical Review Letters **22**, 1304 (1969).



- [16] A. Le Bris and J.-F. Guillemoles, *Applied Physics Letters* **97**, 113506 (2010).
- [17] Y. Feng, R. Patterson, S. Lin, S. Shrestha, S. Huang, M. Green, and G. J. Conibeer, *Applied Physics Letters* **102**, 243901 (2013).
- [18] L. C. Hirst and N. J. Ekins-Daukes, *Progress in Photovoltaics: Research and Applications* **19**, 286 (2011).
- [19] C. Nelson, N. R. Monahan, and X.-Y. Zhu, *Energy and Environmental Science* **6**, 3508 (2013).
- [20] W. Shockley and H. J. Queisser, *Journal of Applied Physics* **32**, 510 (1961).
- [21] G. J. Conibeer, *Materials Today* **10**, 42 (2007).
- [22] T. Takamoto, M. Kaneiwa, M. Imaizumi, and M. Yamaguchi, *Progress in Photovoltaics: Research and Applications* **13**, 495 (2005).
- [23] R. R. King, D. C. Law, K. M. Edmondson, C. M. Fetzer, G. S. Kinsey, H. Yoon, R. A. Sherif, and N. H. Karam, *Applied Physics Letters* **90**, 183516 (2007).
- [24] T. Nozawa and Y. Arakawa, *Applied Physics Letters* **98**, 171108 (2011).
- [25] T. S. Navruz and M. Saritas, *Solar Energy Materials and Solar Cells* **92**, 273 (2008).
- [26] A. S. Brown and M. A. Green, *Journal of Applied Physics* **94**, 6150 (2003).
- [27] V. I. Klimov, *Applied Physics Letters* **89**, 123118 (2006).
- [28] M. C. Hanna and A. J. Nozik, *Journal of Applied Physics* **100**, 074510 (2006).
- [29] A. J. Nozik, *Physica E Low-dimensional Systems and Nanostructures* **14**, 115 (2002).
- [30] T. Trupke, M. A. Green, and P. Würfel, *Journal of Applied Physics* **92**, 1668 (2002).
- [31] T. Trupke, M. A. Green, and P. Würfel, *Journal of Applied Physics* **92**, 4117 (2002).
- [32] S. Kahmann and M. A. Loi, *Journal of Materials Chemistry C* **7**, 2471 (2019).
- [33] I. Ahmed, L. Shi, H. Pasanen, P. Vivo, P. Maity, M. Hatamvand, and Y. Zhan, *Light: Science & Applications* **10**, 174 (2021).
- [34] S. S. Prabhu and A. S. Vengurlekar, *Physical Review B* **53**, 7815 (1996).

- [35] C. K. Choi, Y. H. Kwon, J. S. Krasinski, G. H. Park, G. Setlur, J. J. Song, and Y. C. Chang, *Physical Review B* **63**, 115315 (2001).
- [36] J. M. Richter, F. Branchi, F. Valduga de Almeida Camargo, B. Zhao, R. H. Friend, G. Cerullo, and F. Deschler, *Nature Communications* **8**, 376 (2017).
- [37] G. Conibeer, D. König, M. Green, and J. Guillemoles, *Thin Solid Films* **516**, 6948 (2008).
- [38] G. J. Conibeer, S. Shrestha, S. Huang, R. Patterson, H. Xia, Y. Feng, P. Zhang, N. Gupta, M. Tayebjee, S. Smyth, Y. Liao, S. Lin, P. Wang, X. Dai, and S. Chung, *Solar Energy Materials and Solar Cells* **135**, 124 (2015).
- [39] P. G. Klemens, *Physical Review* **148**, 845 (1966).
- [40] M. Neges, K. Schwarzburg, and F. Willig, *Solar Energy Materials and Solar Cells* **90**, 2107 (2006).
- [41] F. Chen, A. N. Cartwright, H. Lu, and W. J. Schaff, *Applied Physics Letters* **83**, 4984 (2003).
- [42] W. S. Pelouch, R. J. Ellingson, P. E. Powers, C. L. Tang, D. M. Szmyd, and A. J. Nozik, *Physical Review B* **45**, 1450 (1992).
- [43] Y. Rosenwaks, M. C. Hanna, D. H. Levi, D. M. Szmyd, R. K. Ahrenkiel, and A. J. Nozik, *Physical Review B* **48**, 14675 (1993).
- [44] H. Yu, S. Lycett, C. Roberts, and R. Murray, *Applied Physics Letters* **69**, 4087 (1996).
- [45] F. Adler, M. Geiger, A. Bauknecht, D. Haase, P. Ernst, A. Dörnen, F. Scholz, and H. Schweizer, *Journal of Applied Physics* **83**, 1631 (1998).
- [46] P. Würfel, *Solar Energy Materials and Solar Cells* **46**, 43 (1997).
- [47] T. E. Humphrey, R. Newbury, R. P. Taylor, and H. Linke, *Physical Review Letters* **89**, 116801 (2002).
- [48] M. O'Dwyer, T. Humphrey, R. Lewis, and C. Zhang, *Microelectronics Journal* **39**, 656 (2008).

- [49] J. A. R. Dimmock, M. Kauer, J. Wu, H. Liu, P. N. Stavrinou, and N. J. Ekins-Daukes, *Semiconductor Science and Technology* **34**, 064001 (2019).
- [50] M. Li, J. Fu, Q. Xu, and T. C. Sum, *Advanced Materials* **31**, 1802486 (2019).
- [51] P. Roy, N. Kumar Sinha, S. Tiwari, and A. Khare, *Solar Energy* **198**, 665 (2020).
- [52] J. Jeong, M. Kim, J. Seo, H. Lu, P. Ahlawat, A. Mishra, Y. Yang, M. A. Hope, F. T. Eickemeyer, M. Kim, Y. J. Yoon, I. W. Choi, B. P. Darwich, S. J. Choi, Y. Jo, J. H. Lee, B. Walker, S. M. Zakeeruddin, L. Emsley, U. Rothlisberger, A. Hagfeldt, D. Kim, M. Grätzel, and J. Y. Kim, *Nature* **592**, 381 (2021).
- [53] J.-P. Correa-Baena, M. Saliba, T. Buonassisi, M. Graetzel, A. Abate, W. Tress, and A. Hagfeldt, *Science* **358**, 739 (2017).
- [54] S. D. Stranks, G. E. Eperon, G. Grancini, C. Menelaou, M. J. P. Alcocer, T. Leijtens, L. M. Herz, A. Petrozza, and H. J. Snaith, *Science* **342**, 341 (2013).
- [55] J. Ball, S. D. Stranks, M. T. Hörantner, S. Hüttner, W. Zhang, E. J. W. Crossland, I. Ramirez, M. Riede, M. B. Johnston, R. H. Friend, and H. J. Snaith, *Energy and Environmental Science* **8**, 602 (2015).
- [56] M. Saliba, J.-P. Correa-Baena, M. Grätzel, A. Hagfeldt, and A. Abate, *Angewandte Chemie International Edition* **57**, 2554 (2018).
- [57] A. K. Jena, A. Kulkarni, and T. Miyasaka, *Chemical Reviews* **119**, 3036 (2019).
- [58] C. Müller, T. Glaser, M. Plogmeyer, M. Sendner, S. Döring, A. A. Bakulin, C. Brzuska, R. Scheer, M. S. Pshenichnikov, W. Kowalsky, A. Pucci, and R. Lovrinčić, *Chemistry of Materials* **27**, 7835 (2015).
- [59] D. Cortecchia, H. A. Dewi, J. Yin, A. Bruno, S. Chen, T. Baikie, P. P. Boix, M. Grätzel, S. Mhaisalkar, C. Soci, and N. Mathews, *Inorganic Chemistry* **55**, 1044 (2016).
- [60] M. Lyu, J. H. Yun, M. Cai, Y. Jiao, P. V. Bernhardt, M. Zhang, Q. Wang, A. Du, H. Wang, G. Liu, and L. Wang, *Nano Research* **9**, 692 (2016).
- [61] M. B. Price, J. Butkus, T. Jellicoe, A. Sadhanala, A. Briane, J. E. Halpert, K. Broch, J. M. Hodgkiss, R. H. Friend, and F. Deschler, *Nature Communications* **6**, 8420 (2015).

- 
- [62] G. Xing, N. Mathews, S. Sun, S. Lim, Y. M. Lam, M. Grätzel, S. Mhaisalkar, and T. C. Sum, *Science* **342**, 344 (2013).
- [63] O. Flender, J. R. Klein, T. Lenzer, and K. Oum, *Physical Chemistry Chemical Physics* **17**, 19238 (2015).
- [64] H. H. Fang, S. Adjokatse, S. Shao, J. Even, and M. A. Loi, *Nature Communications* **9**, 243 (2018).
- [65] X. Deng, X. Wen, S. Huang, R. Sheng, T. Harada, T. W. Kee, M. Green, and A. Ho-Baillie, *Journal of Physical Chemistry C* **120**, 2542 (2016).
- [66] S. Nah, B. M. Spokoyny, C. M. M. Soe, C. C. Stoumpos, M. G. Kanatzidis, and E. Harel, *Nano Letters* **18**, 1044 (2018).
- [67] Y. Yang, D. P. Ostrowski, R. M. France, K. Zhu, J. van de Lagemaat, J. M. Luther, and M. C. Beard, *Nature Photonics* **10**, 53 (2016).
- [68] H. Shi, X. Zhang, X. Sun, and X. Zhang, *Applied Physics Letters* **116**, 151902 (2020).
- [69] A. Gold-Parker, P. M. Gehring, J. M. Skelton, I. C. Smith, D. Parshall, J. M. Frost, H. I. Karunadasa, A. Walsh, and M. F. Toney, *Proceedings of the National Academy of Sciences* **115**, 11905 (2018).
- [70] J. M. Frost, L. D. Whalley, and A. Walsh, *ACS Energy Letters* **2**, 2647 (2017).
- [71] N. Lu, L. Li, D. Geng, and M. Liu, *Organic Electronics* **61**, 223 (2018).
- [72] D. Niesner, H. Zhu, K. Miyata, P. P. Joshi, T. J. S. Evans, B. J. Kudisch, M. T. Trinh, M. Marks, and X.-Y. Zhu, *Journal of the American Chemical Society* **138**, 15717 (2016).
- [73] J. Yang, X. Wen, H. Xia, R. Sheng, Q. Ma, J. Kim, P. Tapping, T. Harada, T. Kee, F. Huang, Y. B. Cheng, M. Green, A. Ho-Baillie, S. Huang, S. Shrestha, R. Patterson, and G. J. Conibeer, *Nature Communications* **8**, 14120 (2017).
- [74] J. Fu, Q. Xu, G. Han, B. Wu, C. H. A. Huan, M. L. Leek, and T. C. Sum, *Nature Communications* **8**, 1300 (2017).

- [75] M. Li, S. Bhaumik, T. W. Goh, M. S. Kumar, N. Yantara, M. Grätzel, S. Mhaisalkar, N. Mathews, and T. C. Sum, *Nature Communications* **8**, 14350 (2017).
- [76] S. Mildner, J. Hoffmann, P. E. Blöchl, S. Techert, and C. Jooss, *Physical Review B* **92**, 035145 (2015).
- [77] G. Saucke, J. Norpoth, C. Jooss, D. Su, and Y. Zhu, *Physical Review B* **85**, 165315 (2012).
- [78] M. Sotoudeh, S. Rajpurohit, P. Blöchl, D. Mierwaldt, J. Norpoth, V. Roddatis, S. Mildner, B. Kressdorf, B. Iffland, and C. Jooss, *Physical Review B* **95**, 235150 (2017).
- [79] D. Raiser, S. Mildner, B. Iffland, M. Sotoudeh, P. Blöchl, S. Techert, and C. Jooss, *Advanced Energy Materials* **7**, 1602174 (2017).
- [80] A. Sharma, M. Chauhan, V. Bharti, M. Kumar, S. Chand, B. Tripathi, and J. P. Tiwari, *Physical Chemistry Chemical Physics* **19**, 26169 (2017).
- [81] J. R. Sun, B. G. Shen, Z. G. Sheng, and Y. P. Sun, *Applied Physics Letters* **85**, 3375 (2004).
- [82] G. Li, D. B. Huang, S. W. Jin, Y. Q. Ma, and X. G. Li, *Solid State Communications* **150**, 1737 (2010).
- [83] A. Sawa, T. Fujii, M. Kawasaki, and Y. Tokura, *Applied Physics Letters* **86**, 112508 (2005).
- [84] T. Susaki, N. Nakagawa, and H. Y. Hwang, *Physical Review B* **75**, 104409 (2007).
- [85] X.-Y. Li, L. Zhao, X.-Y. Wei, H. Li, and K.-X. Jin, *Chinese Physics B* **27**, 117501 (2018).
- [86] B. Iffland, J. Hoffmann, B. Kressdorf, V. Roddatis, M. Seibt, and C. Jooss, *New Journal of Physics* **19**, 063046 (2017).
- [87] S. Hoffmann-Urlaub, U. Ross, J. Hoffmann, A. Belenchuk, O. Shapoval, V. Roddatis, Q. Ma, B. Kressdorf, V. Moshnyaga, and C. Jooss, *Advanced Materials Interfaces* **8**, 2002049 (2021).

- 
- [88] B. Kressdorf, T. Meyer, A. Belenchuk, O. Shapoval, M. ten Brink, S. Melles, U. Ross, J. Hoffmann, V. Moshnyaga, M. Seibt, P. Blöchl, and C. Jooss, *Physical Review Applied* **14**, 054006 (2020).
- [89] Z. Jiráček, S. Krupička, Z. Šimša, M. Dlouhá, and S. Vratislav, *Journal of Magnetism and Magnetic Materials* **53**, 153 (1985).
- [90] M. Planck, *Annalen der Physik* **309**, 553 (1901).
- [91] N.-P. Harder and P. Würfel, *Semiconductor Science and Technology* **18**, S151 (2003).
- [92] P. Würfel, *Journal of Physics C: Solid State Physics* **15**, 3967 (1982).
- [93] M. I. Hossain, W. Qarony, S. Ma, L. Zeng, D. Knipp, and Y. H. Tsang, *Nano-Micro Letters* **11**, 58 (2019).
- [94] R. A. Sinton and R. M. Swanson, *IEEE Trans. Electron Devices* **34**, 1380 (1987).
- [95] A. W. Bett, F. Dimroth, R. Lockenhoff, E. Oliva, and J. Schubert, in *2008 33rd IEEE Photovoltaic Specialists Conference (IEEE, 2008)* pp. 1–5.
- [96] S. Liu, X. H. Zhao, C. M. Campbell, M. B. Lassise, Y. Zhao, and Y. H. Zhang, *Applied Physics Letters* **107**, 2 (2015).
- [97] S. Ruehle, *Solar Energy* **130**, 139 (2016).
- [98] U. Rau, B. Blank, and T. Kirchartz, *2017 IEEE 44th Photovoltaic Specialist Conference, PVSC 2017*, 1 (2017).
- [99] T. Kirchartz, J. Mattheis, and U. Rau, *Physical Review B - Condensed Matter and Materials Physics* **78**, 1 (2008).
- [100] S. N. Agbo, T. Merdzhanova, U. Rau, and O. Astakhov, *Solar Energy Materials and Solar Cells* **159**, 427 (2017).
- [101] F. H. Alharbi and S. Kais, *Renewable and Sustainable Energy Reviews* **43**, 1073 (2015).
- [102] P. T. Landsberg and G. Tonge, *Journal of Applied Physics* **51**, R1 (1980).
- [103] T. Markvart, *Physica Status Solidi (A) Applications and Materials Science* **205**, 2752 (2008).

- [104] T. Markvart, *IEEE Journal of Photovoltaics* **9**, 1614 (2019).
- [105] T. Meyer, PhD Thesis: Structural and Electronic Investigation of Strongly Correlated Transition Metal Oxide Perovskite Thin Films and Interfaces using In-situ Transmission Electron Microscopy (2020).
- [106] B. Kressdorf, T. Meyer, M. Ten Brink, C. Seick, S. Melles, N. Ottinger, T. Titze, H. Meer, A. Weisser, J. Hoffmann, S. Mathias, H. Ulrichs, D. Steil, M. Seibt, P. E. Blöchl, and C. Jooss, *Physical Review B* **103**, 1 (2021).
- [107] A. M. Glazer, *Acta Crystallographica Section B* **28**, 3384 (1972).
- [108] J. B. Goodenough, *Physical Review* **100**, 564 (1955).
- [109] H. A. Jahn and E. Teller, *Proc. R. Soc. Lond.* **A161**, 220 (1937).
- [110] C. C. Wang and L. W. Zhang, *New Journal of Physics* **9**, 0 (2007).
- [111] L. Wu, R. F. Klie, Y. Zhu, and C. Jooss, *Physical Review B* **76**, 174210 (2007).
- [112] P. W. Anderson, *Physical Review* **79**, 350 (1950).
- [113] J. Kanamori, *Journal of Physics and Chemistry of Solids* **10**, 87 (1959).
- [114] A. J. Millis, P. B. Littlewood, and B. I. Shraiman, *Physical Review Letters* **74**, 5144 (1995).
- [115] J. Hoffmann, P. Moschkau, S. Mildner, J. Norpoth, C. Jooss, L. Wu, and Y. Zhu, *Materials Research Express* **1**, 046403 (2014).
- [116] C. Jooss, L. Wu, T. Beetz, R. F. Klie, M. Beleggia, M. A. Schofield, S. Schramm, J. Hoffmann, and Y. Zhu, *Proceedings of the National Academy of Sciences of the United States of America* **104**, 13597 (2007).
- [117] R. Mathieu, J. P. He, X. Z. Yu, Y. Kaneko, M. Uchida, Y. S. Lee, T. Arima, A. Asamitsu, and Y. Tokura, *Europhysics Letters (EPL)* **80**, 37001 (2007).
- [118] M. Ibarra, R. Retoux, M. Hervieu, C. Autret, A. Maignan, C. Martin, and B. Raveau, *Journal of Solid State Chemistry* **170**, 361 (2003).
- [119] K. Kalantar-zadeh, J. Z. Ou, T. Daeneke, A. Mitchell, T. Sasaki, and M. S. Fuhrer, *Applied Materials Today* **5**, 73 (2016).

- 
- [120] T. Nachtrab, S. Heim, M. Moeßle, R. Kleiner, O. Waldmann, R. Koch, P. Mueller, T. Kimura, and Y. Tokura, *Journal of Applied Physics* **91**, 7520 (2002).
- [121] T.-H. Kim, M. Angst, B. Hu, R. Jin, X. G. Zhang, J. F. Wendelken, E. W. Plummer, and A.-P. Li, *Proceedings of the National Academy of Sciences* **107**, 5272 (2010).
- [122] J. Kim, J. Huang, J.-S. Zhou, J. B. Goodenough, H. Zheng, J. F. Mitchell, and A. de Lozanne, *Physical Review Letters* **110**, 217203 (2013).
- [123] Z. He, H. Tian, G. Deng, Q. Xu, and G. Van Tendeloo, *Applied Physics Letters* **102**, 212902 (2013).
- [124] M. A. Majidi, E. Thoeng, P. K. Gogoi, F. Wendt, S. H. Wang, I. Santoso, T. C. Asmara, I. P. Handayani, P. H. M. van Loosdrecht, A. A. Nugroho, M. Rübhausen, and A. Rusydi, *Physical Review B* **87**, 235135 (2013).
- [125] F. Masee, S. de Jong, Y. Huang, W. K. Siu, I. Santoso, A. Mans, A. T. Boothroyd, D. Prabhakaran, R. Follath, A. Varykhalov, L. Patthey, M. Shi, J. B. Goedkoop, and M. S. Golden, *Nature Physics* **7**, 978 (2011).
- [126] E. Dagotto, *Science* **309**, 257 (2005).
- [127] Y. Tokura, *Reports on Progress in Physics* **69**, 797 (2006).
- [128] D. Polli, M. Rini, S. Wall, R. W. Schoenlein, Y. Tomioka, Y. Tokura, G. Cerullo, and A. Cavalleri, *Nature Materials* **6**, 643 (2007).
- [129] H. Ichikawa, S. Nozawa, T. Sato, A. Tomita, K. Ichiyangi, M. Chollet, L. Guerin, N. Dean, A. Cavalleri, S.-i. Adachi, T.-h. Arima, H. Sawa, Y. Ogimoto, M. Nakamura, R. Tamaki, K. Miyano, and S.-y. Koshihara, *Nature Materials* **10**, 101 (2011).
- [130] V. Kiryukhin, D. Casa, J. P. Hill, B. Keimer, A. Vigliante, Y. Tomioka, and Y. Tokura, *Nature* **386**, 813 (1997).
- [131] B. Raveau, A. Maignan, and C. Martin, *Journal of Solid State Chemistry* **130**, 162 (1997).
- [132] A. Asamitsu, Y. Tomioka, H. Kuwahara, and Y. Tokura, *Nature* **388**, 50 (1997).
- [133] K. X. Jin, C. L. Chen, S. G. Zhao, and Z. M. Song, *Journal of Materials Science* **41**, 3881 (2006).



- [134] W. Prellier, P. Lecoeur, and B. Mercey, *Journal of Physics: Condensed Matter* **13**, R915 (2001).
- [135] A.-M. Haghiri-Gosnet and J.-P. Renard, *Journal of Physics D: Applied Physics* **36**, R127 (2003).
- [136] A. J. Millis, T. Darling, and A. Migliori, *Journal of Applied Physics* **83**, 1588 (1998).
- [137] T. Elovaara, S. Majumdar, H. Huhtinen, and P. Paturi, *Advanced Functional Materials* **25**, 5030 (2015).
- [138] Z. J. Yue, K. Zhao, H. Ni, S. Q. Zhao, Y. C. Kong, H. K. Wong, and A. J. Wang, *Journal of Physics D: Applied Physics* **44**, 095103 (2011).
- [139] H. Yada, Y. Ijiri, H. Uemura, Y. Tomioka, and H. Okamoto, *Physical Review Letters* **116**, 076402 (2016).
- [140] M. Scherff, J. Hoffmann, B. Meyer, T. Danz, and C. Jooss, *New Journal of Physics* **15**, 103008 (2013).
- [141] Z. G. Sheng, M. Nakamura, W. Koshibae, T. Makino, Y. Tokura, and M. Kawasaki, *Nature Communications* **5**, 4584 (2014).
- [142] Z. G. Sheng, B. C. Zhao, W. H. Song, Y. P. Sun, J. R. Sun, and B. G. Shen, *Applied Physics Letters* **87**, 242501 (2005).
- [143] C. Luo, K. X. Jin, C. L. Chen, and T. Wu, *Applied Physics Letters* **103**, 212401 (2013).
- [144] T. Meyer, B. Kressdorf, V. Roddatis, J. Hoffmann, C. Jooss, and M. Seibt, *Small Methods* **5**, 2170042 (2021).
- [145] S. Mokkaapati and K. R. Catchpole, *Journal of Applied Physics* **112**, 101101 (2012).
- [146] H. A. Atwater and A. Polman, *Nature Materials* **9**, 205 (2010).
- [147] S. Rajpurohit, C. Jooss, and P. E. Blöchl, *Physical Review B* **102**, 1 (2020).
- [148] K. Miyano, T. Tanaka, Y. Tomioka, and Y. Tokura, *Physical Review Letters* **78**, 4257 (1997).

- [149] P. Beaud, A. Caviezel, S. O. Mariager, L. Rettig, G. Ingold, C. Dornes, S.-W. Huang, J. A. Johnson, M. Radovic, T. Huber, T. Kubacka, A. Ferrer, H. T. Lemke, M. Chollet, D. Zhu, J. M. Glowina, M. Sikorski, A. Robert, H. Wadati, M. Nakamura, M. Kawasaki, Y. Tokura, S. L. Johnson, and U. Staub, *Nature Materials* **13**, 923 (2014).



## Author Contribution

In this Chapter the contribution of the authors to the articles presented in Chapter 4 – 6 of this thesis are clarified. All articles present original research by the authors.

### Chapter 4

B. Kressdorf, T. Meyer, A. Belenchuk, O. Shapoval, M. ten Brink, S. Melles, U. Ross, J. Hoffmann, V. Moshnyaga, M. Seibt, P. Blöchl, C. Jooss, "*Room-Temperature Hot-Polaron Photovoltaics in the Charge-Ordered State of a Layered Perovskite Oxide Heterojunction*", Phys. Rev. Applied **14**, 054006 (2020)

As the first author B.K. supplied a main contribution to the physical interpretations of the individual experiments as well as data analysis in order to develop an overall unified scientific concept and interpretation.

The manuscript draft was prepared by B.K. in collaboration with J.H. and C.J. and revision of the draft by M.S., P.E.B., V.M. and A.B.. All authors read and agreed on the written paper and declare no conflict of interest.

The thin films prepared by means of MAD were prepared by A.B. and O.S. under supervision of V.M. and the IBS thin films were prepared by B.K. and S.M. Optical, XRD and photovoltaic measurements were performed by B.K. TEM measurements were collected by U.R. and T.M. and the simulation for the density of states were done by M.t.B. under supervision of P.E.B.. The transport measurements were performed by S.M and the analysis was conducted by B.K. and J.H. under revision by V.M. and C.J..

### Chapter 5

B. Kressdorf, T. Meyer, M. ten Brink, C. Seick, S. Melles, N. Ottinger, T. Titze, H. Meer, A. Weisser, J. Hoffmann, S. Mathias, H. Ulrichs, D. Steil, M. Seibt, P. E. Blöchl, C. Jooss, "*Orbital-order phase transition in  $\text{Pr}_{1-x}\text{Ca}_x\text{MnO}_3$  probed by photovoltaics*", Phys. Rev. B **103**, 235122 (2021)

B.K. brought together the different experiments to create a unified overall picture of scientific questions raised in the article. Therefore, B.K. was involved in the interpretation of all data and has made a major contribution to the development overall concept and scientific interpretation.

This article is the result of a fruitful collaboration between many authors and different groups. The idea and interpretation behind the publication has been developed in joint cooperation between B.K., J.H., C.J., T.M., M.S., M.t.B. and P.E.B.. The introduction and discussion section of the manuscript were prepared in collaboration of C.J., P.B., B.K. and under revision by M.S..

B.K. prepared the thin films for all measurements except for one thin film for transport measurements as well as the powder for the temperature dependent XRD measurements. The optical, photovoltaic and XRD measurements were carried out by B.K. and B.K. prepared the overall draft of the manuscript in collaboration with J.H. and C.J.; specifically the sections for characterization, photovoltaic, transport, magnetic, optical and temperature dependent structure.

T.M. contributed the TEM measurements and structural simulations/calculations as well as contributed the corresponding sections to the manuscript. The tight-binding DFT calculations and simulations for the orbital order parameter were done by M.t.B. under supervision P.B.. Additionally M.t.B. contributed the corresponding sections to the manuscript under revision by P.E.B..

The transient pump probe measurements were performed by T.T., A.W., D.S. under supervision of S.M and the accompanying temperature model simulations were contributed by H.U.. The corresponding sections of the manuscript were written by H.U. and D.S. under revision by S.M. and C.J.. The magnetic property measurements were performed by C.S. and the analysis was conducted in collaboration with C.S., J.H. and B.K.. The electrical measurements as well as the film preparation for this measurement were performed by S.M. and the corresponding analysis was done in collaboration of S.M. and J.H. The temperature dependent XRD measurements and first data preparation was contributed by N.O. and the detailed analysis of XRD data was done by J.H. and B.K.. All authors read and agreed on the written paper and declare no conflict of interest.

## Chapter 6

B. Kressdorf, J. Hoffmann, M. Seibt, C. Jooss, *Power Density and Spectral Photovoltaic Response in a Hot Polaron Solar Cell*, to be published

B. K. performed all measurements and data analysis for the article and has made a major contribution in the development of the scientific concept as well as the physical interpretation of the results. The manuscript was prepared in collaboration with J.H. and C.J. and under revision by M.S..



## List of abbreviations

CER	colossal electroresistance
CMR	colossal magnetoresistance
CO	charge order
CT	charge transfer
DOS	density of states
EELS	electron energy loss spectroscopy
$E_g$	band gap
$E_{ph}$	photon energy
IBS	ion beam sputtering
$J_{sc}$	short circuit current density
JT	Jahn–Teller
MAD	metal aerosol deposition
OO	orbital order
PV	photovoltaic
PCMO	$Pr_{1-x}Ca_xMnO_3$
RP	Ruddlesden-Popper
RP PCMO	$Pr_{0.5}Ca_{1.5}MnO_4$
SEM	scanning electron microscope
STO	$SrTiO_3$
STNO	$Nb$ doped $SrTiO_3$
TEM	transmission electron microscope
$T_{CO}$	charge order transition temperature
$T_N$	Néel temperature
$U_{oc}$	open circuit voltage
XRD	X-ray diffraction





## Danksagung

An dieser Stelle möchte ich allen Personen danken, die mich im Laufe meiner Promotion sowie bei der Anfertigung meiner Doktorarbeit unterstützt haben.

Mein besonderer Dank gilt Prof. Dr. Christian Jooß für die ausgezeichnete Betreuung, das Bereitstellen eines überaus spannenden Themas und den kompetenten Rat bei der Durchführung der gesamten Arbeit. Ich möchte an dieser Stelle die Gelegenheit ergreifen und mich für die Begleitung und die fortwährende Unterstützung auf meinem wissenschaftlichen Werdegang von Bachelor bis zur Doktorarbeit bedanken.

Für viele fruchtbare Gespräche und die stete Hilfsbereitschaft danke ich Prof. Dr. Michael Seibt, der meine Doktorarbeit als zweiter Gutachter betreut hat, vielmals.

Ein besonderer Dank geht an Dr. Jörg Hoffmann, der für meine großen und kleinen Probleme immer ein offenes Ohr hatte und mir stets mit Rat und Tat zur Seite stand. Ich bedanke mich herzlich für die tatkräftige Unterstützung, für die vielen Stunden, die wir gemeinsam diskutiert haben sowie für seine aufbauenden Worte.

Außerdem möchte ich mich bei Prof. Dr. Peter Blöchl bedanken, der mich auf meinem Weg mit Rat und vielen produktiven Gesprächen begleitet hat. Ich bedanke mich für die Geduld und die Bereitschaft, einem Experimental-Physiker theoretische Konzepte zu erläutern.

Weiterhin gilt mein Dank Prof. Dr. Vasily Moshneyaga für die hilfreiche Unterstützung und die Zusammenarbeit bei der Herstellung der Ruddlesden-Popper PCMO Filme. Ich danke für viele anregende Diskussionen zum Thema der Filmherstellung mit MAD, PLD und IBS.

Des Weiteren danke ich meiner gesamten Prüfungskommission.

Hier möchte ich mich insbesondere bei meinem Projektpartner Tobias Meyer für die geniale Zusammenarbeit und die vielen gemeinsamen Vorträge bedanken und darüber hinaus danke ich dem gesamten B02 Team Benne Iland, Stephan Melles und Christoph Flathmann.

Ich möchte nicht versäumen, meiner aktuellen sowie der ehemaligen Arbeitsgruppe für die angenehme und hilfsbereite Arbeitsatmosphäre zu danken. Hier gilt mein besonderer Dank Max Baumung und Frederik Stender für die herzlichen Gespräche bei einem Kaf-

fee und für die Aufmunterungen, wenn es mal nicht so lief. Für die vielen förderlichen Ratschläge und spannenden Gespräche, auch außerhalb der Wissenschaft, danke ich Sarah Hoffmann-Urlaub.

Für die finanzielle Unterstützung danke ich der DFG / SFB 1073. Ich danke dem gesamten Institut für Materialphysik für die gemeinsamen Aktivitäten und Ausflüge. Für vielfältige Unterstützung bei den Experimenten bin ich besonders Lutz Kirchhof, Michael Malchow und Conni Mewes verbunden. Des Weiteren möchte ich mich bei allen Co-Autoren der Veröffentlichungen für die produktive Zusammenarbeit und für die konstruktiven Anregungen bedanken.

Meiner Familie und meinen Freunden danke ich für ihre Geduld, Ermutigung und Unterstützung während der Arbeit an dieser Doktorarbeit.

Ich möchte mich insbesondere auch bei allen bedanken, die mich in den letzten Wochen des Zusammenschreibens auf die verschiedenste Art und Weise unterstützt haben. Schließlich möchte ich allen anderen, die mich bei der Erstellung dieser Dissertation auf unterschiedlichste Weise unterstützt haben und die hier ungenannt bleiben, für die erwiesene Hilfe danken.